

Topics in Current Chemistry Collections

Rüdiger-A. Eichel *Editor*

Electrochemical Energy Storage

Next Generation Battery Concepts

 Springer

Topics in Current Chemistry Collections

Journal Editors

Massimo Olivucci, Siena, Italy and Bowling Green, USA

Wai-Yeung Wong, Hong Kong, China

Series Editors

Hagan Bayley, Oxford, UK

Greg Hughes, Codexis Inc, USA

Christopher A. Hunter, Cambridge, UK

Seong-Ju Hwang, Seoul, South Korea

Kazuaki Ishihara, Nagoya, Japan

Barbara Kirchner, Bonn, Germany

Michael J. Krische, Austin, USA

Delmar Larsen, Davis, USA

Jean-Marie Lehn, Strasbourg, France

Rafael Luque, Córdoba, Spain

Jay S. Siegel, Tianjin, China

Joachim Thiem, Hamburg, Germany

Margherita Venturi, Bologna, Italy

Chi-Huey Wong, Taipei, Taiwan

Henry N.C. Wong, Hong Kong, China

Vivian Wing-Wah Yam, Hong Kong, China

Chunhua Yan, Beijing, China

Shu-Li You, Shanghai, China

Aims and Scope

The series *Topics in Current Chemistry Collections* presents critical reviews from the journal *Topics in Current Chemistry* organized in topical volumes. The scope of coverage is all areas of chemical science including the interfaces with related disciplines such as biology, medicine and materials science.

The goal of each thematic volume is to give the non-specialist reader, whether in academia or industry, a comprehensive insight into an area where new research is emerging which is of interest to a larger scientific audience.

Each review within the volume critically surveys one aspect of that topic and places it within the context of the volume as a whole. The most significant developments of the last 5 to 10 years are presented using selected examples to illustrate the principles discussed. The coverage is not intended to be an exhaustive summary of the field or include large quantities of data, but should rather be conceptual, concentrating on the methodological thinking that will allow the non-specialist reader to understand the information presented.

Contributions also offer an outlook on potential future developments in the field.

More information about this series at <http://www.springer.com/series/14181>

Rüdiger-A. Eichel
Editor

Electrochemical Energy Storage

Next Generation Battery Concepts

With contributions from

Philipp Adelhelm • Isidora Cekic-Laskovic • Helmut Ehrenberg
Yair Ein-Eli • Christian Friebe • Danny Gelman • Laura Imholt
Serife Kaymaksiz • Karin Kleiner • Lukas Medenbach
Kristina Oldiges • Babak Razaee Rad • Ulrich S. Schubert
Boris Shvartsev • Martin Winter • Natascha von Aspern

 Springer

Editor

Rüdiger-A. Eichel
Forschungszentrum Jülich GmbH
Institut für Energie- und Klimaforschung (IEK-9)
D-52425 Jülich
Germany

Partly previously published in *Top Curr Chem (Z)* Volume 374 (2016), *Top Curr Chem (Z)* Volume 375 (2017)

ISSN 2367-4067
Topics in Current Chemistry Collections
ISBN 978-3-030-26128-3

© Springer Nature Switzerland AG 2019

This work is subject to copyright. All rights are reserved by the Publisher, whether the whole or part of the material is concerned, specifically the rights of translation, reprinting, reuse of illustrations, recitation, broadcasting, reproduction on microfilms or in any other physical way, and transmission or information storage and retrieval, electronic adaptation, computer software, or by similar or dissimilar methodology now known or hereafter developed.

The use of general descriptive names, registered names, trademarks, service marks, etc. in this publication does not imply, even in the absence of a specific statement, that such names are exempt from the relevant protective laws and regulations and therefore free for general use.

The publisher, the authors, and the editors are safe to assume that the advice and information in this book are believed to be true and accurate at the date of publication. Neither the publisher nor the authors or the editors give a warranty, express or implied, with respect to the material contained herein or for any errors or omissions that may have been made. The publisher remains neutral with regard to jurisdictional claims in published maps and institutional affiliations.

This Springer imprint is published by the registered company Springer Nature Switzerland AG
The registered company address is: Gewerbestrasse 11, 6330 Cham, Switzerland

Contents

Preface	vii
Synergistic Effect of Blended Components in Nonaqueous Electrolytes for Lithium Ion Batteries	1
Isidora Cekic-Laskovic, Natascha von Aspern, Laura Imholt, Serife Kaymaksiz, Kristina Oldiges, Babak Razaei Rad and Martin Winter: Top Curr Chem (Z) 2017, 2019:37 (15, March 2017) DOI 10.1007/s41061-017-0125-8	
High-Power-Density Organic Radical Batteries	65
Christian Friebe and Ulrich S. Schubert: Top Curr Chem (Z) 2017, 2019:19 (1, February 2017) DOI 10.1007/s41061-017-0103-1	
Cell Concepts of Metal–Sulfur Batteries (Metal = Li, Na, K, Mg): Strategies for Using Sulfur in Energy Storage Applications	101
Lukas Medenbach and Philipp Adelhelm: Top Curr Chem (Z) 2017, 2019:81 (29, September 2017) DOI 10.1007/s41061-017-0168-x	
Challenges and Prospect of Non-aqueous Non-alkali (NANA) Metal–Air Batteries	127
Danny Gelman, Boris Shvartsev and Yair Ein-Eli: Top Curr Chem (Z) 2016, 2019:82 (22, November 2016) DOI 10.1007/s41061-016-0080-9	
Challenges Considering the Degradation of Cell Components in Commercial Lithium-Ion Cells: A Review and Evaluation of Present Systems	169
Karin Kleiner and Helmut Ehrenberg: Top Curr Chem (Z) 2017, 2019:54 (3, May 2017) DOI 10.1007/s41061-017-0139-2	

Preface

Isidora Cekic-Laskovic¹ and Martin Winter^{1,2}

Electrochemical energy storage in batteries has been recognized as the most promising technology for portable electronics as well as stationary and (auto-)motive applications. Although often perceived and applied as a simple electrochemical device, batteries are inherently complex and dynamic systems. Existing technologies still face performance and cost challenges, including barriers in specific energy, energy density, service life and energy efficiency at high rates. A proper selection of a battery system involves comparison with a set of goals, which pull in different directions, but need to be fulfilled simultaneously. The energy and power performance goals need to be well-balanced against the goals of long life and safety. The overall performance of battery cells is limited by the fundamental behavior of the used materials, including electrode active materials, electrolytes, separators and other supporting components. In addition, successful operation of batteries relies significantly on a series of interrelated mechanisms, some involving instability of the constituting components induced by charge/discharge cycles and some also encompassing formation/reaction of metastable phases. With this in line, the ability to achieve long-term stability requires careful elucidation of the physical and chemical processes governing charge/discharge cycling and storage. The key performance requirements of a battery for different applications might look very similar at first sight, however, each application calls for different requirement prioritization. Frequently, they conflict with one another and call for inevitable trade-offs. The objective of advanced battery research and development relates to obtaining the best compromise among the goals, followed by a decision whether the balanced system should be implemented instead of a competing technology.

¹ Helmholtz Institute Münster, IEK-12, Forschungszentrum Jülich GmbH, 48149 Münster, Germany

² Westfälische Wilhelms-Universität Münster, MEET Battery Research Center, Institute of Physical Chemistry, 48149 Münster, Germany

This topical collection is devoted to research and development stages of four different battery systems, namely lithium ion battery, non-aqueous non-alkali metal/air battery, metal/sulfur battery and organic radical battery, highlighting main advantages and limitations thereof. In this spirit, the topical collection comprises contributions from five research teams, connected by a unifying theme of batteries as advanced electrochemical energy storage systems. Each contribution provides a profound example of a given battery chemistry, its performance suitable for specific application and main remaining challenges still left unresolved.

The first contribution on specific aspects of non-aqueous electrolytes for lithium ion batteries (LIBs), highlights chemical and synergistic effects of blended electrolyte components (conducting salts, solvents/co-solvents and functional additives) and their relevant structural, physicochemical, electrochemical as well as safety properties tailoring the advanced performance of a battery through the ability of blended components to compensate/eliminate for each other's disadvantages.

In the second contribution, Friebe and Schubert comprehensively review organic radical batteries (ORBs), considered to be a high-power alternative to the benchmark Li-ion battery systems. In respect to materials developed so far, key properties, significant characteristics, housing approaches and applied additives, not neglecting the main drawbacks and limitations of these environmentally friendly energy storage systems of similar or higher charge capacity and similar or shorter charge time compared to LIB counterparts have been collected in this chapter.

Medenbach and Adelhelm set the focus on the complex electrochemistry of sulfur, different strategies enabling alternative lithium-, sodium-, potassium- and magnesium/sulfur cell concepts for energy storage applications and limitations hindering the further development and commercialization progress.

Ein-Eli and co-workers critically discuss main challenges and concerns hindering the scientific advance in the leading non-aqueous non-alkali (NANA) metal/air batteries, namely magnesium/air, aluminum/air, silicon/air and all-solid-state metal/air battery systems, pointing out to possible directions towards desired improvements that will positively affect the overall performance of these systems.

In the last contribution, Kleiner and Ehrenberg highlight the challenges and limitations related to the degradation processes of active and inactive components in commercial lithium ion batteries systems, stressing out the significance for understanding and evaluating the main factors, parameters and operation conditions leading to overall performance drop and increased safety risks.

It is our anticipation that this fine selection and collection of manuscripts will be a valuable resource for Topics in Current Chemistry Collections readers and will encourage further research into the promising field of advanced rechargeable batteries for diverse application possibilities. We would like to thank all who kindly contributed their manuscripts for this topical collection, Prof. Rüdiger A. Eichel for the selection and invitation of authors and the editorial office as well as the publishing and production teams of Topics in Current Chemistry for their assistance in the preparation and publishing processes.



Synergistic Effect of Blended Components in Nonaqueous Electrolytes for Lithium Ion Batteries

Isidora Cekic-Laskovic¹ · Natascha von Aspern¹ ·
Laura Imholt¹ · Serife Kaymaksiz¹ · Kristina Oldiges¹ ·
Babak Razaei Rad¹ · Martin Winter^{1,2}

Received: 29 November 2016 / Accepted: 21 February 2017 / Published online: 15 March 2017
© Springer International Publishing Switzerland 2017

Abstract Application of different electrolyte components as blends in nonaqueous electrolyte formulations represents a viable approach towards improving the overall performance and reliability of a lithium ion battery cell. By combining the advantages of different electrolyte constituents, cell chemistry can be optimized and tailored for a specific purpose. In this paper, the current progress on possibilities, advantages, as well as limitations of blended nonaqueous electrolyte formulations, including solvent, salt and additive blends is reviewed and discussed. Emphasis is set on the physicochemical, electrochemical, and safety aspects. In addition, the aim of this review is to provide perspective and possible strategy for further and future development of blended nonaqueous electrolytes with long life, high energy density, high power, and adequate safety at competitive manufacturing costs. The provided overview and perspective on blended nonaqueous electrolyte formulations should encourage researchers to proceed with further and deeper investigations in this promising field of advanced batteries.

Keywords Blends · Synergistic effect · Nonaqueous electrolytes · Electrolyte solvent · Conducting salt · Additive

Chapter 1 was originally published as Cekic-Laskovic, I., von Aspern, N., Imholt, L., Kaymaksiz, S., Oldiges, K., Rad, B. R. & Winter, M. Top Curr Chem (Z) (2017) 375: 37. DOI 10.1007/s41064-017-0125-8.

✉ Isidora Cekic-Laskovic
i.cekcic-laskovic@fz-juelich.de

¹ Helmholtz Institute Münster, IEK-12, Forschungszentrum Jülich GmbH, 48149 Münster, Germany

² MEET Battery Research Center, Institute of Physical Chemistry, Westfälische Wilhelms-Universität Münster, 48149 Münster, Germany

1 Introduction

Among a wide variety of different storage technologies for electric energy, electrochemical energy storage in batteries was recognized as the most promising for portable electronics, stationary and (auto-)motive applications [1]. Thanks to the high energy efficiency [2, 3] and outstanding scalability, batteries are key elements in all energy scenarios nowadays. Twenty-five years after the commercialization by Sony Corporation, lithium ion batteries (LIBs) have significantly improved in performance, reliability, as well as safety, thus representing an accustomed part of our everyday life [4].

The key performance requirements of a battery cell for different applications might look very similar at first sight; however, each application has different performance requirement priorities. The cycle life of a rechargeable battery cell is strongly influenced by the long-term reversibility of the redox reactions represented by the cell chemistry. The crucial factor maintaining this reversibility is related to chemical as well as electrochemical stability of the used electrolyte formulation. The nonaqueous electrolyte is the key component for the development of novel and improved cell chemistries, custom-tailored for the specific application. One of the crucial points for next-generation lithium batteries is associated with the development of high-performance electrolyte components, namely solvents, conducting salts, and additives in replacing the current state-of-the-art (SOTA) organic carbonate solvent-based [5] electrolyte formulations with lithium hexafluorophosphate (LiPF_6) as conducting salt [6]. These novel and improved electrolyte formulations should assure high ionic conductivity as well as high thermal and electrochemical stability, long-term stability vs. anode and cathode over a wide state of charge (SoC) range and lead to formation of effective solid electrolyte interphases (SEI) [7] and cathode electrolyte interphases (CEI). At the same time, the aforementioned (ideal) electrolyte components should be non-flammable, nontoxic and environmentally friendly (Fig. 1).

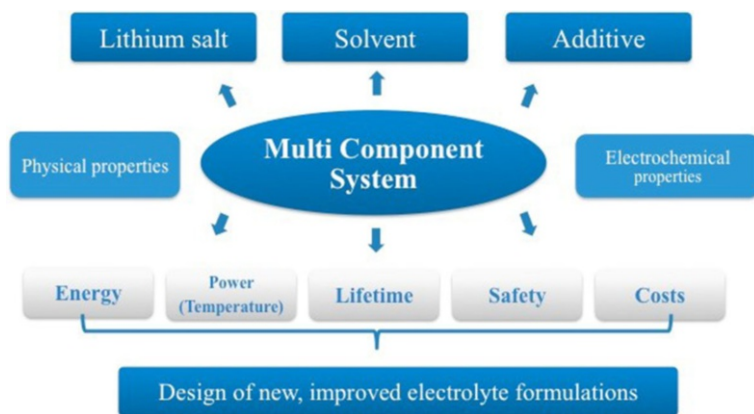


Fig. 1 Nonaqueous electrolyte as core and key component of a lithium ion battery (LIB) cell

One way in improving the SOTA nonaqueous electrolyte formulations is to synthesize and thoroughly characterize new electrolyte components to determine their physicochemical properties and electrochemical behavior. With this in line, the focus of many research activities is set on development of new electrolyte formulations through new solvents, new salts, or on modifying conventional systems with adequate electrolyte additives. However, functionalities with the beneficial impact on the cell performance are usually obtained at the cost of other characteristics. For this reason, blends containing at least two chemical substances with different molecular structures of the same electrolyte component (solvent, salt, and additive) can be used.

The utilization of blended component electrolytes represents an alternative approach towards maximizing the performance of lithium ion cells by combining the advantages of each constituent. The synergy between two or more different solvents, conductive salts or various additives, as a blend in an electrolyte formulation, has the potential to significantly contribute to the desired advancements of the lithium ion technology. In this regard, blends of electrolyte components selected in adequate amounts, perform complementary functions to each other. By definition, a synergistic effect arises from the interaction between two or more substances, agents, entities or factors that produces an effect greater than the sum of the individual ones. Taking the term synergy as a word to its roots, “syn” has the meaning of together whereas “ergon” means work. A strong synergistic effect of properly selected components may have a positive outcome on the overall performance, as blending of ‘right’ electrolyte components enhances the physicochemical, thermal, as well as electrochemical properties of all of them. In this regard, a mixture of high dielectric solvents (HDS—solvate ions and favor salt dissociation, but highly viscous) and a low viscosity (LVS—facilitate ion transport, low permittivity) solvents used in common SOTA electrolytes is a well-known example of the synergistic effect influencing the ionic conductivity of the electrolyte. This important measure of the conductivity through ionic charge carriers, which determines internal resistance and electrochemical behavior of the cell, is dependent on the nature as well as on the ratio of the solvents in the electrolyte system. In order to reach the maximum ionic conductivity, an optimum HDS + LVS composition has to be identified (Fig. 2a). Beside properly selected solvent mixture in an electrolyte formulation, a Li salt (LiX) concentration plays an important role in maximizing the ionic conductivity. As depicted in Fig. 2b, at low salt concentrations, which is in solvent excess, the number of ions as charge carriers will be low. However, it will consequently increase with the increase of salt concentration until reaching a maximum at certain point. The location of this conductivity maximum is dependent on the dielectric constant of the solvent(s) used in the electrolyte as well as the temperature. In solvent-mixed electrolytes containing solvent with high dielectric constant or at higher temperatures at which electrolyte viscosity is decreased, the conductivity maximum will be shifted to higher LiX concentrations. After passing through a conductivity maximum, the number of free charge carriers as well as the ionic mobility will decrease with further increase of the LiX concentration, due to the intense ion pair formation and

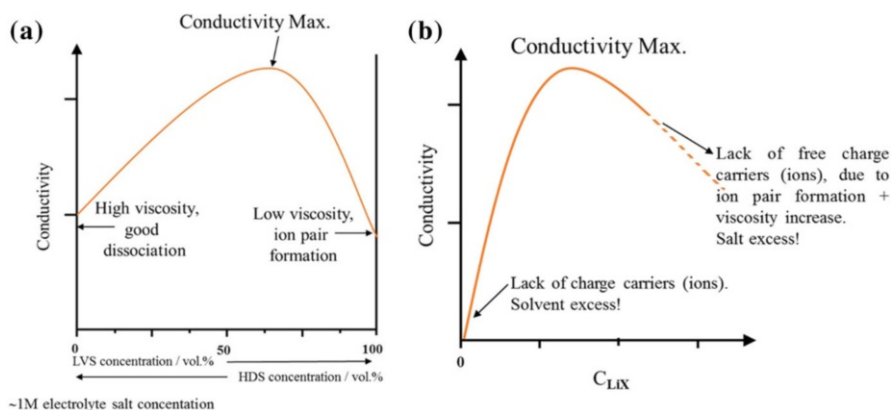


Fig. 2 Ionic conductivity dependency on concentration of **a** HDS and LVS in mixed electrolyte solution and **b** lithium salt [8]

higher viscosity of the electrolyte formulation. At very high LiX concentrations, the salt may even precipitate.

This survey aims to highlight the opportunities and perspectives of nonaqueous electrolyte formulations containing different classes of solvents, salts and additives as blends in LIB cells, without neglecting their limitations.

2 Solvent Blends in Nonaqueous Electrolytes

Despite the fact that the organic carbonate-based nonaqueous electrolyte is the most suitable choice for graphite-based LIBs due to formation of an effective SEI layer on the graphite surface, the safety problems at only moderately elevated temperatures (>40 °C) are a matter of concern for industry as well as for consumers [9, 10]. Furthermore, the electrochemical stability of the SOTA organic carbonate solvent-based electrolyte limits the high-voltage operation, required for high-energy LIBs in electric vehicles to extend energy density and driving range. Thus, there is an unmet need for development of alternative electrolyte formulations with higher electrochemical stabilities and improved safety properties [11]. A possible solution for substituting carbonate-based solvents refers to selection of other classes of compounds. Among them, nitriles and ionic liquids (ILs), showed significant potential due to their thermal stability over a broad temperature range, wide electrochemical stability window (ESW) and in case of the ILs and many (but not all) nitriles, negligible vapor pressure [12–17]. In recent years, mono- and dinitriles received considerable attention as promising solvents for LIB electrolytes [18, 19]. Due to the high thermal and good anodic stabilities, especially in domain of high-voltage operation, special focus was set on dinitriles, such as glutaronitrile (GLN), adiponitrile (ADN), or sebaconitrile (SEN). The importance of the solvent flash point was emphasized by Wrodnigg et al. [20] as early as 1999. Abu-Lebdeh et al. [15, 16] and Nagahama et al. [17] proposed GLN, ADN, and SEN as possible

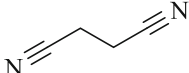
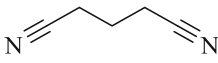
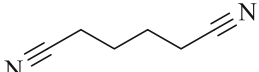
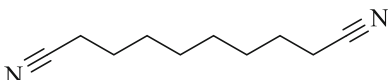
solvents for electrolytes in LIBs. Among them, GLN and ADN were recognized as the most attractive candidates owing to the highest values of boiling and flash points, highest dielectric constants and lowest viscosities. However, nitriles as in single solvent electrolytes resulted in a low ionic conductivity (3.6 mS cm^{-1} for GLN and 1.8 mS cm^{-1} for ADN at $25 \text{ }^\circ\text{C}$) and are incompatible with graphite, as shown by Li et al. [21]. Abu-Lebdeh et al. [15] revealed that ADN as single solvent, either with lithium bis(trifluoromethylsulfonyl)imide (LiTFSI) alone or together with the SEI-promoting additive, lithium bis(oxalato)borate (LiBOB), led to only limited capacities in graphite/LiCoO₂ (LCO) full cells. Moreover, the melting points were too high for battery applications. The drawbacks of using nitriles as single solvents in LIB cells clearly indicated that for better battery performance, blending is required. Besides nitriles, systematic research on the application of ILs as electrolyte solvents in energy storage devices was increased in recent years. The most popular cations of room temperature ionic liquids (RTILs) are quaternary ammonium-based such as tetraalkylammonium, aromatic cyclic amines (pyridinium, imidazolium) and saturated cyclic amines (pyrrolidinium, piperidinium), whereas the most used counter anions refer to non-coordinating anions such as [B(CN)₄], bis(trifluoromethylsulfonyl)imide (TFSI) and bis(fluorosulfonyl)imide (FSI)—very large anions with small charge to radius ratios. This leads to weaker electrostatic bonding between cation and anion as well as to lower melting points. Low lithium ion mobility, which is a direct consequence of the higher viscosity of RTILs, is in fact, one of the main obstacles in performance of LIBs using RTIL-based electrolytes [22, 23].

2.1 Nitrile-Based and Ionic Liquid-Based Solvent Blends

2.1.1 Aim of Solvent Blending

As listed in Table 1, the melting points of the dinitriles $\text{CN}(\text{CH}_2)_n\text{CN}$ with $n = 2, 3, 4, 8$ follow no regularity and the values for succinonitrile (SCN), ADN and SEN are

Table 1 Melting and flash point values of selected dinitriles $\text{CN}(\text{CH}_2)_n\text{CN}$ with $n = 2, 3, 4, 8$

Name	$\text{CN}(\text{CH}_2)_n\text{CN}$ $n =$	Structural formula	Melting point ($^\circ\text{C}$)	Flash point ($^\circ\text{C}$)
Succinonitrile	2		50–54 [23]	113 [23]
Glutaronitrile	3		–29 [22]	113 [22]
Adiponitrile	4		1–3 [21]	163 [21]
Sebaconitrile	8		7–8 [24]	>113 [24]

in the positive range, limiting their performance at low temperatures. For this reason, blending nitriles with other solvents enables the utilization of nitriles for LIB application.

Ethylene carbonate (EC), a cyclic carbonate which is present in conventional carbonate-based electrolytes in LIBs, has a high melting point (35–38 °C [25]) and can therefore not be used as single solvent at room temperature. Blending of EC and nitrile led to a binary eutectic blend with a lower melting point [≈ -60 °C for EC/ acetonitrile (ACN)] [26]. It is well known that the linear carbonates, e.g., dimethyl carbonate (DMC) and EC also form an eutectic blend with a lower melting point [27]. The addition of a nitrile to the carbonate blend generates a ternary eutectic blend. Based on the EC/DMC/ACN blends, Cho et al. showed that by using ≈ 60 vol% ACN and ≈ 40 vol% EC or EC/DMC (1:1 v/v), the eutectic point can be attained [26]. Moreover, the eutectic point at ≈ -60 °C could be reached with a binary or a ternary blend. The phase diagram, shown in Fig. 3c, was generated by plotting the temperatures of the endothermic peaks versus volume fraction of EC/ DMC obtained from the differential scanning calorimetry (DSC) thermograms (Fig. 3a, b).

A single solvent nitrile system most often fails to fulfill major demands for the commercial applications. An exception was constituted by a single-solvent electrolyte based on cyanoesters which combined adequate electrochemical performance with improved safety [28]. Nevertheless, blending of several solvents brings multifunctional solution to electrolyte formulation. Nitriles have high boiling and flash points, whereas conventional carbonate-based solvents suffer from relatively lower boiling and flash points; thus their high flammability is an issue, which endangers safe operation of a LIB. For this reason, blending represents a promising way to improve the safety of nonaqueous electrolyte formulations. Additionally, a solvent blend containing nitrile and carbonate has a reduced viscosity due to the low viscosities of nitriles. In such solvent blend, carbonates take

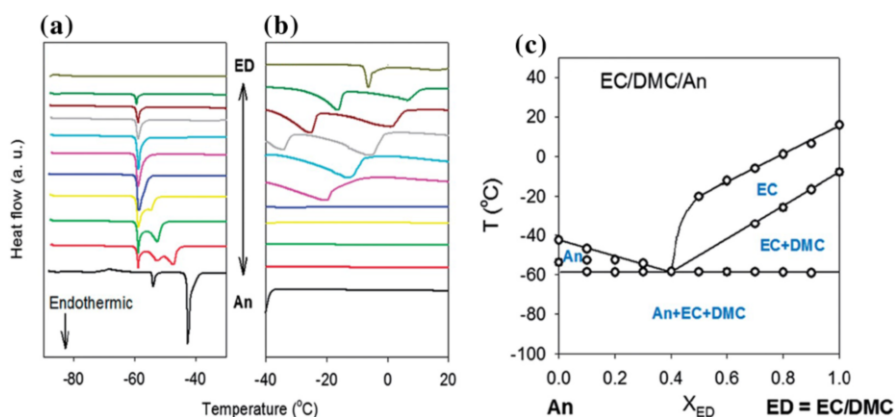
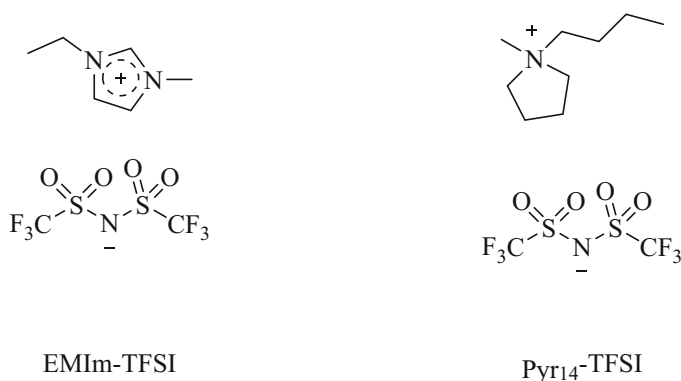


Fig. 3 Thermograms for ACN/EC/DMC solvent blends measured by DSC. Endothermic heat flow is downward (a, b). Heat flow was normalized in b to clarify the peaks. c Resulting phase diagram, ED = EC/DMC (1:1 v/v). X_{ED} = volume fraction of ED. Reprinted from Ref. [26]. Copyright (2014) with permission of Royal Society of Chemistry



Scheme 1 Molecular structures of 1-ethyl-3-methylimidazolium bis(trifluoromethylsulfonyl)imide (EMIm-TFSI) and *N*-butyl-*N*-methylpyrrolidinium bis(trifluoromethylsulfonyl)imide (Pyr₁₄⁺-TFSI)

over the task related to the formation of an effective SEI and make the electrolyte more conductive. This leads to an assumption that nitriles and carbonates complement each other, thus resulting in a better electrochemical performance.

To clarify the effect of RTILs on the safety of LIBs, Guerfi et al. investigated the flammability of RTILs and carbonate solvent blends [29]. They prepared several electrolyte blends of the IL 1-ethyl-3-methylimidazolium bis(trifluoromethylsulfonyl)imide (EMIm-TFSI, Scheme 1) and 1 M LiPF₆ in EC/diethyl carbonate (DEC) (1:1 by wt.) containing 2% vinylene carbonate (VC), with different concentrations of RTIL. The electrolyte with 100% organic carbonate started to burn in the first second of ignition, whereas in pure RTIL, no combustion occurred even after 20 s of flame exposure. The flame exposure time was increased with addition of EMIm-TFSI to the carbonate-based electrolyte. The flammability of the blended electrolyte was prevented by addition of 40% or more EMIm-TFSI. An optimum composition for better battery performance (low viscosity and high conductivity) and higher safety (no flammability) was proposed with 40–60% EMIm-TFSI.

Arbizzani et al. carried out flammability studies in blends composed of 1 M LiPF₆ in EC/DMC (1:1 by wt.) as carbonate-based electrolyte and various concentrations of the *N*-butyl-*N*-methylpyrrolidinium bis(trifluoromethylsulfonyl)imide (Pyr₁₄⁺-TFSI, Scheme 1) with a slightly different setup (Fig. 2) [30]. A glass fiber mat (Whatman, GF/F) was soaked with the investigated electrolyte blends and exposed to the flame placed at a distance of 123 mm from the top of the burner tube so that the ignition was only due to the temperature increase. The flame was turned on for 5 s.

Each sample was measured six times and the average value ($\approx 10\%$ error) of the self-extinguishing time (SET) was used. Table 2 lists the reproducibility data of the ignition occurrence as an indication of the flame inhibition effect of different electrolyte blends. At least 30 wt% RTIL should be added to a carbonate-based electrolyte in order to observe the flame-inhibition effect. With addition of more than 50 wt%, the tendency to ignite was significantly reduced. Considering the

Table 2 Ignition occurrence and the mean values of the SET of several blends of 1 M LiPF₆ in EC/DMC (1:1 by wt.) and Py_rF₁₄-TFSI. Reprinted from Ref. [30]. Copyright (2011) with permission of Elsevier

Py _r F ₁₄ -TFSI (wt%)	Ignition occurrence	SET (s g ⁻¹)
0	6/6	55
10	6/6	67
30	4/6	109
50	2/6	125
70	2/6	127
100	0/6	–

major safety problems of carbonate-based electrolytes as well as certain unfavorable physicochemical properties (melting point and viscosity) of single solvent electrolytes containing nitriles and RTILs, blending of carbonate solvents with nitriles or RTILs could be a solution to overcome afore-described drawbacks.

2.2 Effect of Blending on Physicochemical Features

In order to formulate an electrolyte with a higher flash point and at least steady electrochemical performance, Isken et al. [31] mixed EC with ADN in 1:1 (by wt.) ratio. The flash point of this blend was found to be more than 110 °C higher than blends of EC with a linear carbonate like DMC or DEC. Furthermore, the vapor pressure of such blend is much lower and has a positive effect on the safety of cells.

Duncan et al. [32] revealed viscosity values of 1 M LiTFSI in pure dinitrile to be much higher than in the binary solvents EC/dinitrile (1:1 v/v) at room temperature. Due to the fact that LiBOB as co-salt leads to very good cycling performance, the authors used the ternary solvent blend containing EC/DMC/dinitrile (1:1:2 v/v/v) in combination with a salt blend [1 M lithium tetrafluoroborate (LiBF₄) + 0.1 M LiBOB] to obtain the lowest viscosities (Fig. 4).

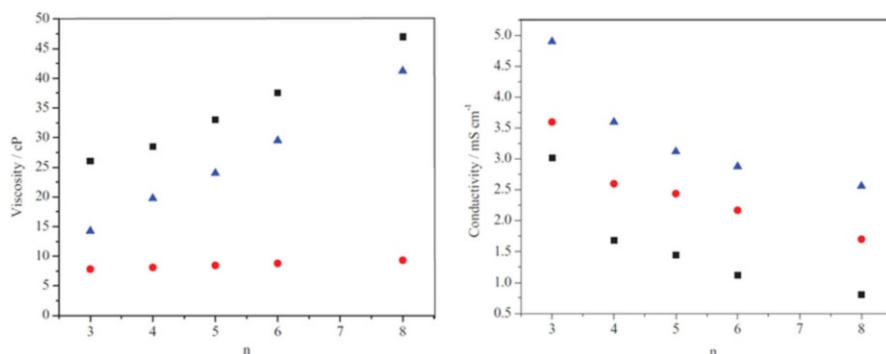


Fig. 4 Viscosity (left) and conductivity (right) values of 1 M LiTFSI in pure dinitrile (black filled square), 1 M LiTFSI in EC/dinitrile (1:1 v/v) (blue filled triangle) and 1 M LiBF₄, 0.1 M LiBOB in EC/DMC/dinitrile (1:1:2 v/v/v) (red filled square) at room temperature. Dinitriles with different chain lengths: NC-(CH₂)_n-CN with n = 3–8. Reprinted from Ref. [32]. Copyright (2013) with permission of ECS

It became apparent that a longer alkyl chain of the dinitrile gives rise to a higher viscosity of the electrolyte. The longer alkyl chain is related to a bigger molecular size, which leads to decreased mobility and conductivity. The electrolytes containing 1 M LiTFSI in a single dinitrile (NC-(CH₂)_n-CN with $n = 3-8$) showed the lowest conductivities whereas the investigated EC/dinitrile blends with 1 M LiTFSI revealed the highest conductivities. Furthermore, the conductivities of the electrolytes with binary solvent blends were higher than those with ternary solvent blends (1 M LiBF₄ + 0.1 M LiBOB in EC/DMC/dinitrile), although the last-named had the lowest viscosities. The reason behind this is associated with the fact that the ternary blend has a lower dielectric constant than the binary blend; and LiBF₄, as a different conducting salt, has a lower dissociation constant. As a result of weak salt dissociation, the ionic conductivity of the electrolyte significantly decreased.

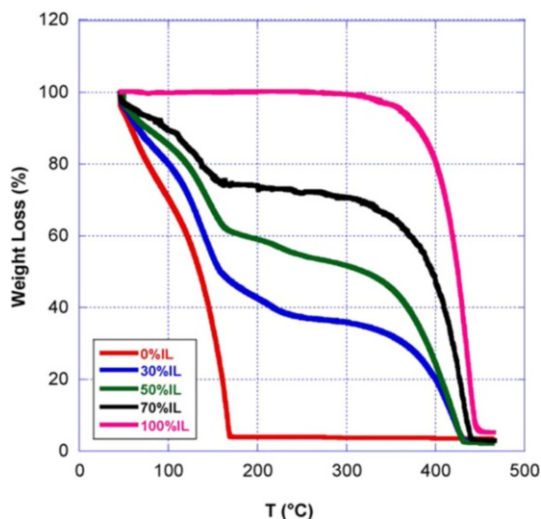
Abu-Lebdeh et al. [16] showed that addition of EC to GLN led to an increase in conductivity and to a decrease in viscosity. The temperature dependence as well as the dependence on the salt concentration of LiTFSI was found to be similar for both electrolytes. Increase in temperature resulted in higher conductivity values. At room temperature, the highest conductivity was reached with a 1 M solution of LiTFSI in EC/GLN (1:1 v/v) amounting to 4.9 mS cm⁻¹. Higher concentrations caused lower conductivities, most probably due to ion pairing or increased viscosity.

Isken et al. [31] revealed that a blend of 0.9 M LiBF₄ in EC/ADN (1:1 by wt.) showed better conductivities at room temperature compared to the 1 M LiBF₄ in EC/DEC (3:7 by wt.) electrolyte.

MacFarlane et al. [33] introduced pyrrolidinium-saturated cations [33] with higher cathodic stability on the graphite electrode as well as better interfacial behavior on lithium metal anodes. However, compared to imidazolium-based ILs, conductivity values were lower and viscosities higher. IL blends of electrolytes with carbonate-based solvents can tune the physicochemical and electrochemical properties of different types of RTILs to achieve better performance in the cell. The carbonate solvents could improve the SEI formation capability of the blended electrolytes and in the same time increase the conductivity. Many groups investigated the improvements in conductivity of solvent blended electrolytes and the obtained results pointed out the positive effect of carbonate solvents on reducing the viscosities and improving the conductivities [29, 34].

Thermal stability of the nonaqueous electrolytes is the key to better performance of the battery cell as internal heat is always produced during charge and discharge. As mentioned above, SOTA electrolytes suffer from low thermal stability of LiPF₆ and organic carbonate-based solvents. The thermal decomposition of organic electrolytes as well as blended electrolytes with RTILs was investigated by many groups [29, 30, 35–37]. The general conclusion of these investigations was that the addition of RTILs to the carbonate-based electrolytes have positive effects on the thermal stability of electrolyte blends, but the presence of the RTIL cannot stop the thermal decomposition of LiPF₆ and the carbonate molecules. Guerfi et al. investigated the thermal stability of the pure solvent and solvent blended electrolytes by means of thermogravimetric analysis (TGA) as depicted in Fig. 5 [29].

Fig. 5 Thermogravimetric analysis of 1 M LiPF₆ in EC/DEC and 2% VC with different EMIm-TFSI ratios. Reprinted from Ref. [29]. Copyright (2010) with permission of Elsevier



The pure RTIL showed less than 3% weight loss up to 350 °C. In contrast, 30% weight loss was observed in case of the carbonate-based electrolyte using LiPF₆ as conducting salt, when the temperature was raised up to 100 °C and furthermore about 80% loss at 160 °C. Although the addition of RTILs enhanced the thermal stability of the solvent blended electrolytes, the thermal stability in the temperature range from 25 to 100 °C was not improved.

Arbizzani et al. investigated the thermal decomposition of blended electrolytes under N₂ and N₂/O₂ atmosphere, the latter to simulate air conditions (Fig. 6) [30]. The influence of the atmosphere was found to be negligible. Furthermore, it was shown that DMC and EC evaporated sequentially based on their boiling points (89

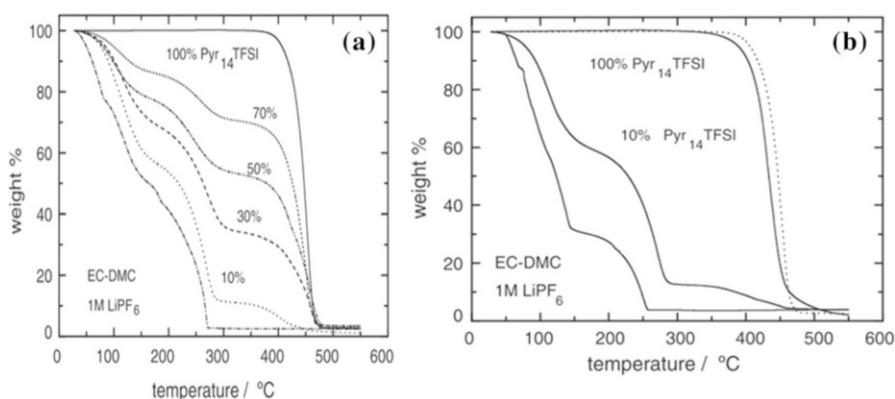
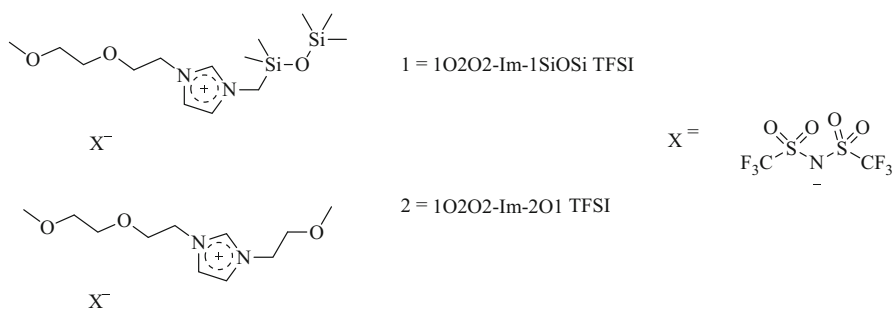


Fig. 6 TGA curves of **a** 1 M LiPF₆ in EC/DMC (1:1 by wt.) and Pyr₁₄-TFSI solutions with different wt% of Pyr₁₄-TFSI under N₂ atmosphere and **b** 1 M LiPF₆ in EC/DMC (1:1 by wt.), Pyr₁₄-TFSI and a solution with 10% Pyr₁₄-TFSI under N₂/O₂; for comparison the curve of Pyr₁₄-TFSI under N₂ atmosphere (dotted line) is also reported. Reprinted from Ref. [30]. Copyright (2011) with permission of Elsevier



Scheme 2 Ether–ether and ether–siloxane ILs [41]

and 260 °C) and the thermal decomposition of LiPF_6 in electrolyte solution starting at temperatures below 107 °C [38–40].

Chavan et al. investigated thermal decomposition of two newly synthesized RTILs (Scheme 2) and their blends with propylene carbonate (PC, 55 mol%) in electrolyte containing 1 M LiTFSI as conductive salt [41].

Both, pure ILs and ILs in combination with LiTFSI lost 90% of weight in the temperature range from 350 to 530 °C. The IL + PC solvent blended electrolytes with LiTFSI showed two major weight loss steps at ≈ 246 °C (15% weight loss), which could be due to decomposition of the PC component, and at 350 °C with 75% weight loss originating from IL decomposition. The addition of LiTFSI to blends of PC and investigated ILs led to the improvement of thermal stability of ether–ether IL + PC blends (from 110 to 150 °C, Fig. 7a) and for ether–siloxane IL + PC blends (from 100 to 130 °C, Fig. 7b). Similar improvements resulted from addition of LiTFSI to ILs (309–355 °C for ether–ether IL and 307–329 °C for ether–siloxane IL). Chavan et al. additionally showed that an ether–ether substituent IL has a higher thermal stability than an ether–siloxane IL under similar conditions.

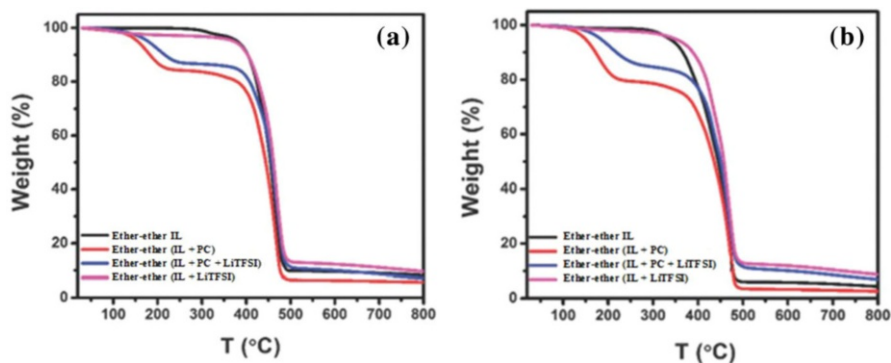


Fig. 7 TGA analysis of **a** ether–ether IL; **b** ether–siloxane IL. Redrawn from Ref. [41]. Copyright (2016) with permission of Royal Society of Chemistry

2.3 Effect of Blending on Electrochemical Performance

2.3.1 Cycling Performance and Electrochemical Stability

Aliphatic nitriles are known for their incompatibility with the graphite anode, as they are not able to form an effective SEI. Abu-Lebdeh et al. suggested that graphite can only be stabilized vs. nitriles by using a blend with SEI forming components (solvents and salts) and proposed to mix ADN and EC together with 1 M LiTFSI + 0.1 M LiBOB salt blend, as the solvent blend only is not sufficient to insure good electrochemical performance [15]. LiBOB is known as a very strong SEI-promoting electrolyte component [42]. ADN and EC decompose at 0.4 and 0.7 V vs. Li/Li⁺ respectively, whereas BOB⁻ reduction occurs at more positive potentials (1.5 V vs. Li/Li⁺), thus stabilizing the surface of the graphitic structure. Xu et al. reported that the presence of EC and LiBOB influences the formation of an effective SEI [42]. With this in line, the authors investigated electrochemical performance of EC/ADN blends (1:1 v/v) compared to pure ADN in the presence of 1 M LiTFSI as conducting salt. Cycling results obtained in graphite/LCO full cells at a C-rate of C/12 showed much higher initial capacity for the EC/ADN blends (1:1 v/v). Using 0.1 M LiBOB as co-salt reduced the capacity fading. The blend of 1 M LiTFSI, 0.1 M LiBOB in EC/ADN (1:1 v/v) showed the best cycling performance with an initial specific discharge capacity of 108 mAh/g and a capacity retention of 90% after 50 cycles (Fig. 8). The reductive decomposition of ADN on graphite was prevented by the synergistic effect between EC, BOB⁻ and TFSI⁻ anions resulting in an effective SEI formation [15].

Isken et al. revealed that an EC/ADN (1:1 by wt.) solvent blend containing 0.9 M LiBF₄ shows good cycling performance without considerable capacity fading [31].

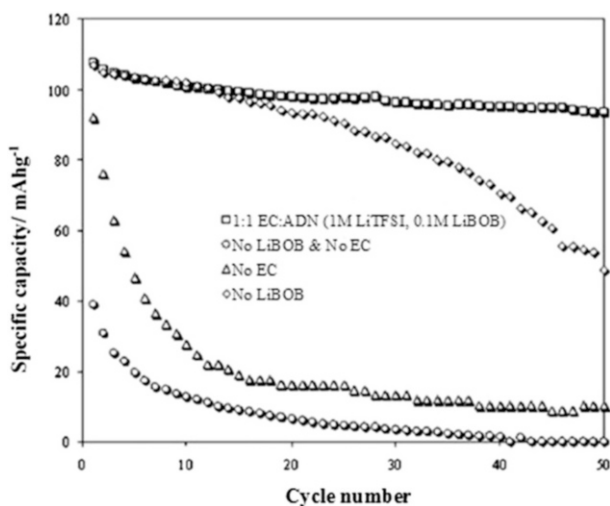


Fig. 8 Effect of electrolyte components on cycling performance of ADN-based electrolytes at C/12 in graphite/LCO full cells. Redrawn from Ref. [15]. Copyright (2009) with permission of Elsevier

Graphite/Li half-cells showed almost the theoretical capacity, even at high C-rate (5 C). After 50 cycles, the capacity was still more than 98% of the initial value. In case of LiNiMnCoO₂ (NMC)/Li half-cells, a capacity retention of 97% was obtained after 50 cycles. The anodic stability of the EC/ADN blend (6.4 V vs. Li/Li⁺) was 0.3 V higher than that of the standard electrolyte 1 M LiPF₆ in EC/DEC (3:7 by wt.) (6.1 V vs. Li/Li⁺), which better enables the use of high-voltage electrodes. The standard electrolyte showed ≈ 0.2 V higher cathodic stability compared to the dinitrile blend. However, this might be attributed to an additional reduction process that gives rise to passivation of the platinum (Pt) working electrode. The addition of a third solvent, a linear carbonate, such as DMC or ethyl methyl carbonate (EMC), to the binary blend could also have a significant impact on the electrochemical performance of the electrolyte. Duncan et al. disclosed that LiNi_{0.5}Mn_{1.5}O₄ (LMNO)/Li half-cells operate only when DMC as third solvent, LiBF₄ as salt and LiBOB as co-salt are used [32]. Furthermore, they indicated that higher capacities could be reached with shorter alkane dinitriles such as ADN than with longer alkane dinitriles such as SEN. Nevertheless, all investigated electrolyte blends showed similar capacity fading.

Nagahama et al. [17] investigated ternary blends consisting of 1 M LiBF₄ in EC/DMC/SEN (1:1:2 v/v/v). They showed that the ternary blend has unique features such as a wide electrochemical stability window of ≈ 6 V (0.5–6.5 V vs. Li/Li⁺) and a good electrochemical compatibility with Li₄Ti₅O₁₂ (LTO), LiMn₂O₄ (LMO), LiCoPO₄ (LCP) and LiFePO₄ (LFP).

Over the last decade, electrochemical properties of ILs were investigated by many groups [33, 34, 43–45]. Most of the imidazolium-based ILs suffer from a narrow ESW, which results in a poor cycling performance of the cell. This is due to low cathodic stability, which makes this type of RTILs inappropriate for applications in graphite-based lithium ion systems and to the formation of an ineffective SEI layer on the graphite surface, which results in the phenomenon of solvent intercalation and resulting into exfoliation, i.e., severe damage to graphite anodes by shedding of graphene layers or graphene layer packages [46]. However, imidazolium-based ILs have lower viscosities and higher conductivities as effect of the charge delocalization in the cations. Most importantly, the electrochemical performance of solvent blended electrolytes was investigated using different electrode materials. Guerfi et al. studied electrochemical properties of blended carbonate solvents with EMIm-TFSI on LFP cathode and mesocarbon microbeads (MCMB) anodes [29]. Although no solvent intercalation occurred at potentials lower than 0.25 V vs. Li/Li⁺, exfoliation of graphite was observed and the first cycle efficiency was very low when pure EMIm-TFSI-based electrolyte was used. The addition of carbonate solvents to EMIm-TFSI could improve the formation of an effective SEI layer due to the EC decomposition at ≈ 0.8 V vs. Li/Li⁺. The addition of an IL to the carbonate solvent clearly affected the first cycle Coulombic efficiency of the investigated electrolytes. The same was valid for first and second cycle capacity values, as summarized in Table 3.

The use of pure EMIm-TFSI and a LFP cathode resulted in lower first cycle Coulombic efficiencies, which could be due to high viscosity and low wettability of pure IL. Furthermore, the authors studied 40% EMIm-TFSI blends of 1 M LiPF₆ in

Table 3 The first cycle electrochemical characteristics of MCMB graphite anode in carbonate-based electrolyte blends and EMIm TFSI. Reprinted from Ref. [29]. Copyright (2010) with permission of Elsevier

IL (wt%)	Discharge cap. 1st/2nd	Charge cap. 1st/2nd	Ah. eff. 1st/2nd
100	141/94	96/79	68/84
50	311/255	250/248	80/97
30	377/314	315/312	85/99
20	388/324	337/331	87/102
10	362/306	329/302	91/99
0	362/306	316/312	92/102

EC/DEC (1:1 by wt.) and 2% VC as nonflammable electrolyte in a cell using LFP and LTO as cathode and anode. The formation cycle at C/24 rate had 89% Coulombic efficiency in the first cycle and a specific capacity of 115 mAh g⁻¹.

Kühnel et al. investigated the ESW of PC+ Py₁₄-TFSI solvent blended electrolytes with different concentrations of 0.3 M LiTFSI using Pt as working electrode [35]. No difference in electrochemical stability was observed in the blended electrolytes. The discharge capacities of all electrolytes with different concentrations were investigated in a half-cell setup using LFP as working electrode and C-rates between 0.1C and 5C. There is a good correlation between the percent amount of IL and the capacity; following the trend: the higher the IL amount, the lower the capacity (Fig. 9a).

Conductivity and wettability were found as two important factors influencing discharge capacity values of the nonaqueous electrolytes as claimed by the authors. The effect of electrode wetting on discharge capacities in galvanostatic cycling of blended electrolytes through the initial cycles is known in literature [47].

The performance of blended solvent electrolytes was investigated at high temperature (60 °C) by means of constant current cycling at 5 C. As an interesting

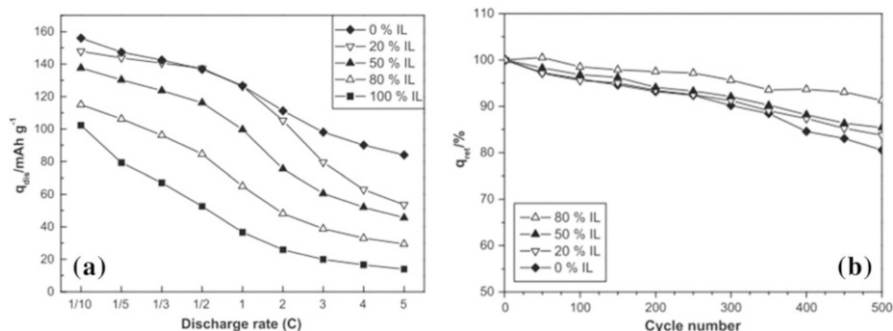
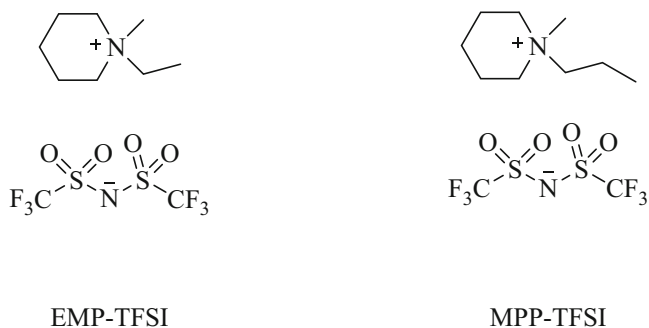


Fig. 9 **a** Specific discharge capacity (q_{dis}) of LFP electrodes with PC/Py₁₄-TFSI, 0.3 M LiTFSI blend electrolytes. The electrodes were cycled at RT with different discharge rates. Reprinted from Ref. [35]. Copyright (2011) with permission of Elsevier; **b** discharge capacity retention (q_{ret}) of LFP with PC/Py₁₄-TFSI, 0.3 M LiTFSI blend electrolytes. The electrodes were cycled at 60 °C with 5 C charge/discharge rate. Reprinted from Ref. [35]. Copyright (2011) with permission of Elsevier



Scheme 3 Molecular structures of 1-ethyl-1-methylpiperidinium bis(trifluoromethylsulfonyl)imide (EMP-TFSI) and 1-methyl-1-propyl-piperidinium bis(trifluoromethylsulfonyl)imide (MPP-TFSI)

result, the higher capacity retention for electrolytes with higher IL amounts during cycling was obtained (Fig. 9b). Kühnel et al. claimed that the lower capacity loss during cycling with higher amounts of Py₁₄-TFSI could be attributed to less dendrite formation or less solvent evaporation.

Kim et al. [48] published a paper on the high-voltage application of two different piperidinium-based ILs, namely 1-ethyl-1-methylpiperidinium bis(trifluoromethylsulfonyl)imide (EMP-TFSI) and 1-methyl-1-propyl-piperidinium bis(trifluoromethylsulfonyl)imide (MPP-TFSI) (molecular structures depicted in Scheme 3) in carbonate-based solvent using LMNO cathode.

Conductivity measurements revealed higher conductivity of the EMP-TFSI-based electrolyte with 1.5 M LiPF₆ in EC/DEC (1:1 v/v) compared to MPP-TFSI-based electrolytes. This has an obvious effect on galvanostatic cycling at different C-rates as the electrolyte with the lowest conductivity (MPP-TFSI blended electrolyte) had the largest over-potential, lower capacities as well as Coulombic efficiencies (Fig. 10).

Charge/discharge cycling at 0.5 C demonstrated very steady performance for both pure carbonate-based electrolyte and EMP-TFSI blended electrolyte, but MPP-TFSI blended electrolyte displayed very unstable cycling stability and Coulombic efficiencies over 50 cycles (Fig. 11).

2.3.2 Aluminum Dissolution in Presence of Nitriles

In electrolytes containing LiTFSI as conducting salt, anodic aluminum (Al) dissolution takes place [49–51]. Krämer et al. [52] showed that a blend of nitrile and carbonate slows down Al dissolution in LiTFSI-based electrolyte. The authors investigated dissolution behavior of Al at high potentials of 1 M LiTFSI-based [EC/EMC (1:1 by wt.), EC/DMC (1:1 by wt.), EC/DEC (1:1 by wt.), EC/DEC (3:7 by wt.)], pure ADN and EC/ADN (1:1 by wt.) electrolytes. They performed linear sweep voltammetry (LSV) measurements with a scan rate of 1 mV/s until a potential of 5.0 V vs. Li/Li⁺ was reached and thereafter kept constant for 24 h. The carbonate-based electrolytes showed a much higher electric charge (≈ 14 C after 24 h) whereas the EC/ADN blend led to an electric charge of ≈ 7.5 C. As

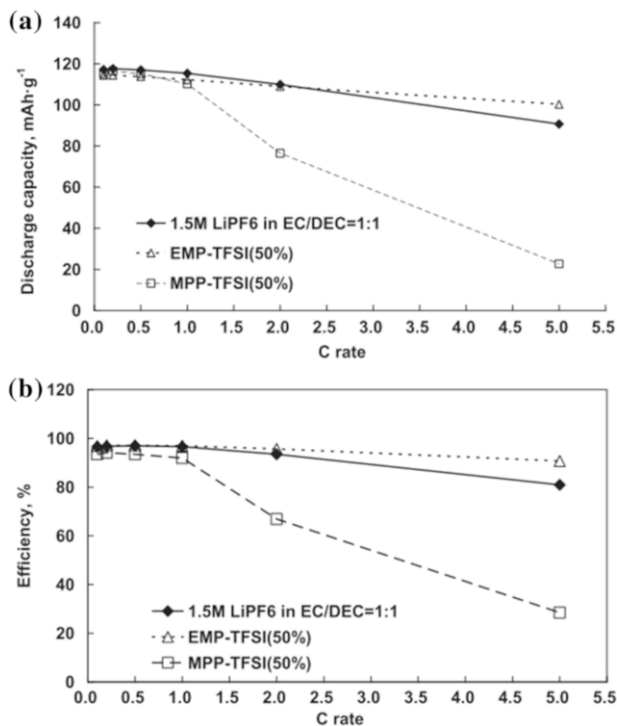


Fig. 10 The rate capability tests with 50% ILs and a pure carbonate electrolyte using LMNO working electrodes. **a** The discharge values versus the discharge rate and **b** the Coulombic efficiency versus the discharge rate. Prior to the measurements, five formation cycles at a rate of 0.1 C were performed for each measurement. Reprinted from Ref. [48]. Copyright (2013) with permission of Elsevier

comparison, 1 M LiTFSI in ADN as single solvent only reached an electric charge of ≈ 2.0 C. The dissolution of the current collector caused a weight loss, which was detected by weighting the Al electrode before and after the potentiostatic experiment. With pure ADN, no significant weight loss was observed, indicating negligible Al dissolution. The investigated EC/ADN blend led to a much higher weight losses, whereas carbonate-based electrolytes showed the highest weight loss and therefore the largest advance towards anodic Al dissolution. The fact that the anodic Al dissolution was slowed down, but remained apparent in EC/ADN blends with 1 M LiTFSI, led to the conclusion that LiTFSI is not a suitable conducting salt for EC/dinitrile blends. As LiPF₆ is soluble in ADN and GLN (<1 M) only in small quantities, even after adding carbonates, Isken et al. used LiBF₄ as conducting salt [31]. They revealed that 0.9 M LiBF₄ in EC/ADN (1:1 by wt.) electrolyte forms a stable protective film on the Al current collector, which prevents Al dissolution at 4.3 V vs. Li/Li⁺.

This issue was further investigated by Abu-Lebdeh et al. [15] in a 1 M LiTFSI in EC/ADN blend (1:1 v/v). They claimed that a higher open-circuit potential (OCP) indicates improved ability of the electrolyte to passivate Al surface. In order to further strengthen their idea, they employed the cyclic voltammetry (CV) technique

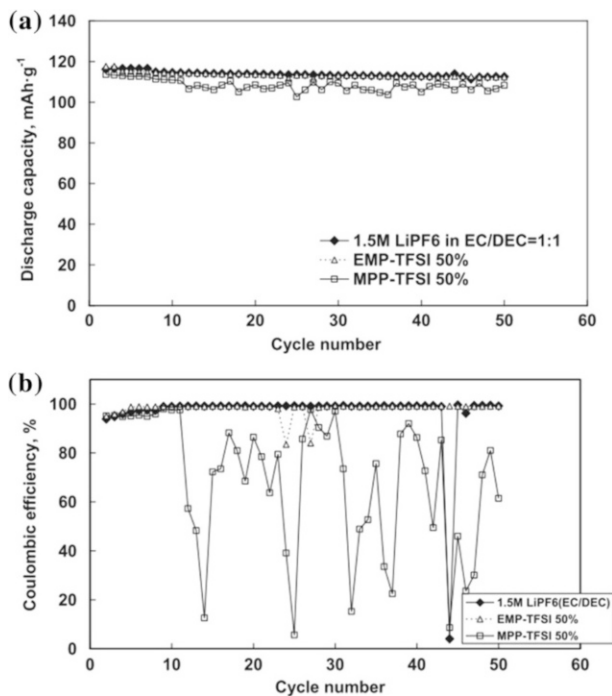


Fig. 11 Cycle life studies with IL blended electrolytes and a pure carbonate electrolyte using LMNO working electrodes. Both the charge and discharge rates for experiments were 0.5 C. Reprinted from Ref. [48]. Copyright (2013) with permission of Elsevier

in a three-electrode configuration with an Al wire as working electrode and a silver wire as a reference and counter electrode. The OCP of the cell containing the EC/ADN blend as solvent was reported as 2.51 V vs. Li/Li⁺ which is higher than that of the cell with pure ADN (2.2 V vs. Li/Li⁺). In light of these results, it was suggested that the solvent blend-based electrolyte formed a better passivation layer on Al. The passivation ability of the blended solvent electrolyte was better than that of 1 M LiTFSI in EC/DMC (1.63 V vs. Li/Li⁺) [53]. Furthermore, by exchanging ADN with GLN, Abu-Lebdeh et al. [16] observed an OCP of 2.2 and 2.3 V vs. Li/Li⁺ for pure GLN and EC/GLN blend (1:1 v/v), respectively, which is again higher than for the carbonate-based electrolyte.

Kühnel et al. has also investigated the anodic dissolution of Al current collector in electrolyte blends containing PC with different concentrations of 0.3 M LiTFSI in Py₁₄-TFSI. They used Al disks as working electrodes and lithium metal as counter and reference electrode to perform LSV measurements. It is well known that anodic dissolution of Al current collector is less pronounced in ionic liquid media probably due to low solubility of Al(TFSI)₃ species [54–56]. Here, the authors showed a correlation between the IL amount in solvent blended electrolyte formulations and anodic dissolution potentials. The values for blended electrolytes lay in between as listed in Table 4. The potential ranged from 3.8 V vs. Li/Li⁺ in case of pure PC

Table 4 Maximum potentials (E_{\max}) applied to Al foil electrode in electrolytes before the Faradaic reactions start. Reprinted from Ref. [35]. Copyright (2011) with permission of Elsevier

IL (wt%)	E_{\max} vs. (Li/Li ⁺) (V)
0	3.8
20	3.8
50	4.1
80	4.2
100	5.4

electrolyte with 0.3 M LiTFSI up to 5.4 V vs. Li/Li⁺ in case of pure Py₁₄-TFSI. For electrolytes with higher amount of IL, maximum potentials applied prior to Al anodic dissolution were higher than potential values in case of electrolytes with lower amount of IL.

2.4 Summary

Blending nitriles and ILs with carbonates enables their application as electrolyte co-solvents. In this way, better physicochemical and electrochemical properties required for the performance in a LIB cell can be achieved. Nitrile/carbonate solvent blends have lower melting points than the single solvents as well as higher flash points, thus leading to improved safety conditions. In addition, due to suppression of anodic Al dissolution and a broader electrochemical stability window, good electrochemical performance can be attained. Blending of RTILs with carbonate solvents influences the safety properties of the nonaqueous electrolytes. The addition of EC to the dinitrile and/or increase of the temperature lead to higher conductivity values. The capacity values are higher compared to pure dinitrile as solvent, but a solvent blend itself is not enough to insure adequate cycling performance. For this reason, a combination with a salt blend is required. Blends of RTILs and carbonate solvents contribute to more effective SEI layer formation on graphite electrodes and improve the conductivity and rate capability of the electrolyte. However, the addition of carbonate solvents to RTILs has a negative influence on safety properties of the electrolyte blend such as lower thermal stability and higher flammability. In summary, taking into account all investigated functional aspects, the combination of nitriles and RTILs with carbonates seems to be a good solution to overcome the drawbacks of the respective single solvents, as summarized in Table 5.

3 Blended Conducting Salts in Nonaqueous Electrolytes

All commercial nonaqueous LIB electrolytes require a conducting salt that, in the ideal case, fulfills the following requirements: high purity, low molecular weight, the ability to completely dissolve and dissociate in a nonaqueous solvent medium, intrinsic thermal stability, chemical stability vs. the solvent, stability over a wide electrochemical potential window, high mobility of the solvated ions (especially solvated Li⁺ ions), effective SEI and CEI formation on graphite and on the cathode

Table 5 Major roles of discussed solvent blend-based electrolytes

Solvent blend	Target improvement	Investigated electrolyte	References
EC/dinitrile	Higher flash point	1 M LiBF ₄ in EC/ADN (1:1 by wt.)	[31]
	Lower vapor pressure		
	Lower viscosity	1 M LiTFSI in EC/dinitrile (1:1 v/v)	[32]
	Higher conductivity	(NC-(CH ₂) _n -CN with <i>n</i> = 3–8)	
		1 M LiTFSI in EC/GLN (1:1 v/v)	[16]
		0.9 M LiBF ₄ in EC/ADN (1:1 by wt.)	[31]
	Suppressed Al dissolution	1 M LiTFSI in EC/ADN (1:1 by wt.)	[52]
	Effective SEI formation	0.9 M LiBF ₄ in EC/ADN (1:1 by wt.)	[31]
		1 M LiTFSI in EC/ADN (1:1 v/v)	[15]
		1 M LiTFSI in EC/GLN (1:1 v/v)	[16]
	Broader electrochemical stability window	0.9 M LiBF ₄ in EC/ADN (1:1 by wt.)	[31]
	Higher capacities	1 M LiTFSI in EC/ADN (1:1 v/v)	[15]
	Reduced capacity fading	1 M LiTFSI, 0.1 M LiBOB in EC/ADN (1:1 v/v)	
		0.9 M LiBF ₄ in EC/ADN (1:1 by wt.)	[31]
EC/DMC/dinitrile	Lower viscosity	1 M LiBF ₄ , 0.1 M LiBOB in EC/DMC/dinitrile (1:1:2 v/v/v)	[32]
	Higher conductivity		
	Higher capacities	1 M LiBF ₄ , 0.1 M LiBOB in EC/DMC/dinitrile (1:1:2 v/v/v)	[32]
		(NC-(CH ₂) _n -CN with <i>n</i> = 1–8)	
	Broader electrochemical stability window	1 M LiBF ₄ in EC/DMC/SEN (1:1:2 v/v/v).	[17]
EMIm-TFSI in EC/DEC (1:1 wt%)	Flame inhibition effect	EMIm-TFSI (40% or more) + 1 M LiPF ₆ in EC/DEC	[29]
	Optimum viscosity and conductivity values	EMIm-TFSI (40–60%) + 1 M LiPF ₆ in EC/DEC	
	Optimum charge/discharge capacity (MCMB/Li half-cell)	EMIm-TFSI (20–30%) + 1 M LiPF ₆ in EC/DEC	

Table 5 continued

Solvent blend	Target improvement	Investigated electrolyte	References
Pyr ₁₄ -TFSI in EC/ DMC (1:1 wt%)	Flame inhibition effect	Pyr ₁₄ -TFSI (30% or more) + 1 M LiPF ₆ in EC/DMC	[30]
	Higher thermal stability	Pyr ₁₄ -TFSI + 1 M LiPF ₆ in EC/DMC	
Pyr ₁₄ -TFSI in PC	Higher anodic dissolution of Al current collector	PC+ 0.3 M LiTFSI in Pyr ₁₄ -TFSI (50% or more)	[35]
	Lower discharge capacities	PC+ 0.3 M LiTFSI in Pyr ₁₄ -TFSI (by addition of IL)	
	Higher capacity retention during galvanostatic cycling at 60 °C (LFP, 5C)	PC+ 0.3 M LiTFSI in Pyr ₁₄ -TFSI (by addition of IL)	
EMP-TFSI MPP-TFSI in EC/DEC (1:1 wt%)	Higher conductivity and better rate capability of EMP than MPP	50% IL (EMP or MPP) + 1.5 M LiPF ₆ in EC/DEC	[48]
	Improved galvanostatic cycling performance and higher Coulombic efficiency of EMP than MPP	50% IL (EMP or MPP) +1.5 M LiPF ₆ in EC/DEC	

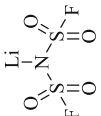
surface, passivation of the Al current collector to circumvent anodic Al dissolution, as well as low cost. Over the past three decades, various lithium salts (e.g. LiPF₆, LiBF₄, LiBOB, lithium difluoro(oxalato)borate—LiDFOB, LiTFSI, lithium bis(fluoro-sulfonyl)imide—LiFSI) were subjected to an extensive investigation in nonaqueous (aprotic) solvents or solvent blends in respect to their physicochemical, electrochemical and safety features [42]. Nevertheless, a lithium salt, which fulfills all the above demanded criteria at the same time, has not been identified so far. Moreover, compared to the wide variety of aprotic organic solvents available, the selection of an appropriate lithium salt is rather limited. Table 6 summarizes the most investigated lithium salts accompanied by their main physicochemical features.

The commercially dominant conducting salt in carbonate-based electrolytes is still LiPF₆. This domination has not been driven by any single outstanding property, but by the combination of a series of well-balanced properties [24]. However, its thermal and chemical instability has drawn the attention of the LIB society to search for alternatives [65]. In particular, the tendency of LiPF₆ to form toxic and chemically aggressive HF in the presence of water (as impurity in the LIB cell and the electrolyte itself) [66], which is accelerated by heat are a concern. LiPF₆ therefore cannot only deteriorate electrochemical performance, by e.g. increased cathode dissolution [67, 68], but can furthermore react with the organic solvents yielding even more toxic components such as fluorophosphates and organophosphates [5, 69–71].

Table 6 Main characteristics of the lithium salts discussed in the paper

Conducting salt	Molecular weight	Melting temperature (°C)	Decomposition temperature (°C) in solution	Al dissolution	Ionic conductivity (mS cm ⁻¹)	References
$\left[\begin{array}{c} \text{F} \\ \\ \text{F}-\text{P}-\text{F} \\ \\ \text{F} \end{array} \right]^{-} \text{Li}^{+}$	151.9	200	80 in EC/DMC	No	10.7 in EC/DMC	[24, 42, 57]
LiPF₆ $\left[\begin{array}{c} \text{F} \\ \\ \text{F}-\text{P}-\text{F} \\ \\ \text{F} \end{array} \right]^{-} \text{Li}^{+}$	93.9	293	>100	No	4.9 in EC/DMC	[24, 25, 42]
LiBF₄ $\left[\begin{array}{c} \text{O} \\ // \\ \text{O}-\text{B}-\text{O} \\ // \\ \text{O} \end{array} \right]^{-} \text{Li}^{+}$	193.8	300	300–370	No	4.7 in EC/DMC	[25, 58–60]
LiBOB $\left[\begin{array}{c} \text{O} \\ // \\ \text{O}-\text{B}-\text{O} \\ // \\ \text{O} \end{array} \right]^{-} \text{Li}^{+}$	143.8	265–271	240	No	4.5 in EC:DEC	[24, 61, 62]
LiDFOB $\begin{array}{c} \text{O} \\ // \\ \text{O}-\text{N}-\text{S}-\text{O} \\ // \quad // \\ \text{O} \quad \text{O} \end{array} \text{Li}^{+}$	286.9	234	>100	Yes	9.0 in EC:DMC	[24, 57, 63]
LiTFSI						

Table 6 continued

Conducting salt	Molecular weight	Melting temperature (°C)	Decomposition temperature (°C) in solution	Al dissolution	Ionic conductivity (mS cm ⁻¹)	References
 LiFSI	187.1	135	>200	Yes	9.8 in EC:EMC	[24, 64]

3.1 Aim of Blending Lithium Salts

The electrochemical performance and safe operation of a battery cell mainly depend on the chemical and electrochemical stability of each individual cell component. Lithium salts, being responsible for (Li^+) ion conduction, may have strengths and weaknesses with respect to physicochemical and electrochemical features, which most likely restrict their application in future LIB systems. Substitution of LiPF_6 with new salts, addition of salt additives, or utilization of salt blends, is expected to improve electrolyte performance. With respect to salt blends, the known advantages of the individual conducting salts can be exploited by combining them. Salt blends exhibit improved thermal stability, ionic conductivity, electrochemical performance and safety characteristics as compared to their single constituents. Many interesting literature examples of blended salts that mainly shed light on the effect of salt blends on anode, cathode, suppression or inhibition of Al dissolution as well as the overall system performance were reported so far [72, 73]. The idea of blending various lithium salts in different amounts is generating considerable interest for future electrolyte formulation in LIB research. However, there is still much controversy surrounding the influence of salt blends on electrolyte properties. In addition, a common approach in improving electrolyte formulations is related to the addition of the sacrificial anions, so-called salt additives, which degradation results in a considerable improvement of battery performance [74]. By combining the advantages of two different salts, cell chemistry and cell performance can be optimized and tailored for a specific purpose. Lithium salts were used as blends in various concentrations and combinations to suppress the adverse effects of the single salt in electrolyte formulation. The purpose of blending salts can be listed as (1) achieving higher ionic conductivity by combining several lithium salts in one pot, (2) adjusting physicochemical features of the resulting electrolyte blends, e.g. boiling, freezing points, solubility, (3) forming an effective SEI on the surface of the negative electrode, thus improving its cycling efficiency in lithium ion or lithium metal batteries, (4) preventing metal dissolution from the cathode, (5) increasing anodic potential stability window, (6) forming a passivation layer on the surface of the Al current collector and preventing anodic Al dissolution and (7) improving cell safety.

3.2 Physicochemical Features of Blended Salt-Based Electrolytes

3.2.1 Transport Properties: Viscosity and Conductivity

The viscosities of $\text{LiPF}_6 + \text{LiBOB} + \text{LiDFOB}$ in EC/DMC (1:1 by wt.) and EC/dimethyl sulfone (DMSN) (4:1 by wt.) were systematically investigated by Hofmann et al. [75]. Their findings indicated an increase in viscosity and a decrease in ionic conductivity for the following binary and ternary blended salts: $\text{LiPF}_6 + \text{LiBOB}$, $\text{LiPF}_6 + \text{LiDFOB}$ and $\text{LiPF}_6 + \text{LiBOB} + \text{LiDFOB}$, as compared to the single-salt system (LiPF_6). As summarized in Table 7, no significant difference could be observed.

Table 7 Physicochemical features of binary and ternary blended salts over single salt by Hofmann et al. Reprinted from Ref. [75]. Copyright (2015) with permission of Elsevier

Electrolyte	LiPF ₆ EC/DMC	LiPF ₆ EC/DMSN	LiPF ₆ + LiBOB EC/DMSN	LiPF ₆ + LiDFOB EC/DMSN	LiPF ₆ + LiBOB + LiDFOB EC/DMSN
Melting point (°C)	-19.4	16.0	18.1	18.6	18.8
Freezing point (°C)	-56.1	-26.1	-12.3	-19.1	-17.3
Density (25 °C) (g cm ⁻³)	1.27	1.40	1.39	1.36	1.37
Viscosity (20 °C) (mPas)	4.4	11.4	11.0	11.4	11.4
Conductivity (mS cm ⁻¹)	10.67	5.95	5.38	5.95	5.76

The physicochemical features of a series of electrolytes containing LiBF_4 + LiBOB salt blends were reported by Lai et al. with an attempt to improve the operation temperature range of LIBs. In their study, the investigated electrolyte formulations contained salt blends of LiBF_4 + LiBOB (8:2) in PC/EC/EMC, PC/EC/EMC/MB, PC/EC/methyl butyrate (MB) solvent systems [76]. At moderate and high temperatures, ionic conductivity values of the blended salt electrolytes were lower than that of single component salt (LiPF_6). However, at lower temperatures (-40 and -20 °C), no considerable difference could be observed due to the high mobility of BF_4^- . Electrolyte blends of LiBF_4 + LiBOB (8:2) PC/EC/EMC/MB (1:1:1:2 v/v/v/v) showed ionic conductivity of 4.34 and 2.16 mS cm^{-1} at -20 and -40 °C, respectively.

The discrepancy in ionic conductivities of LiBF_4 + LiBOB salt blends as compared to the single constituents and LiDFOB salts was discussed by Schedbauer et al. [62]. The specific conductivities of the LiBF_4 containing electrolyte blends were found to be lower as compared to non- BF_4^- containing electrolytes in the temperature ranging from -40 to 60 °C. Moreover, 0.5 M LiBOB in EC/DEC (3:7 by wt.) and 1 M LiDFOB in EC/DEC (3:7 by wt.) electrolytes showed almost identical behavior in the investigated temperature range. Furthermore, the trend in conductivities of LiBOB + LiBF_4 salt blends depicted a descending behavior with the increasing LiBF_4 concentration.

In the study published by Zhang et al., the effect of the increasing LiFSI concentration on the electrochemical performance of LiPF_6 -based EC/EMC (3:7 v/v) electrolyte was discussed [77]. Ionic conductivity of the resulting blend showed a parallel trend with the concentration of LiFSI up to 0.2 mol L^{-1} ($\sigma_{0.1 \text{ mol L}^{-1}}$: 9.33 mS cm^{-1} , $\sigma_{0.2 \text{ mol L}^{-1}}$: 9.60 mS cm^{-1}). However, at concentrations higher than 0.2 mol L^{-1} a fast decrease in ionic conductivity of the electrolyte was observed, which could be attributed to the detrimental effect of the high salt concentration, giving rise to ionic interactions.

A similar trend was observed for LiBF_4 + LiDFOB salt blends in EC/EMC/DMC (1:1:1 by wt.) [78]. Concentration changes of LiDFOB and LiBF_4 were found to influence the ionic conductivity in a different manner. An increase of the LiDFOB concentration (up to 0.8 M) led to higher ionic conductivities in the temperature range from 30 to 70 °C compared to that of the pure LiBF_4 -based electrolyte [79, 80]. At contrast, in the temperature range from 20 to -20 °C, the ionic conductivity of the aforementioned system gradually deteriorated. However, an increase of the LiBF_4 concentration (up to 0.8 M) in this low temperature range had a positive influence on ionic conductivity, due to the lower van der Waals volume of the BF_4^- ion and its correlation to electrolyte viscosity [81]. An equimolar blend of LiBF_4 and LiDFOB in EC/PC/DMC (1:1:3) at a concentration of 10 wt%, provided a good overall ionic conductivity (in the order of $10^{-3} \text{ S cm}^{-1}$) over the temperature range from 20 to 80 °C as stated by Zygadło-Monikowska et al. [82]. Besides, a LiPF_6 + LiDFOB blend in EC/PC/DMC (1:1:3 v/v/v) could not compete with the pure LiPF_6 -based electrolyte in the temperature range from 0 to 40 °C, as showed by Zhang et al. [83]. This is due to the larger van der Waals volume of the ODFB^- ion compared to PF_6^- as well as the lower ionic dissociation

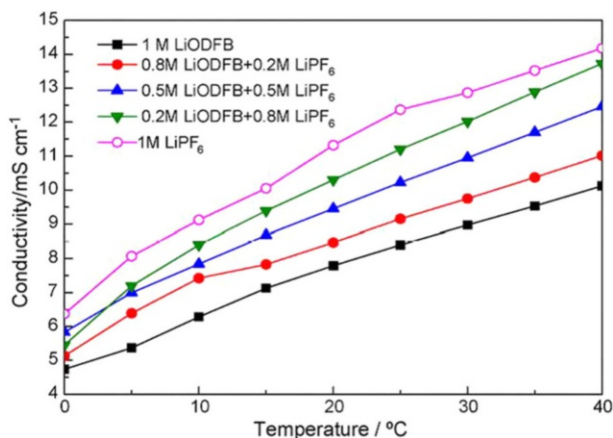


Fig. 12 Ionic conductivity (κ) of electrolytes with different LiDFOB + LiPF₆ salt blend ratios in EC/PC/DMC (1:1:3) solution (0–40 °C). Reprinted from Ref. [83]. Copyright (2010) with permission of Elsevier

ability of LiDFOB compared to LiPF₆, leading to higher viscosity of the electrolyte, thus resulting in conductivity decrease. With this in mind, the conductivity of the LiDFOB-based electrolytes could be enhanced by addition of LiPF₆, as depicted in Fig. 12 [83].

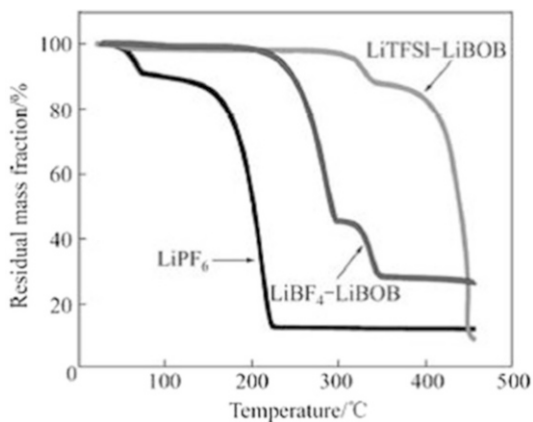
In another study by Park et al., the ionic conductivity of (EC/DEC 3:7 v/v) electrolyte containing blend of LiFSI and LiDFOB salts was determined over the temperature range from 10 to 60 °C and compared to the pure LiFSI and LiPF₆-based electrolytes [84]. In consistence with literature data, the conductivity of the LiFSI-based electrolyte was higher than that of LiPF₆-based electrolyte [64, 85]. In line with this, the ionic conductivity of the 0.8 M LiFSI + 0.2 M LiDFOB in EC/DEC (3:7 v/v) was found to be higher than the pure LiPF₆-based electrolyte over the aforementioned temperature range indicating that addition of LiDFOB had no significant impact on the superior ionic conductivity of the pure LiFSI-based electrolyte [84].

Using the synergistic effect of LiDFOB and LiTFSI salts in EC/EMC (4:6 by wt.), Li et al. pointed out the minor difference in ionic conductivity of equimolar blend (7 mS cm⁻¹) compared to the pure LiTFSI-based electrolyte (7.8 mS cm⁻¹) at 20 °C [86].

3.2.2 Thermal Stability of Blended Salt-Based Electrolytes

It is of great importance to introduce thermally stable electrolyte blends for achieving risk-free operation of LIBs. Several approaches aimed at suppressing the low thermal stability of the LiPF₆-based electrolyte by using thermally more stable salt blends including LiBOB, LiBF₄, LiDFOB and LiTFSI. Furthermore, in few studies LiBOB + LiPF₆ salt blends were used for elucidating the effect of LiBOB on suppressing the thermal instability of LiPF₆ salt [72, 73]. The influence of LiBOB on the thermal stability of MCMB/spinel LIBs was attained from the

Fig. 13 TGA profiles of LiBOB + LiTFSI and LiBOB + LiBF₄ salt blends compared to pure LiPF₆. Reprinted from Ref. [87] Copyright (2015) with permission of Elsevier



corresponding cycling curve at 55 °C, which depicted more steady behavior as compared to the pure LiPF₆ salt-based electrolyte.

Zhang et al. [87] reported several thermally stable salt blends, namely LiBF₄ + LiBOB and LiTFSI + LiBOB as compared to the SOTA salt, LiPF₆. The thermal stability of the aforementioned blended salt electrolytes is illustrated in Fig. 13.

Another example related to the effect of blending on the thermal stability for LiBF₄ containing electrolyte was disclosed by Hong et al. [88]. As already mentioned, LiBF₄ suffers from low ionic conductivity but it provides good cycling performance at higher (50–80 °C) and lower temperatures (–20 °C) [89]. A study published by Zhang et al. pointed out that blending LiBOB salt with LiBF₄ and LiTFSI enables effective SEI formation and Al current collector passivation, which can successfully compensate the drawbacks of LiBF₄ and LiTFSI. According to their results, the thermal stabilities of the investigated salt systems followed the ascending order of LiPF₆ < LiBF₄ + LiBOB < LiTFSI + LiBOB [89, 90].

By blending LiPF₆ with LiDFOB in EC/PC/DMC (1:1:3 v/v/v), Zhang et al. showed remarkable improvement in performance of the artificial graphite (AG)/LFP cells at 65 °C compared to the pure LiPF₆-based electrolyte formulation. This superior behavior, expressed through higher capacity and capacity retention values, was attributed to an effective SEI film-formation in the presence of the high LiDFOB concentration (LiDFOB/LiPF₆ in ratio 4:1) as well as the thermal stability enhancement of the electrolyte. The presence of LiDFOB inhibited the autocatalytic decomposition of the electrolyte and synergistic effect of both salts enhanced the thermal stability of the electrolyte. This was achieved by a disproportionation reaction of LiDFOB, in which lithium tetrafluoroaluminate (LiPF₄C₂O₄), which sequestered PF₅ formed during thermal decomposition of LiPF₆, was generated [91]. The addition of LiPF₆ in smaller amount contributed to an improved electrolyte conductivity and increased capacity [83]. The beneficial influence of LiDFOB + LiBF₄ blends in EC/DMC/EMC (1:1:3 by wt.) was confirmed in graphite/LiNi_{0.5}Mn_{1.5}O₄ (LNMO) full cells at low (–20 °C) and elevated (60 °C) temperatures [78]. Moreover, the improved low temperature performance at high

C-rate charging and discharging was attributed to a diminished charge transfer impedance in presence of LiBF_4 ($\text{LiDFOB}/\text{LiBF}_4 = 4:1$, in molar).

3.3 Electrochemical Features of Blended Salt-Based Electrolytes

3.3.1 Cathodic Stability of Blended Salt-Based Electrolytes

The cathodic stability of the blended salt-based electrolytes was mainly characterized by means of CV and/or galvanostatic charging on the surface of a graphite electrode. The performance assessment of such electrolyte blends was derived based on: (1) a SEI forming features, (2) irreversible capacity, (3) Coulombic efficiency and (4) capacity retention.

As initially emphasized, the blending concept significantly influences cell chemistry and electrochemical features of the electrolyte system. A well-known example is given for a PC containing electrolyte formulations in combination with graphitic anodes. The superior features of PC-based electrolytes such as enhanced rate capability, lower and higher temperature stability make this solvent an important component for electrolyte formulations [92]. Nevertheless, its incompatibility to the graphitic electrode, due to solvent co-intercalation and intense gas evolution surface is a well-known issue [93, 94]. In this respect, a blended salt system that contains sufficient amounts of LiBOB (1–5 mol%) in LiPF_6 or LiBF_4 -based electrolytes, may serve as a promising solution to cope with PC reduction and graphite exfoliation. Xu et al. investigated two electrolyte formulations that contained 50 and 30% PC, which in the normal case prevent intercalation of Li^+ into graphite. In the additive free case, the graphite potential leveled off at 0.8 V vs. Li/Li^+ which is in the characteristic reduction potential range of PC (Fig. 14). However, in the presence of LiBOB, the reversible lithiation potential of graphite (0.2 V vs. Li/Li^+) could be reached [58]. Another example for a PC containing electrolyte recipe was related to the LiBOB + LiBF_4 salt blend which was considered as solution to enable the application of a LiBF_4/PC -based electrolyte in graphite-based LIBs [95], by introducing LiBOB as a SEI forming additive. A cathodic signal at 1.75 V vs. Li/Li^+ indicated the reduction of BOB^- forming an

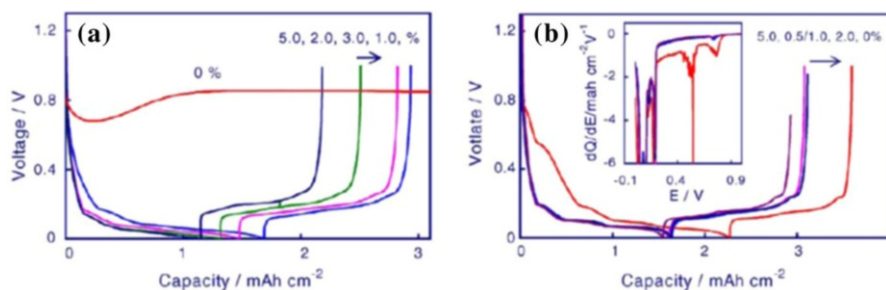


Fig. 14 Voltage-capacity curves of the first cycle for Li/graphite cells with different LiBF_4/PC electrolytes, in which the numbers present molar percentage of LiBOB in the mixed salt. *Inset in b* is a part of the plots of differential capacities vs. cell voltage. **a** 1.0 m LiBF_4 PC/EC (1:1) and **b** 1.0 m LiBF_4 PC/EC/EMC (1:1:3). Reprinted from Ref. [95]. Copyright (2006) with permission of Elsevier

effective SEI on the negative electrode [96, 97]. As reported by Panitz et al. reduction of LiBOB gave rise to capacity loss and higher charge-transfer impedance as compared to the SOTA salt [98]. Moreover, in the same study it was reported that the state of the graphite anode surface, e.g. surface chemistry [99–102], specific surface area [103–106], have a decisive role in the intensity of this reduction process. The opportunity to tailor SEI chemistry of a carbonaceous electrode by a boron rich surface layer made LiBOB a good electrolyte candidate for blending purposes.

A similar study reporting on the superiority of LiBOB with regard to the SEI film-formation, was performed by Zhang et al. [95]. When LiBOB was used as co-salt, it sufficiently stabilized the surface of the graphitic anode and in this way enabled the application of LiBF_4/PC electrolytes in LIBs. Additionally, it was indicated that LiBOB, when used even in small amount (1–5 mol%), formed an effective SEI film on the graphite electrode [107] in LiBF_4 -based PC/EC/EMC and LiBF_4 -based PC/EC electrolytes. The effectiveness of LiBOB in circumventing the solvent reduction at potential regimes of 0.8–0.4 V vs. Li/Li^+ was investigated by means of the CV technique. In the absence of LiBOB, solvent reduction peaks within the indicated potential range were clearly observable, whereas in the presence of 1 mol% LiBOB the peaks were suppressed and Li^+ intercalation into graphite could take place at ≈ 0.3 V vs. Li/Li^+ . Even at low concentrations of LiBOB (0.5 mol%), the SEI was sufficient to suppress further reduction of the investigated electrolyte. The superior feature of the BOB^- originated SEI was reported to advance the thermal reactivity of the lithiated graphite towards the nonaqueous electrolyte and in this way, an improvement in the safety characteristics of the negative electrode could be observed. In a further study performed by Jiang et al., the thermal stability of the lithiated graphite electrodes was investigated by means of accelerated rate calorimetry (ARC). According to the obtained results, the exothermic reaction between lithiated MCMB and the electrolyte began at 80 °C in a LiPF_6 salt-based electrolyte system, whereas in the presence of LiBOB it took place at 180 °C [59, 108, 109].

An interesting study involving a $\text{LiPF}_6 + \text{LiFSI} + \text{LiBOB}$ ternary salt blend for achieving improved electrochemical performance of MCMB/LFP full cells was conducted by Zhang et al. [77]. They indicated outstanding capacity retention (99.6% after 100 cycles) of an MCMB electrode in a 1 mol L^{-1} LiFSI-based EC/EMC (3:7 v/v) electrolyte which served as major reason to include LiFSI in the electrolyte; however, Al current collector dissolution in presence of the FSI^- anion limits application of these electrolyte formulations. In fact, the authors presented that LFP-based cells could only be cycled for seven cycles in $\text{LiFSI} + \text{LiPF}_6$ salt-blended electrolyte (1 mol L^{-1} LiPF_6 and 0.2 mol L^{-1} LiFSI) due to the severe Al dissolution. For this reason, the addition of LiBOB salt into this binary blend to effectively passivate Al surface with an optimum concentration of $\text{LiPF}_6 + \text{LiFSI} + \text{LiBOB}$ (0.8:0.2:0.2 mol L^{-1}) was proposed. The capacity retention values after 120 cycles in graphite-based cells containing LiPF_6 , $\text{LiPF}_6 + \text{LiFSI}$, $\text{LiPF}_6 + \text{LiFSI} + \text{LiBOB}$ as single, binary and ternary salt blends were reported to be 88.2, 93.5 and 97.0%, which was another proof for the effectiveness of the ternary blends on the cycling performance of graphite. Nevertheless, the rate

capability of the MCMB electrode in the $\text{LiPF}_6 + \text{LiFSI}$ salt blend-based electrolyte was slightly lower than that of the ternary blend ($\text{LiPF}_6 + \text{LiFSI} + \text{LiBOB}$), which could be explained by the higher SEI resistance caused by BOB.

Schedbauer et al. conducted a study on the composition of the SEI on copper surface in the presence of a $\text{LiBF}_4 + \text{LiBOB}$ salt blend-based electrolyte [62]. Results obtained by means of X-ray photoelectron spectroscopy (XPS) measurements showed that with increasing the LiBF_4 amount in the $\text{LiBF}_4 + \text{LiBOB}$ blend, the composition of the SEI displays similarity to that containing the LiDFOB salt. The interaction between LiBF_4 and LiBOB resulted in a trace amount of LiDFOB formation at room temperature as was confirmed by NMR measurements.

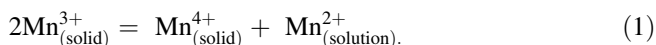
Cycling stability of lithium-metal batteries was limited by the lithium dendrite growth on lithium metal during repeated cycling which causes severe safety risks for commercial applications [110–113]. It is known that the SEI films on Li metal and lithiated graphite differ considerably [114, 115]. An electrolyte based on a $\text{LiTFSI} + \text{LiBOB}$ salt blend was investigated by Xiang et al. with an aim to improve the charging capability of $\text{LiNi}_{0.8}\text{Co}_{0.15}\text{Al}_{0.05}\text{O}_2$ (NCA)/Li half-cells [116]. In the investigated electrolyte system, LiBOB played a crucial role in forming an effective SEI film on Li metal and the mandatory Al current collector passivation, whereas LiTFSI functioned in modifying the features of the SEI film on the lithium metal by increasing ionic conductivity.

As stated by Zhang et al., blending of LiPF_6 and LiDFOB salts in a ternary carbonate-based electrolyte, contributed to improved performance of both artificial graphite (AG)/Li half- and AG/LFP 063048-type full cells [83]. Compared to a pure LiPF_6 -based electrolyte, in the presence of LiDFOB , a more effective SEI was formed in the initial cycles, resulting in a superior Coulombic efficiency of 98.2% in the third cycle and a reversible capacity of 339 mAh g^{-1} over 100 cycles in the AG/Li half-cell. The obtained CV results indicated a strong influence of LiDFOB on the Li^+ de-intercalation step. The optimized $\text{LiPF}_6/\text{LiDFOB}$ ratio was set to 1:4 (0.2 M:0.8 M). In the AG/LFP full cell setup, the obtained discharge capacity values were significantly higher compared to the pure LiPF_6 -based electrolyte. Furthermore, the presence of LiPF_6 in a blended salt system was found to compensate the poor ionic conductivity of the LiDFOB -based electrolyte. The authors even stated that it might additionally have a positive influence on the capacity values. After 100 cycles, the cell containing 0.2 M $\text{LiPF}_6 + 0.8 \text{ M LiDFOB}$ in EC/PC/DMC (1:1:3 v/v/v) electrolyte showed a capacity higher than the cell with the pure salt electrolyte. In addition, at elevated temperature (65°C), both discharge capacity and capacity retention of the optimized salt-blended electrolyte (351.3 mAh, 88.7%) were superior compared to the single salt containing electrolyte (121 mAh, 52%).

3.3.2 Anodic Stability of the Blended Salt-Based Electrolytes

In a study performed by Shieh et al., the effect of $\text{LiBOB} + \text{LiPF}_6$ salt blend on thermal stability, cycle life stability and Mn dissolution of LMO electrode was discussed [72]. Mn^{2+} dissolution from the LMO cathode material in the SOTA

electrolyte system (1 M LiPF₆ EC/DMC) at elevated temperatures and its consequences on cell chemistry are a well-known issue [117, 118]. At elevated temperature, decomposition of LiPF₆ triggers the Mn²⁺ dissolution from LMO via the Hunter's mechanism [119]:



Cycling investigations showed no significant difference in capacity fading of the single-salt containing systems (LiBOB or LiPF₆) with 79% capacity retention, whereas the capacity retention of the blended salt electrolytes (82% for 0.5 M LiBOB + 0.5 M LiPF₆) was reported to be superior to the single salt-based electrolyte after 100 cycles.

An electrolyte containing LiBOB + LiPF₆ salt blend, enabled a Mn²⁺ dissolution decrease from the LMO cathode thus stabilizing the LiPF₆ salt decomposition during cycling at elevated temperature as well as enhancing the electrochemical performance of the cell. In conclusion, the blended salt concept potentially allowed for application of LMO at elevated temperatures (>55 °C). A similar study, performed by Chen et al. [73], confirmed the findings of Shieh et al. [72]. Their results showed that the power capability of lithium ion cells decreases with increasing LiBOB concentration; however capacity retention of the cells at 55 °C increased with LiBOB concentration which is in line with the results obtained by Shieh et al. [52]. Furthermore, they specified the optimum concentration of LiBOB as 0.1 M, using MCMB/NMC full cells at 55 °C. MCMB/spinel full cell cycling at 55 °C with 0.1 C current rate showed a clear evidence of poor cycling behavior in the SOTA electrolyte formulation (1.2 M LiPF₆ in EC/PC/DMC) that led to more than 50% capacity loss in 300 cycles, most probably due to Mn²⁺ migration from the positive to the negative electrode and deterioration of the SEI. However, the pure LiBOB and blended (LiPF₆ + LiBOB) salt systems significantly improved the cycling stability of the cell, which pointed out an effective CEI formation and suppressed Mn²⁺ dissolution in presence of LiBOB.

A ternary salt blend containing LiPF₆ as main salt, with LiFSI and LiBOB as co-salts was investigated by Zhang et al. for improved electrochemical performance of a graphite/LFP full cell [77]. The aim of their study was to tailor the electrolyte by using LiFSI (high conductivity and good cycling stability) + LiBOB (beneficial Al current collector passivation behavior) blend. Graphite/LFP full cells cycled in this ternary salt blend-based electrolyte exhibited improved cycling characteristics; the Coulombic efficiency was close to 100% over 200 cycles.

LiFSI, as conducting salt, generated widespread interest in LIB science owing to its promising features, e.g. absence of hydrogen fluoride (HF) release, enabling good electrolyte conductivity, high-rate capability and low electrolyte viscosity [85, 120]. However, a key challenge is addressed to the Al current collector dissolution, thus limiting the application of this salt [121].

An electrolyte based on LiTFSI + LiBOB blend was suggested by Xiang et al. to improve the charging capabilities of NCA/Li half-cells [116]. In such electrolyte system, LiBOB takes part in formation of an effective SEI film and passivation of

the Al current collector, whereas LiTFSI functioned in modifying the SEI on lithium metal by increasing its ionic conductivity.

In view of the realization of high voltage LIBs, it is important to introduce electrochemically stable electrolyte systems that operate beyond 5 V vs. Li/Li⁺. Li et al. investigated a blended salt-based electrolyte formulation with an aim to improve the cycling stability of the LNMO cathode at high potentials [122]. In their study, LiBOB had a role of a main conducting salt, whereas lithium difluoro(-sulfato)borate (LiBSO₄F₂) was used as a co-salt in 0.1 M to create an effective CEI at the LNMO cathode surface. As suggested by the authors, LiBSO₄F₂ formed a smooth and uniform, thus low resistive CEI. Their findings indicated that the LiBSO₄F₂ + LiBOB-based electrolyte exhibited a lower charge-transfer impedance with LNMO due to the formation of a CEI, which was found to be rich in sulfurous compounds. The oxidation stability increased from 5.3 to 5.6 V vs. Li/Li⁺. Moreover, the influence of the co-salt was further proven by electrochemical impedance spectroscopy results showing that the LiBSO₄F₂ salt reduced the charge-transfer impedance. The capacity retention of LNMO electrodes in this blended salt system was reported to be 98.9% after 100 cycles, whereas only 92.8% retention could be achieved in the single salt electrolyte. Finally, the C-rate capability was improved with the salt blend-based electrolyte.

In a recent study, Zhou et al. indicated the LiDFOB + LiBF₄ salt blend as a promising candidate for enabling the high voltage LNMO cathode active material [78]. The authors reported enhanced electrochemical kinetics at room temperature of the LNMO electrodes in the electrolyte containing high amount of LiDFOB compared to the pure LiBF₄-based electrolyte as well as the strong influence of this salt on reaction reversibility and capacity retention of the investigated graphite/LNMO full cells. As a result of the effective CEI formation in presence of LiDFOB (LiDFOB/LiBF₄ ratio = 4:1), the specific capacity and capacity retention after 100 cycles amounted to 120.7 mAh g⁻¹ and 95.2%, respectively. SEM results of the pristine and cycled LNMO electrodes confirmed the formation of thin CEI layer in the presence of LiDFOB + LiBF₄ salt-blended electrolyte, whereas in case of the pure LiBF₄-containing electrolyte, continuous electrolyte decomposition led to a formation of thick and dense CEI layer which had a detrimental effect on the capacity retention at elevated temperature. In addition, the fluoroborate salts LiBF₄ and LiDFOB in an equimolar blend of 0.1 M in DMC showed an oxidation stability up to 4.9 V vs. Li/Li⁺ [82]. By combining the advantages of both conducting salts, the LiTFSI + LiDFOB blend in EC/EMC (4:6 by wt.)-based electrolyte formulation was found to significantly improve the electrochemical performance of the LFP electrode. The optimum amount was determined to be 1 M LiTFSI_{0.6} + LiDFOB_{0.4}. Although the increase of LiDFOB concentration improved the cycling performance, concentrations higher than 0.4 M would lead to the higher cell impedance. Figure 15 illustrates the voltage profiles of LFP/Li half-cells at different C-rates of the salt blend containing electrolyte compared to the pure LiPF₆-based electrolyte.

The reasons behind the improved Coulombic efficiencies were related to superior water and thermal stabilities of both the LiBF₄ and LiDFOB salt resulting in suppressed iron dissolution and weak parasitic reactions.

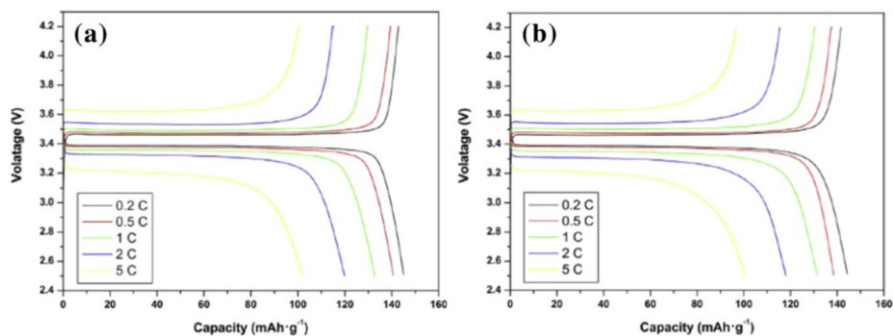


Fig. 15 Rate capability of LFP/Li half-cells in electrolytes containing **a** 1 M LiTFSI_{0.6} + LiODFB_{0.4} and **b** 1 M LiPF₆. Reprinted from Ref. [86]. Copyright (2015) with permission from Elsevier

3.3.3 C-Rate Capability and Capacity Retention of the Blended Salt-Based Electrolytes

As reported by Chen et al. [73], no considerable change in cycling stability between the investigated single and binary salts containing electrolytes was observed, whereas differences in capacity retention at elevated temperatures (55 °C) were clearly visible, as reflected from Fig. 16. The LiBOB containing electrolyte presented a better cycling performance in graphite/NMC full cells (10% capacity loss over 60 cycles in LiBOB free electrolyte). Similarly, a poor capacity retention was reported for the graphite/spinel full cells (50% loss in 300 cycles) at 55 °C. The ternary salt blend (LiPF₆ + LiBOB + LiFSI) exhibited a capacity retention close to 100% with a specific discharge capacity of 153.9 mAh g⁻¹ for graphite/LFP full cells [77].

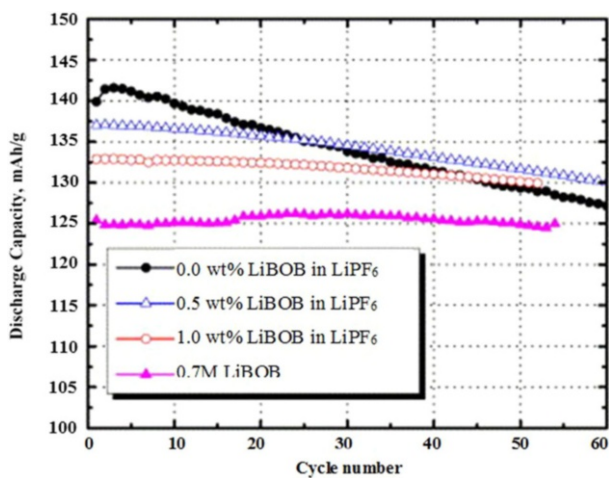


Fig. 16 Capacity retention of graphite/NMC (MCMB-1028/L333 cells at 55 °C). The cells were cycled with a constant current of C/2 (~1.2 mA). Redrawn from Ref. [73]. Copyright (2006) with permission of Elsevier

Cycling stabilities of graphite/LiNiO₂ cells containing LiBOB + LiBF₄ salt blend in PC/EC/EMC-based electrolyte were reported by Zhang et al. [95]. The results indicated that the cell maintained 90% of the initial capacity after 180 cycles at room temperature in 2 mol% LiBOB containing electrolyte formulation. Another study on LiBOB + LiPF₆ blends stated that the capacity loss for the blended salt-based electrolyte (0.75 M LiPF₆ + 0.25 M LiBOB) was 16%, whereas 23% was observed in the LiPF₆ case over 250 cycles at 55 °C [72].

The capacity retentions of several blended electrolyte systems containing LiBF₄ + LiBOB (8:2) in various solvent blends with LiPF₆ as reference were reported by Lai et al. [76]. Their findings indicated that at elevated temperature (65 °C) the LiPF₆-based electrolyte presented 77% capacity retention in LFP/Li half-cells, whereas LiBF₄ and LiBOB blends maintained the capacities at 79–85% of the initial value. In this respect, 1 M LiBF₄ + LiBOB (8:2) salt blend in EC/PC/EMC (1:1:3) was identified as the most promising electrolyte formulation. A similar study performed by Zhang et al. disclosed a capacity retention of the LiBF₄ + LiBOB salt blend for the LFP/Li half-cell as 87.5% as compared to LiTFSI + LiBOB with 85.1% and LiPF₆ with 79.3% over 100 cycles at 65 °C, [87]. With these findings in line, blended salt electrolytes demonstrated better capacity retention at high temperature as compared to the single-salt system.

3.3.4 Suppression of Aluminum Dissolution by Blended Salt-Based Electrolytes

To ensure safe and long-lasting performance, a compact protective passivation layer must be formed on the surface of the Al current collector. The following factors mainly determine the passivation process: the upper cut-off potential, the electrolyte solvents, additives, and the used conducting salt. The potential at which the oxidation dissolution current rapidly increases in reference to the background current is called ‘pitting potential (E_p)’. Only at potentials higher than E_p , the oxidation currents vary with the conducting salt. The presence of LiBF₄ and LiPF₆ suppresses this current at higher potential values, thus enabling effective passivation of the Al surface and preventing further oxidation. On the contrary, lithium imide salts (LiIm) are known for promoting severe Al current collector dissolution [123, 124]. Among them, LiFSI was reported as promising salt to overcome the well-known limitations of LiPF₆ [120, 121]. With this in line, Park et al. systematically investigated the inhibition of dissolution in LiFSI in EC/DEC (3:7 v/v) electrolytes by addition of selected Li borate salts and revealed the following order of their inhibition ability: LiDFOB > LiBF₄ ≈ LiPF₆ > LiBOB [84]. Furthermore, a 0.8 M LiFSI + 0.2 M LiDFOB salt blend in EC/DEC (3:7 v/v) showed remarkable inhibition of Al dissolution, even comparable to a 1 M LiPF₆ electrolyte. As depicted in Fig. 17, the superior inhibition ability of LiDFOB, compared to other investigated borate salts, was assigned to the increased thickness (~24.4 nm) of the passivation surface layer compared to the layer in other blends (<1 nm) as well as to the nature of its constituents, Al–F, Al₂O₃ and B–O/B–F species [84]. B–O compounds are known for their ability to protect Al surface from dissolution caused by LiIm salt-based electrolytes [125]. LiDFOB was suggested as the most effective complementary salt to LiFSI for improving Al stability.

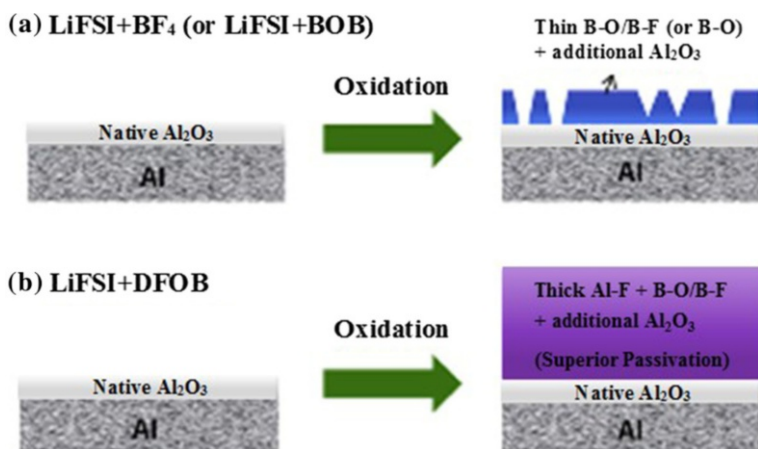


Fig. 17 Schematic diagram of passive layer formation on an Al electrode cycled in EC/DEC (3:7 v/v) electrolyte containing **a** LiFSI + LiBF₄ or LiFSI + LiBOB and **b** LiFSI + LiDFOB salt blends. Redrawn from Ref. [84] Copyright (2015) with permission of Elsevier

A study by Li et al. revealed the effective suppression of Al dissolution in 1 M LiTFSI in EC/EMC (4:6 by wt.) electrolyte by addition of LiDFOB as co-salt (2 wt%), comparable to the pure 1 M LiPF₆-based electrolyte.

The performed XPS measurements revealed the presence of B, F, O, N and S elements in the passivation layer as a result of LiDFOB and LiTFSI decomposition, thus pointing out the presence of B–O species as meritorious for this protection effect [86]. Besides LiDFOB, the presence of LiBF₄ had a positive influence on Al dissolution behavior due to the tendency of passive layer formation [126]. As stated by Zhang et al., the following stability order of salts was established in a EC/DME solvent blend: LiBF₄ > LiPF₆ > LiIm [124]. The Al pitting in LiTFSI-based electrolyte could be depressed by LiBF₄ as co-salt, as shown by Song et al. [127]. By means of electrochemical quartz crystal microbalance (EQCM)—CV and SEM techniques, the authors revealed passivation of the Al current collector to take place as well as suppression of the dissolution process in a 0.5 M LiTFSI + 0.5 M LiBF₄ in EC/DMC (1:1 by wt.) electrolyte. FT-IR spectroscopy and EDX analysis indicated Al[N(SO₂CF₃)₂]_{3-y}(OH)_y (y = 0, 1, 2) as the main dissolution product, RCO₂M (M = Al and/or Li) as organic species and lithium oxalate as well as B-F containing compounds as Al current collector passivation products. In view of these findings, the LiTFSI + LiBF₄ salt blend was assumed to increase the resistance of the Al current collector by passivation [127]. When Al was polarized to high potential values (5.5 V vs. Li/Li⁺), a passivation film, formed on the Al surface, mainly contained Al_xBO₃ species [128]. LiBOB was included in several salt blends, e.g. blends with LiTFSI and LiFSI, due to its Al passivation features [77, 87].

Various approaches were suggested to improve the stability of the Al current collector at high potentials (>3.8 V vs. Li/Li⁺) in LiFSI- and LiTFSI-based electrolytes, for instance by using new solvents [52, 129, 130] or by blending several salts with LiFSI or LiTFSI, e.g. with LiPF₆ [49], LiBF₄ [127] and LiBOB [125].

3.4 Summary

The conducting salt LiPF_6 was identified as the skeletal electrolyte component of SOTA electrolytes; however, its well-known drawbacks limit the performance of the lithium ion cells beyond the temperature range: -20 to 50 °C. The blending concept contributes to overcoming the handicaps of the single salt-based electrolyte with the aim to achieve improvements in the transport properties as well as the thermal stability of the nonaqueous electrolyte, enhancement of cycling efficiency of the cell and finally for bringing more safety to consumer electronics. Under the synergistic effect, salt blends combine the advantages of the individual salts and result in improved overall cell performance. In this chapter, the effect of different salt blends on the physicochemical and electrochemical features of nonaqueous electrolytes for LIB was discussed and compared to the single salt formulations. Literature examples of blended salt electrolytes that revealed the influence of blending on anode and cathode performance, suppression or inhibition of Al dissolution as well as the overall cell performance are summarized in Table 8.

Although a salt-blend approach seems as a promising strategy for tuning the nonaqueous electrolytes towards improved performance, there are still important questions left unanswered. Among them, the exact mechanisms of the synergistic effect of blended salts remain unclear as well as whether the beneficial effect on electrochemical performance can be maintained at high and low temperatures or not.

4 Blended Additive Containing Electrolytes

For improvement of SOTA electrolyte formulations, the addition of small amounts of electrolyte additives is a low cost and effective strategy. The specific function of the additives is directed to: (1) improvement of the interfaces/interphases at anode and cathode, (2) stabilization of the lithium salt, (3) improvement of safety such as overcharge protection and flame retardant, (4) improvement of wetting properties, (5) trapping of undesired components and (6) improvement of electrolyte conductivity [131]. In recent years, research expanded from single additives on the electrolyte additive blends for combining different functions in one electrolyte formulation. With this in line, in this chapter, the status of research in the field of blended additive systems is reviewed and comparatively discussed.

4.1 Safety Protection Agents

4.1.1 Flame Retardant Additive Blends

Safety is still a major issue in LIBs due to the high flammability of the nonaqueous organic solvents present in SOTA electrolytes [131, 132]. Any attempt to decrease the flammability of the electrolyte, will pave the way for safer LIBs, for instance by using flame retardant additives [131] or fluorinated compounds as electrolyte solvents [133–136]. Among flame retardant additives, organophosphorous compounds, i.e. trimethylphosphate (TMP) [137] were well studied for the application in

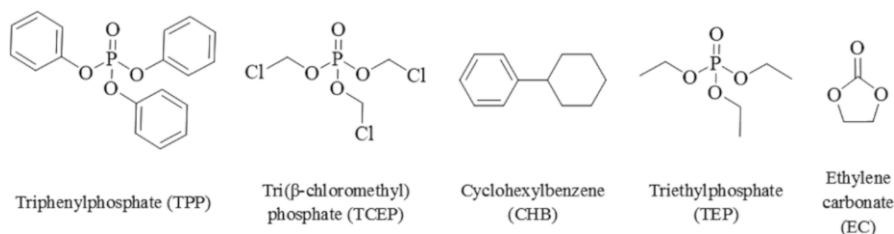
Table 8 Major roles of the discussed lithium salt blends in investigated electrolytes

Lithium salt blend	Target improvement	Investigated electrolyte	References
	Promoted SEI formation	5 mol% LiBOB in LiPF ₆ -based EC/PC (1:1 v/v)	[107]
LiPF ₆	LiBOB	5 mol% LiBOB in LiPF ₆ -based EC/PC/EMC (3:3:4 v/v/v)	
	Suppressed Mn dissolution in LMO	0.5 M LiBOB + 0.5 M LiPF ₆ -based EC/EMC (1:1 v/v)	[72]
	Improved thermal stability of the graphite/LMO		
	Improved conductivity of the electrolyte for high power applications		
	Improved capacity retention of MCMB/NMC full cells at 55 °C	0.5, 1.0 wt% LiBOB + 1.2 M LiPF ₆ in EC/PC/DMC (1:1:3 by wt.)	[73]
LiPF ₆	LiBOB, LiFSI	0.8 M LiPF ₆ + 0.2 M LiFSI + 0.2 M LiBOB in EC/EMC (3:7 v/v)	[77]
	Promoted SEI formation		
	Stabilization of the Al surface		
	Improved cycling performance in graphite/Li and graphite/LFP full cells		
LiPF ₆	LiBOB, LiDFOB	0.65 mol kg ⁻¹ LiPF ₆ + 0.05 mol kg ⁻¹ LiBOB + 0.05 mol kg ⁻¹ LiDFOB in EC/DMSN (80:20 wt.)	[75]
	Achieving high C-rates up to 1.5C with >80% of the initial specific discharge capacity for carbon/NMC full cells		
LiPF ₆	LiDFOB	0.2 M LiPF ₆ + 0.8 M LiDFOB in EC/PC/DMC (1:1:3 v/v/v)	[83]
	Distinct improvement in cycling efficiency and specific capacity of artificial graphite (AG)/Li half-cells		
	Improvement in cycling performance of AG/LFP 063048-type cells at 65 °C		
	Promoted SEI formation	1–5 mol% LiBOB + 1 m LiBF ₄ in PC/EC/EMC (1:1:3)	[95]
	Improved cycling performance in graphite/Li half-cells	1–5 mol% LiBOB in 1 m LiBF ₄ in PC/EC (1:1)	
LiBF ₄	LiBOB	0.5 M LiBF ₄ + 0.5 M LiBOB in EC/DEC (3:7 by wt.)	[62]
	Promoted SEI formation	LiBF ₄ + LiBOB blend in PC/EC/EMC (1:1:3 v/v)	[87]
	Improved thermal stability		
	Suppressed Al dissolution		
	Promoted SEI formation	1 M LiBF ₄ + LiBOB (8:2) in PC/EC/EMC (1:1:3 v/v)	[76]
	Wide operating temperature range	1 M LiBF ₄ + LiBOB (8:2) in PC/EC/EMC:MB (1:1:2:1 v/v/v/v)	

Table 8 continued

Lithium salt blend	Target improvement	Investigated electrolyte	References
LiBF ₄ LiTFSI	Suppressed Al dissolution	0.2 M LiBF ₄ + 0.8 M LiTFSI in EC/DMC (1:1) 0.5 M LiBF ₄ + 0.5 M LiTFSI in EC/DMC (1:1)	[127]
LiBF ₄ LiDFOB	Improved capacity and capacity retention of graphite/LNMO full cells at RT and 60 °C Improved cycling ability in high rate cycling at -20 °C Improved ionic conductivity, high thermal stability and wide potential window	0.2 M LiBF ₄ + 0.8 M LiDFOB in EC/DMC/EMC (1:1:1 by wt.) 0.8 M LiBF ₄ + 0.2 M LiDFOB in EC/DMC/EMC (1:1:1 by wt.) 0.5 M LiBF ₄ + 0.5 M LiDFOB in EC/PC/DMC (1:1:3)	[78] [82]
LiBOB LiBSO ₄ F ₂	Increased anodic stability of the electrolyte for high potential applications Stabilized surface of NMO electrode	0.1 M (LiBSO ₄ F ₂) + 0.7 M LiBOB in EC/DMC (1:1 v/v)	[109]
LiFSI LiDFOB	Inhibited Al dissolution Comparable rate capability to LiPF ₆ -based electrolyte	0.8 M LiFSI + 0.2 M LiDFOB in EC/DEC (1:1 v/v)	[84]
LiTFSI LiDFOB	Effective suppression of Al dissolution Improved Coulombic efficiencies Outstanding thermal and water stability, suppression of iron dissolution in LFP-based cells	0.6 M LiTFSI + 0.4 M LiDFOB in EC/EMC (4:6 by wt.)	[86]

LIBs, however a high concentration (>35 wt%) was necessary to suppress the flammability of the electrolyte formulation [137–140], unfortunately leading to higher viscosity, lower ionic conductivity and poor graphitic compatibility. One way to overcome the poor cathodic stability was related to fluorination of organophosphorous compounds. This resulted in a formation of an effective SEI [43, 141–143]. Another advantage of the fluorinated compounds refers to their ability to suppress flammability. The additives investigated in this behalf are displayed in Scheme 4.

**Scheme 4** Molecular structures of the flame retardant additives

Several additive blends combining flame retardant and SEI/CEI formation features were reported by Nam et al. [144] and Shim et al. [145]. These studies investigated the performance of 3 wt% triphenylphosphate (TPP) with different film-forming additives as blends in 1.1 M LiPF₆ EC/EMC (4:6 v/v) electrolyte for graphite/LCO full cells. In an additive blend, TPP had the role of a flame retardant [146–152] by scavenging hydrogen radicals in the flame, thus prohibiting chain reactions and flame propagation [138, 153]. Additionally, it formed a fire resisting char layer that suffocated the flame but the flash point was not significantly altered. This finding indicated decomposition of TPP essential for the action as a flame retardant [146]. The thermal stability was investigated by means of DSC measurements. Nam et al. [144] and Shim et al. [145] showed that in case of the TPP containing blended electrolyte formulation, the endothermic peak could be shifted to higher temperature by 20 °C compared to the standard electrolyte. The blend of TPP and vinyl acetate (VA) showed even higher thermal stability since the endothermic peak could be shifted to higher temperature by 25 °C. Another example of a flame retardant and film-forming additive blends was reported by He et al. [154]. Their study focused on the additive blend tri(β-chloromethyl) phosphate (TCEP) together with cyclohexylbenzene (CHB) in 1 M LiPF₆ EC/DMC/EMC (1:1:1 by wt.) electrolyte. TCEP is known as a flame retardant [154], whereas CHB is an additive that protects the cell during overcharge [155]. He et al. showed that TCEP absorbs hydrogen radicals during the decomposition and therefore reduces the possibility of endothermic chain reaction induced by free radicals. As shown in Fig. 18, the addition of TCEP to the electrolyte reduced the flammability, whereas the addition of CHB led to an increase. The blend of 5 wt% TCEP and 5 wt% CHB showed the lowest flammability, indicating a high impact of TCEP on the SET and therefore improved safety characteristic of the investigated electrolyte.

So far, there has always been a trade-off between achieving non-flammability and, at the same, time decreasing cell performance (faster capacity fading/lower

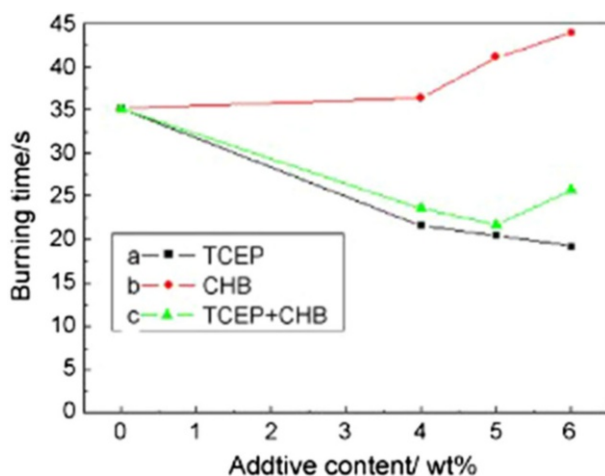
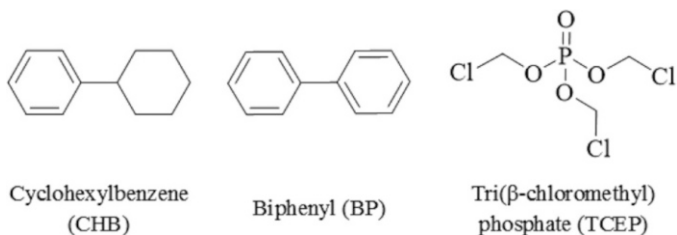


Fig. 18 SET determination of the 1 M LiPF₆ EC/DMC/EMC (1:1:1 by wt.) electrolyte with TCEP and CHB as additives. Reprinted from Ref. [154]. Copyright (2007) with permission of Elsevier

power) or deteriorating physical influences (high melting point/high viscosity) by using flame retardants in combination with organic solvents [138, 156]. Therefore, RTILs are considered as one of the safest electrolyte components since they are flammable only at very high temperatures, non-volatile, and relatively thermally stable [157, 158], depending on the respective IL composition. Furthermore, they have a wide liquidus range and relatively wide ESW, in particular a high oxidation stability of ILs with fluorinated anions [159, 160]. However, IL-based LIB electrolytes are often highly viscous and thus exhibit low ionic conductivity compared to conventional nonaqueous electrolytes [22, 161]. Using a small amount of organic compound as an additive is an alternative way to overcome aforementioned limitations. On the one hand, these additives will improve the conductivity by reducing the viscosity. On the other hand, the addition of organic solvents will significantly affect the flammability and thermal properties of the electrolyte. For this reason, a non-flammable additive is required to guarantee safe operation of the cell. Lalia et al. [162] investigated *N*-methyl-*N*-propylpiperidinium bis(trifluoromethylsulfonyl)imide (PP₁₃-TFSI) with addition of triethylphosphate (TEP) and EC in a volume ratio of 80:10:10 in graphite/LMO full cells. The alkylphosphate TEP showed low viscosity, low melting point, high boiling point, non-flammability and a relatively high dielectric constant [137]. TEP as an additive was added to suppress the flammability of the organic electrolyte, to improve the ionic conductivity, viscosity and thermal stability of the PP₁₃-TFSI-based electrolyte. The disadvantage of this compound was related to the instability towards reductive decomposition on the graphite anode surface and a poor long-term cycling stability [162]. EC, commonly used as electrolyte solvent [163], whereas here in additive amounts, had the role to form an effective SEI between a graphite-based negative electrode and the nonaqueous electrolyte. The direct flame test of TEP and EC binary blend in 0.4 M LiTFSI/PP₁₃-TFSI electrolyte showed that with an equal ratio of TEP and EC, the system was completely non-flammable and could thus serve as a safe electrolyte for LIBs. Furthermore, TEP with a high dielectric constant and low viscosity was able to increase the ionic conductivity and to improve the electrochemical performance, as well.

4.1.2 Overcharge Protection Additive Blends

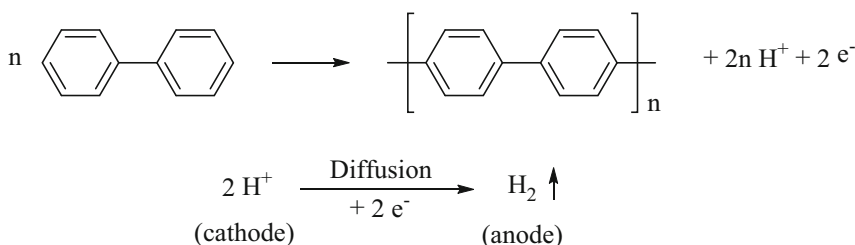
Unlike aqueous electrolyte batteries, where the decomposition of the solvent water is the basis for ‘the oxygen-cycle’ [164, 165], the nonaqueous (water-free) electrolyte LIB technology has no intrinsic chemical/electrochemical overcharge protection included in the battery solvent [166]. Overcharge can result in severe performance degradation and safety problems [167]. Overcharge protection additives can be categorized as reversible redox shuttle- and irreversible shut down additives [131]. One promising class of the latter category are compounds that polymerize electrochemically on the surface of the cathode or create, by decomposition, reactive species that induce the polymerization of the base electrolyte [155, 168–170]. Vinylene [171–174] and isocyanate [175] compounds are known to electrochemically polymerize both during reduction [176] or oxidation [177]. The over-charge additives discussed in this behalf are displayed in Scheme 5.



Scheme 5 Molecular structures of the overcharge protection additives

Biphenyl (BP), for instance, was studied as an aromatic shutdown additive [144, 168, 178]. The mechanism can be described as follows: (1) BP is oxidized at the cathode side, (2) the oxidized products form through radical coupling a poly(*p*-phenylene)-type polymer that is depositing on the cathode surface and growing through the separator to anode side, creating an electronic short circuit that carries a part of the over-charge current, (3) the co-generated protons diffuse through the electrolyte and to the anode side, (4) at the anode are reduced to hydrogen increasing the internal and cell pressure and (5) the pressure increase in the cell is activating a current interrupt device (CID) that is interrupting the external current circuit, this the current causing over-charge is interrupted (Scheme 6) [168, 179].

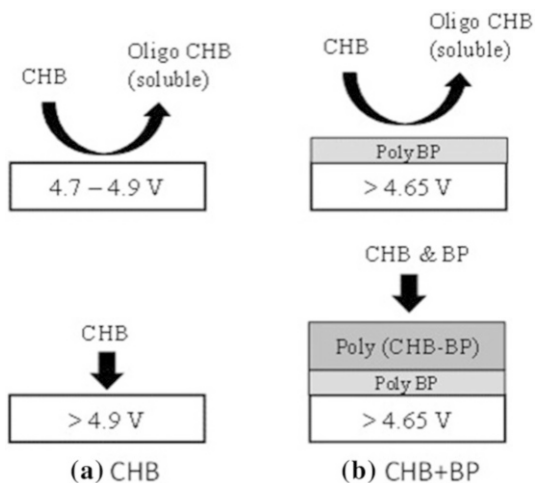
The oxidation products can be described as condensed aromatic compounds with a widespread π -electron conjugation system and the bond formation mainly occurs at the *ortho*-positions of the phenyl group [178]. However, a high concentration of BP within the electrolyte would lead to a decrease in lithium cycling efficiency. The hydrogenated form of BP is CHB and has a higher oxidation potential than BP, making it more inert towards undesirable side reactions during operation in the normal voltage range of the cell. CHB also shows higher lithium cycling efficiency than BP, allowing the interpretation that it is more stable towards charged anode electrodes [155]. BP and CHB both belong to overcharge protection agents called non-redox shuttle type, with the same overcharge protection mechanism during electrochemical oxidation [178]. Lee et al. found that the co-use of CHB and BP in 1 M LiPF₆ EC/EMC (1:2 v/v) in graphite/LCO full cells is much more effective for overcharge protection than using BP or CHB alone (Table 9) [180]. The synergistic effect in overcharge protection was proven in pouch cells with a nominal capacity of 760 mAh by applying a constant current with a voltage limit of



Scheme 6 Proposed mechanism of electropolymerization and hydrogen evaluation of BP

Table 9 Number of the passes over total trials during overcharge tests for graphite/LCO full cells with various CHB and BP composition in 1 M LiPF₆ EC/EMC (1:2 v/v) Adapted from [180]

CHB (%)	BP (%)	12 V and 1 A passes/trials	12 V and 2 A passes/trials
0.0	0.0	0/3	0/3
3.0	0.0	0/1	1/2
4.0	0.0	2/2	8/10
3.5	0.5	–	10/10
3.0	1.0	3/3	3/3
3.0	2.0	3/3	3/3

Fig. 19 Electropolymerization process for **a** CHB and **b** CHB + PB on Pt electrodes. Redrawn from Ref. [180]

12 V and a magnitude of the current among 0.5, 1 and 2 A. Prior to the overcharge test, cells were cycled to 4.2 V several times and were fully discharged in the last cycle. It was shown that the addition of CHB helps to increase the safety in case of overcharge but the electrolyte containing blend with BP is much more effective than the CHB containing electrolyte. The blend of CHB and BP expanded the safety region up to 12 V and 2 A, which the single additive CHB could never reach. This synergistic effect was studied in electropolymerization measurements on Pt electrodes and explained as following (Fig. 19): CHB alone formed a polymer film on the Pt surface above 4.9 V. At lower values, the oxidation products of CHB seem to be too soluble to precipitate or the adhesion to the Pt surface is too weak. By increasing the concentration of the oxidation products, a polymer film can be formed on the surface.

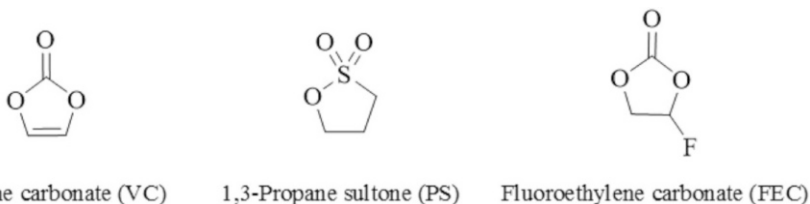
In contrast, when using the blend, BP formed a polymer film from 4.65 V. The formed poly-BP film, resulting in much more effective polymer deposition on the surface, catalyzes the oxidation of CHB and probably BP. The application of a shutdown and flame retardant additive at the same time was disclosed by He et al. [154]. Here, the electrolyte blend contained 5 wt% CHB as shutdown and 5 wt%

TCEP as flame retardant additive to improve the safety characteristics of the investigated cells. Hereby, the surface analysis of LiCoO_2 electrodes after overcharge indicates a polymer film on the surface, which can be attributed to CHB. Furthermore, the temperature change during overcharge showed an exothermic peak after 30 min, which proves the exothermic polymerization process of CHB. This generated heat can be absorbed by chloroethane, a decomposition product of TCEP. Through this synergistic effect, the increase of temperature can be delayed.

4.2 SEI and CEI Film-Forming Additive Blends

Utilization of electrolyte additives that form in situ SEI on the anode/CEI on the cathode side is one of the most effective methods to suppress further electrolyte decomposition and protect the electrode active material from degradation, thus decreasing the internal resistance of the cell [131, 181, 182]. A blend of different film-forming additives can be used either to form an effective SEI and CEI at the same time or to strengthen the surface film-formed by one single additive. Small amounts of organic solvents as additives were used to form an electrochemically effective SEI prior to reduction of IL [131, 183, 184]. With this in line, Kim et al. investigated a binary additive blend based on 1-butyl-1-methylpyrrolidinium bis(trifluoromethylsulfonyl)imide (BMP-TFSI) with 10% (1:1 by wt.) VC and 1,3-propane sultone (PS) (Scheme 7) in LTO/LCO full cells [185]. VC is a well-known and intensively studied SEI additive [143, 174, 186–188]. It improves thermal stability of the surface layer due to the formation of polymeric species [189], well known also for other vinylene compounds [138–141]. Furthermore, PS is able to form an SEI on the anode [184, 190–192]. Xu et al. [184] reported PS containing electrolyte formulations to modify the cathode surface, which resulted in an improved cycling performance. The addition of organic solvents suppresses the reductive decomposition of BMP-TFSI. Moreover, high discharge capacities and improved capacity retention could be achieved by using the combination of VC + PS. FTIR measurements of the blended system showed that the film on the LTO electrode surface consists of a polymeric/organic and inorganic salt species blend and was more compact and dense when using the additive blend instead of VC or PS alone [185].

Additionally, VC is a well-known and studied SEI additive for silicon (Si)-based electrodes [193, 194]. This alternative anode material displayed a high theoretical Li storage capacity, volumetric capacity as well as gravimetric capacity [195, 196].



Scheme 7 Molecular structures of the film-forming additives

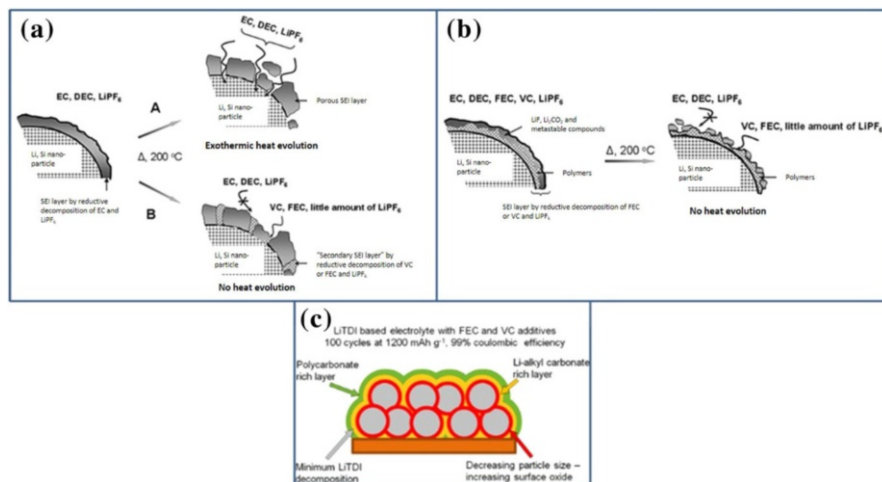
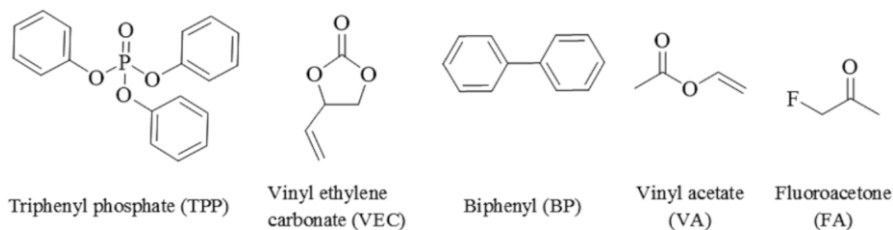


Fig. 20 **a** A schematic diagram showing the thermal events in the Li_xSi -Ref system that occur while heating up to $200\text{ }^\circ\text{C}$ (route A). Thermal degradation of the SEI layer makes it porous and permeable to the electrolyte components, such as EC, DEC, and LiPF_6 . Direct contact between the components and Li_xSi initiates the thermal runaway. The thermal reactions of Li_xSi that was lithiated in the Ref electrolyte, washed, dried and heated in contact with either FEC10 or VC10 are shown in route B. Upon thermal degradation, the FEC and VC additives in contact with Li_xSi provide the “secondary SEI” layer, which does not allow direct interaction between Li_xSi and the electrolyte. **b** A schematic diagram showing the protective function of the FEC- and VC-derived SEI layers on the surface of the lithiated Si nano-particles during heating up to $200\text{ }^\circ\text{C}$. The SEI layer, which forms electrochemically, is mostly composed of a polymeric species and shows excellent stability at elevated temperatures. **c** A schematic drawing of the formed SEI in the presence of both additives FEC and VC. The inner shell mainly consists out of lithium alkyl carbonates (yellow), whereas the outer shell mainly consists out of polycarbonates (green). Redrawn from Ref [143, 202]. Copyright (2013 and 2016) with permission of Elsevier and ACS

However, large volume expansion upon extraction and insertion of Li led to a decreased electronic conductivity resulting in capacity fading [197]. Besides VC, fluoroethylene carbonate (FEC) (Scheme 7) is another thoroughly studied SEI additive for Si-based electrodes [198–201]. The thermal stability of VC and FEC was studied by Profatilova et al. [143]. The authors showed that the SEI formed by the 1 M LiPF_6 in EC:DEC (3:7 by wt.) electrolyte cracked open by heating up to $200\text{ }^\circ\text{C}$, thus resulting in a formation of a permeable SEI layer. This allowed the electrolyte to interact with the Li_xSi nano-particles. When using the electrolyte containing either 10 wt% VC or FEC, a so-called secondary SEI layer could be formed. The decomposition reactions driven by VC or FEC were similar and resulted in formation of polycarbonates, thus preventing direct contact between the electrolyte formulation and Li_xSi nano-particles. It was induced immediately when the SEI cracked open at elevated temperatures (Fig. 20a). Furthermore, VC and FEC formed a so-called primary SEI layer during charge, which was mainly formed by polycarbonate species. The decomposition layer of 1 M LiPF_6 in EC:DEC (3:7 by wt.) was formed on top of it. By heating up this electrode to $200\text{ }^\circ\text{C}$ only the outer shell of the primary SEI cracked open. Nevertheless, the Li_xSi nano-particles were still protected by the polymers formed by either VC or FEC, preventing the contact between the electrode and electrolyte (Fig. 20b).

The combination of both SEI additives for the application of Si anode materials was first studied by Mazouzi et al. [203]. The investigated electrolyte was 1 M LiPF₆ in either EC/DMC (1:1 by wt.) or EC/DEC (1:1 by wt.) with 10 wt% FEC and 2 wt% VC in Si/Li half-cells. They showed that using this additive blended electrolyte formulation, the kinetics of the electrolyte degradation was slowed down due to the prior reduction of VC and FEC compared to EC. The reduction products were more stable and limited the EC reduction, thus resulting in a strongly improved cycling performance. The work of Gauthier et al. [204] confirmed those results. They used 1 M LiPF₆ in EC/DEC (1:1 by wt.) with 10 wt% FEC and 2 wt% VC as a blended electrolyte formulation in Si/Li half-cells. The cells could be charged up to 900 cycles with a Coulombic efficiency of 99%. The synergistic effect of both SEI additives was studied by Lindgren et al. in Si/Li half-cells containing 0.6 M 4,5-dicyano-2-(trifluoromethyl) imidazolid (LiTDI) in EC/DMC (2:1 v/v) with 5 vol% FEC and 1 vol% VC [202]. Besides the improved cycling performance up to 100 cycles with a Coulombic efficiency of 99%, they showed the importance of LiTDI and the blended electrolyte formulation. The additive blend significantly contributed the SEI formation; otherwise, an ineffective SEI was formed and accelerated lithium silicate formation. LiTDI was only partially involved in the SEI formation, whereas the main part was LiF, formed by decomposition of FEC. The formed SEI consisted of an inner and outer shell. The inner shell mainly consisted of the decomposition products driven by the lithium alkyl carbonates, whereas the outer shell mainly of polycarbonates (Fig. 20c). They claimed that the high content of LiF as well as the large extent of polycarbonates was essential for the cycling performance of Si anodes. Furthermore, as mentioned above, Nam et al. [144] and Shim et al. [145] studied blended additive electrolytes containing the flame retardant TPP together with different film-forming additives such as vinyl ethylene carbonate (VEC), biphenyl (BP), VA and VC. Their molecular structures are displayed in Scheme 8.

VEC could be reduced at potentials above 1 V vs. Li/Li⁺ due to the electron-rich double bond and was therefore found to be a good SEI-film-forming additive [127, 205–211]. During reduction on the anode, VEC polymerizes with the major film components Li₂CO₃ and ROCO₂Li. When the concentration of VEC is low, ROCO₂Li formation will be small. This results in an improved electrochemical performance, whereas a high content of VEC suppresses the formation of Li₂CO₃ causing an adverse effect on the cycling performance [208]. Additionally, VEC is able to form a CEI layer even at elevated temperatures [206, 212, 213]. BP is able to



Scheme 8 Molecular structures of the film-forming additives

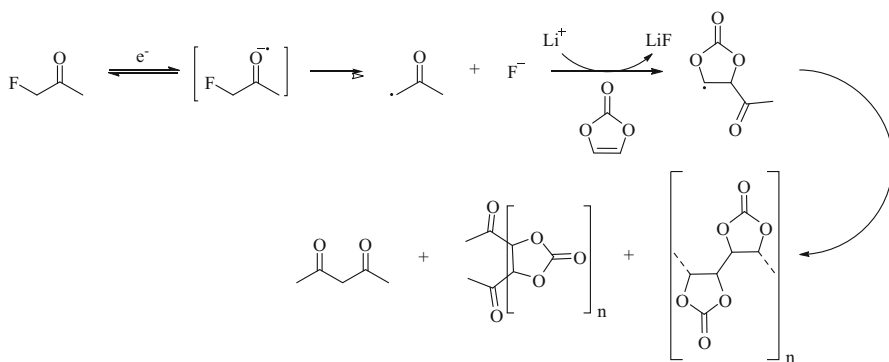
form a thin CEI film when only present in small amounts (0.1 wt%), which prevents further electrolyte decomposition on the cathode side [214]. However, the use of BP had several drawbacks, e.g. poor lithium cycling efficiency due to the reaction with lithium metal and no oxidation stability during prolonged storage or cycling [168, 169]. VA is known to form a SEI layer on the anode surfaces, resulting in an enhancement of cycling performance [215, 216]. This film-formation was due to the reduction of the vinyl group induced by electro-polymerization [171–173, 216]. As previously stated, TPP was used as a flame retardant additive to increase the thermal stability. However, in an amount of up to 10 vol%, TPP influenced the surface chemistry on both electrodes, whereas the cycling performance and capacity retention were not affected [146, 148]. On the cathode side, high additive concentration gave rise to the formation of a thick protective layer. On the anode side, TPP did not go through electrochemical reduction but it participated in the SEI layer formation by chemical reaction [147, 217]. Furthermore, the cell impedance increased which affects the cycling performance and the electrochemical stability up to 5 V vs. Li/Li⁺ [148, 150, 152, 217]. Nam et al. [144] and Shim et al. [145] found that all blended additive electrolyte formulations of 3 wt% TPP with 1 wt% VEC, VA, VC or 0.1% BP in 1.1 M LiPF₆ in EC/EMC (4:6 v/v) showed an improved cell performance compared to the single additive electrolyte formulations containing TPP. Furthermore, the electrochemical stability, the irreversible capacity, the Coulombic efficiency and the rate capability were improved, as listed in Table 11. The TPP + BP containing electrolyte showed better cycling stability than the electrolyte with TPP + VEC blend. Moreover, the electrolyte formulation containing TPP + BP was able to maximize the discharge capacity and to reduce the cell impedance. This showed that BP can improve the cell performance and thermal stability better than VEC [144]. By comparing the effect of VA or VC in the binary electrolyte formulation, the VC containing formulation showed the best enhancement in thermal stability and cell performance [145]. In addition, Shim et al. [218] investigated the ternary blend of TPP with VA + VC and the blend of TPP with VEC + BP. Both additive blended electrolytes displayed high electrochemical stability up to 4.9 V vs. Li/Li⁺. The impedance of a cell containing TPP + VEC + BP could be reduced during cycling and therefore the specific discharge capacity was maximized. Furthermore, the cycle life performance was better for the TPP + VEC + BP blend than for the TPP + VA + VC blend. With this in line, Shim et al. [218] reported TPP + VEC + BP additive blend in organic carbonate-based electrolyte formulation to contribute to the improved cell performance and thermal stability (Table 10).

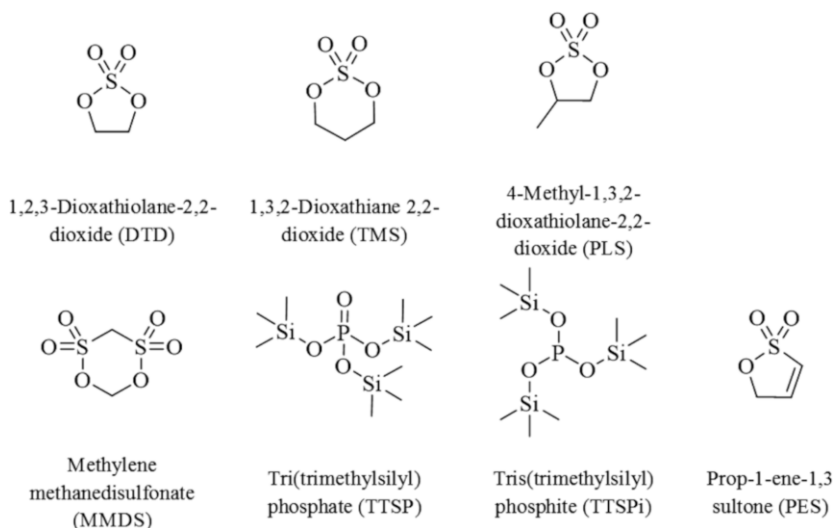
VC, known as one of the most common SEI forming additives, could only be used in concentrations up to 2% as higher concentrations led to a larger charge transfer resistance, especially at the graphite electrode [219]. For this reason, other SEI forming additives were investigated in combination with VC. For instance, Krämer et al. [220, 221] investigated 1 wt% VC with 1 wt% fluoroacetone (FA) in 1 M LiPF₆ in PC electrolyte using graphite/Li half-cells. PC-based electrolyte formulations showed a poor comparability with graphite electrodes, because the PC molecules co-intercalated into the graphite structure thus resulting in exfoliation [187]. FA was able to suppress this phenomenon by forming a protective SEI [220].

Table 10 Comparison of the effects of the addition of one or two film-forming additives (VEC, BP, VA, VC) to the electrolyte formulation containing 3 wt% TPP in terms of irreversible capacity, Coulombic efficiency and capacity retention

Electrolyte formulation	Irreversible capacity	Coulombic efficiency (%)	Capacity retention (40 cycles) (%)
1.1 M LiPF ₆ EC/EMC (4:6 v/v)	2.5 mAh g ⁻¹ [144], 0.39 mAh [145]	98.1 [144], 89.0 [145]	68 [144], 67 [145, 218]
1.1 M LiPF ₆ EC/EMC (4:6 v/v) + 3% TPP	3.3 mAh/g [144], 0.83 mAh [145]	97.4 [144], 77.0 [145]	65 [144], 64 [145, 218]
1.1 M LiPF ₆ EC/EMC (4:6 v/v) + 3% TPP + 1% VEC	2.1 mAh g ⁻¹ [144]	98.4 [144]	70 [144]
1.1 M LiPF ₆ EC/EMC (4:6 v/v) + 3% TPP + 0.1% BP	0.8 mAh g ⁻¹ [144]	99.4 [144]	75 [144]
1.1 M LiPF ₆ EC/EMC (4:6 v/v) + 3% TPP + 1% VA	0.72 mAh [145]	81.0 [145]	70 [145]
1.1 M LiPF ₆ EC/EMC (4:6 v/v) + 3% TPP + 1% VC	0.31 mAh [145]	91.0 [145]	68 [145]
1.1 M LiPF ₆ EC/EMC (4:6 v/v) + 3% TPP + 1% VA + 1% VC	–	–	69 [218]
1.1 M LiPF ₆ EC/EMC (4:6 v/v) + 3% TPP + 1% VEC + 0.1% BP	–	–	71 [218]

Reactive species like radical anions, formed during reduction, were able to eliminate fluorine anions. This resulted in an increase of the LiF amount in the formed SEI [221]. The combination of two different SEI additives in 1 M LiPF₆ in PC led to stable cycling performance in graphite/Li half-cells. Furthermore, a higher capacity retention, a higher first cycle charge/discharge efficiency and a good discharge rate could be achieved [220]. The formed acetone and VC radical species reacted with each other and formed copolymers responsible for the aforementioned improvements [221]. The postulated mechanism is illustrated in Scheme 9.

**Scheme 9** Postulated reductive decomposition mechanism of FA in the presence of VC. Redrawn from [221]



Scheme 10 Molecular structures of the film-forming additives

Another possibility to improve the SEI formation by VC was to add sulfur-containing additives, known for SEI formation on the negative electrode [133, 174, 222–224]. Li et al. [223] and Ota et al. [222] suggested that the formed SEI in presence of sulfur containing additives contained both inorganic materials like Li_2SO_3 and organic compounds like ROSO_2Li . These organic sulfur-containing additives reacted at the graphite surface in such a way that sulfur was incorporated into the SEI film. Zhang et al. [225] and Han et al. [226] studied the combination of 1.5 wt% VC and PS in 1 M LiPF_6 in EC/EMC (3:7 by wt.) in graphite/NMC and graphite/Li half-cells (Scheme 10). This additive blend led to a SEI formation that combines the advantages of both electrolyte additives resulting in an improved cycling performance: (1) PS was responsible for the formation of lithium alkylsulfonate which gave rise to higher conductivity and (2) VC led to the formation of poly(VC) resulting in an improved stability of the SEI. Additionally, Xia et al. [219, 227] studied the effect of the homologous series of cyclic sulfate additives including ethylene sulfate (or 1,3,2-dioxathiolane-2,2-dioxide) (DTD), trimethylene sulfate (or 1,3,2-dioxathiane 2,2-dioxide) (TMS), propylene sulfate (or 4-methyl-1,3,2-dioxathiolane-2,2-dioxide) (PLS) and PS either as a single additive or in combination with VC in 1 M LiPF_6 EC/EMC (3:7 by wt.) electrolyte (Scheme 10). As DTD, TMS and PLS have the same SO_4 unit bonded to a different position in hydrocarbon ring, the impact of the ring size could be studied. DTD has a low LUMO energy and could therefore be easily reduced forming a SEI film which prevented further electrolyte decomposition [228]. Sano et al. suggested that the SEI formed by DTD is due to one electron reduction of the sulfur atom to form a DTD anion radical which could react further with another DTD molecule to form a PEO like polymer and Li_2SO_3 [229]. Furthermore, it was possible to use DTD as a co-solvent for a PC containing electrolyte formulation to fully prevent solvent co-

intercalation and graphite exfoliation [230] and to reduce the volume expansion due to gas formation [228], which was reported to happen in PC electrolytes without the additive [231, 232]. No positive influence on the cycling performance of the graphite could be achieved in the presence of TMS as a single additive, due to the formation of a small amount of sulfate compounds at the electrode surfaces [233]. For the PLS additive containing electrolyte formulation, no improvement compared to the VC containing electrolyte blend could be observed [219]. The results of the blended additive-containing electrolytes were compared with the results from other groups on methylene methanedisulfonate (MMDS) (Scheme 10). MMDS containing electrolyte is able to form a thinner CEI film on the cathode surface, as compared to the reference electrolyte. This resulted in a reduction of the charge transfer impedance and in a high Li^+ ion mobility [234, 235]. Amounting to 1–3 wt%, the additive components were added into the LiPF_6 -based EC/EMC (3:7 by wt.) electrolyte and investigated in graphite/NMC pouch cells. Xia et al. [219] showed that DTD can compete with VC as a single additive, however large amount of gas generation during the formation had to be considered. PLS was not effective neither alone nor in combination with VC and the blend of VC with either DTD, TMS or MMDS led to a better performance. The TMS + VC additive blend containing electrolyte did not give rise to a significant amount of gas generation during the formation step of graphite/NMC full cell, balanced to operate at 4.2 V. Figure 21 depicts the direct comparison between the three different blended electrolyte formulations in the Coulombic inefficiency, the charge end point capacity slippage, the charge transfer resistance and the voltage drop. Furthermore, Xia et al. demonstrated that the synergistic effect could be either beneficial or detrimental in the additive combination of either PS + VC or MMDS + VC [227]. The electrolyte formulation containing MMDS + VC blend was able to improve

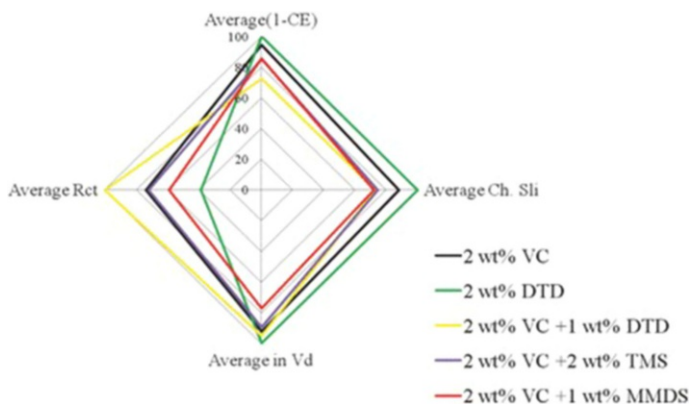


Fig. 21 A “spider” plot that compares the best blends of the additive VC with DTD, TMS and MMDS. The four axes represent the Coulombic inefficiency (1-CE), the charge end point capacity slippage (Ch. Sli), the charge transfer resistance after cycling (R_{CT}) and the voltage drop during storage (V_d). The axes have been scaled so that 100% is the value of the additive that has the largest value of each parameter. The best additive blend would have values closest to the center of the plot. Reprinted from Ref. [219]. Copyright (2014) with permission of ECS

the cycling performance and decreased the swelling of the cell compared to the single additive containing electrolyte formulation. In the case of the of PS + VC additive blended electrolyte, no improvement compared to the single additive containing electrolyte formulation could be achieved in respect to the cycling performance. Furthermore, the PS + VC blend-containing electrolyte showed a drastic increase in the cell impedance, whereas the electrolyte formulation with MMDS + VC additive blend resulted in a decrease compared to the single additive electrolyte formulation. In case of the ternary VC + PS + MMDS blend-containing electrolyte, a decrease of the cell impedance compared to the binary PS + VC blended electrolyte could be observed, but compared to the binary MMDS + VC blend-containing electrolyte, the cell impedance was increased. It could be concluded that the additive PS has a detrimental influence on electrochemistry in combination with VC and MMDS.

The work performed by Sinha et al. focused on organophosphorous compounds, containing a tris(trimethylsilyl) (TMS) group, as additives regarding their possible application as high-voltage additives [236]. TMS-based additives found multiple considerations in research [237, 238]. It was suggested that tris(trimethylsilyl) phosphate (TTSP) and tris(trimethylsilyl) phosphite (TTSPi) as additives could help to improve the cycling performance of lithium ion cells at high voltage and/or elevated temperature (Scheme 10) [239].

TTSP was reported to be able to replace EC in the Li^+ solvation shell and to form a CEI film without increasing the acidity at the cathode interface; acidity, which would be the result of electrolyte solvent oxidation. This effect can be explained by a proton transfer to another TTSP molecule or an intramolecular oxidation instead of a proton transfer to the electrode surface. The presence of this CEI was the reason behind the significant improvement in cycling performance, the decrease in cell impedance and the reduction of transition metal dissolution [240–244]. TTSPi is involved in formation of the CEI film on the cathode surface [245–249] due to the lower oxidation and reduction potential compared to EC [248], resulting in preferential oxidation [249]. Sinha et al. compared the performance of 1, 2 or 3 wt% TTSP or TTSPi together with 2 wt% VC as a binary additive blended 1 M LiPF_6 EC/EMC (3:7 by wt.) electrolyte in graphite/NMC pouch cells [236]. They showed that TTSP or TTSPi do reduce the overall cell impedance. However, in the binary blends of either VC + TTSP or VC + TTSPi, the cell impedance was increased. The best-blended system among investigated, consisted of 2 wt% VC and 1 wt% TTSPi and could lead to a longer cycle life, longer calendar life and reduced impedance compared to cells with electrolytes containing only VC. Ma et al. [250] and Wang et al. [251] combined sulfur and phosphorus containing film-forming additives (mentioned above) with organophosphorus compounds and studied their impact on the cycling performance as a ternary or quaternary systems. As listed in Table 11, all investigated electrolyte blends showed higher Coulombic efficiencies and lower charge end-point capacity slippage rates compared to electrolyte formulations containing VC as a single additive, thus pointing out a reduction in parasitic reaction rates. Furthermore, the self-heating rate was decreased indicating a thermally stable SEI on the anode. A more effective passivation layer on both electrodes was formed, represented by lower charge transfer impedance after

Table 11 Summary of the electrolyte additive combinations discussed in the text and their amount in the electrolyte formulation 1 M LiPF₆ EC/EMC (3:7 by wt.) in graphite/NMC full cells

VC (%)	TMS (%)	DTD (%)	MMDS (%)	TTSP (%)	TTSPi (%)
2.0	1.0	–	–	0.5	0.5
2.0	1.0	–	–	–	–
2.0	–	1.0	–	0.5	0.5
2.0	–	1.0	–	–	1.0
2.0	–	–	1.0	0.5	0.5
2.0	–	–	1.0	–	1.0

cycling compared to the single additive formulation. Additionally, the gas generation during cycling was the same or less as compared to the VC containing electrolyte formulation. All investigated blended electrolyte formulations led to improved safety and longer cycle life with better power capability of the resulting LIBs.

The additives MMDS (1 wt%) and TTSPi (1 wt%) were also investigated together with 2 wt% prop-1-ene-1,3 sultone (PES) in 1 M LiPF₆ EC/EMC (3:7 by wt.) using graphite/NMC full cells by Ma et al. [252, 253], Nie et al. [254] and Madec et al. [255] (Scheme 10). These additive blended electrolyte formulations improved the capacity retention, reduced the cell impedance as well as suppressed gas formation significantly. PES has a similar structure compared to PS, but has a more positive reduction potential, which made the resulting SEI more effective [256, 257]. However, Madec et al. also reported that blend of 2 wt% PES + 1 wt% MMDS + 1 wt% TTSPi displayed a capacity loss and an impedance increase when the cell was charged for a long time at potentials above 4.4 V vs. Li/Li⁺ due to the relatively poor stability of the sulfite species [255]. XPS studies showed that the preferential reaction of MMDS and PES was responsible for more effective SEI and CEI formation. Therefore, a better capacity retention could be achieved, accompanied by reduced gas formation. In addition, they found that TTSPi reacted at the graphite surface before the cell was fully charged. Furthermore, Ma et al. compared the impact of VC or PES in the combination with MMDS and TTSPi in 1 M LiPF₆ EC/EMC (3:7 by wt.) as a blended electrolyte formulation [258]. The PES containing blended additive electrolyte formulations showed a better capacity retention as compared to that of the VC containing one (Fig. 22). The cells containing the additive blend 2 wt% PES + 1 wt% MMDS + 1 wt% TTSPi showed the highest capacity retention which is more than 80% of the initial capacity after 900 cycles at 55 °C. The thermal reactivity for the charged graphite electrode was lower for the PES + VC containing blends, which resulted in a significant life improvement of these LIBs. This was investigated by means of an ARC experiment where 140 mg lithiated graphite reacted with 140 mg of the electrolyte formulation containing 2 wt% of the selected additive. For both additive blended electrolyte formulations, the exothermic feature was significantly decreased.

Burns et al. investigated a binary additive blend containing VC in combination with trimethoxyboroxine (TMOBX) in 1 M LiPF₆ EC/EMC (3:7 by wt.)

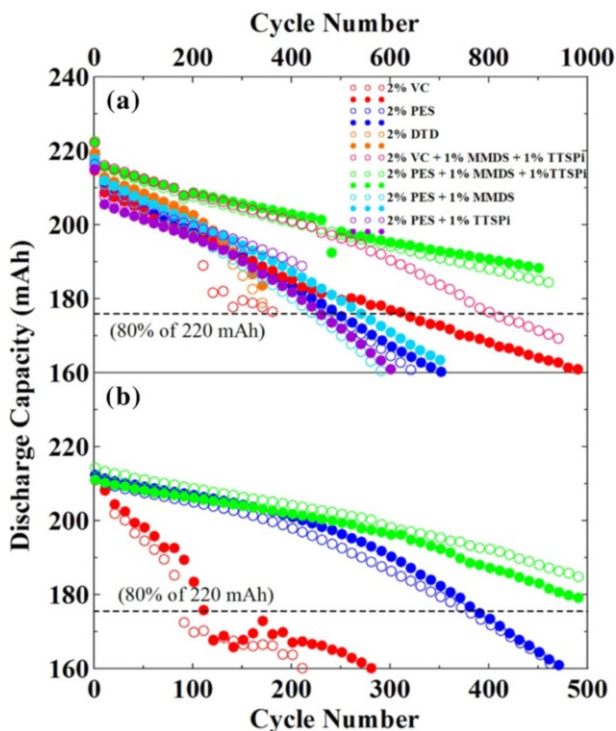
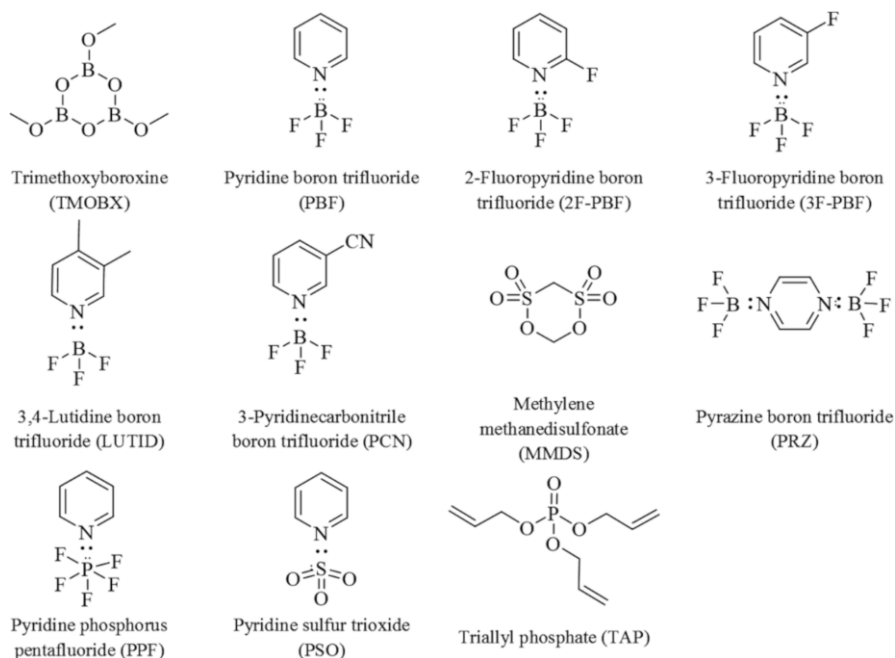


Fig. 22 **a** Capacity versus cycle number for graphite/NMC111 pouch cells (unclamped) containing selected additives or additive blends in the range from 2.8 and 4.2 V, at 55 °C and 80 mA. **b** Capacity versus cycle number for graphite/NMC442 pouch cells (unclamped) containing selected additives or additive blends. The cycling was performed between 3.0 and 4.4 V at 45 °C and at 100 mA. Reprinted from Ref. [258]. Copyright (2015) with permission of ECS

(Scheme 11) [259]. Mao et al. showed that the presence of this methoxy-group in TMOBX helps to reduce the capacity loss during cycling more effectively than the $(\text{BO})_3$ ring alone [260]. Furthermore, TMOBX in amounts of less than 1% is a very useful additive to decrease the cell impedance [261]. Graphite/Li half-cell investigations showed that the presence of TMOBX increases the rate of parasitic reactions. The first cycle irreversible capacity was increased and no effective SEI layer could be formed [262]. However, Burns et al. [259] and Petibon et al. [263] pointed out that 2 wt% VC together with 0.3 wt% TMOBX reduced the cell impedance but the Coulombic efficiency became slightly lower in case of graphite/LCO full cells. When cycling in graphite/NMC full cells, the cell impedance and Coulombic efficiency remained unchanged whereas the capacity retention at elevated temperature was slightly improved. It could be concluded that the impact of TMOBX as an additive strongly depends on the used electrode and electrolyte formulation.

To improve the cycling stability, additives based on an organic heterocyclic ring structure were electrochemically studied. Nie et al. investigated pyridine boron trifluoride type molecules such as pyridine boron trifluoride (PBF) as additives for



Scheme 11 Molecular structures of the film-forming additives

high-voltage applications (Scheme 11) [264]. The structure of PBF consists of two major functional groups, BF_3 as a Lewis acid and an amine Lewis base. Amine functional groups are known as corrosion inhibitors for metals and were therefore considered to decrease the transition metal dissolution from NMC electrode [265]. The BF_3 group as an anion receptor was speculated to react with LiF and dissolve it out of the surface layer resulting in lower impedance [266]. For this reason, PBF type molecules were assumed to be able to control the impedance growth during cycling [131, 254]. The blended electrolyte formulations containing 1 wt% PBF-type molecules together with MMDS or DTD (1 wt%) were investigated in graphite/NMC full cells containing 1 M LiPF_6 EC/EMC (3:7 by wt.) electrolyte (Scheme 11). In presence of MMDS and the PBF-type additives as blend, the impedance of the cells could be reduced. Furthermore, the PBF-type additives helped to increase the Coulombic efficiency of the investigated blends. The PBF + MMDS and PBF + DTD additive blends seemed to be a promising candidate for high-voltage application. However, the electrolyte oxidation could not be suppressed [264]. In addition, by introducing another nitrogen atom into the ring structure a second Lewis acid such as BF_3 is necessary, as studied by Nie et al. [264] and Ma et al. [252]. The authors combined 0.5 wt% pyrazine di-boron trifluoride (PRZ) with 1 wt% MMDS or DTD in 1 M LiPF_6 EC/EMC (3:7 by wt.) in graphite/NMC full cells (Scheme 11). The cycling performance was found to be improved and PRZ + MMDS additive blend was found to be a very effective for LIBs regarding Coulombic efficiency, impedance control and capacity loss. Recently, Nie

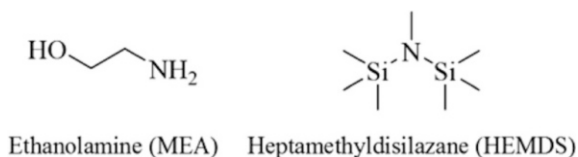
et al. [265] investigated additives consisting of the same amine Lewis base group as PBF but they varied the Lewis acid group. Pyridine phosphorus pentafluoride (PPF) containing a PF_5 instead of BF_3 and pyridine sulfur trioxide (PSO) using a SO_3 as a Lewis acid (Scheme 11). The 1 M LiPF_6 in EC/EMC (3:7 by wt.) electrolyte formulation was enriched either with a single additive or in combination with DTD, VC or triallyl phosphate (TAP) (Scheme 11). TAP was already studied as a single additive for high voltage lithium-ion cells and it was shown that TAP leads to higher Coulombic efficiency since it polymerizes at the surface of the anode and the cathode creating thick stable surface films. However, large amounts of TAP (>3 wt%) led to increased cell impedance [267]. The obtained results indicated high impedance in the cells containing the combination of TAP with PBF or PPF in investigated electrolyte. When comparing the open circuit potential (OCP) after storage at 4.5 V and 60 °C for 500 h, the blend of 2 wt% VC with 1 wt% PSO showed improved storage properties compared to electrolyte containing VC alone. The combination of 2 wt% VC and 1 wt% PBF or PPF did not show any improvement. However, the investigated DTD + PBF and DTD + PFB additive blend-containing electrolytes displayed a significant improvement as confirmed by the higher Coulombic efficiency, lower charge end point capacity slippage, low and stable impedance and no gassing during tests at 4.5 V and 40 °C. In summary aforementioned combination showed high potential for further investigations in high voltage graphite/NMC full cells [265].

4.3 Blended Electrolytes with Salt Stabilizer Additives

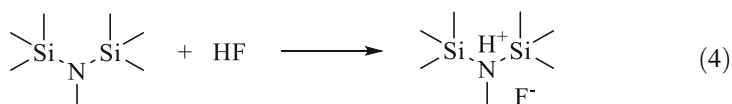
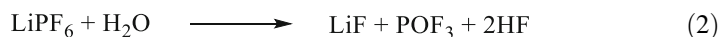
Residual trace amounts of impurities such as water and HF cannot be completely prevented from nonaqueous electrolytes, as well as other LIB cell components even for battery grade products. The formed HF is known as the main reason for the dissolution of cathode materials [67, 131]. For instance, LMO suffers from severe capacity fading after storage at elevated temperature, associated to Mn^{2+} dissolution induced by HF [268, 269]. One solution is based on decreasing the water and HF content by stabilizing the electrolyte. H_2O and HF can be stabilized through hydrogen bonding bridge with molecules such as ethanolamine (MEA) leading to an improved cycling performance [270]. Yamane et al. [271] and Li et al. [272] used single additives hexamethyldisilazane (HMDS) and heptamethyldisilazane (HEMDS) in LiPF_6 -based electrolytes to successfully eliminate HF from the electrolyte. The binary blend of both mentioned additives, MEA + HEMDS, as an electrolyte salt stabilizer was studied by Wu et al. (Scheme 12) [273].

The same group investigated the storage behavior of LMO exposed in air as well as in LMO/Li half-cells at a temperature of 60 °C. The blend of 1 vol% MEA and

Scheme 12 Molecular structures of the salt stabilizer additives



3 vol% HEMDS in 1 M LiPF₆ EC/DMC/EMS (1:1:1) electrolyte was found to suppress Mn²⁺ dissolution as well as the formation of amorphous LMO/electrolyte degradation products, i.e., as λ-MnO₂ with small amounts of MnF₂ and LiF, thus resulting in improved storage performance. The authors proposed the following mechanism: (1) LiPF₆ reacts with water and produces HF (2) and (2) the mentioned degradation products will be generated through a disproportionation reaction of Mn³⁺ at the surface of LiMn₂O₄ induced by HF (3). Theoretical calculations performed by Zhang et al. [274] showed that both H₂O and HF can be stabilized by MEA through hydrogen bridge bonding. HEMDS can eliminate HF by forming the salt compound (4). Since both additives were able to interact with the formed HF simultaneously in different ways, HF can be effectively removed.



4.4 Summary

Using selected additive blends can be more effective than using a single additive, as indicated through the described and discussed examples. This approach represents a very promising way to optimize electrolyte functionalities as selected and investigated additives show ability to compensate for each other's disadvantages. All, in this chapter, reviewed additive blends in corresponding electrolyte formulations are listed in Table 12.

Although, many research groups have been and are still working in this field, additive blended electrolyte formulations still require further and deeper investigation. With this in line, the synergistic effect of the used additives has to be studied in more detail in order to completely understand their main operation, failure mechanisms as well as the synergistic interplay in the electrolyte matrix.

5 Concluding Remarks and Perspectives

One of the critical barriers hindering the further progress and development of LIBs for custom tailored applications is addressed to the electrolyte. In this respect, chemistry and synergy between different electrolyte components are playing a significant role. This review paper highlighted activities in the field of nonaqueous electrolytes containing solvent, salt, as well as additive blends towards improved overall lithium ion cell performance. Blending of properly selected electrolyte constituents appears to be a very promising way to optimize electrolyte functions

Table 12 Overview of the investigated additive blends including the used electrolyte formulation, electrode system as well as their function

Additive blend	Electrolyte	Electrodes	Target improvement	References
TPP + VEC TPP + BP TPP + VA TPP + VC	1.1 M LiPF ₆ EC/EMC (4/6 v/v)	Graphite/ LCO	Flame retardant, SEI	[144, 145]
TCEP + CHB	1 M LiPF ₆ EC/DMC/ EMC (1:1:1 by wt.)	Graphite/ LCO	TCEP: reduced flammability CHB: overcharge protection	[154]
TEP + EC	0.4 M LiTFSI/ PP13-TFSI	Graphite/ LMO	EC: Lower viscosity and increased conductivity TEP: Reduced flammability	[162]
BP + CHB	1 M LiPF ₆ EC/EMC (1:2 v/v)	Graphite/ LCO	Overcharge protection	[180]
VC + PS	BMP-TFSI	LTO/LCO	SEI	[185]
FEC + VC	1 M LiPF ₆ EC/DMC (1:1 by wt.) 1 M LiPF ₆ EC/DEC (1:1 by wt.) 0.6 M LiTDI EC/DMC (2:1 v/v)	Si/Li	SEI Improved cycling performance	[202–204]
VC + FA	1 M LiPF ₆ PC	Graphite/Li	SEI	[220, 221]
VC + PS	1 M LiPF ₆ EC/EMC (3:7 v/v) 1 M LiPF ₆ EC/EMC (3:7 by wt.)	Graphite/ NMC Graphite/Li Graphite/ LCO	SEI SEI	[225, 226]
VC + DTD VC + TMS VC + PLS VC + PS VC + MMDS	1 M LiPF ₆ EC/EMC (3:7 by wt.)	Graphite/ NMC	SEI and CEI	[219, 227]
VC + TTSP VC + TTSPi	1 M LiPF ₆ EC/EMC (3:7 by wt.)	Graphite/ NMC	Improved cycling performance	[236]
VC + TMS VC + DTD MMDS + TTSP MMDS + TTSPi	1 M LiPF ₆ EC/EMC (3:7 by wt.)	Graphite/ NMC	SEI Improved cycling performance	[250, 251]

Table 12 continued

Additive blend	Electrolyte	Electrodes	Target improvement	References
PES + MMDS + TTSPi	1 M LiPF ₆ EC/EMC (3:7 by wt.)	Graphite/ NMC442	SEI Improved cycling performance	[250, 252, 254, 255]
VC + MMDS + TTSPi	1 M LiPF ₆ EC/EMC	Graphite/ NMC111	PES: improved cycling performance	[258]
PES + MMDS + TTSPi	(3:7 by wt.)	(4.4 V), Graphite/ NMC442 (4.7 V)	compared to VC	
VC + TMOBX	1 M LiPF ₆ EC/EMC (3:7 by wt.)	Graphite/ LCO Graphite/ NMC	Improved cycling performance	[259, 263]
PBF-type + MMDS	1 M LiPF ₆ EC/EMC (3:7 by wt.)	Graphite/ NMC	Improved cycling performance	[252, 264]
PBF-type + DTD				
PRZ + MMDS				
PRZ + DTD				
PBF + DTD	1 M LiPF ₆ EC/EMC (3:7 by wt.)	Graphite/ NMC	TAP + PBF, TAP + PPF: High impedance	
PBF + VC				
PBF + TAP				
PPF + DTD				
PPF + VC				
PPF + TAP				
PSO + DTD				
PSO + VC				
PSO + TAP				
VC + PBF, VC + PPF:	[265]			
No improvement				
DTD + PBF, DTD + PPF:				
Improved cycling performance				
MEA + HEMDS	1 M LiPF ₆ EC/DMC/ EMS (1:1:1 by wt.)	LMO/Li	Decreased Mn dissolution Stabilization of HF and water	[273, 274]

through the ability of blended components to compensate for each other's disadvantages or to eliminate undesired disadvantages. With this in line, the effect of different solvent, salt as well as additive blends on the physicochemical and electrochemical features of nonaqueous electrolyte formulations was discussed using interesting literature examples, pointing out the influence on anode, cathode, suppression or inhibition of Al dissolution, thermal stability as well as the overall cell performance.

However, in respect to the synergistic effect of afore described and discussed electrolyte blends, there are still many questions left unanswered, thus acting as a barrier towards desired improvements and refined electrolyte optimization. In order to systematically develop novel blended nonaqueous electrolyte formulations, the following points must be taken in consideration and studied in more detail: correlation between the molecular and electronic structure of the electrolyte components and their reactivity, the synergistic effects of the blended components, main operation and failure processes, study on intermediate species, investigation of the different plausible reaction pathways as well as the analysis of the limiting and determining steps which provide rationalization of the obtained results. Integrating the knowledge gained from profound studies of the aforementioned parameters and processes will lead to desired improvements that positively affect lithium ion cell chemistry and LIB performance.

We hope that this review provides a good overview and clear perspective on blended nonaqueous electrolyte formulations thus raising the motivation in encouraging researchers to proceed with further and deeper investigations in this promising field.

References

1. Wagner R, Preschitschek N, Passerini S, Leker J, Winter M (2013) *J Appl Electrochem* 43:481–496
2. Jia H, Kloepsch R, He X, Evertz M, Nowak S, Li J, Winter M, Placke T (2016) *Acta Chim Slov* 63:470–483
3. Meister P, Jia H, Li J, Kloepsch R, Winter M, Placke T (2016) *Chem Mater* 28:7203–7217
4. Besenhard JO, Winter M (1998) *Pure Appl Chem* 70:603–608
5. Winter M, Imhof R, Joho F, Novák P (1999) *J Power Sources* 81–82:818–823
6. Lux SF, Lucas IT, Pollak E, Passerini S, Winter M, Kostecki R (2012) *Electrochem Commun* 14:47–50
7. Winter M (2009) *Z Phys Chem* 223:1395–1406
8. Winter M (2006) Second International symposium on LLIBTA, AABC-06 Baltimore Inner Harbor
9. Scrosati B, Garche J (2010) *J Power Sources* 195:2419–2430
10. Chagnes A, Diaw M, Carré B, Willmann P, Lemordant D (2005) *J Power Sources* 145:82–88
11. Xu K (2014) *Chem Rev* 114:11503–11618
12. Sato T, Maruo T, Marukane S, Takagi K (2004) *J Power Sources* 138:253–261
13. Xu J, Yang J, NuLi Y, Wang J, Zhang Z (2006) *J Power Sources* 160:621–626
14. Wang M, Shan Z, Tian J, Yang K, Liu X, Liu H, Zhu K (2013) *Electrochim Acta* 95:301–307
15. Abu-Lebdeh Y, Davidson I (2009) *J Electrochem Soc* 156:A60–A65
16. Abu-Lebdeh Y, Davidson I (2009) *J Power Sources* 189:576–579
17. Nagahama M, Hasegawa N, Okada S (2010) *J Electrochem Soc* 157:A748–A752
18. Rohan R, Kuo T-C, Lin J-H, Hsu Y-C, Li C-C, Lee J-T (2016) *J Phys Chem C* 120:6450–6458
19. Luo R, Ren W, Jiang Y-M, Liao S-J (2014) *Xian Dai Hua Gong* 34:36–40
20. Wrodnigg GH, Reisinger C, Besenhard JO, Winter M (1999) *ITE Battery Lett* 1:110
21. Li S, Zhao D, Chen R (2016) *EMCPE*, Zhengzhou, China, pp 334–337
22. Galiński M, Lewandowski A, Stępniański I (2006) *Electrochim Acta* 51:5567–5580
23. Wilkes JS (2002) *Green Chem* 4:73–80
24. Younesi R, Veith GM, Johansson P, Edstrom K, Vegge T (2015) *Energy Environ Sci* 8:1905–1922
25. Amereller M, Multerer M, Schreiner C, Lodermeier J, Schmid A, Barthel J, Gores HJ (2009) *J Chem Eng Data* 54:468–471
26. Cho Y-G, Kim Y-S, Sung D-G, Seo M-S, Song H-K (2014) *Energy Environ Sci* 7:1737–1743
27. Ding MS, Xu K, Jow TR (2000) *J Electrochem Soc* 147:1688–1694

28. Brox S, Roser S, Husch T, Hildebrand S, Fromm O, Korth M, Winter M, Cekic-Laskovic I (2016) *ChemSusChem* 9:1704–1711
29. Guerfi A, Dontigny M, Charest P, Petitclerc M, Lagacé M, Vijn A, Zaghbi K (2010) *J Power Sources* 195:845–852
30. Arbizzani C, Gabrielli G, Mastragostino M (2011) *J Power Sources* 196:4801–4805
31. Isken P, Dippel C, Schmitz R, Schmitz RW, Kunze M, Passerini S, Winter M, Lex-Balducci A (2011) *Electrochim Acta* 56:7530–7535
32. Duncan H, Salem N, Abu-Lebdeh Y (2013) *J Electrochem Soc* 160:A838–A848
33. MacFarlane DR, Huang J, Forsyth M (1999) *Nature* 402:792–794
34. Vogl T, Menne S, Balducci A (2014) *Phys Chem Chem Phys* 16:25014–25023
35. Kühnel RS, Böckenfeld N, Passerini S, Winter M, Balducci A (2011) *Electrochim Acta* 56:4092–4099
36. Yang B, Li C, Zhou J, Liu J, Zhang Q (2014) *Electrochim Acta* 148:39–45
37. Patra J, Wang C-H, Lee T-C, Wongthitharom N, Lin Y-C, Ting-Kuo Fey G, Majumder SB, Hsieh C-T, Chang J-K (2015) *RSC Adv* 5:106824–106831
38. Sloop SE, Pugh JK, Wang S, Kerr JB, Kinoshita K (2001) *Electrochem Solid-State Lett* 4:A42–A44
39. Campion CL, Li W, Lucht BL (2005) *J Electrochem Soc* 152:A2327–A2334
40. Yang H, Zhuang GV, Ross PN (2006) *J Power Sources* 161:573–579
41. Chavan SN, Tiwari A, Nagaiah TC, Mandal D (2016) *Phys Chem Chem Phys* 18:16116–16126
42. Xu K, Lee U, Zhang S, Allen JL, Jow TR (2004) *Electrochem Solid-State Lett* 7:A273–A277
43. Xu K (2004) *Chem Rev* 104:4303–4418
44. Shin J (2003) *Electrochem Commun* 5:1016–1020
45. Shin J-H, Henderson WA, Passerini S (2005) *Electrochem Solid-State Lett* 8:A125–A127
46. Winter M, Appel WK, Evers B, Hodal T, Möller K-C, Schneider I, Wachtler M, Wagner MR, Wrodnigg GH, Besenhard JO (2001) *Monatshfte für Chemie/Chem Mon* 132:473–486
47. Lux SF, Jeong S-S, Kim G-T, Passerini S, Winter M, Balducci A (2010) *ECS Trans* 25:21–25
48. Kim K, Cho Y-H, Shin H-C (2013) *J Power Sources* 225:113–118
49. Morita M, Shibata T, Yoshimoto N, Ishikawa M (2002) *Electrochim Acta* 47:2787–2793
50. Krause LJ, Lamanna W, Summerfield J, Engle M, Korba G, Loch R, Atanasoski R (1997) *J Power Sources* 68:320–325
51. Kramer E, Schedlbauer T, Hoffmann B, Terborg L, Nowak S, Gores HJ, Passerini S, Winter M (2012) *J Electrochem Soc* 160:A356–A360
52. Krämer E, Passerini S, Winter M (2012) *ECS Electrochem Lett* 1:C9–C11
53. Garcia B, Armand M (2004) *J Power Sources* 132:206–208
54. Lombardo L, Brutti S, Navarra MA, Panero S, Reale P (2013) *J Power Sources* 227:8–14
55. Peng C, Yang L, Zhang Z, Tachibana K, Yang Y (2007) *J Power Sources* 173:510–517
56. Mun J, Yim T, Choi CY, Ryu JH, Kim YG, Oh SM (2010) *Electrochem Solid-State Lett* 13:A109–A111
57. Ue M, Mori S (1995) *J Electrochem Soc* 142:2577–2581
58. Xu K, Zhang S, Jow TR (2003) *Electrochem Solid-State Lett* 6:A117–A120
59. Jiang J, Dahn JR (2004) *Electrochim Acta* 49:4599–4604
60. Schmidt M, Heider U, Kuehner A, Oesten R, Jungnitz M, Ignat'ev N, Sartori P (2001) *J Power Sources* 97–98:557–560
61. Shui Zhang S (2006) *Electrochem Commun* 8:1423–1428
62. Schedlbauer T, Krüger S, Schmitz R, Schmitz RW, Schreiner C, Gores HJ, Passerini S, Winter M (2013) *Electrochim Acta* 92:102–107
63. Dominey LA, Koch VR, Blakley TJ (1992) *Electrochim Acta* 37:1551–1554
64. Han H-B, Zhou S-S, Zhang D-J, Feng S-W, Li L-F, Liu K, Feng W-F, Nie J, Li H, Huang X-J, Armand M, Zhou Z-B (2011) *J Power Sources* 196:3623–3632
65. Böttcher T, Duda B, Kalinovich N, Kazakova O, Ponomarenko M, Vlasov K, Winter M, Rösenthaller GV (2014) *Prog Solid State Chem* 42:202–217
66. Schmitz RW, Murmann P, Schmitz R, Müller R, Krämer L, Kasnatscheew J, Isken P, Niehoff P, Nowak S, Rösenthaller G-V, Ignatiev N, Sartori P, Passerini S, Kunze M, Lex-Balducci A, Schreiner C, Cekic-Laskovic I, Winter M (2014) *Prog Solid State Chem* 42:65–84
67. Gallus DR, Schmitz R, Wagner R, Hoffmann B, Nowak S, Cekic-Laskovic I, Schmitz RW, Winter M (2014) *Electrochim Acta* 134:393–398
68. Evertz M, Horsthemke F, Kasnatscheew J, Börner M, Winter M, Nowak S (2016) *J Power Sources* 329:364–371

69. Kraft V, Weber W, Streipert B, Wagner R, Schultz C, Winter M, Nowak S (2016) *RSC Adv* 6:8–17
70. Kraft V, Grütze M, Weber W, Menzel J, Wiemers-Meyer S, Winter M, Nowak S (2015) *J Chromatogr A* 1409:201–209
71. Terborg L, Weber S, Passerini S, Winter M, Karst U, Nowak S (2014) *J Power Sources* 245:836–840
72. Shieh D-T, Hsieh P-H, Yang M-H (2007) *J Power Sources* 174:663–667
73. Chen Z, Lu WQ, Liu J, Amine K (2006) *Electrochim Acta* 51:3322–3326
74. Jow RT, Xu K, Borodin O, Ue M (2014) *Electrolytes for lithium and lithium-ion batteries*. Springer, New York
75. Hofmann A, Hanemann T (2015) *J Power Sources* 298:322–330
76. Lai Y, Peng B, Zhang Z, Li J (2014) *J Electrochem Soc* 161:A875–A879
77. Zhang L, Chai L, Zhang L, Shen M, Zhang X, Battaglia VS, Stephenson T, Zheng H (2014) *Electrochim Acta* 127:39–44
78. Zhou H, Xiao K, Li J (2016) *J Power Sources* 302:274–282
79. Zugmann S, Moosbauer D, Amereller M, Schreiner C, Wudy F, Schmitz R, Schmitz R, Isken P, Dippel C, Müller R, Kunze M, Lex-Balducci A, Winter M, Gores HJ (2011) *J Power Sources* 196:1417–1424
80. Abraham DP, Furczon MM, Kang SH, Dees DW, Jansen AN (2008) *J Power Sources* 180:612–620
81. Ding MS, Richard Jow T (2004) *J Electrochem Soc* 151:A2007–A2015
82. Zygadlo-Monikowska E, Florjańczyk Z, Kubisa P, Biedroń T, Tomaszewska A, Ostrowska J, Langwald N (2010) *J Power Sources* 195:6202–6206
83. Zhang Z, Chen X, Li F, Lai Y, Li J, Liu P, Wang X (2010) *J Power Sources* 195:7397–7402
84. Park K, Yu S, Lee C, Lee H (2015) *J Power Sources* 296:197–203
85. Li L, Zhou S, Han H, Li H, Nie J, Armand M, Zhou Z, Huang X (2011) *J Electrochem Soc* 158:A74–A82
86. Li F, Gong Y, Jia G, Wang Q, Peng Z, Fan W, Bai B (2015) *J Power Sources* 295:47–54
87. Zhang Z-A, Zhao X-X, Peng B, Lai Y-Q, Zhang Z-Y, Li J (2015) *Trans Nonferrous Met Soc China* 25:2260–2265
88. Hong E-S, Okada S, Sonoda T, Gopukumar S, Yamaki J-I (2004) *J Electrochem Soc* 151:A1836–A1840
89. Zhang S, Xu K, Jow T (2003) *J Solid State Electrochem* 7:147–151
90. Zhang SS, Xu K, Jow TR (2002) *J Electrochem Soc* 149:A586–A590
91. Xu M, Zhou L, Hao L, Xing L, Li W, Lucht BL (2011) *J Power Sources* 196:6794–6801
92. Zhang SS, Xu K, Allen JL, Jow TR (2002) *J Power Sources* 110:216–221
93. Wagner MR, Albering JH, Moeller KC, Besenhard JO, Winter M (2005) *Electrochem Commun* 7:947–952
94. Wagner MR, Raimann PR, Trifonova A, Moeller K-C, Besenhard JO, Winter M (2004) *Electrochem Solid-State Lett* 7:A201–A205
95. Zhang SS, Xu K, Jow TR (2006) *J Power Sources* 156:629–633
96. Wachtler M, Wohlfahrt-Mehrens M, Ströbele S, Panitz J-C, Wietelmann U (2006) *J Appl Electrochem* 36:1199–1206
97. Zhuang GV, Xu K, Jow TR, Ross PN (2004) *Electrochem Solid-State Lett* 7:A224–A227
98. Panitz J-C, Wietelmann U, Wachtler M, Ströbele S, Wohlfahrt-Mehrens M (2006) *J Power Sources* 153:396–401
99. Blyth RIR, Buqa H, Netzer FP, Ramsey MG, Besenhard JO, Winter M (2001) *J Power Sources* 97–98:171–173
100. Buqa H, Golob P, Winter M, Besenhard JO (2001) *J Power Sources* 97–98:122–125
101. Buqa H, Blyth RIR, Golob P, Evers B, Schneider I, Santis Alvarez MV, Hofer F, Netzer FP, Ramsey MG, Winter M, Besenhard JO (2000) *Ionics* 6:172–179
102. Blyth RIR, Buqa H, Netzer FP, Ramsey MG, Besenhard JO, Golob P, Winter M (2000) *Appl Surf Sci* 167:99–106
103. Olivier JP, Winter M (2001) *J Power Sources* 97–98:151–155
104. Placke T, Siozios V, Rothermel S, Meister P, Colle C, Winter M (2015) *Z Phys Chem* 229:1451
105. Placke T, Siozios V, Schmitz R, Lux SF, Bieker P, Colle C, Meyer HW, Passerini S, Winter M (2012) *J Power Sources* 200:83–91
106. Winter M, Novák P, Monnier A (1998) *J Electrochem Soc* 145:428–436
107. Xu K, Zhang S, Jow TR (2005) *Electrochem Solid-State Lett* 8:A365–A368
108. Jiang J, Dahn JR (2003) *Electrochem Solid-State Lett* 6:A180–A182

109. Jiang J, Dahn JR (2004) *Electrochem Commun* 6:39–43
110. Gallagher KG, Goebel S, Greszler T, Mathias M, Oelerich W, Eroglu D, Srinivasan V (2014) *Energy Environ Sci* 7:1555–1563
111. Xu W, Wang J, Ding F, Chen X, Nasybulin E, Zhang Y, Zhang J-G (2014) *Energy Environ Sci* 7:513–537
112. Ryou M-H, Lee YM, Lee Y, Winter M, Bieker P (2015) *Adv Funct Mater* 25:834–841
113. Bieker G, Winter M, Bieker P (2015) *Phys Chem Chem Phys* 17:8670–8679
114. Heine J, Hilbig P, Qi X, Niehoff P, Winter M, Bieker P (2015) *J Electrochem Soc* 162:A1094–A1101
115. Winter M, Besenhard JO (1999) In: Besenhard JO (ed) *Handbook of battery materials*. VCH, Weinheim, pp 383–418
116. Xiang H, Shi P, Bhattacharya P, Chen X, Mei D, Bowden ME, Zheng J, Zhang J-G, Xu W (2016) *J Power Sources* 318:170–177
117. Blyr A, Sigala C, Amatucci G, Guyomard D, Chabre Y, Tarascon JM (1998) *J Electrochem Soc* 145:194–209
118. Börner M, Klamor S, Hoffmann B, Schroeder M, Nowak S, Würsig A, Winter M, Schappacher FM (2016) *J Electrochem Soc* 163:A831–A837
119. Hunter JC (1981) *J Solid State Chem* 39:142–147
120. Guerfi A, Duchesne S, Kobayashi Y, Vijh A, Zaghbi K (2008) *J Power Sources* 175:866–873
121. Abouimrane A, Ding J, Davidson IJ (2009) *J Power Sources* 189:693–696
122. Li S, Li L, Liu J, Jing J, Li X, Cui X (2015) *Electrochim Acta* 155:321–326
123. Myung S-T, Hitoshi Y, Sun Y-K (2011) *J Mater Chem* 21:9891–9911
124. Zhang SS, Jow TR (2002) *J Power Sources* 109:458–464
125. Chen X, Xu W, Engelhard MH, Zheng J, Zhang Y, Ding F, Qian J, Zhang J-G (2014) *J Mater Chem A* 2:2346–2352
126. Behl WK, Plichta EJ (1998) *J Power Sources* 72:132–135
127. Song S-W, Richardson TJ, Zhuang GV, Devine TM, Evans JW (2004) *Electrochim Acta* 49:1483–1490
128. Zhang X, Devine TM (2006) *J Electrochem Soc* 153:B365–B369
129. Wang X, Yasukawa E, Mori S (2000) *Electrochim Acta* 45:2677–2684
130. Kawamura T, Tanaka T, Egashira M, Watanabe I, Okada S, Yamaki J-I (2005) *Electrochem Solid-State Lett* 8:A459–A463
131. Zhang SS (2006) *J Power Sources* 162:1379–1394
132. Hess S, Wohlfahrt-Mehrens M, Wachtler M (2015) *J Electrochem Soc* 162:A3084–A3097
133. Wrodnigg GH, Wrodnigg TM, Besenhard JO, Winter M (1999) *Electrochem Commun* 1:148–150
134. Appel WK, Besenhard JO, Pasenok S, Winter M, Lie LH. Electrolyte system for lithium batteries, the use thereof, and method for enhancing the safety of lithium batteries. German Patent DE19858925A1 (19.12.1998) (**related European, US and international patents**)
135. Appel WK, Besenhard JO, Pasenok S, Winter M, Lie LH. Electrolyte system for lithium batteries and its use and also a method of increasing the safety of lithium batteries. German Patent DE19858924A1 (19.12.1998) (**related European, US and international patents**)
136. Möller KC, Hodal T, Appel WK, Winter M, Besenhard JO (2001) *J Power Sources* 97–98:595–597
137. Xu K, Ding MS, Zhang SS, Allen JL, Jow TR (2002) *J Electrochem Soc* 149:A622–A626
138. Wang X, Yasukawa E, Kasuya S (2001) *J Electrochem Soc* 148:A1058–A1065
139. Yao XL, Xie S, Chen CH, Wang QS, Sun JH, Li YL, Lu SX (2005) *J Power Sources* 144:170–175
140. Murmann P, Mönninghoff X, von Aspern N, Janssen P, Kalinovich N, Shevchuk M, Kazakova O, Rösenthaller G-H, Cekic-Laskovic I, Winter M (2016) *J Electrochem Soc* 163:A751–A757
141. Xu K, Zhang SS, Allen JL, Jow TR (2003) *J Electrochem Soc* 150:A170–A175
142. Kasnatscheew J, Schmitz RW, Wagner R, Winter M, Schmitz R (2013) *J Electrochem Soc* 160:A1369–A1374
143. Profatilova IA, Stock C, Schmitz A, Passerini S, Winter M (2013) *J Power Sources* 222:140–149
144. Nam T-H, Shim E-G, Kim J-G, Kim H-S, Moon S-I (2007) *J Electrochem Soc* 154:A957–A963
145. Shim E-G, Nam T-H, Kim J-G, Kim H-S, Moon S-I (2007) *J Power Sources* 172:901–907
146. Dunn RP, Kafle J, Krause FC, Hwang C, Ratnakumar BV, Smart MC, Lucht BL (2012) *J Electrochem Soc* 159:A2100–A2108
147. Ciosek Högström K, Lundgren H, Wilken S, Zavalis TG, Behm M, Edström K, Jacobsson P, Johansson P, Lindbergh G (2014) *J Power Sources* 256:430–439
148. Ping P, Wang QS, Sun JH, Xia X, Dahn JR (2012) *J Electrochem Soc* 159:A1467–A1473

149. Xia X, Ping P, Dahn JR (2012) *J Electrochem Soc* 159:A1834–A1837
150. Shim E-G, Nam T-H, Kim J-G, Kim H-S, Moon S-I (2007) *J Power Sources* 172:919–924
151. Smart MC, Krause FC, Hwang C, West WC, Soler J, Prakash GKS, Ratnakumar BV (2011) *ECS Trans* 35:1–11
152. Hyung YE, Vissers DR, Amine K (2003) *J Power Sources* 119–121:383–387
153. Granzow A (1978) *Acc Chem Res* 11:177–183
154. He Y-B, Liu Q, Tang Z-Y, Chen Y-H, Song Q-S (2007) *Electrochim Acta* 52:3534–3540
155. Tobishima S, Ogino Y, Watanabe Y (2003) *J Appl Electrochem* 33:143–150
156. Wang X, Yasukawa E, Kasuya S (2001) *J Electrochem Soc* 148:A1066–A1071
157. Pyschik M, Kraft V, Passerini S, Winter M, Nowak S (2014) *Electrochim Acta* 130:426–430
158. Pyschik M, Schultz C, Passerini S, Winter M, Nowak S (2015) *Electrochim Acta* 176:1143–1152
159. Placke T, Fromm O, Lux SF, Bieker P, Rothermel S, Meyer H-W, Passerini S, Winter M (2012) *J Electrochem Soc* 159:A1755–A1765
160. Rothermel S, Meister P, Schmuelling G, Fromm O, Meyer H-W, Nowak S, Winter M, Placke T (2014) *Energy Environ Sci* 7:3412–3423
161. Armand M, Endres F, MacFarlane DR, Ohno H, Scrosati B (2009) *Nat Mater* 9:621–629
162. Lalia BS, Yoshimoto N, Egashira M, Morita M (2010) *J Power Sources* 195:7426–7431
163. Tasaki K, Goldberg A, Winter M (2011) *Electrochim Acta* 56:10424–10435
164. Winter M, Besenhard JO (1999) *Chem unserer Zeit* 33:252–266
165. Winter M, Besenhard JO (1999) *Chem unserer Zeit* 33:320–332
166. Vogl U, Schmitz A, Stock C, Badillo JP, Gores HJ, Winter M (2014) *J Electrochem Soc* 161:A1407–A1414
167. Krueger S, Kloepsch R, Li J, Nowak S, Passerini S, Winter M (2013) *J Electrochem Soc* 160:A542–A548
168. Xiao L, Ai X, Cao Y, Yang H (2004) *Electrochim Acta* 49:4189–4196
169. Watanabe Y, Morimoto H, Tobishima S (2006) *J Power Sources* 154:246–254
170. Dippel C, Schmitz R, Müller R, Böttcher T, Kunze M, Lex-Balducci A, Rösenthaller G-V, Passerini S, Winter M (2012) *J Electrochem Soc* 159:A1587–A1590
171. Korepp C, Santner HJ, Fujii T, Ue M, Besenhard JO, Möller KC, Winter M (2006) *J Power Sources* 158:578–582
172. Santner HJ, Korepp C, Winter M, Besenhard JO, Möller K-C (2004) *Anal Bioanal Chem* 379:266–271
173. Möller KC, Santner HJ, Kern W, Yamaguchi S, Besenhard JO, Winter M (2003) *J Power Sources* 119–121:561–566
174. Wrodnigg GH, Besenhard JO, Winter M (1999) *J Electrochem Soc* 146:470–472
175. Korepp C, Kern W, Lanzer EA, Raimann PR, Besenhard JO, Yang M, Möller KC, Shieh DT, Winter M (2007) *J Power Sources* 174:628–631
176. Korepp C, Kern W, Lanzer EA, Raimann PR, Besenhard JO, Yang MH, Möller KC, Shieh DT, Winter M (2007) *J Power Sources* 174:387–393
177. Besenhard JO, Moller K-C, Fauler G, Winter M (2002) *US Patent US20040029017A1*
178. Shima K, Shizuka K, Ue M, Ota H, Hatozaki T, Yamaki J-I (2006) *J Power Sources* 161:1264–1274
179. Lee H, Kim S, Jeon J, Cho J-J (2007) *J Power Sources* 173:972–978
180. Lee H, Lee JH, Ahn S, Kim H-J, Cho J-J (2006) *Electrochem Solid-State Lett* 9:A307–A310
181. Kawaguchi T, Fukuda K, Tokuda K, Sakaide M, Ichitsubo T, Oishi M, Mizuki J, Matsubara E (2015) *Phys Chem Chem Phys* 17:14064–14070
182. Liu W, Oh P, Liu X, Lee M-J, Cho W, Chae S, Kim Y, Cho J (2015) *Angew Chem Int Ed* 54:4440–4457
183. Herstedt M, Andersson AM, Rensmo H, Siegbahn H, Edstrom K (2004) *Electrochim Acta* 49:4939–4947
184. Xu M, Li W, Lucht BL (2009) *J Power Sources* 193:804–809
185. Kim JH, Bae S-Y, Min J-H, Song S-W, Kim D-W (2012) *Electrochim Acta* 78:11–16
186. Balducci A, Schmuck M, Kern W, Rupp B, Passerini S, Winter M (2008) *ECS Trans* 11:109–114
187. Jeong S-K, Inaba M, Mogi R, Iriyama Y, Abe T, Ogumi Z (2001) *Langmuir* 17:8281–8286
188. Wang Y, Nakamura S, Tasaki K, Balbuena PB (2002) *J Am Chem Soc* 124:4408–4421
189. Ota H, Sakata Y, Inoue A, Yamaguchi S (2004) *J Electrochem Soc* 151:A1659–A1669
190. Kim H, Grugeon S, Gachot G, Armand M, Sannier L, Laruelle S (2014) *Electrochim Acta* 136:157–165

191. Tarnopolskiy V, Kalhoff J, Nádherná M, Bresser D, Picard L, Fabre F, Rey M, Passerini S (2013) *J Power Sources* 236:39–46
192. Leggesse EG, Jiang J-C (2012) *RSC Adv* 2:5439–5446
193. Chen L, Wang K, Xie X, Xie J (2007) *J Power Sources* 174:538–543
194. Chen L, Wang K, Xie X, Xie J (2006) *Electrochem Solid-State Lett* 9:A512–A515
195. Wen CJ, Huggins RA (1981) *J Solid State Chem* 37:271–278
196. Winter M, Besenhard JO, Albering JH, Yang J, Wachtler M (1998) *Prog Batt Batt Mater* 17:208–213
197. Ryu JH, Kim JW, Sung Y-E, Oh SM (2004) *Electrochem Solid-State Lett* 7:A306–A309
198. Etacheri V, Haik O, Goffer Y, Roberts GA, Stefan IC, Fasching R, Aurbach D (2012) *Langmuir* 28:965–976
199. Dalavi S, Guduru P, Lucht BL (2012) *J Electrochem Soc* 159:A642–A646
200. Vogl US, Lux SF, Crumlin EJ, Liu Z, Terborg L, Winter M, Kostecki R (2015) *J Electrochem Soc* 162:A603–A607
201. Nakai H, Kubota T, Kita A, Kawashima A (2011) *J Electrochem Soc* 158:A798–A801
202. Lindgren F, Xu C, Niedzicki L, Marcinek M, Gustafsson T, Björefors F, Edström K, Younesi R (2016) *ACS Appl Mater Interfaces* 8:15758–15766
203. Mazouzi D, Delpuech N, Oumellal Y, Gauthier M, Cerbelaud M, Gaubicher J, Dupré N, Moreau P, Guyomard D, Roué L, Lestriez B (2012) *J Power Sources* 220:180–184
204. Gauthier M, Mazouzi D, Reyter D, Lestriez B, Moreau P, Guyomard D, Roue L (2013) *Energy Environ Sci* 6:2145–2155
205. Ma L, Xia J, Xia X, Dahn JR (2014) *J Electrochem Soc* 161:A1495–A1498
206. Li B, Wang Y, Lin H, Liu J, Xing L, Xu M, Li W (2014) *Electrochim Acta* 141:263–270
207. Wang Z, Hu Y, Chen L (2005) *J Power Sources* 146:51–57
208. Xu S-D, Zhuang Q-C, Wang J, Xu Y-Q, Zhu Y-B (2013) *Int J Electrochem Sci* 8:8058–8076
209. Hu Y, Kong W, Wang Z, Li H, Huang X, Chen L (2004) *J Electrochem Soc* 7:A442–A446
210. Nam ND, Park IJ, Kim JG, Kim HS (2012) *Mater Res Bull* 47:2811–2814
211. Liu J, Chen Z, Busking S, Belharouak I, Amine K (2007) *J Power Sources* 174:852–855
212. Li J, Yao W, Meng YS, Yang Y (2008) *J Phys Chem C* 112:12550–12556
213. Chen G, Zhuang GV, Richardsson TJ, Liu C, Ross PN Jr (2005) *Electrochem Solid-State Lett* 8:A334–A347
214. Abe K, Ushigoe Y, Yoshitake H, Yoshio M (2006) *J Power Sources* 153:328–335
215. Abe K, Yoshitake H, Kitakura T, Hattori T, Wang H, Yoshio M (2004) *Electrochim Acta* 49:4613–4622
216. Santner HJ, Möller KC, Ivančo J, Ramsey MG, Netzer FP, Yamaguchi S, Besenhard JO, Winter M (2003) *J Power Sources* 119–121:368–372
217. Xia X, Ping P, Dahn JR (2012) *J Electrochem Soc* 159:A1460–A1466
218. Shim E-G, Nam T-H, Kim J-G, Kim H-S, Moon S-I (2007) *Electrochim Acta* 53:650–656
219. Xia J, Sinha NN, Chen LP, Dahn JR (2014) *J Electrochem Soc* 161:A264–A271
220. Krämer E, Schmitz R, Passerini S, Winter M, Schreiner C (2012) *Electrochem Commun* 16:41–43
221. Krämer E, Schmitz R, Niehoff P, Passerini S, Winter M (2012) *Electrochim Acta* 81:161–165
222. Ota H, Akai T, Namita H, Yamaguchi S, Nomira M (2003) *J Power Sources* 119–121:567–571
223. Xing L, Li W, Xu T, Li T, Zhou L (2011) *J Power Sources* 196:7044–7047
224. Wrodnigg GH, Besenhard JO, Winter M (2001) *J Power Sources* 97–98:592–594
225. Zhang B, Metzger M, Solchenbach S, Payne M, Meini S, Gasteiger HA, Garsuch A, Lucht BL (2015) *J Phys Chem C* 119:11337–11348
226. Han G, Li B, Ye Z, Cao C, Guan S (2012) *Int J Electrochem Sci* 7:12963–12973
227. Xia J, Harlow JE, Petibon R, Burns JC, Chen LP, Dahn JR (2014) *J Electrochem Soc* 161:A547–A553
228. Ding Z, Li X, Wei T, Yin Z, Li X (2016) *Electrochim Acta* 196:622–628
229. Sano A, Maruyama S (2009) *J Power Sources* 192:714–718
230. Janssen P, Schmitz R, Müller R, Isken P, Lex-Balducci A, Schreiner C, Winter M, Cekic-Laskovic I, Schmitz R (2014) *Electrochim Acta* 125:101–106
231. Winter M, Wrodnigg GH, Besenhard JO, Biberacher W, Novák P (2000) *J Electrochem Soc* 147:2427–2431
232. Wagner MR, Raimann PR, Trifonova A, Moller KC, Besenhard JO, Winter M (2004) *Anal Bioanal Chem* 379:272–276

233. Madec L, Xia J, Petibon R, Nelson KJ, Sun J-P, Hill IG, Dahn JR (2014) *J Phys Chem C* 118:29608–29622
234. Huang T, Wu M, Wang W, Pan Y, Fang G (2014) *J Power Sources* 262:303–309
235. Zuo X, Fan C, Xiao X, Liu J, Nan J (2012) *J Power Sources* 219:94–99
236. Sinha NN, Burns JC, Dahn JR (2014) *J Electrochem Soc* 161:A1084–A1089
237. Gallus DR, Wagner R, Wiemers-Meyer S, Winter M, Cekic-Laskovic I (2015) *Electrochim Acta* 184:410–416
238. Qi X, Tao L, Hahn H, Schultz C, Gallus DR, Cao X, Nowak S, Roser S, Li J, Cekic-Laskovic I, Rad BR, Winter M (2016) *RSC Adv* 6:38342–38349
239. Bhat V, Cheng G, Kaye S, Li B, Olugible R, Yang JH (2012) US Patent 0315536: A1
240. Rong H, Xu M, Xie B, Huang W, Liao X, Xing L, Li W (2015) *J Power Sources* 274:1155–1161
241. Delp SA, Borodin O, Olguin M, Eisner CG, Allen JL, Jow TR (2016) *Electrochim Acta* 209:498–510
242. Rong H, Xu M, Xing L, Li W (2014) *J Power Sources* 261:148–155
243. Zhang J, Wang J, Yang J, NuLi Y (2014) *Electrochim Acta* 117:99–104
244. Yan G, Li X, Wang Z, Guo H, Wang C (2014) *J Power Sources* 248:1306–1311
245. Zhu Y, Luo X, Xu M, Zhang L, Yu L, Fan W, Li W (2016) *J Power Sources* 317:65–73
246. Song Y-M, Kim C-K, Kim K-E, Hong SY, Choi N-S (2016) *J Power Sources* 302:22–30
247. Song Y-M, Han J-G, Park S, Lee KT, Choi N-S (2014) *J Mater Chem A* 2:9506–9513
248. Han Y-K, Yoo J, Yim T (2015) *J Mater Chem A* 3:10900–10909
249. Mai S, Xu M, Liao X, Hu J, Lin H, Xing L, Liao Y, Li X, Li W (2014) *Electrochim Acta* 147:565–571
250. Ma L, Wang DY, Downie LE, Xia J, Nelson KJ, Sinha NN, Dahn JR (2014) *J Electrochem Soc* 161:A1261–A1265
251. Wang DY, Dahn JR (2014) *J Electrochem Soc* 161:A1890–A1897
252. Ma L, Self J, Nie M, Glazier S, Wang DY, Lin Y-S, Dahn JR (2015) *J Power Sources* 299:130–138
253. Ma L, Xia J, Dahn JR (2014) *J Electrochem Soc* 161:A2250–A2254
254. Nie M, Xia J, Dahn JR (2015) *J Electrochem Soc* 162:A1186–A1195
255. Madec L, Ma L, Nelson KJ, Petibon R, Sun J-P, Hill IG, Dahn JR (2016) *J Electrochem Soc* 163:A1001–A1009
256. Li B, Xu M, Li T, Li W, Hu S (2012) *Electrochem Commun* 17:92–95
257. Li B, Xu M, Li B, Liu Y, Yang L, Li W, Hu S (2013) *Electrochim Acta* 105:1–6
258. Ma L, Xia J, Dahn JR (2015) *J Electrochem Soc* 162:A1170–A1174
259. Burns JC, Sinha NN, Gaurav J, Ye H, VanElzen CM, Lamanna WM, Xiao A, Scott E, Choi J, Dahn JR (2012) *J Electrochem Soc* 159:A1105–A1113
260. Mao H, Sacken UV, Reimers J (1999) US Patent 5,891,592
261. Ping P, Xia X, Wang QS, Sun JH, Dahn JR (2014) *J Electrochem Soc* 160:A426–A429
262. Burns JC, Xia X, Dahn JR (2013) *J Electrochem Soc* 160:A383–A386
263. Petibon R, Aiken CP, Sinha NN, Burns JC, Ye H, VanElzen CM, Jain G, Trussler S, Dahn JR (2013) *J Electrochem Soc* 160:A117–A124
264. Nie M, Xia J, Dahn JR (2015) *J Electrochem Soc* 162:A1693–A1710
265. Nie M, Ma L, Xia J, Xiao A, Lamanna WM, Smith K, Bahn JR (2016) *J Electrochem Soc* 163:A2124–A2130
266. Zuo X, Fan C, Liu J, Xiao J, Wu J, Nan J (2013) *J Electrochem Soc* 160:A1199–A1204
267. Xia J, Madec L, Ma L, Ellis LD, Qiu W, Nelson KJ, Lu Z, Dahn JR (2015) *J Power Sources* 295:203–211
268. Zhang SS, Jow TR, Amine K (2002) *J Power Sources* 107:18–23
269. Yoshio M, Xia Y, Kumada N (2001) *J Power Sources* 101:79–85
270. Zuo XX, Su DG, Liu JS (2005) *Battery* 35:366–367
271. Yamme H, Inoue T, Fujita M, Sano M (2001) *J Power Sources* 99:60–65
272. Li Y, Zhang R, Liu J, Yang C (2009) *J Power Sources* 189:685–688
273. Wu X, Li X, Wang Z, Guo H, Yue P, Zhang Y (2013) *Appl Surf Sci* 268:349–354
274. Zhang Z, Xu X, Zuo XX (2007) *Acta Phys Chim Sin* 23:526–530



High-Power-Density Organic Radical Batteries

Christian Friebe^{1,2} · Ulrich S. Schubert^{1,2}

Received: 11 November 2016 / Accepted: 5 January 2017 / Published online: 1 February 2017
© Springer International Publishing Switzerland 2017

Abstract Batteries that are based on organic radical compounds possess superior charging times and discharging power capability in comparison to established electrochemical energy-storage technologies. They do not rely on metals and, hence, feature a favorable environmental impact. They furthermore offer the possibility of roll-to-roll processing through the use of different printing techniques, which enables the cost-efficient fabrication of mechanically flexible devices. In this review, organic radical batteries are presented with the focus on the hitherto developed materials and the key properties thereof, e.g., voltage, capacity, and cycle life. Furthermore, basic information, such as significant characteristics, housing approaches, and applied additives, are presented and discussed in the context of organic radical batteries.

Keywords Electrochemical energy storage · Organic radical batteries · Lithium-organic batteries · High-power devices

Abbreviations

MWCNT Multi-walled carbon nanotubes
ORB Organic radical battery
PANI Poly(aniline)

Chapter 2 was originally published as Friebe C. & Schubert U. S. Top Curr Chem (Z) (2017) 375: 19. DOI 10.1007/s41061-017-0103-1.

✉ Ulrich S. Schubert
ulrich.schubert@uni-jena.de

¹ Laboratory of Organic and Macromolecular Chemistry (IOMC), Friedrich Schiller University Jena, Humboldtstraße 10, 07743 Jena, Germany

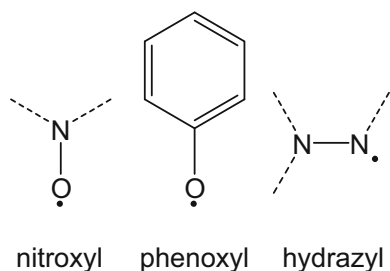
² Center for Energy and Environmental Chemistry Jena (CEEC Jena), Friedrich Schiller University Jena, Philosophenweg 7a, 07743 Jena, Germany

PEG	Poly(ethylene glycol)
PPy	Poly(pyrrole)
PROXYL	2,2,5,5-Tetramethylpyrrolidin- <i>N</i> -oxyl radical
PT	Poly(thiophene)
PTAm	Poly(2,2,6,6-tetramethyl-4-piperidinyl- <i>N</i> -oxyl acrylamide)
PTGE	Poly(2,2,6,6-tetramethyl-4-piperidinyl- <i>N</i> -oxyl glycidyl ether)
PTMA	Poly(2,2,6,6-tetramethyl-4-piperidinyl- <i>N</i> -oxyl methacrylate)
RFID	Radio-frequency identification
TEMPO	2,2,6,6-Tetramethyl-4-piperidinyl- <i>N</i> -oxyl radical

1 Introduction

Current battery technologies are based on the usage of metals such as lead, lithium, cobalt, and nickel. They suffer, on the one hand, from a restricted availability, which potentially leads to new dependencies, as already present for fossil fuels [1]. On the other hand, modern applications, e.g., RFID tags, smart clothes, smart packaging, and the Internet of Things, require modified demands, namely rapid charging, a persistent cycle life, mechanical flexibility, non-toxic materials, environmentally friendly production from sustainable resources, and material-saving processing through roll-to-roll or additive manufacturing techniques. Thus, more and more scientific effort focuses on batteries that rely on organic compounds to store electric charges. These materials allow for a detailed tailoring of their properties with regard to an optimization of the whole battery system. Furthermore, they have the potential to be prepared from renewable resources in the future [2], which directly tackles the sustainability issue. Among the classes of batteries based on organic compounds, organic radical batteries (ORBs) belong to the most promising. They rely on stable organic radicals, which possess an unpaired electron in the ground state [3–6]. The intrinsic stability problems of such systems, namely the formation of single bonds between radicals, are usually overcome by the introduction of sterically hindering groups and electron resonance in the molecule. Related charging products that are obtained by one-electron oxidation or reduction feature no unpaired electrons and are, hence, more stable than redox products of comparable non-radical compounds. Also, organic radicals enable simple redox reactions that necessitate only the transfer of a single electron per active unit without any intercalation processes, as they are present, e.g., in Li-ion batteries, or structural changes, which are observable for alternative organic compounds. Thus, these systems possess superior redox kinetics with high electron-transfer rates, which allow for high charging and discharging currents and, hence, high power densities. Also, the amount of generated heat is reduced, thus avoiding the risk of thermal runaways.

By far the most ORBs that were published up to now use nitroxyl, phenoxy, and hydrazyl radicals (Fig. 1), in particular, the 2,2,6,6-tetramethyl-4-piperidinyl-*N*-oxyl radical (TEMPO). The first battery based on the concept of organic radicals was published by Nakahar et al. in 2002 [6]. Poly(2,2,6,6-tetramethyl-4-piperidinyl-*N*-oxyl methacrylate) (PTMA) and lithium were the active materials used in a metal–organic hybrid cell. This system has since become the standard system for

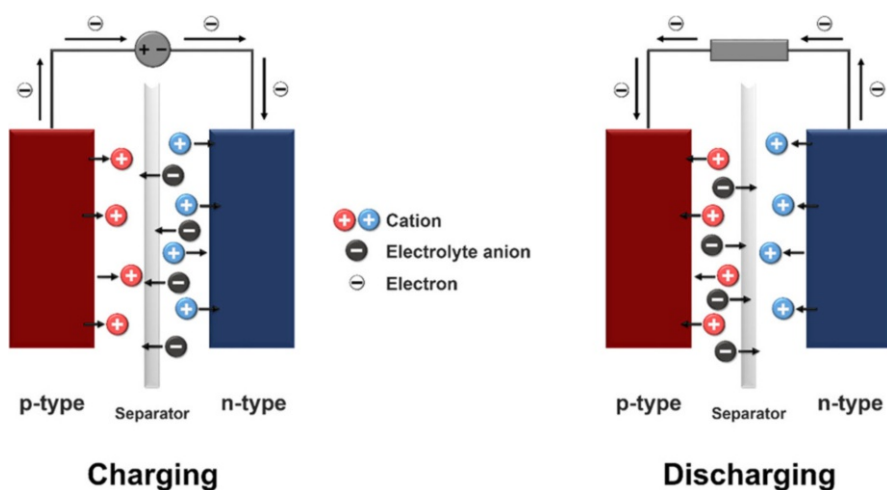
Fig. 1 Molecular structures of stable organic radical units

metal–organic ORBs due to its favorable reliability and stability. The first all-organic ORB, featuring organic active materials for both electrodes, was presented in 2009 by Nishide et al. [7]. It likewise relied on a TEMPO-based polymer, but on a galvinoxyl radical for the second electrode.

2 Basic Concepts of Thin-Film Batteries

In an electrochemical cell, two materials with different redox potentials are placed in an electrolyte solution, separated by a salt bridge or a semipermeable membrane and connected by an electrical conductor. As long as possible, electrons move from the electrode that features the redox couple with the lower redox potential (n-type) to the electrode that shows the higher redox potential (p-type); the former is oxidized, while the latter is reduced. Applying a reverse electric current inverts the process and the system is charged again. The electrolyte is able to provide and receive anions and cations to maintain charge neutrality (Fig. 2).

In an organic radical battery, at least one electrode contains persistent organic radical compounds as active material. In contrast to metallic materials, which show

**Fig. 2** Illustration of an electrochemical cell

sufficient intrinsic electrical conductivity, organic radicals are mostly insulators and must, therefore, be dispersed in a conductive phase. Hence, these electrodes are composite electrodes that contain, besides the active radical, a conductive additive, which provides sufficient electron transport, and a binder, which ensures mechanical stability and homogenous film formation (cf. Sect. 4.1). Furthermore, the solubility of the organic radical compound in all its employed redox states is a crucial matter. Dissolved active material can act as a charge shuttle and leads to self-discharge and lowered capacities. Hence, most of the applied organic materials are (crosslinked) polymers, which usually possess a lower solubility than comparable small molecules.

Most of the ORBs that have been published up to now are metal–organic systems, which possess an organic composite electrode and a metal (mostly lithium, zinc, sodium, magnesium) electrode, as well as a respective metal-ion-containing electrolyte. The metal electrode, which usually represents the n-type electrode, relies on a M^{n+}/M redox couple—the metal is deposited during the charging and dissolved in the form of cations during the discharging process (Fig. 3). Metal–organic cells show usually a higher reproducibility and are more reliable than all-organic systems since the used metal redox couples are established and well known. Thus, they are used to carry out basic characterization routines and performance tests for new organic materials.

The final goal, of course, is a fully organic battery, where both electrodes are composite electrodes containing organic radical active materials. In general, organic redox-active materials are classified into one of three categories, depending on the type of electrochemical reaction they can undergo during the charging process: n-type materials, p-type materials, and b-type (bipolar) materials, whereas the latter can either be oxidized or reduced and thus can be used in both electrodes [8]. The composite electrodes are separated by an ion-permeable membrane and immersed in a suitable electrolyte (Fig. 4).

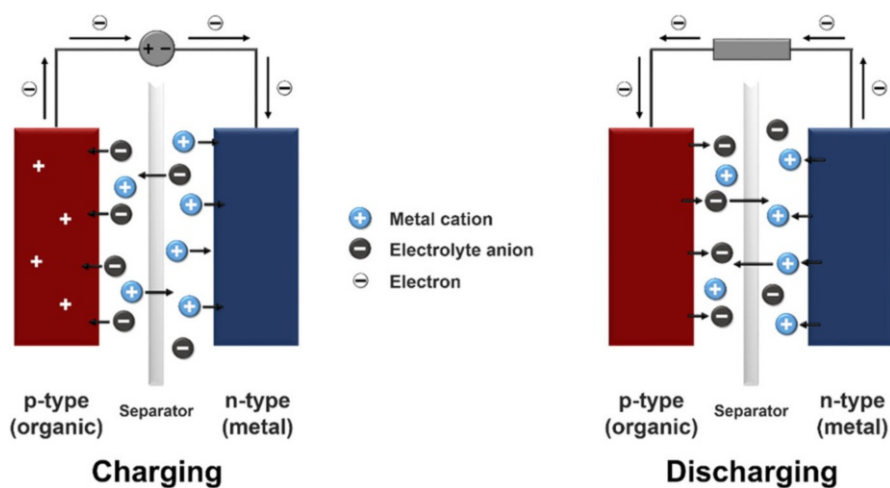


Fig. 3 Illustration of the charging and discharging process of a metal–organic cell

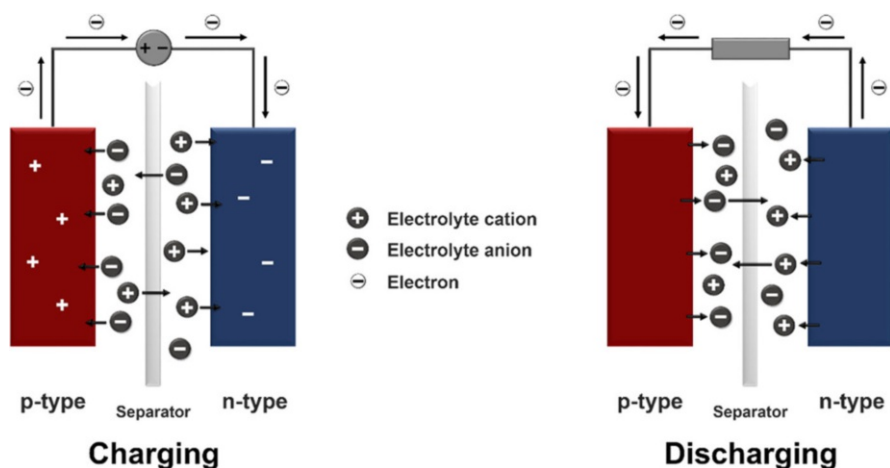


Fig. 4 Illustration of the charging and discharging process of an all-organic cell

2.1 Battery Setup and Housing

In a thin-film organic radical battery, the active materials are applied in thin, solid films of around 2–100 μm . Through charging and discharging, redox reactions take place at the electrodes, and electrons are transferred via the electric circuit. To enable charge neutrality, the films are immersed in an electrolyte, i.e., a conducting salt in a solvent or solvent mixture, which allows the permeation of charge carriers (ions) into and their release out of the electrodes. The whole setup has to ensure charge transport toward both electrodes, but it must also prevent leakage of electrolyte and ingress of moisture and oxygen, as well as short circuits. Several setups have been developed for both laboratory test scale and commercial products.

The most common housing type is the coin cell, which can be used for test experiments, as well as final applications. The single layers of current collectors, electrodes, and separator are stacked, immersed in the electrolyte, and pressed together by a steel spring in a sealed metal casing (Fig. 5). The sealing allows the use of oxygen- and/or water-sensitive materials, if the coin cell is assembled under an inert atmosphere (e.g., in a glovebox) and is, therefore, suitable for a wide range of materials, in particular for first tests.

For experimental test usage, a system that allows further investigations on the used materials after the cell tests is desirable. The so-called SwagelokTM cell, for example, represents such a system. The material layer assembly is locked by screws (Fig. 6a), which enables the disassembling after the cell's examination. For more comprehensive electrochemical tests of the cell, a SwagelokTM T-cell is advised, which allows the usage of a third electrode, i.e., a reference electrode (Fig. 6b). Thus, the electrodes, in particular the applied cell potentials, can be monitored separately to enable a more detailed analysis of the processes that occur in the cell.

A more application-oriented design is the pouch-cell setup. It was developed in 1995 and is simple, flexible, and lightweight [10]. The interior layers of the battery, rounded off by the metal current collectors, are stacked in a sandwich assembly and

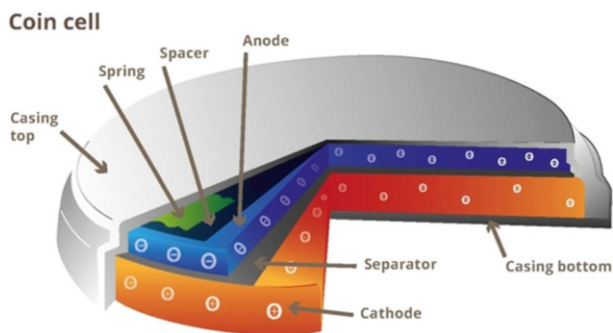


Fig. 5 Illustration of a coin-cell assembly. Reprinted with permission from Ref. [9]. Copyright 2016 American Chemical Society

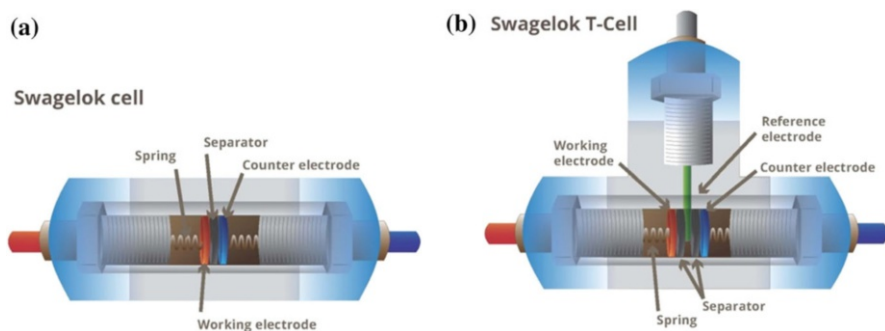


Fig. 6 Illustration of a SwagelokTM-cell (a) and a SwagelokTM T-cell (b) assembly. Reprinted with permission from Ref. [9]. Copyright 2016 American Chemical Society

enclosed by an aluminized plastic pouch (Fig. 7). The latter is subsequently sealed to protect the interior against moisture and oxygen. Thus, a packaging efficiency of more than 90% is achieved, which is the highest among all housing designs.

A widely known housing setup is the cylindrical cell, e.g., the 18650 type. The electrodes and a separating porous membrane are twisted and placed in a cylindrical casing. The setup stands out due to its high mechanical stability and easy assembling. However, up to now no organic radical batteries were fabricated using this design.

2.2 Characteristics

After assembly, independent of the used setup/housing, several basic key parameters have to be determined to decide on the quality and the operability of the battery [11, 12]:

- The *theoretical voltage* (V_{theo} in V) of a battery is the maximum cell voltage that can be achieved with the used redox systems. It is calculated according to

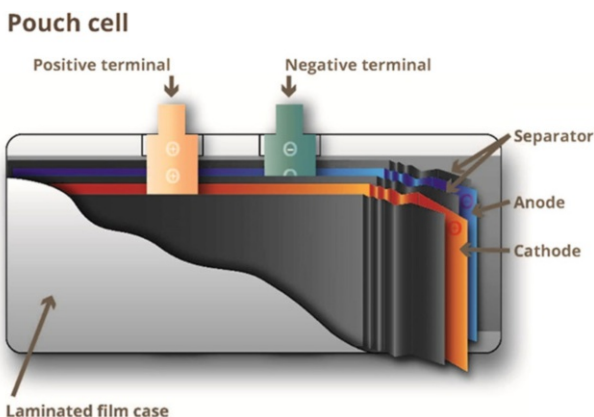


Fig. 7 Illustration of a pouch cell assembly. Reprinted with permission from Ref. [9]. Copyright 2016 American Chemical Society

$V_{\text{theo}} = E_{\text{cathode}} - E_{\text{anode}}$, with E being the redox potential of the respective electrode's redox couple.

- The *theoretical capacity* (C_{theo} in C or Ah) describes the maximum amount of charge that can be stored in the cell if all the active material is accessed.
- The *specific capacity* (C_{spec} in Ah kg⁻¹) is the amount of storable charge per mass of active material. It is calculated according to $C_{\text{spec}} = \frac{nF}{M_w}$, with n being the number of transferred electrons per redox reaction, F the Faraday constant (96,485 C mol⁻¹), and M_w the molar mass of the redox-active moiety. In a cell, both of the electrodes possess single specific capacities, which are not necessarily equal. Usually, the limiting, i.e., the lower, capacity is stated, in particular in cells where one electrode material is used in excess, like in metal–organic cells. The specific capacity of the entire cell can be calculated via $C_{\text{spec,cell}}^{-1} = C_{\text{spec,anode}}^{-1} + C_{\text{spec,cathode}}^{-1}$.
- The *theoretical energy* (E_{theo} in J or Wh) describes the maximum energy that a cell can store, according to $E_{\text{theo}} = C_{\text{theo}} \cdot V$.
- The *specific energy* (E_{spec} in Wh kg⁻¹) is the provided energy per mass of the active material, $E_{\text{spec}} = \frac{E}{m}$. Alternatively, the energy can be referred to the volume of the active material, yielding the *energy density* (E_{dens} in Wh L⁻¹), $E_{\text{dens}} = \frac{E}{\text{volume}}$.

In a real battery, just a fraction of the stated, ideal values can be obtained due to only partial activities of the active material, an insufficient depth of discharge, or electrode polarization, which all result in a decreased provided energy. Additionally, to assess the real performance parameters, the specific capacity and energy have to refer to the whole battery system including the non-active components, e.g., conductive additive, binder, electrolyte, current collector, separator, housing, and seals, which increase the mass and the volume of the battery, thus significantly decreasing both the specific capacity and energy. Hence, optimized, but real

batteries usually provide energies at about 25–35% of the theoretical value [12]. The performance of a battery is thus characterized by the real, experimentally determined values:

- The *cell voltage* (V in V) is the actual voltage that is achieved by a cell. It ranges from about 1–3.6 V for commercially available batteries. Systems that are based on organic radicals exhibit similarly high voltages (up to 3.6 V), if they are run with a lithium electrode. All-organic radical batteries currently show voltages up to 1.3 V, which can be further raised by the introduction of suitable functional groups [13].
- The *capacity* (C in Ah) is the amount of charges that can be stored in the battery. It can be stated separately for each electrode as well as for the charging and the discharging. Accordingly, the *energy* (E in Wh) of the battery describes the energy that is stored (charging) or released (discharging). Both values can also be stated as specific value, i.e., per mass of the active material or, more practically, per mass of the whole battery setup. The specific charges of ORBs that are presented in the literature up to now reach values of about 185 Ah kg^{-1} for metal-containing hybrid systems and 44 Ah kg^{-1} for all-organic radical batteries. (Noteworthy, these values are calculated for the mass of only the p-type and of both electrodes, respectively.)
- The *Coulombic efficiency* (η_c in %) is the ratio of discharging and charging capacity, $\eta_c = \frac{C_{\text{discharge}}}{C_{\text{charge}}}$, and thus depicts the reversibility of the charging process. For a usable battery, the efficiency should be nearly 100%.
- The *rate capability* describes the ability of the battery to be charged/discharged at certain (high) currents; usually, the highest current density that still results in a capacity that is similar to the capacities at significantly lower currents is stated. It is given by the C-rate, which gives the applied current relative to the current that is necessary to charge the battery within 1 h (C-rate = $\frac{i_{\text{applied}}}{i_{1\text{h}}}$). ORBs are capable to show very high charging/discharging rates of 10–400C with only a minor loss of capacity.

3 Active Materials

The core demand to a battery active material is the availability of at least one reversible electrochemical process with stable species in both the oxidized and the reduced form. The respective redox potential should be appropriate, i.e., as high (p-type material) or low (n-type material) as possible, but still manageable with regard to the used electrolyte, current collector, etc., to achieve a cell voltage that is as high as possible. Organic compounds offer a large pool of available structures and possibilities of functionalization, which enable the tuning of the redox processes of interest, in particular with regard to the redox potentials. Thus, compounds that can either serve as p-type or n-type material or even both (b-type) can be prepared, although most of the organic materials that were developed up to now are more

a two-step electron transfer [16–18]: firstly, a heterogeneous electron transfer from the current collector or conductive additive to the TEMPO unit occurs. This step is facilitated by the only small alterations of the structure of the radical moiety. Respective standard transfer rate constants were determined to be around $10^{-1} \text{ cm s}^{-1}$ [15], which is in the range of redox processes related to transition metal ions [19, 20]. In a polymer, the second step is a concentration-gradient-driven charge transfer among the radical moieties based on self-exchange between neighboring units with a bimolecular rate constant of $1.8 \times 10^5 \text{ M}^{-1} \text{ s}^{-1}$ [18]. Accordingly, TEMPO-containing polymers show intrinsic electrical conductivity along the polymer chain in the solid state [21].

Several examples of TEMPO-bearing active materials that were used in batteries are shown in Table 1. The most common radical-based active material is the TEMPO-containing polymer poly(2,2,6,6-tetramethyl-4-piperidinyl-*N*-oxyl methacrylate) (PTMA). Like all organic active materials, it was mostly used in metal-containing hybrid batteries up to now, usually with lithium, where a cell voltage of ca. 3.6 V with an only small gap of around 100 mV between the charging and discharging is achieved [22, 23]. The theoretical specific capacity of 111 Ah kg^{-1} is reached for many presented examples and a stability of several hundred cycles can be accomplished. Another promising material class is represented by TEMPO-functionalized poly(norbornene)s. The usage of two TEMPO units per norbornene monomer leads to a theoretical specific capacity of 109 Ah kg^{-1} . Noteworthy, the usable capacity depends strongly on the endo/exo configuration of the two TEMPO moieties: due to a small radical–radical distance of 10 Å in the endo/endo species, only half of the theoretical capacity is achieved [24]. In contrast, the endo/exo isomer allows for full material activity.

The charge compensation during charging/discharging via inclusion or release of counterions represents a crucial process with regard to the overall kinetics. Because of its good swelling property and superior ionic transport ability along the main chain, the PEG-analogous PTGE is used enabling efficient charge transport and thus a diminished amount of required conductive additive [25]. Alternatively, micelles with a poly(styrene) core and a PTMA corona were studied and permit an easier access of the counterions to the active radical units; however, the poly(styrene) block is “dead” material decreasing the overall specific capacity [26]. When sulfonate-containing co-monomers are used, the counterions for charge compensation are included in the active material itself. Thus, the electrolyte’s ion concentration remains stable throughout the charge/discharge process and the required amount of conducting salt is decreased [27].

In the course of a usual composite preparation, the particles of the conductive additive are homogeneously coated with the active material, which is only non- or semiconductive. Thus, the conductive particles are electrically isolated and the charge transfer is limited [28]. One approach to overcome this problem is the application of vertically aligned carbon nanotubes that are grown from the current collector, thus preventing the formation of an isolating polymer layer and enabling charging rates up to 100C [29]. Alternatively, the homogeneity of the mixture of active material and carbon particles can be increased, for example, by the melt-polymerization of TEMPO methacrylate in the presence of nanostructured carbons [30].

Table 1 Characteristics of batteries based on TEMPO-containing active materials

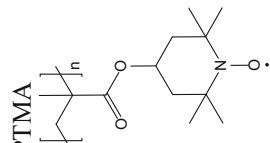
Compound	Discharge voltage	Initial discharge capacity (material activity)	Applied current	Cycles	Capacity loss (%)	Remarks	References	
 <p>PTMA</p>	3.5 V vs. Li ⁺ /Li	77 Ah kg ⁻¹ (69%)	1 A m ⁻²	500	12		[6]	
	3.5 V vs. Li ⁺ /Li	110 Ah kg ⁻¹ (99%)	1C	100	8		[22]	
	3.6 V vs. Li ⁺ /Li	- ^a	20C	1000	11		[23]	
	3.4 V vs. graphite	80 Ah kg ⁻¹ (72%)	59 A kg ⁻¹	100	18		[36]	
	3.9 V vs. Li ⁺ /Li	39 Ah kg ⁻¹ (35%)	100C	- ^a	- ^a		[37]	
	3.6 V vs. Li ⁺ /Li	111 Ah kg ⁻¹ (100%)	10C	150	2		[38]	
	3.6 V vs. Li ⁺ /Li	109 Ah kg ⁻¹ (98%)	50C	10	1		[39]	
	3.6 V vs. Li ⁺ /Li	133 Ah kg ⁻¹ (120%)	1C	500	20		[40]	
							Significant contribution by the conductive additive's capacitance	
		3.6 V vs. Li ⁺ /Li	63 Ah kg ⁻¹ (57%)	100C	- ^a	- ^a		[29]
	3.6 V vs. Li ⁺ /Li	53 Ah kg ⁻¹ (48%)	10C	1200	15		[30]	
	3.6 V vs. Li ⁺ /Li	97 Ah kg ⁻¹ (87%)	2C	200	5		[41]	
	3.7 V vs. Li ⁺ /Li	15 Ah kg ⁻¹ (14%)	1C	80	30		[26]	
	3.5 V vs. Li ⁺ /Li	77 Ah kg ⁻¹ (69%)	10 A m ⁻²	1000	- ^a		[42]	
	3.6 V vs. Li ⁺ /Li	111 Ah kg ⁻¹ (100%)	30C	100	16		[43]	
	3.6 V vs. Li ⁺ /Li	78 Ah kg ⁻¹ (70%)	1C	100	2		[44]	
	3.6 V vs. Li ⁺ /Li	55–111 Ah kg ⁻¹ (50–100%)	10C (lowest thickness)	100	10–30	Different film thicknesses	[45]	
	3.6 V vs. Li ⁺ /Li	79–111 Ah kg ⁻¹ (71–100%)	20C (lowest content)	200	15	Different active-material contents	[46]	

Table 1 continued

Compound	Discharge voltage	Initial discharge capacity (material activity)	Applied current	Cycles	Capacity loss (%)	Remarks	References
Poly(TMA-GMA)	3.6 V vs. Li ⁺ /Li	110 Ah kg ⁻¹ (99%)	10C	400	15		[47]
	3.6; 2.5–3.2 V vs. Li ⁺ /Li	222 Ah kg ⁻¹ (200%)	1C	100	24	Contribution by a 2nd TEMPO redox process	[48]
	3.6 V vs. Li ⁺ /Li	110 Ah kg ⁻¹ (99%)	1C	50	10		[49]
	3.6 V vs. Li ⁺ /Li	94 Ah kg ⁻¹ (85%)	10C	300	4	Polymer brushes	[50]
	3.6 V vs. Li ⁺ /Li	97 Ah kg ⁻¹ (87%)	10C	50	10	Polymer brushes	[51]
	3.6 V vs. Li ⁺ /Li	4.9 Ah dm ⁻³	5C	250	4	Polymer brushes	[52]
	3.65 V vs. Li ⁺ /Li	94 Ah kg ⁻¹ (85%)	20C	100	3	Polymer brushes	[53]
	3.65 V vs. Li ⁺ /Li	94 Ah kg ⁻¹ (85%)	0.5C	^a	^a	Polymer brushes on MWCNTs	[54]
	0.8 V vs. AgCl/Ag	70 Ah kg ⁻¹	100C	500	^a	Grafting onto ITO	[55]
	Poly(TEMPO norbornene)	3.5 V vs. Li ⁺ /Li	109 Ah kg ⁻¹ (100%)	100 A kg ⁻¹	^a	^a	
3.6 V vs. Li ⁺ /Li		106 Ah kg ⁻¹ (97%)	10C	1000	^a	Photocrosslinking	[56]
3.6 V vs. Li ⁺ /Li		7–109 Ah kg ⁻¹ (6–100%)	0.088 mA cm ⁻²	500	10	Different monomer substitution patterns	[57]
0.66 V vs. Poly(galvinoxyl styrene)		32 Ah kg ⁻¹ (92% total amount)	360C	250	20	Fully organic	[7]

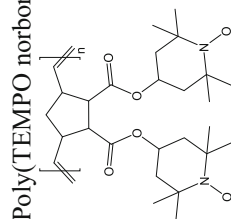
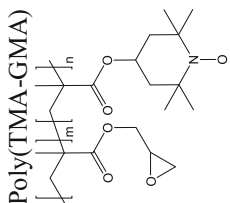


Table 1 continued

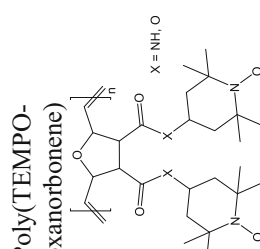
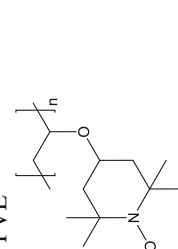
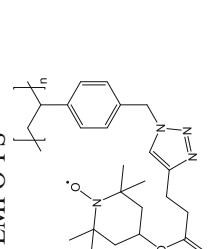
Compound	Discharge voltage	Initial discharge capacity (material activity)	Applied current	Cycles	Capacity loss (%)	Remarks	References
Poly(TEMPO-oxanorbonene)  X = NH, O	3.5 V vs. Li ⁺ /Li	74 Ah kg ⁻¹ (68%) (last value)	1C	100	-60 ^b	Ionic-liquid electrolyte	[58]
	3.6 V vs. Li ⁺ /Li	93 (X=NH), 107 (X=O) Ah kg ⁻¹ (85, 98%)	100 A kg ⁻¹	100	-11 (X=NH) ^b , 10 (X=O)		[59]
PTVE 	1.7 V vs. Zn ²⁺ /Zn	131 Ah kg ⁻¹ (97%)	60C	500	35	Aqueous electrolyte	[60]
	3.5 V vs. Li ⁺ /Li	114 Ah kg ⁻¹ (84%)	0.6C	- ^a	- ^a		[61]
	3.5 V vs. Li ⁺ /Li	104 Ah kg ⁻¹ (77%)	1C	- ^a	- ^a		[62]
	0.75 V vs. AgCl/Ag	131 Ah kg ⁻¹ (97%)	60C	1000	25	Aqueous electrolyte	[63]
TEMPO-PS 	3.6 V vs. Li ⁺ /Li	31 Ah kg ⁻¹ (48%)	0.25C	30	~0		[64]

Table 1 continued

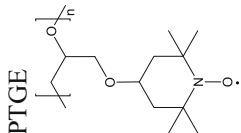
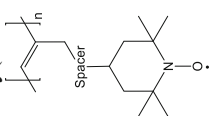
Compound	Discharge voltage	Initial discharge capacity (material activity)	Applied current	Cycles	Capacity loss (%)	Remarks	References
 PTGE	3.5 V vs. Li ⁺ /Li	80 Ah kg ⁻¹ (68%)	1C	200	30		[25]
	3.5 V vs. Li ⁺ /Li	77 Ah kg ⁻¹ (65%)	10C	1000	— ^a		[65]
 Poly(TEMPO acetylene)	3.6 V vs. Li ⁺ /Li	23–82 Ah kg ⁻¹	100 A kg ⁻¹	— ^a	— ^a	Different spacer	[24]
	3.6 V vs. Li ⁺ /Li	21–108 Ah kg ⁻¹ (20–100%)	96 A kg ⁻¹	— ^a	— ^a	Different spacer	[66]
	3.6 V vs. Li ⁺ /Li	43–84 Ah kg ⁻¹ (33–98%)	95 A kg ⁻¹	100	15	Different spacer	[67]

Table 1 continued

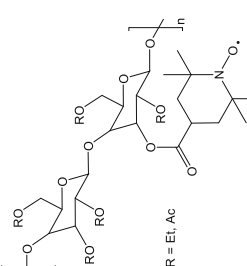
Compound	Discharge voltage	Initial discharge capacity (material activity)	Applied current	Cycles	Capacity loss (%)	Remarks	References
<p>TEMPO-cellulose</p>  <p>R = Et, Ac</p>	3.6; 2.8–2.4 V vs. Li ⁺ /Li	43 (R=Et), 61 (R=Ac) Ah kg ⁻¹ (139, 153%)	500 A kg ⁻¹	100	30 (R=Et), 7 (R=Ac)	Contribution by a 2nd TEMPO redox process	[68]
TEMPO-DNA complex	3.6; 2.8 V vs. Li ⁺ /Li	41–60 Ah kg ⁻¹ (124–192%)	400 A kg ⁻¹	100	<10	Contribution by a 2nd TEMPO redox process	[69]
TEMPO-polyallene	3.6 V vs. Li ⁺ /Li	41 Ah kg ⁻¹	100 A kg ⁻¹	50	1.4		[70]

Table 1 continued

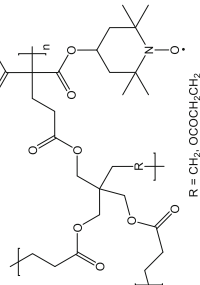
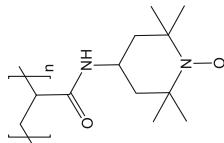
Compound	Discharge voltage	Initial discharge capacity (material activity)	Applied current	Cycles	Capacity loss (%)	Remarks	References
<p>TEMPO-poly(β-ketoester)</p>  <p>R = CH₂, OCOCH₂CH₂</p>	0.8 V vs. AgCl/Ag	54 (R=CH ₂), 55 (R=OCOCH ₂ CH ₂) Ah kg ⁻¹	1C	20	10		[71]
<p>PTAm</p> 	1.2 V vs. Poly(viologen)	110 Ah kg ⁻¹ (98%)	60C	2000	20	Fully organic	[72]

Table 1 continued

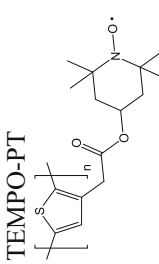
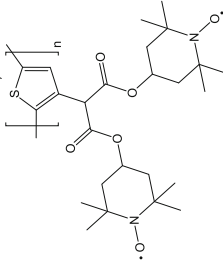
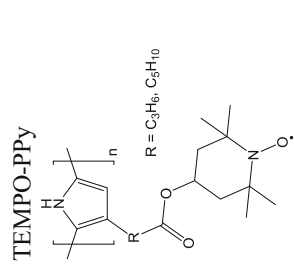
Compound	Discharge voltage	Initial discharge capacity (material activity)	Applied current	Cycles	Capacity loss (%)	Remarks	References
 TEMPO-PT	3.6 V vs. Li ⁺ /Li	79 Ah kg ⁻¹	0.05 mA	50	23		[73]
 TEMPO-PPy	3.6 V vs. Li ⁺ /Li	89 Ah kg ⁻¹ (81%)	1C	10	14		[74]
 TEMPO-PPy R = C ₃ H ₆ , C ₆ H ₁₀	3.6; 3.0–2.6 V vs. Li ⁺ /Li	87 (R=C ₃ H ₆), 115 (R=C ₅ H ₁₀) Ah kg ⁻¹	20 A kg ⁻¹	50	45 (R=C ₃ H ₆), 25 (R=C ₅ H ₁₀)		[75]

Table 1 continued

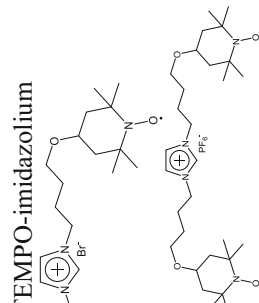
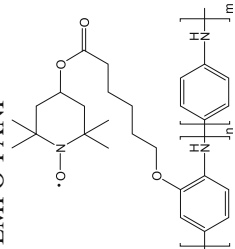
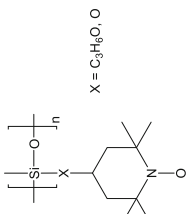
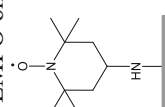
Compound	Discharge voltage	Initial discharge capacity (material activity)	Applied current	Cycles	Capacity loss (%)	Remarks	References
	3.5 V vs. Li ⁺ /Li	59 Ah kg ⁻¹ (100%)	1C	300	24		[76]
	3.5 V vs. Li ⁺ /Li	80 Ah kg ⁻¹ (100%)	1C	50	1		[76]
	3.7–3.0 V vs. Li ⁺ /Li	44–77 Ah kg ⁻¹	20 A kg ⁻¹	20	15–20	Different co-monomer ratios; sloping discharging plateau	[77]

Table 1 continued

Compound	Discharge voltage	Initial discharge capacity (material activity)	Applied current	Cycles	Capacity loss (%)	Remarks	References
<p>TEMPO-PMS</p>  <p>X = C₃H₆O</p>	3.6 V vs. Li ⁺ /Li	46 (X=C ₃ H ₆ O), 89 (X=O) Ah kg ⁻¹ (47, 77%)	1C	100	<2 (X=O)		[78]
<p>TEMPO on carbon</p> 	0.9 V vs. Naphthalimide	8.3 Ah kg ⁻¹	0.1 mA	50	30	Fully organic	[79]

^a Not given

^b Capacity increase during cycling

To increase the rate capability and capacity, hybrid systems that combine TEMPO polymers with established charge-storage technologies were developed. Aiming at higher charging rates, a hybrid TEMPO-supercapacitor electrode based on a gel that formed from crosslinked PTMA, high-surface-area carbon particles, and a carbonate-based electrolyte was prepared [31]. In combination with a lithium electrode, total capacities of 40 Ah kg^{-1} (with respect to the overall mass of both electrodes) and discharging rates of 100C with reasonable capacity loss were observed. Alternatively, PTMA was combined with LiFePO_4 to form a hybrid electrode that allows for faster charging (10C) and higher long-term stability (>1500 cycles) compared to a LiFePO_4 electrode and for higher specific capacities (130 Ah kg^{-1}) than for PTMA-based systems [32].

In addition to the well-known, reversible oxidation of the TEMPO radical, a reduction toward the aminoxyl anion is possible, too. Under usual conditions, this process is irreversible and thus inappropriate for the application in a battery. However, efforts were made to utilize this process, which would make the TEMPO a b-type material. The presented approaches are mostly based on the stabilization of the reduced species by mesoporous carbon networks or graphene [33–35].

3.2 Other Nitroxide Radicals

Although TEMPO is the by far most frequently used organic radical for battery active materials, other nitroxyl radicals represent promising alternatives and additions, in particular with regard to all-organic systems [80]; several examples are provided in Table 2. The 2,2,5,5-tetramethyl-2,5-dihydro-1*H*-pyrrol-*N*-oxyl and the saturated 2,2,5,5-tetramethylpyrrolidin-*N*-oxyl (PROXYL) radicals possess five- instead of six-membered rings, thus featuring a lower molar mass than TEMPO derivatives. Hence, higher theoretical capacities can be achieved, e.g., 147 Ah kg^{-1} for a 2,2,5,5-tetramethyl-2,5-dihydro-1*H*-pyrrol-*N*-oxyl-decorated PEG polymer, which is comparable to LiCoO_2 in classical lithium-ion batteries [81, 82]. However, subsequently built batteries exhibited only half the expected capacity [83]. The approach to increase the specific capacity via the introduction of a second nitroxyl in a spiro-*bis*(nitroxide) failed likewise, since only one radical unit undergoes a reversible redox reaction [84]. Furthermore, a series of *N*-*tert*-butyl-nitroxyl styrene derivatives was proposed to serve as active material that can be, depending on additional functional groups, used either as p-type or n-type material [85]. Though, up to now, these materials were not applied in a battery. The nitronyl nitroxide radical is of particular interest, since it features two reversible redox processes in an applicable potential range. Hence, it can be used as a b-type material. Nishide et al. presented a battery based on poly(nitronyl nitroxyl styrene) as active material for both electrodes [86]. It showed a cell voltage of 1.3 V and a specific capacity of 29 Ah kg^{-1} , which corresponds to 91% of the theoretical value. Furthermore, a reversible pole change was demonstrated, proving that the battery is “pole-less”.

Table 2 Characteristics of batteries based on other radical active materials

Compound	Discharge voltage (stability)	Initial discharge capacity (material activity)	Current	Cycles	Capacity loss (%)	Remarks	References
Poly(2,2,5,5-tetramethyl-3,4-dihydro-pyrrolidin- <i>N</i> -oxy ether)	3.6 V vs. Li ⁺ /Li	75 Ah kg ⁻¹ (60%)	10C	100	10		[99]
	3.7 V vs. Li ⁺ /Li	70 Ah kg ⁻¹ (48%)	10C	1000	20		[83]
Poly(PROXYL acetylene)	3.5 V vs. Li ⁺ /Li	103 (R=Me, X=O; helical),	1C	100	15		[67]
		112 (R=Me, X=O; non-helical) Ah kg ⁻¹ (92, 100%)					
		117 (R=H, X=O), 95 (R=H, X=NH) Ah kg ⁻¹ (98, 79%)					
	3.5 V vs. Li ⁺ /Li			100	25		[100]

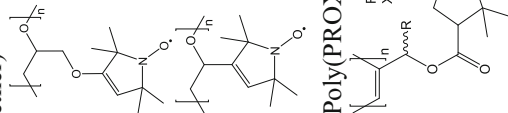


Table 2 continued

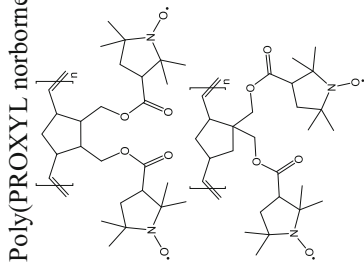
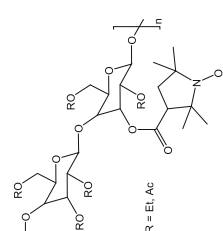
Compound	Discharge voltage (stability)	Initial discharge capacity (material activity)	Current	Cycles	Capacity loss (%)	Remarks	References
Poly(PROXYL norbornene) 	3.5 V vs. Li ⁺ /Li	89 to 107 Ah kg ⁻¹ (81–98%)	0.089 mA cm ²	100	35–0	endo/endo and endo/exo isomer	[100]
	3.5 V vs. Li ⁺ /Li	85 Ah kg ⁻¹ (78%)	0.089 mA cm ²	100	25		[100]
PROXYL-cellulose 	3.6; 2.8–2.4 V vs. Li ⁺ /Li	59 (R=Et), 45 (R=Ac) Ah kg ⁻¹ (140, 111%)	500 A kg ⁻¹	100	30 (R=Et), 10 (R=Ac)	Contribution by a 2nd PROXYL redox process	[68]

Table 2 continued

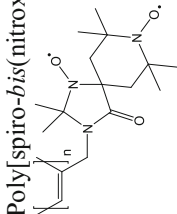
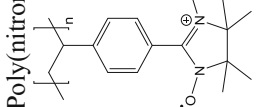
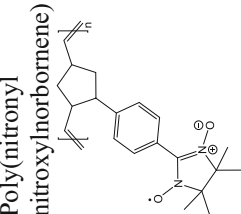
Compound	Discharge voltage (stability)	Initial discharge capacity (material activity)	Current	Cycles	Capacity loss (%)	Remarks	References
Poly[spiro-bis(nitroxide)] 	~3.6; ~4.3 V vs. Li ⁺ /Li	73 (only 1st process), 90 Ah kg ⁻¹ (85, 52%)	1C	15	60		[84]
Poly(nitronyl nitroxyl/styrene) 	1.3 V vs. Poly(nitronyl nitroxyl styrene) 0.6 V vs. Poly(galvinoxyl-styrene)	44 Ah kg ⁻¹ (86%, total amount) 29 Ah kg ⁻¹ (91%, total amount)	10C	250	33	Pole-less, fully organic	[86]
Poly(nitronyl nitroxylnorbornene) 	0.8; -0.8 V vs. AgCl/Ag	59, 44 Ah kg ⁻¹ (71, 54%)	40C	100	25 (only 1st process)	Half cell	[101]

Table 2 continued

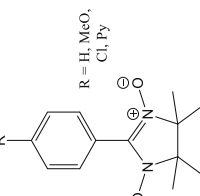
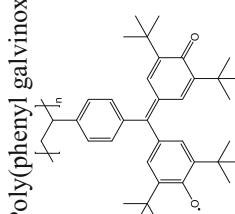
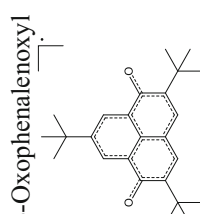
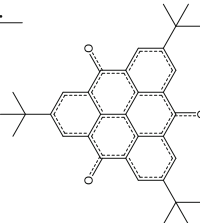
Compound	Discharge voltage (stability)	Initial discharge capacity (material activity)	Current	Cycles	Capacity loss (%)	Remarks	References
Aryl(nitronyl nitroxide)	3.5; 2.5 V (R=H, MeO), 3.6; 2.6 V (R=Cl, Py) vs. Li ⁺ /Li	143 (R=H), 180 (R=MeO), 143 (R=Cl), 185 (R=Py) Ah kg ⁻¹ (62, 88, 72, 81%)	50 A kg ⁻¹	4	55 (R=H), 15 (R=MeO), 65 (R=Cl, Py)		[102]
							
Poly(phenyl galvinoxyl)	0.66 V vs. Poly (TEMPO norbornene)	32 Ah kg ⁻¹ (91%, total amount)	10C	250	25	Fully organic	[7]
	0.6 V vs. Poly (nitronyl nitroxylstyrene)	29 Ah kg ⁻¹ (91%, total amount)	10C	250	–	Fully organic	[86]
							
6-Oxophenalenoxyl	3.5; 2.2 V vs. Li ⁺ /Li	152 Ah kg ⁻¹ (103%)	1C	100	80		[89]
							

Table 2 continued

Compound	Discharge voltage (stability)	Initial discharge capacity (material activity)	Current	Cycles	Capacity loss (%)	Remarks	References
Trioxotriangulene 	3.0; 2.2 V vs. Li^+/Li	169 Ah kg^{-1} (65%) (2nd cycle)	0.3C	100	60		[89]

^a Not given

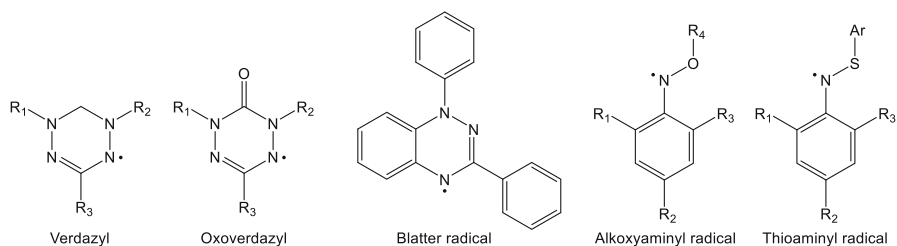


Fig. 10 Molecular structures of selected organic radicals as potential candidates for ORBs

3.3 Other Radicals

Only very few organic radical compounds besides nitroxides were considered for the usage in batteries up to now (cf. Table 2). Phenoxy radicals, namely the galvinoxyl radical, were used as n-type active material for all-organic radical batteries, exploiting the phenoxy/phenolate redox couple [7, 86–88]. The applied poly(phenyl galvinoxyl) possesses a theoretical specific capacity of only 51 Ah kg⁻¹; thus, although material activities over 90% were achieved, the obtained all-organic batteries showed specific capacities of only about 30 Ah kg⁻¹ (referred to the total amount of active material in both electrodes). Targeting higher specific capacities requires either a lower molar mass, which is rather challenging with regard to the radical stability, or multi-electron redox processes. The latter can be fulfilled using suitable polycyclic compounds, like the 6-oxophenalenoxyl and trioxotriangulene, which allow a two- and four-electron oxidation, respectively, leading to high specific capacities of 152 and 169 Ah kg⁻¹, but suffer from multi-step discharge voltages and severe capacity losses over cycling [89].

For future developments, new classes of radicals that are suitable for electrochemical energy storage should be developed to enlarge the scope of available active materials and thus of the application possibilities. Here, computational methods could assist in finding stable radical structures and support an effective optimization of the material's characteristics through the simulation of applicable functionalization patterns. Nitrogen heterocycles turned out to be a promising class of organic radicals for battery application. In particular, the verdazyl and oxoverdazyl radicals (Fig. 10) are conceivable candidates to extend the toolbox of active materials, with the oxoverdazyl being more stable than its methylene-bridged counterpart [90, 91]. The 1,3-diphenyl-1,4-dihydro-1,2,4-benzotriazin-4-yl radical, the so-called Blatter radical (Fig. 10), represents an additional promising alternative, which offers high radical stability and further possibilities of functionalization with regard to a desirable fine-tuning of the radical's electrochemical properties [92–95]. Besides heterocycles, stable nitrogen-based radicals can also be achieved in the form of alkoxyaminy radicals and thioaminy radicals (Fig. 10) [96–98], which likewise offer various possibilities of functionalization with regard to an optimized stability, redox potential, and solubility. Both the presented *N*-heterocycle and the aminyl radicals offer a reversible one-electron oxidation and reduction of the radical species, which allows the usage as p-type and

n-type, as well as bipolar material. The theoretical specific capacities of active materials based on verdazyl, oxoverdazyl, Blatter, alkoxyaminy, and thioaminy radicals are, depending on additional functionalization, <130, <120, <95, <120, and <110 Ah kg⁻¹, respectively (assuming at least two iso-propyl groups for the verdazyl systems and at least one aryl substituent for the aminyl compounds to achieve stable radicals), which is comparable to the established nitroxide materials. However, these systems are mere candidates so far.

4 Non-Active Materials

4.1 Conductive Additive and Binder

Organic radical compounds usually lack intrinsic electrical conductivity. Some systems show electron-hopping mechanisms, which allow for restricted electron-transfer pathways, but the resulting conductivity is usually not sufficient to enable long-range electron migration [15, 17]. One approach to ensure a high activity of the active material is the application of thin films directly on the current collectors. The films are applied either by polymerization onto the surface, e.g., through electropolymerization [73, 103, 104] and surface-initialized polymerization [52, 53], or as polymers via classical coating techniques, like spincoating [7, 18, 56, 105]. Such a setup is convenient to determine characteristics of the electrochemical surface process, e.g., the diffusion coefficient or electron-exchange rates [106, 107], and consequently to gain deeper insights into the material's interactions with its environment, but it is not suitable for a commercial battery due to its insufficient, ultra-low capacity [56].

In an organic battery, the active material is mixed with a conductive additive to obtain a composite electrode. The additives allow for electron migration between the redox-active molecules and the current collector and, furthermore, are able to counterbalance volume changes during the electrochemical processes. They must thus provide high intrinsic electrical conductivity and a large surface to interact effectively with the active material, and they have to enable the formation of a flexible network [46]. During the charge-storage process, the redox-active moiety not only has to take up or release electrons, but the change of charge must also be balanced simultaneously through the insertion or the release of counter ions [28]. Hence, the composite must possess porosity to enable the electrolyte to penetrate the entire material and to allow counter ions to enter and to leave the active material network. Redox units that are not accessible either by electrons or counter ions cannot participate in the charging and discharging process and have to be considered as dead material.

Most of the applied conductive additives are nanostructured carbon materials, e.g., carbon nanoparticles [108, 109], mesoporous carbon [34, 40, 110], vapor-grown carbon fibers [23, 62, 111, 112], graphene [35, 48, 113–115], and carbon nanotubes [116–118].

A binder material can be necessary to ensure intermixing of the active material and the carbon conductive additive, as well as to enhance the mechanical stability of

the composite electrode. It thus has an essential impact on the battery performance and stability [119]. When organic solvents are applied in the electrode processing or the battery electrolyte, fluorinated polymers, e.g., poly(tetrafluoroethylene) (PTFE) and poly(vinylidene difluoride) (PVdF), are mostly used due to their electrochemical stability, binding capability, and electrolyte absorption ability [23]. For water-based systems, carboxymethyl cellulose (CMC) is the most frequently used binder. Metal salts of CMC, poly(acrylate)s, or PEDOT:PSS represent alternatives that enhance the composite performance by the introduction of additional ions or semiconductivity [120, 121].

Processing the composite is crucial for the performance of the resulting battery. The more homogenous the electrode components are mixed, the more redox units are able to participate in the charge-storage process. Different processing approaches that aim at an optimized mixing exist, depending on the used materials [9]. Solid–solid mixing, e.g., in a ball mill, leads to large interfaces between the active material and the conductive additive, in particular if the former does not constitute too large particles and the latter consists of spherical or porous materials. If fibrous additives and soluble active materials are used, liquid–solid mixing, i.e., the preparation and homogenization of a solution/dispersion of the active radical compound and the additives, is preferred. The fibers are coated with the active material and form a conductive network upon drying [23]. Even water can be used as solvent, applying carboxymethyl cellulose as binder [22, 36], although, in this case, the active materials have to be applied in the form of nanometer-sized particles to ensure a large contact area with the additives. However, if the drying conditions are not chosen carefully, brittle or cracked electrodes can result, in particular, if the polymer reveals strong swelling in the solvent [62]. Alternatively, in-situ polymerization of the active material onto particles of the conductive additive proved to be suitable for the preparation of large redox material–additive interfaces [30].

4.2 Electrolytes

The electrolyte is crucial for maintenance of the charge balance during the redox processes of the charging/discharging. Besides the fundamental requirement to provide ions of the necessary type and with a maximum mobility, the electrolyte has to be electrochemically and chemically inert under the applied conditions and used materials. Furthermore, it must be stable regarding evaporation and flammability, show a low toxicity, and feature good swellability and affinity toward the composite electrode to ensure effective ion exchange [9].

Two components form the electrolyte: a conducting salt, which is dissolved in a solvent. The latter must thus provide high solubility of the salt to ensure a sufficient number of mobile charge carriers (ions). This usually necessitates a high dipole moment and a high relative permittivity of the solvent to interact with the free salt ions. On the other hand, in a thin-film battery, the solvent must not be able to dissolve the active organic material to prevent self-discharge and capacity fading. Noteworthy, all involved redox states of the active compounds have to be taken into consideration. Additionally, a low viscosity is necessary to assure high ion mobility.

The most common organic solvents that are used in thin-film batteries are carbonates, mainly propylene carbonate, ethylene carbonate (EC), dimethyl carbonate, diethyl carbonate (DEC), and ethylmethyl carbonate [122]. They show high dielectric constants and lead to the formation of protective layers on the current collector, which prevents its electrochemical decomposition [122, 123]. While linear carbonates show, in general, lower viscosities but also lower permittivities, cyclic carbonates are more viscous but possess higher dielectric constants. Hence, usually mixtures are applied. In addition, organic ethers (1,2-dimethoxyethane, 1,3-dioxolane) [122], acetonitrile [7, 86], and water [60, 124, 125] are used. The latter is in particular applied with regard to toxicity and environmental sustainability within the subject of “green” batteries, but possesses only a limited electrochemical window and thus a restricted available voltage range.

In addition to the general demands toward an electrolyte component with regard to stability, compatibility, and sustainability, the used conducting salt has to fulfill particular requests. Most important, it must be well soluble in the used solvent. It has to show a high ion mobility, which is favored by small ion radii. If an electrode that is based on a metal/metal ion redox couple is used, the respective metal cation must be present in the electrolyte. In case of an organic composite electrode, counter ions have to compensate the charge change during the redox processes. Hence, the ions must be able to effectively diffuse into/out of the composite material and have to be present in excess of at least 100–1000 times to ensure an optimal charging/discharging [9]. For organic electrolytes, mostly metal or quaternary ammonium salts of tetrafluoroborates, perchlorates, hexafluorophosphates, trifluoromethanesulfonates (triflates), *bis*(trifluoromethane)-sulfonimides are applied, while in aqueous solutions, metal chlorides or perchlorates are usually used.

Already described organic radical batteries are either based on organic carbonates, mostly EC/DEC with LiPF₆, in case of lithium-organic cells, on an aqueous ZnCl₂ solution for zinc-organic batteries [60], or, in the case of an all-organic battery, on acetonitrile with tetrabutylammonium perchlorate [7, 86].

5 Concluding Remarks

Batteries that are based on stable organic radicals stand out primarily due to their eco-friendliness, both with respect to production and disposal of the materials, due to their ability to be processed via roll-to-roll techniques, and due to their high rate capability. Environmental friendliness is given in particular with regard to the required resource basis, which can potentially rest completely on renewable resources in the future, and regarding the disposal by thermal recycling, i.e., by complete incineration, leaving only harmless CO₂, H₂O, etc., and combustion energy behind. Roll-to-roll processing allows for a low-cost mass production and the incorporation into flexible organic electronics. Thus, for example, organic photovoltaics, organic light-emitting diodes, or organic field-effect transistors with integrated energy-storage units can be produced in large amounts. A superior rate capability in comparison to lithium-ion systems (cf. Table 3) enables a rapid

Table 3 Comparison of the key characteristics of established Li-ion batteries [126] to current lithium-organic and all-organic ORBs

	LiCoO ₂ /Li	LiFePO ₄ /Li	Hybrid ORB	All-organic ORB
Voltage	3.8 V	3.45 V	≤3.6 V	≤1.3 V
Specific capacity	~140 Ah kg ⁻¹	170 Ah kg ⁻¹	≤185 Ah kg ^{-1a}	≤44 Ah kg ^{-1a, b}
Rate capability	0.1–5C	0.1–5C	≤100C	≤360C
Cycle life	1000–2000	1500–2400	≤2000	≤2000

^a Effective value is lower due to non-active additives

^b Referred to the total amount of active material

charging and discharging of organic radical-based batteries, and the absence of the risk of thermal runaways increases the consumer safety.

On the downside, ORBs, in particular all-organic ORBs, feature usually lower specific capacities than metal-based batteries since the used organic molecules possess higher molar masses relative to the transferred electrons. Additionally, organic electrodes necessitate non-active materials, namely conductive additives and binders, which further increases the effective mass without increasing the amount of storable charges. Both the reduction of the molar masses of the used redox-active radical molecules and an increase of the content of the active material in the composite electrode have to be targeted in future works. Alternatively, the introduction of redox systems that provide multi-electron processes represents a promising approach to improve the capacities of ORBs. Another critical point is the low voltage of fully organic ORBs, which is caused by the fact that most of the stable active organic materials possess a relatively high redox potential, making them convenient candidates for an application as p-type material but not suitable for n-type electrodes. This problem can be overcome, on the one hand, by the development of stable, low-redox-potential molecules, as already achieved for non-radical organic materials [127], or, more facile, by the construction of devices that possess several cells that are connected in series. As a consequence, most ORBs that are presented in the literature are metal-hybrid systems—fully organic batteries that feature high voltages and capacities remain to be challenging.

The most promising field of applications is found among the so-called smart devices, like smart clothes, smart packaging, or active RFID tags. A low environmental impact and mechanical flexibility are of preeminent importance, while low capacities and low voltages are bearable, which makes the advantages of the ORBs exceeding their disadvantages for these kinds of application. Nevertheless, the fully organic radical battery still needs to be further developed and optimized not only regarding the active materials themselves but the whole battery as a complex integrated system that consists of numerous different interacting components.

References

- Andersson BA, Råde I (2001) Metal resource constraints for electric-vehicle batteries. *Transp Res Part D Transp Environ* 6:297

2. Gandini A, Lacerda TM (2015) From monomers to polymers from renewable resources: recent advances. *Prog Polym Sci* 48:1
3. Nishide H, Oyaizu K (2008) Toward flexible batteries. *Science* 319:737
4. Nishide H, Suga T (2005) Organic radical battery. *Electrochem Soc Interface* 14:32
5. Satoh M (2005) Organic radical battery and its technology. *NEC J Adv Technol* 2:262
6. Nakahara K, Iwasa S, Satoh M, Morioka Y, Iriyama J, Suguro M, Hasegawa E (2002) Rechargeable batteries with organic radical cathodes. *Chem Phys Lett* 359:351
7. Suga T, Ohshiro H, Sugita S, Oyaizu K, Nishide H (2009) Emerging n-type redox-active radical polymer for a totally organic polymer-based rechargeable battery. *Adv Mater* 21:1627
8. Song Z, Zhou H (2013) Towards sustainable and versatile energy storage devices: an overview of organic electrode materials. *Energy Environ Sci* 6:2280
9. Muench S, Wild A, Friebe C, Häupler B, Janoschka T, Schubert US (2016) Polymer-based organic batteries. *Chem Rev* 116:9438
10. Kumaresan K, Guo Q, Ramadass P, White RE (2006) Cycle life performance of lithium-ion pouch cells. *J Power Sources* 158:679
11. Friebe C, Schubert US (2015) Development of active organic and polymeric materials for batteries and solar cells: introduction to essential characterization techniques. *Adv Energy Mater* 5:1500858
12. Linden D, Reddy TB (2002) *Handbook of Batteries*. McGraw-Hill, New York
13. Nakahara K, Iwasa S, Iriyama J, Morioka Y, Suguro M, Satoh M, Cairns EJ (2006) Electrochemical and spectroscopic measurements for stable nitroxyl radicals. *Electrochim Acta* 52:921
14. Janoschka T, Teichler A, Häupler B, Jähnert T, Hager MD, Schubert US (2013) Reactive inkjet printing of cathodes for organic radical batteries. *Adv Energy Mater* 3:1025
15. Nakahara K, Oyaizu K, Nishide H (2011) Organic radical battery approaching practical use. *Chem Lett* 40:222
16. Kemper TW, Larsen RE, Gennett T (2014) Relationship between molecular structure and electron transfer in a polymeric nitroxyl-radical energy storage material. *J Phys Chem C* 118:17213
17. Oyaizu K, Nishide H (2009) Radical polymers for organic electronic devices: a radical departure from conjugated polymers? *Adv Mater* 21:2339
18. Oyaizu K, Ando Y, Konishi H, Nishide H (2008) Nernstian adsorbate-like bulk layer of organic radical polymers for high-density charge storage purposes. *J Am Chem Soc* 130:14459
19. Satoh M, Nakahara K, Iriyama J, Iwasa S, Suguro M (2004) High power organic radical battery for information systems. *IEICE Trans Electron* 87:2076
20. Suga T, Pu Y-J, Oyaizu K, Nishide H (2004) Electron-transfer kinetics of nitroxide radicals as an electrode-active material. *Bull Chem Soc Jpn* 77:2203
21. Rostro L, Wong SH, Boudouris BW (2014) Solid state electrical conductivity of radical polymers as a function of pendant group oxidation state. *Macromolecules* 47:3713
22. Nakahara K, Iriyama J, Iwasa S, Suguro M, Satoh M, Cairns EJ (2007) Cell properties for modified PTMA cathodes of organic radical batteries. *J Power Sources* 165:398
23. Nakahara K, Iriyama J, Iwasa S, Suguro M, Satoh M, Cairns EJ (2007) High-rate capable organic radical cathodes for lithium rechargeable batteries. *J Power Sources* 165:870
24. Katsumata T, Satoh M, Wada J, Shiotsuki M, Sanda F, Masuda T (2006) Polyacetylene and polynorbornene derivatives carrying TEMPO. Synthesis and properties as organic radical battery materials. *Macromol Rapid Commun* 27:1206
25. Sukegawa T, Sato K, Oyaizu K, Nishide H (2015) Efficient charge transport of a radical polyether/SWCNT composite electrode for an organic radical battery with high charge-storage density. *RSC Adv* 5:15448
26. Hauffman G, Maguin Q, Bourgeois J-P, Vlad A, Gohy J-F (2014) Micellar cathodes from self-assembled nitroxide-containing block copolymers in battery electrolytes. *Macromol Rapid Commun* 35:228
27. Chae IS, Koyano M, Oyaizu K, Nishide H (2013) Self-doping inspired zwitterionic pendant design of radical polymers toward a rocking-chair-type organic cathode-active material. *J Mater Chem A* 1:1326
28. Yoshihara S, Isozumi H, Kasai M, Yonehara H, Ando Y, Oyaizu K, Nishide H (2010) Improving charge/discharge properties of radical polymer electrodes influenced strongly by current collector/carbon fiber interface. *J Phys Chem B* 114:8335
29. Lin C-H, Lee J-T, Yang D-R, Chen H-W, Wu S-T (2015) Nitroxide radical polymer/carbon-nanotube-array electrodes with improved C-rate performance in organic radical batteries. *RSC Adv* 5:33044

30. Vlad A, Rolland J, Hauffman G, Ernould B, Gohy J-F (2015) Melt-polymerization of TEMPO methacrylates with nano carbons enables superior battery materials. *Chem Sus Chem* 8:1692
31. Vlad A, Singh N, Melinte S, Gohy J-F, Ajayan PM (2016) Carbon redox-polymer-gel hybrid super capacitors. *Sci Rep* 6:22194
32. Vlad A, Singh N, Rolland J, Melinte S, Ajayan PM, Gohy J-F (2014) Hybrid supercapacitor-battery materials for fast electrochemical charge storage. *Sci Rep* 4:4315
33. Du ZZ, Ai W, Xie LH, Huang W (2014) Organic radical functionalized graphene as a superior anode material for lithium-ion batteries. *J Mater Chem A* 2:9164
34. Huang Q, Choi D, Cosimbescu L, Lemmon JP (2013) Multi-electron redox reaction of an organic radical cathode induced by a mesopore carbon network with nitroxide polymers. *Phys Chem Chem Phys* 15:20921
35. Guo W, Su J, Li Y-H, Wan L-J, Guo Y-G (2012) Nitroxide radical polymer/graphene nanocomposite as an improved cathode material for rechargeable lithium batteries. *Electrochim Acta* 72:81
36. Nakahara K, Iriyama J, Iwasa S, Suguro M, Satoh M, Cairns EJ (2007) Al-laminated film packaged organic radical battery for high-power applications. *J Power Sources* 163:1110
37. Chae IS, Koyano M, Sukegawa T, Oyaizu K, Nishide H (2013) Redox equilibrium of a zwitterionic radical polymer in a non-aqueous electrolyte as a novel Li^+ host material in a Li-ion battery. *J Mater Chem A* 1:9608
38. Kim J-K, Scheers J, Ahn J-H, Johansson P, Matic A, Jacobsson P (2013) Nano-fibrous polymer films for organic rechargeable batteries. *J Mater Chem A* 1:2426
39. Kim J-K (2013) Micro-fibrous organic radical electrode to improve the electrochemical properties of organic rechargeable batteries. *J Power Sources* 242:683
40. Liu CM, Chen J, Wang FQ, Yi BL (2012) Improvement of electrochemical properties of PTMA cathode by using carbon blacks with high specific surface area. *Russ J Electrochem* 48:1052
41. Bagnon L, Morton CJH, Novak P, Vetter J, Nesvadba P (2007) Synthesis of poly(4-methacryloyloxy-TEMPO) via group-transfer polymerization and its evaluation in organic radical battery. *Chem Mater* 19:2910
42. Nishide H, Iwasa S, Pu Y-J, Suga T, Nakahara K, Satoh M (2004) Organic radical battery: nitroxide polymers as a cathode-active material. *Electrochim Acta* 50:827
43. Kim J-K, Cheruvally G, Choi J-W, Ahn J-H, Choi DS, Song CE (2007) Rechargeable organic radical battery with electrospun, fibrous membrane-based polymer electrolyte. *J Electrochem Soc* 154:A839
44. Deng L-F, Li X-H, Xiao L-X, Zhang Y-H (2003) Synthesis and electrochemical properties of polyradical cathode material for lithium second batteries. *J Cent South Univ Tech* 10:190
45. Kim J-K, Cheruvally G, Choi J-W, Ahn J-H, Lee SH, Choi DS, Song CE (2007) Effect of radical polymer cathode thickness on the electrochemical performance of organic radical battery. *Solid State Ion* 178:1546
46. Kim J-K, Cheruvally G, Ahn J-H, Seo Y-G, Choi DS, Lee S-H, Song CE (2008) Organic radical battery with PTMA cathode: effect of PTMA content on electrochemical properties. *J Ind Eng Chem* 14:371
47. Kim J-K, Ahn J-H, Cheruvally G, Chauhan GS, Choi J-W, Kim D-S, Ahn H-J, Lee SH, Song CE (2009) Electrochemical properties of rechargeable organic radical battery with PTMA cathode. *Metal Mater Int* 15:77
48. Guo W, Yin Y-X, Xin S, Guo Y-G, Wan L-J (2012) Superior radical polymer cathode material with a two-electron process redox reaction promoted by graphene. *Energy Environ Sci* 5:5221
49. Kim Y, Jo C, Lee J, Lee CW, Yoon S (2012) An ordered nanocomposite of organic radical polymer and mesocellular carbon foam as cathode material in lithium ion batteries. *J Mater Chem* 22:1453
50. Lin H-C, Li C-C, Lee J-T (2011) Nitroxide polymer brushes grafted onto silica nanoparticles as cathodes for organic radical batteries. *J Power Sources* 196:8098
51. Wang Y-H, Hung M-K, Lin C-H, Lin H-C, Lee J-T (2011) Patterned nitroxide polymer brushes for thin-film cathodes in organic radical batteries. *Chem Commun* 47:1249
52. Lin C-H, Chou W-J, Lee J-T (2012) Three-dimensionally ordered macroporous nitroxide polymer brush electrodes prepared by surface-initiated atom transfer polymerization for organic radical batteries. *Macromol Rapid Commun* 33:107
53. Hung M-K, Wang Y-H, Lin C-H, Lin H-C, Lee J-T (2012) Synthesis and electrochemical behaviour of nitroxide polymer brush thin-film electrodes for organic radical batteries. *J Mater Chem* 22:1570
54. Ernould B, Devos M, Bourgeois J-P, Rolland J, Vlad A, Gohy J-F (2015) Grafting of a redox polymer onto carbon nanotubes for high capacity battery materials. *J Mater Chem A* 3:8832

55. Takahashi K, Korolev K, Tsuji K, Oyaizu K, Nishide H, Bryuzgin E, Navrotsky A, Novakov I (2015) Facile grafting-onto-preparation of block copolymers of TEMPO and glycidyl methacrylates on an oxide substrate as an electrode-active layer. *Polymer* 68:310
56. Suga T, Konishi H, Nishide H (2007) Photocrosslinked nitroxide polymer cathode-active materials for application in an organic-based paper battery. *Chem Commun* 1370
57. Katsumata T, Qu J, Shiotsuki M, Satoh M, Wada J, Igarashi J, Mizoguchi K, Masuda T (2008) Synthesis, characterization, and charge/discharge properties of polynorbornenes carrying 2,2,6,6-tetramethylpiperidine-1-oxy radicals at high density. *Macromolecules* 41:1175
58. Dai Y, Zhang Y, Gao L, Xu G, Xie J (2011) Electrochemical performance of organic radical cathode with ionic liquid based electrolyte. *J Electrochem Soc* 158:A291
59. Qu JQ, Katsumata T, Satoh M, Wada J, Masuda T (2009) Poly (7-oxanorbornenes) carrying 2,2,6,6-tetramethylpiperidine-1-oxy(TEMPO) radicals: synthesis and charge/discharge properties. *Polymer* 50:391
60. Koshika K, Sano N, Oyaizu K, Nishide H (2009) An aqueous, electrolyte-type, rechargeable device utilizing a hydrophilic radical polymer-cathode. *Macromol Chem Phys* 210:1989
61. Suguro M, Iwasa S, Kusachi Y, Morioka Y, Nakahara K (2007) Cationic polymerization of poly(vinyl ether) bearing a TEMPO radical: a new cathode-active material for organic radical batteries. *Macromol Rapid Commun* 28:1929
62. Suguro M, Iwasa S, Nakahara K (2008) Fabrication of a practical and polymer-rich organic radical polymer electrode and its rate dependence. *Macromol Rapid Commun* 29:1635
63. Koshika K, Sano N, Oyaizu K, Nishide H (2009) An ultrafast chargeable polymer electrode based on the combination of nitroxide radical and aqueous electrolyte. *Chem Commun* 836
64. Sertkol SB, Sinirlioglu D, Esat B, Muftuoglu AE (2015) A novel cathode material based on polystyrene with pendant TEMPO moieties obtained via click reaction and its use in rechargeable batteries. *J Polym Res* 22:136
65. Suga T, Yoshimura K, Nishide H (2006) Nitroxide-substituted polyether as a new material for batteries. *Macromol Symp* 245–246:416
66. Qu J, Katsumata T, Satoh M, Wada J, Igarashi J, Mizoguchi K, Masuda T (2007) Synthesis and charge/discharge properties of polyacetylenes carrying 2,2,6,6-tetramethyl-1-piperidinyloxy radicals. *Chem Eur J* 13:7965
67. Qu JQ, Fujii T, Katsumata T, Suzuki Y, Shiotsuki M, Sanda F, Satoh M, Wada J, Masuda T (2007) Helical polyacetylenes carrying 2,2,6,6-tetramethyl-1-piperidinyloxy and 2,2,5,5-tetramethyl-1-pyrrolidinyloxy moieties: their synthesis, properties, and function. *J Polym Sci A Polym Chem* 45:5431
68. Qu JQ, Khan FZ, Satoh M, Wada J, Hayashi H, Mizoguchi K, Masuda T (2008) Synthesis and charge/discharge properties of cellulose derivatives carrying free radicals. *Polymer* 49:1490
69. Qu J, Morita R, Satoh M, Wada J, Terakura F, Mizoguchi K, Ogata N, Masuda T (2008) Synthesis and properties of DNA complexes containing 2,2,6,6-tetramethyl-1-piperidinyloxy(TEMPO) moieties as organic radical battery materials. *Chem Eur J* 14:3250
70. Zhang XH, Li HQ, Li LT, Lu GL, Zhang S, Gu LN, Xia YY, Huang XY (2008) Polyallene with pendant nitroxyl radicals. *Polymer* 49:3393
71. Ibe T, Frings RB, Lachowicz A, Kyo S, Nishide H (2010) Nitroxide polymer networks formed by Michael addition: on site-cured electrode-active organic coating. *Chem Commun* 46:3475
72. Koshika K, Chikushi N, Sano N, Oyaizu K, Nishide H (2010) A TEMPO-substituted polyacrylamide as a new cathode material: an organic rechargeable device composed of polymer electrodes and aqueous electrolyte. *Green Chem* 12:1573
73. Aydın M, Esat B, Kılıç Ç, Köse ME, Ata A, Yılmaz F (2011) A polythiophene derivative bearing TEMPO as a cathode material for rechargeable batteries. *Eur Polym J* 47:2283
74. Aydın M, Esat B (2015) A polythiophene derivative bearing two electroactive groups per monomer as a cathode material for rechargeable batteries. *J Solid State Electrochem* 19:2275
75. Xu LH, Yang F, Su C, Ji LL, Zhang C (2014) Synthesis and properties of novel TEMPO-contained polypyrrole derivatives as the cathode material of organic radical battery. *Electrochim Acta* 130:148
76. Lee SH, Kim J-K, Cheruvally G, Choi J-W, Ahn J-H, Chauhan GS, Song CE (2008) Electrochemical properties of new organic radical materials for lithium secondary batteries. *J Power Sources* 184:503
77. Xu LH, Ji LL, Wang GS, Zhang C, Su C (2016) A novel nitroxide radical polymer-containing conductive polyaniline as molecular skeleton: its synthesis and electrochemical properties as organic cathode. *Ionics* 22:1377

78. Suguro M, Mori A, Iwasa S, Nakahara K, Nakano K (2009) Syntheses and electrochemical properties of TEMPO radical substituted silicones: active material for organic radical batteries. *Macromol Chem Phys* 210:1402
79. Lebègue E, Brousse T, Gaubicher J, Retoux R, Cougnon C (2014) Toward fully organic rechargeable charge storage devices based on carbon electrodes grafted with redox molecules. *J Mater Chem A* 2:8599
80. Jähnert T, Janoschka T, Hager MD, Schubert US (2014) Polymers with n-type nitroxide side groups: synthesis and electrochemical characterization. *Eur Polym J* 61:105
81. Aricò AS, Bruce P, Scrosati B, Tarascon J-M, van Schalkwijk W (2005) Nanostructured materials for advanced energy conversion and storage devices. *Nat Mater* 4:366
82. Tarascon J-M, Armand M (2001) Issues and challenges facing rechargeable lithium batteries. *Nature* 414:359
83. Oyaizu K, Kawamoto T, Suga T, Nishide H (2010) Synthesis and charge transport properties of redox-active nitroxide polyethers with large site density. *Macromolecules* 43:10382
84. Nesvadba P, Bugnon L, Maire P, Novák P (2010) Synthesis of a novel spirobisnitroxide polymer and its evaluation in an organic radical battery. *Chem Mater* 22:783
85. Suga T, Pu Y-J, Kasatori S, Nishide H (2007) Cathode- and anode-active poly (nitroxylstyrene)s for rechargeable batteries: p- and n-type redox switching via substituent effects. *Macromolecules* 40:3167
86. Suga T, Sugita S, Ohshiro H, Oyaizu K, Nishide H (2011) p- and n-type bipolar redox-active radical polymer: toward totally organic polymer-based rechargeable devices with variable configuration. *Adv Mater* 23:751
87. Jähnert T, Hager MD, Schubert US (2014) Application of phenolic radicals for antioxidants, as active materials in batteries, magnetic materials and ligands for metal-complexes. *J Mater Chem A* 2:15234
88. Jähnert T, Häupler B, Janoschka T, Hager MD, Schubert US (2014) Polymers based on stable phenoxyl radicals for the use in organic radical batteries. *Macromol Rapid Commun* 35:882
89. Morita Y, Nishida S, Murata T, Moriguchi M, Ueda A, Satoh M, Arifuku K, Sato K, Takui T (2011) Organic tailored batteries materials using stable open-shell molecules with degenerate frontier orbitals. *Nat Mater* 10:947
90. Lipunova GN, Fedorchenko TG, Chupakhin ON (2013) Verdazyls: synthesis, properties, application. *Russ Chem Rev* 82:701
91. Gilroy JB, McKinnon SDJ, Koivisto BD, Hicks RG (2007) Electrochemical studies of verdazyl radicals. *Org Lett* 9:4837
92. Morgan IS, Peuronen A, Hänninen MM, Reed RW, Clérac R, Tuononen HM (2014) 1-Phenyl-3-(pyrid-2-yl)benzo[e][1, 2, 4]triazinyl: the first “Blatter Radical” for coordination chemistry. *Inorg Chem* 53:33
93. Berezin AA, Zissimou G, Constantinides CP, Beldjoudi Y, Rawson JM, Koutentis PA (2014) Route to benzo- and pyrido-fused 1,2,4-triazinyl radicals via *N'*-(het)aryl-*N'*-[2-nitro(het)aryl]hydrazides. *J Org Chem* 79:314
94. Constantinides CP, Koutentis PA, Krassos H, Rawson JM, Tasiopoulos AJ (2011) Characterization and magnetic properties of a “super stable” radical 1,3-diphenyl-7-trifluoromethyl-1,4-dihydro-1,2,4-benzotriazin-4-yl. *J Org Chem* 76:2798
95. Blatter HM, Lukaszewski H (1968) A new stable free radical. *Tetrahedron Lett* 9:2701
96. Miura Y, Muranaka Y (2006) Electrochemical study of stable *N*-alkoxyarylaminy radicals. *Electrochim Acta* 52:1053
97. Miura Y, Momoki M, Fuchikami T, Teki Y, Itoh K, Mizutani H (1996) Exceptionally persistent nitrogen-centered free radicals. Syntheses, ESR spectra, isolation, and X-ray crystallographic structures of *N*-(aryltio)-2-*tert*-butyl-4,6-diarylphenylaminy radicals and *N*-(aryltio)-4-*tert*-butyl-2,6-diarylphenylaminy radicals. *J Org Chem* 61:4300
98. Miura Y, Tanaka A (1992) Cyclic voltammetric behaviour of exceptionally persistent nitrogen-centred free radicals. *N*-(aryltio)-2,4,6-triphenylaminy radicals. *Electrochim Acta* 37:2095
99. Oyaizu K, Suga T, Yoshimura K, Nishide H (2008) Synthesis and characterization of radical-bearing polyethers as an electrode-active material for organic secondary batteries. *Macromolecules* 41:6646
100. Qu J, Katsumata T, Satoh M, Wada J, Masuda T (2007) Synthesis and properties of polyacetylene and polynorbornene derivatives carrying 2,2,5,5-tetramethyl-1-pyrrolidinylloxy moieties. *Macromolecules* 40:3136

101. Sukegawa T, Kai A, Oyaizu K, Nishide H (2013) Synthesis of pendant nitronyl nitroxide radical-containing poly (norbornene)s as ambipolar electrode-active materials. *Macromolecules* 46:1361
102. Koizumi T, Ohfujii H, Tanaka S, Shigematsu S, Akutagawa N, Satoh M, Miura Y (2014) Charge-discharge behavior of secondary organic radical battery using 2-aryl nitronyl nitroxides as the cathode active material. *Chem Lett* 43:1092
103. Li F, Zhang YP, Kwon SR, Lutkenhaus JL (2016) Electropolymerized polythiophenes bearing pendant nitroxide radicals. *ACS Macro Lett* 5:337
104. Kunz TK, Wolf MO (2011) Electrodeposition and properties of TEMPO functionalized polythiophene thin films. *Polym Chem* 2:640
105. Takahashi Y, Hayashi N, Oyaizu K, Honda K, Nishide H (2008) Totally organic polymer-based electrochromic cell using TEMPO-substituted polynorbornene as a counter electrode-active material. *Polym J* 40:763
106. Ruff I, Friedrich VJ (1971) Transfer diffusion. I. Theoretical. *J Phys Chem* 75:3297
107. Dahms H (1968) Electronic conduction in aqueous solution. *J Phys Chem* 72:362
108. Donnet J-B (1994) Fifty years of research and progress on carbon black. *Carbon* 32:1305
109. Bourrat X (1993) Electrically conductive grades of carbon black: structure and properties. *Carbon* 31:287
110. Liang C, Li Z, Dai S (2008) Mesoporous carbon materials: synthesis and modification. *Angew Chem Int Ed* 47:3696
111. Choi Y-K, K-i Sugimoto, Song S-M, Gotoh Y, Ohkoshi Y, Endo M (2005) Mechanical and physical properties of epoxy composites reinforced by vapor grown carbon nanofibers. *Carbon* 43:2199
112. Endo M, Kim YA, Hayashi T, Nishimura K, Matusita T, Miyashita K, Dresselhaus MS (2001) Vapor-grown carbon fibers (VGCFs): basic properties and their battery applications. *Carbon* 39:1287
113. Balandin AA, Ghosh S, Bao W, Calizo I, Teweldebrhan D, Miao F, Lau CN (2008) Superior thermal conductivity of single-layer graphene. *Nano Lett* 8:902
114. Stoller MD, Park S, Zhu Y, An J, Ruoff RS (2008) Graphene-based ultracapacitors. *Nano Lett* 8:3498
115. Geim AK, Novoselov KS (2007) The rise of graphene. *Nat Mater* 6:183
116. Cao L, Sadaf S, Beladi-Mousavi SM, Walder L (2013) PolyTEMPO and polyviologen on carbon nanotubes: syntheses, structures and organic battery applications. *Eur Polym J* 49:1923
117. Choi W, Ohtani S, Oyaizu K, Nishide H, Geckeler KE (2011) Radical polymer-wrapped SWNTs at a molecular level: high-rate redox mediation through a percolation network for a transparent charge-storage material. *Adv Mater* 23:4440
118. Hecht DS, Hu L, Irvin G (2011) Emerging transparent electrodes based on thin films of carbon nanotubes, graphene, and metallic nanostructures. *Adv Mater* 23:1482
119. Chou S-L, Pan Y, Wang J-Z, Liu H-K, Dou S-X (2014) Small things make a big difference: binder effects on the performance of Li and Na batteries. *Phys Chem Chem Phys* 16:20347
120. Xu W, Read A, Koech PK, Hu D, Wang C, Xiao J, Padmaperuma AB, Graff GL, Liu J, Zhang J-G (2012) Factors affecting the battery performance of anthraquinone-based organic cathode materials. *J Mater Chem* 22:4032
121. Komaba S, Tanaka T, Ozeki T, Taki T, Watanabe H, Tachikawa H (2010) Fast redox of composite electrode of nitroxide radical polymer and carbon with polyacrylate binder. *J Power Sources* 195:6212
122. Xu K (2004) Nonaqueous liquid electrolytes for lithium-based rechargeable batteries. *Chem Rev* 104:4303
123. Aurbach D, Daroux ML, Faguy PW, Yeager E (1987) Identification of surface films formed on lithium in propylene carbonate solutions. *J Electrochem Soc* 134:1611
124. Sano N, Tomita W, Hara S, Min C-M, Lee J-S, Oyaizu K, Nishide H (2013) Polyviologen hydrogel with high-rate capability for anodes toward an aqueous electrolyte-type and organic-based rechargeable device. *ACS Appl Mater Interfaces* 5:1355
125. Jähnert T, Häupler B, Janoschka T, Hager MD, Schubert US (2013) Synthesis and charge-discharge studies of poly (ethynylphenyl) galvinoxyles and their use in organic radical batteries with aqueous electrolytes. *Macromol Chem Phys* 214:2616
126. Janoschka T, Hager MD, Schubert US (2012) Powering up the future: radical polymers for battery applications. *Adv Mater* 24:6397
127. Wild A, Strumpf M, Häupler B, Hager MD, Schubert US (2016) All-organic battery composed of thianthrene- and TCAQ-based polymers. *Adv Energy Mater* 1601415



Cell Concepts of Metal–Sulfur Batteries (Metal = Li, Na, K, Mg): Strategies for Using Sulfur in Energy Storage Applications

Lukas Medenbach^{1,2} · Philipp Adelhelm^{1,2}

Received: 24 March 2017 / Accepted: 1 September 2017 / Published online: 29 September 2017
© Springer International Publishing AG 2017

Abstract There is great interest in using sulfur as active component in rechargeable batteries thanks to its low cost and high specific charge (1672 mAh/g). The electrochemistry of sulfur, however, is complex and cell concepts are required, which differ from conventional designs. This review summarizes different strategies for utilizing sulfur in rechargeable batteries among membrane concepts, polysulfide concepts, all-solid-state concepts as well as high-temperature systems. Among the more popular lithium–sulfur and sodium–sulfur batteries, we also comment on recent results on potassium–sulfur and magnesium–sulfur batteries. Moreover, specific properties related to the type of light metal are discussed.

Keywords Batteries · Energy storage · Metal-sulfur batteries · Cell concepts · Electrodes

Chapter 3 was originally published as Medenbach, L. & Adelhelm, P. Top Curr Chem (2017) 375: 81. DOI 10.1007/s41061-017-0168-x.

✉ Philipp Adelhelm
philipp.adelhelm@uni-jena.de

¹ Institute for Technical Chemistry and Environmental Chemistry, Friedrich-Schiller-University Jena, Philosophenweg 7a, 07743 Jena, Germany

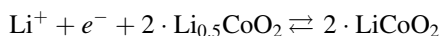
² Center for Energy and Environmental Chemistry Jena (CEEC Jena), Philosophenweg 7a, 07743 Jena, Germany

1 Introduction

1.1 Sulfur as Active Material for Electrochemical Energy Storage: Motivation

Today's market for rechargeable batteries is dominated by lead-acid and Li-ion technology. Lead-acid technology is essentially more than 150 years old and is largely used in automotive applications (starter battery) as well as for uninterruptible power supply. Low cost and robustness are considered as main advantages while its key limitation is the low energy density. Lithium-ion technology is much younger and was commercialized in 1991. Since then it quickly conquered the rapidly growing market for portable applications mainly because of its high energy density and long cycle life. Costs for lithium-ion batteries (LIBs) rapidly decreased within the last years and the technology will be the first choice for the rising markets of electric vehicles, grid storage and mobile robotics. The demand for LIBs will therefore increase manifold times in the near future. The Gigafactory from Tesla/Panasonic alone will double today's battery production capacity once in full operation, for example. On the other hand, concerns have been raised whether this demand will create issues related to element resources and supply chains on the long term [1–4]. Resource limits of different battery chemistries have been studied by Wadia et al. for example [2]. Although discussions on this topic are naturally complex and often controversial, the risk of resource depletion or of restricted access due to political issues has recently resurged interest in alternatives. LIB technology is also expected to reach its physical limits within the next years with energy densities slightly above 300 Wh/kg so other cell concepts have to be considered to significantly increase the energy density. For these and some other reasons, alternative battery concepts among metal-sulfur, metal-air, Na-ion, redox-flow, high temperature or solid-state systems are being considered, each approach having its individual advantages and drawbacks compared to LIB technology [5–15].

It is important to realize that almost all battery technologies rely on positive electrodes in which (transition) metals change their oxidation state. In LIBs, these are active redox centers such as $\text{Co}^{3+/4+}$, $\text{Ni}^{2+/3+}$, or $\text{Fe}^{2+/3+}$, which are fixed at defined positions in crystals of LiCoO_2 , $\text{Li}[\text{Ni}_{1/3}\text{Co}_{1/3}\text{Mn}_{1/3}]\text{O}_2$ or LiFePO_4 , for example. The electrode reaction is essentially based on *cation redox chemistry*. For the example of LiCoO_2 , the reaction for the positive electrode is:



The anions such as O^{2-} or PO_4^{3-} in these electrodes are inactive.¹ The use of transition metal compounds in LIBs is the key to achieve a high cell voltage. On the other hand, the capacity of LIB positive electrodes is limited to around 150–200 mAh/g. The working principle of a lithium-ion battery is sketched in

¹ It is worth to note that anion redox effects in high capacity positive electrode materials has recently become an active research field [16]. Anyway, most of the charge storage is due to the change in oxidation states of the transition metals.

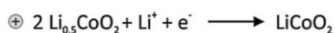
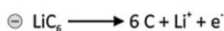
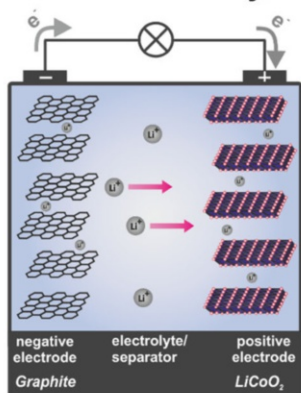
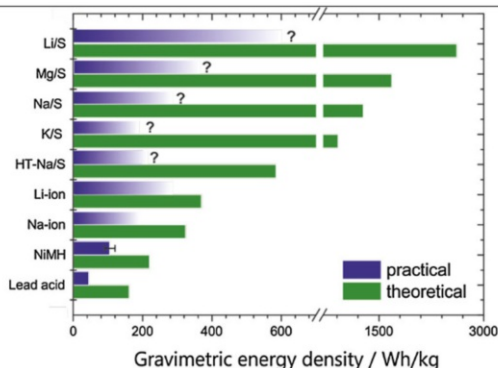
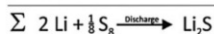
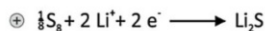
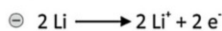
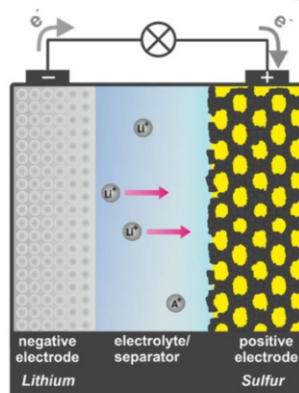
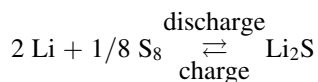
(a) Lithium-ion battery

(b) Lithium-Sulfur battery


Fig. 1 Schematic comparison of **a** the lithium-ion battery concept with graphite and LiCoO_2 as electrode materials and **b** the analogue lithium-sulfur cell. The positive electrode usually consists of sulfur distributed within a porous carbon framework that provides electronic wiring. For the positive electrode, other metals such as Na, K, or Mg might be used instead of lithium. The bottom graph shows a comparison of theoretical and practical energy densities for a variety of battery types (cell level). To date, only the lead acid, the nickel metal hydride, the Li-ion, and the high temperature Na/S battery are commercialized. Practical energy densities of the metal-sulfur cells are estimates

Fig. 1 (left). Graphite usually serves as negative electrode, which forms the intercalation compound LiC_6 upon charging.

The conceptual approach for metal-sulfur batteries is very different. Here, the redox active element of the positive electrode is a non-metal and the electrode reaction is largely based on *anion redox chemistry*.² For the example of a lithium-sulfur battery, the ideal reaction at the positive electrode would be:

² Similar reactions can be formulated for oxygen (metal-oxygen batteries). This type of cells ideally work with a gas diffusion electrode as cathode and ideally utilize atmospheric oxygen. They are therefore



The full reduction of sulfur from S to S²⁻ corresponds to a capacity of 1672 mAh per gram of sulfur, i.e., roughly ten times higher than for many LIB-positive electrode materials. Besides, sulfur is very cheap, more abundant than most transition metals and non-toxic. The redox potential of sulfur is relatively low so that the sulfur electrode is ideally combined with a light metal (Li, Na, Mg) negative electrode. This way, cell voltage and hence energy density are maximized. In view of this, metal–sulfur batteries are among the very few systems that could outrival LIB technology in terms of energy density and/or price. Table 1 summarizes the properties of the idealized cell reaction of sulfur with the light metals Li, Na, K, and Mg. Figure 1 (right) shows the concept of a lithium–sulfur battery as it is currently most studied, i.e., lithium metal is used as negative electrode. Two classes of electrolyte solvents are applied: carbonates, which are well known from LIB technology and ethers. The bottom of Fig. 1 shows a graphical comparison between the theoretical and practical energy density of different battery technologies. The practical energy densities given for the different metal–sulfur batteries are just for orientation. For lithium–sulfur, 600 Wh/kg are considered a best case scenario for the cell concept shown in Fig. 1, which corresponds roughly to around one-fifth of the theoretical value. The same ratio has been applied for Na/S, K/S, and Mg/S, respectively. Today, 400 Wh/kg have been demonstrated on the cell level for the lithium–sulfur battery [19].

The promise of metal–sulfur batteries, however, remains largely unfulfilled so far. The major challenges are rooted in some intrinsic properties of sulfur and its compounds:

- (1) *Sulfur and (Li, Na, K, Mg) sulfides are insulators* Values for the electronic and ionic conductivity are negligible. Large particles will therefore be electrochemically inactive if no countermeasures are taken. The addition of larger amounts of conductive additive combined with nanosizing is therefore a popular strategy for activating the redox reaction. A large variety of nanoporous carbon materials is studied that provide conductivity and confine sulfur as illustrated in Fig. 2. The amount of carbon used is large, often in excess of 40 wt%. The characterization of carbon/sulfur composite materials is challenging due to the high vapor pressure of sulfur [20, 21]. Usually, the more carbon added the better the utilization of sulfur but the extra weight significantly reduces the effective capacity of the electrode and hence a large penalty in energy density has to be paid. For comparison, the content of conductive additives in conventional electrodes for LIBs is typically below 5 wt%.

Footnote 2 continued

fundamentally different from classical rechargeable batteries that are closed systems. More information can be found in Refs. 17 and 18

Table 1 Selected properties for the reaction of sulfur with the elements Li, Na, K, and Mg

Cell reaction	$\Delta_r G^\circ /$ kJ/mol	$E^\circ /$ V	$W_{th} /$ Wh/kg	$W_{th} /$ Wh/l	$\Delta V / \%$	$q_{th, metal} /$ mAh/g	$q_{th, metal} /$ mAh/cm ³
$2 \text{ Li} + 1/8 \text{ S}_8 \xrightleftharpoons[\text{charge}]{\text{discharge}} \text{Li}_2\text{S}$	-432.57	2.24	2615	4289	+80	3861	2062
$2 \text{ Na} + 1/8 \text{ S}_8 \xrightleftharpoons[\text{charge}]{\text{discharge}} \text{Na}_2\text{S}$	-357.77	1.85	1273	2363	+171	1166	1128
$2 \text{ K} + 1/8 \text{ S}_8 \xrightleftharpoons[\text{charge}]{\text{discharge}} \text{K}_2\text{S}$	-362.73	1.88	914	1590	+309	686	587
$\text{Mg} + 1/8 \text{ S}_8 \xrightleftharpoons[\text{charge}]{\text{discharge}} \text{Mg}_2\text{S}$	-341.44	1.77	1683	4509	+36	2206	3834
$\text{Li} + 2 \text{ Li}_{0.5}\text{CoO}_2 \xrightleftharpoons[\text{charge}]{\text{discharge}} 2\text{LiCoO}_2$	-188.14	3.9	534	2723	few%	3861	2062

Gibbs free energies $\Delta_r G^\circ$, theoretical cell voltage E° , theoretical energies w by weight and volume and theoretical capacities of the metals q by weight and volume. The volumetric energy density w_{th} refers to the discharged state. The volume expansion ΔV refers to the difference in molar volumes between sulfur (before discharge) and the corresponding sulfide (after discharge). The cell reaction of $\text{Li}_{0.5}\text{CoO}_2$ with lithium is added for comparison. All values at 25 °C

- (2) *Sulfur forms a number of polysulfides as intermediates during reduction* A number of intermediate polysulfides form during reduction that severely complicate the reaction. Table 2 summarizes the thermodynamically stable phases within the binary systems of Li–S, Na–S, K–S and Mg–S. Besides, a large number of soluble chain-like polysulfide dianions S_n^{2-} and radical monoanions S_n^- as well as other metastable phases exist [22]. It is the solubility of the polysulfide intermediates that causes major problems related to the use of metal–sulfur cells. For the cell concept shown in Fig. 1, this means that soluble polysulfides diffuse out of the electrode leading to fast capacity loss and therefore poor rechargeability. The issue of polysulfide dissolution is shown in Fig. 2. The polysulfides diffuse toward the counter electrode where they become reduced. As a result, surface film formation and so-called shuttling of soluble polysulfides between both electrodes occur [23]. More precisely, during charging, shorter polysulfides are electrochemically oxidized at the positive electrode and form long(er)-chain polysulfides. This causes concentration gradients within the cell and the afore-oxidized polysulfides diffuse to the negative electrode where they become chemically reduced to shorter-chain polysulfides again. The shorter polysulfides then diffuse back to the positive electrode where they re-oxidize again and the process starts over. This shuttle mechanism is essentially a chemical shortcut of the cell which is superimposed onto the electrochemical charging leading to self-discharge and cell ageing. Confinement of sulfur in nanoporous carbon

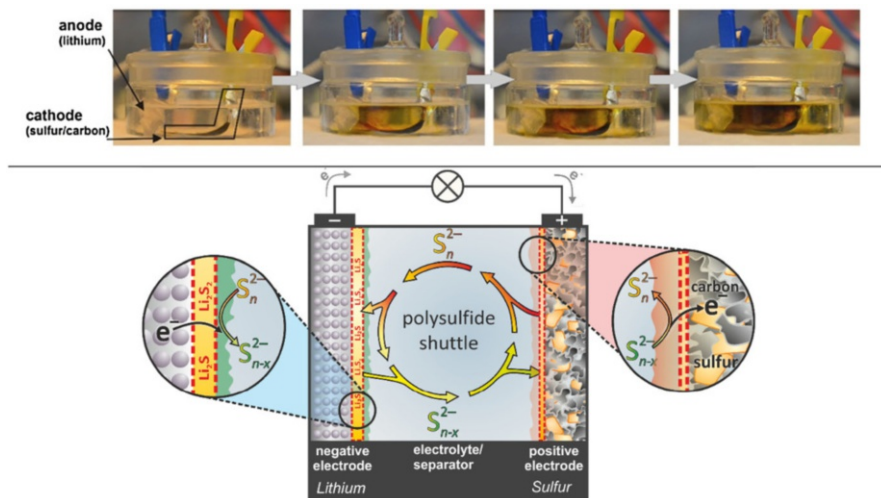


Fig. 2 Top Discharging of a lithium–sulfur cell using the cell concept shown in Fig. 1. Polysulfide formation and dissolution is clearly visible from the coloration of the electrolyte solution. Despite many efforts and improvements, tackling this issue is still one of the major challenges of the cell concept shown in Fig. 1 [37]. Bottom Illustration of the shuttle mechanism in a lithium–sulfur cell after Mikhaylik and Akridge [23]. Polysulfides S_n^{2-} of different length diffuse between both electrodes in a cyclic process during discharging/charging, drawing after [28]. The shuttle mechanism is highly detrimental and leads to intrinsic self-discharge and poor cycle life. It also leads to surface film formation on the negative electrode of highly reduced solid sulfur compounds

Table 2 Overview on thermodynamically stable binary phases at room temperature for different metal–sulfur systems

Phase diagram	Stable binary phases at RT
Li–S [52]	Li_2S
Na–S [53]	Na_2S , Na_2S_2 , Na_2S_4 , Na_2S_5
K–S [54]	K_2S , K_2S_2 , K_2S_3 , K_2S_4 , K_2S_5 , K_2S_6
Mg–S [55]	MgS

In addition, a number of metastable compounds exists as well as a large amount of solubilized polysulfides with chain-like dianions S_n^{2-} as well as radical monoanions S_n^- [22]

or other nanomaterials can delay polysulfide dissolution but often at too many compromises [24, 25].

- (3) *Sulfur/Sulfides are corrosive* Sulfur is reacting with a large number of metals by forming sulfides. This issue is restricting the range of suitable materials for current collectors and cell housing. For example, steel or copper corrosion by sulfur through FeS and CuS formation is a well known phenomenon [26]. Aluminum is therefore often preferred. In the same way, polysulfide intermediates can react with cell components and certain electrolyte solvents. Although it has been reported that sulfur cells containing carbonate solvents such as propylene carbonate (PC) or dimethyl carbonate (DMC) are working

well and show high initial capacities, side reactions with soluble sulfides are suspected as reason for fast capacity fading [27, 28]. Polysulfides can react with the carbonyl group of the solvent molecule by nucleophilic attack [29, 30], for example. Ethers are more stable and a 1:1 mixture of monoglyme and 1,3-dioxolane (DOL) has become popular. Other linear glymes (diglyme, tetraglyme) are also often used [31]. Overall, however, it remains unclear which electrolyte solvents are most suited, as it is quite difficult to separate the different origins of capacity fading and low cycle life. For conductive salts, the popular PF_6^- anion is not suitable for sulfur batteries. The reason being again the instability against polysulfides. Better alternatives are triflate or TFSI salts. Common binders such as PVDF might be attacked also [32, 33], motivating research on binder free electrodes [34, 35].

- (4) *The formation of sulfides from sulfur comes along with a large volume change* Volume expansion is in the range of 80% (S to Li_2S) to 300% (S to K_2S), which means that extra space is needed and solid electrodes might crack. The use of porous materials might mitigate effects related to volume expansion but, again, at cost of energy density.

Another important challenge is the use of metals as negative electrodes. Metals are the preferred choice for maximizing cell voltage and energy density. This is of course also true for LIBs but safety issues related to dendrite formation as well as electrolyte decomposition so far limit the use of lithium metal anodes to primary cells [36]. In principle, the same issues apply to other alkali or Mg metal electrodes. Although it has been reported that Mg does not show dendrite formation a final proof is missing. In rechargeable LIBs, the problems of dendrite formation and electrolyte decomposition are mitigated by using graphite instead of lithium (see Fig. 1). The intercalation of Li^+ into graphite occurs close to the potential of the metal electrode (0.1 V vs. Li/Li^+). In principle, one could use intercalation compounds such as graphite also in sulfur batteries, but given the already low redox potential of sulfur reduction of around 2 V or below (see Table 1), this would lead to more and more unattractive cell voltages. Without a metal electrode, the advantage of metal–sulfur batteries in energy density over LIBs will be difficult to materialize in practical batteries.

Without doubt, these are difficult starting conditions for designing metal–sulfur batteries. So how can one activate sulfur in electrochemical cells without making too many compromises? Different strategies were proposed over the years and a number of different cell concepts for metal–sulfur batteries were developed that aim at mitigating the challenges described above. The cell concepts are based on using sulfur and its compounds either in their solid, dissolved or molten state. A well-known example is the high-temperature Na/S battery, which operates at around 300 °C and is based on liquid electrodes (molten sulfur/polysulfides and molten sodium) that are separated by a solid electrolyte. In fact, this cell concept was developed already in the 1960s. Most research is currently dedicated to room-temperature Li/S batteries. In this case, the traditional design of having two solid electrodes (Li, S) separated by a liquid electrolyte is most commonly applied (see Fig. 1). This concept is now more and more extended by, e.g., introducing

additional membranes that aim at blocking the polysulfide shuttle between the electrodes. Much less is known about room-temperature Na/S batteries and studies on K/S or Mg/S batteries are scarce, however, the same concepts as for Li/S batteries can be applied, in principle. A very recent strategy are all-solid-state concepts in which the liquid electrolyte is replaced by a solid electrolyte [38–41].

The progress in lithium–sulfur batteries is frequently reviewed and comprehensive overviews on the myriad of materials tested can be found in Refs. [28, 42–51], for example. The main focus of this article is on reviewing the principles of the different “metal–sulfur battery concepts” available. Advantages and disadvantages of the different strategies for utilizing sulfur in electrochemical cells will be discussed. In principle, all concepts can be applied to any metal-negative electrode (Li, Na, K, Mg...) so we will first discuss the concept in general and discuss specifics of the individual systems Li/S, Na/S, K/S, and Mg/S. We note that also primary aluminum–sulfur cells have been suggested, however, as hardly any literature is available on rechargeable Al/S batteries, this system is not further considered here.

2 Cell Concepts

In the following, the different cell concepts will be discussed and compared. The starting point is the conventional design shown in Fig. 1, i.e., a cell based on solid electrodes and a liquid electrolyte solution. This design is extended by adding a membrane to block polysulfide diffusion toward the negative electrode (2.1). This concept can be further extended for specifically operating with dissolved polysulfides only (2.2). The all-solid-state concept is discussed in subsection 2.3, whereas high-temperature systems with molten electrodes are discussed in subsection 2.4.

2.1 Conventional Design with Additional Membrane

Most of the recent scientific works about sulfur electrochemistry aim at minimizing or eliminating the parasitic polysulfide shuttle mechanism. An obvious strategy is the integration of an ion selective membrane, which is blocking for dissolved polysulfides (see Fig. 3) but permeable for the metal cations. Such a membrane is directly placed between both electrodes and covers the whole electrodes surface. The membrane therefore might also replace the conventional separator.

The membrane materials have to fulfill different requirements: (1) The membranes must be dense and completely impermeable towards polysulfides but at the same time highly permeable to the metal cations to minimize resistance; (2) The membranes should be as thin as possible to minimize the weight penalty. For comparison, the thickness of separators in commercial LIBs is around 10–20 μm . One also has to be aware that adding a membrane creates additional interfaces between the liquid electrolyte and the membrane. The ion transfer over this new interfaces might be rate limiting [56]; (3) Conceivable membrane materials have to provide sufficient mechanical and chemical stability on the long term.

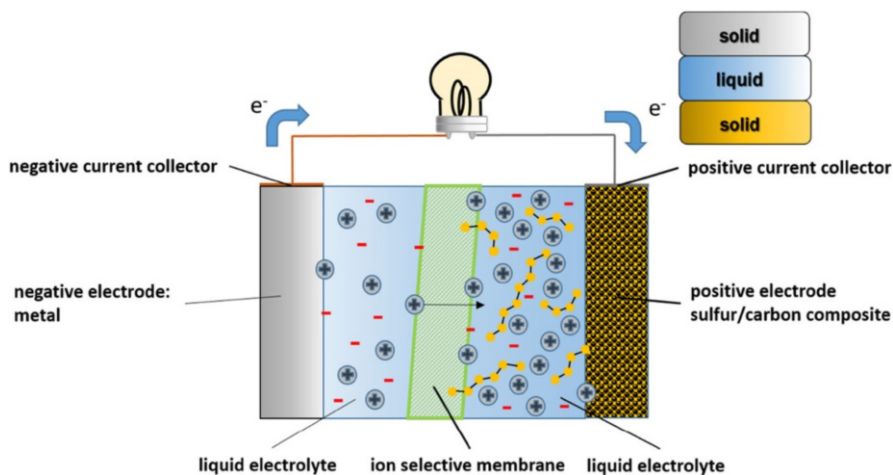
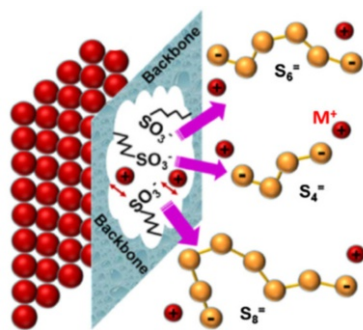


Fig. 3 Scheme of the membrane cell concept with an ion selective membrane. Cations can pass the membrane, while polysulfides (indicated as yellow/black chains) are locked on the positive electrode side. The shuttle mechanism is suppressed and the anode is protected

An advantage of this cell concept is that it requires only little modification compared to the conventional design. In case the membrane replaces the cell separator, the loss in energy density is likely very small. On the other hand, the synthesis and design of membrane materials, which fulfill the requirements outlined above, is a difficult challenge. Above all, the combination of 100% ion selectivity, like it is the case for solid electrolytes, and high mechanical flexibility usually results in too many compromises. Therefore it is unlikely that a thin, polymer-based membrane is able to suppress the parasitic polysulfide shuttle effect completely. Moreover, leaking around the edges of the membrane is a practical challenge. Long-term stability issues make it even more problematic to find reliable materials. If a membrane stays in contact with organic electrolyte, it is probable that swelling takes place, which might reduce the membranes quality to protect the negative electrode from dissolved polysulfides.

One popular polymer-based membrane material is *Nafion*TM. It has been investigated in terms of shuttle effect suppression for Li/S and Na/S electrochemistry as well [57–61]. The main advantage of this material is the possibility to design it especially for several types of cations, while surface functionalization with negative sulfonate groups have a repulsive effect on all anions like polysulfides. According to the efficiency of this material, recent observations show that almost a complete suppression does succeed [57]. The proposed working mechanism is demonstrated in Fig. 4. Another approach is the use of ceramic solid electrolytes as membranes. Monolithic β' -alumina membranes (thickness of 500 μm) have been used to demonstrate the basic functionality of this concept. Better overall cell performance and cycle stability has been demonstrated in case of room-temperature Na/S cells, for example [33, 62]. This solid electrolyte provides optimal ion selectivity and excellent chemical long-term stability. On the downside, solid

Fig. 4 Functionality of an ion-selective NafionTM membrane in a metal–sulfur cell. Reprinted with permission from Ref. [58] Copyright (2016) American Chemical Society



electrolytes are not flexible and therefore more difficult to process in general. A major challenge is to prepare dense membranes with sufficiently small thickness at a competitive cost. Some solid electrolytes also suffer from the problem that they dissolve in certain organic solvents, e.g., some sulfides in ethers or carbonates.

Overall, the membrane concept is a very promising route to improve the performance of metal–sulfur batteries that operate at (close to) room-temperature conditions. Membranes might enable high coulombic efficiency due to complete shuttle suppression as well as only little loss in energy density. The requirements, however, are complex and development and optimization of suitable membrane materials is still necessary.

2.2 Polysulfide Cell Concept

The idea of using a polysulfide blocking membrane for suppressing the shuttle mechanism can be also used to design cells that run completely on dissolved polysulfides. While other concepts try to minimize dissolution of polysulfides, this concept tries to take advantage of their high solubility. The key difference compared to the membrane concept discussed in Sect. 2.1. is that the cell reaction is restricted to intermediates only, i.e. insoluble polysulfides as well as the end members of the reaction (sulfur and fully reduced sulfide) are intentionally avoided. The positive electrode then consists of a conductive carbon framework and the polysulfide redox process takes place on its surface (adsorption → reduction/oxidation → desorption). The polysulfide concept is shown in Fig. 5. During discharge, metal is oxidized and the cations pass the membrane just like in the concept described above, but no solid discharge products are formed.

What can be the expected advantages this approach? In this regard, it is necessary to take a view on sulfur redox kinetics. It has been reported several times that electrochemical reactions between long-chain sulfur/polysulfides (S₈, S₈²⁻) and medium-chain polysulfides (S₆²⁻, S₄²⁻) show much lower overpotentials especially for discharge process (reduction) compared with reactions, where non-soluble sulfides form [28, 47, 63]. Therefore, this method seems to be very attractive due to high energy efficiency. Moreover, detrimental effects related to volume expansion are avoided. So overall, better cycling stability and lifetime can be expected. In addition, the polysulfide solution can be pumped, which makes a semi-flow battery

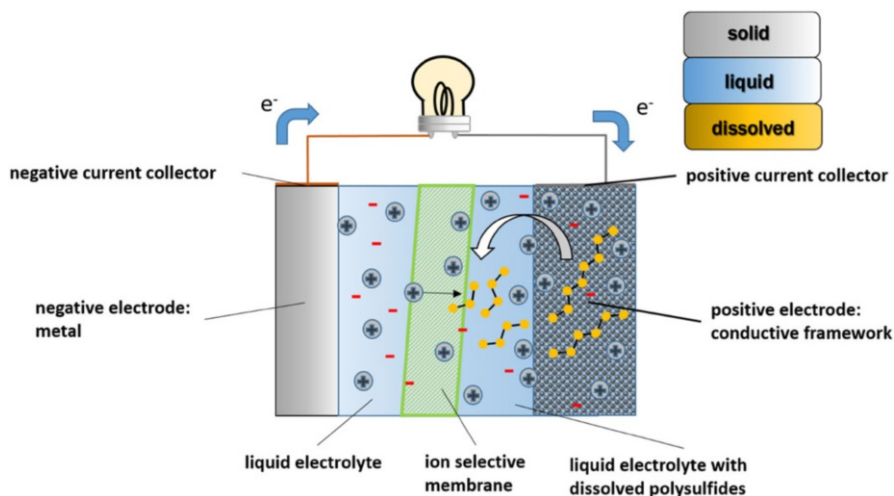


Fig. 5 Scheme of the polysulfide cell concept: Only soluble polysulfides become oxidized and reduced during cycling, no solid-phases form

conceivable. Of course, there are also trade-offs. The most obvious disadvantage is the loss in capacity. For example, reduction/oxidation between S_8^{2-} and S_4^{2-} corresponds to a capacity of 209 mAh/g, which is only one-eighth of the theoretical capacity of sulfur (S^0 to S^{2-}). Polysulfide electrochemistry is naturally also quite complex and it is not trivial to control the reaction in a way that only selected polysulfides are present. Moreover, the use of excess solvent/electrolyte adds extra weight to the cell which negatively impacts energy density. Exact numbers of weight and volume penalty depend on different parameters such as polysulfide solubility limits over a defined cell reaction window and electrolyte viscosity, especially when a flow system is projected. In this matter, Yang et al. estimated for a Li-polysulfide system (Li_2S_n , $8 \geq n \geq 4$) a theoretical energy density of around 170 Wh/kg (190 Wh/l) considering nearly saturated polysulfide solution (7 M, DOL:DME, 1:1) [64]. For comparison, neglecting the extra weight in this estimation would result in a theoretical energy density of more than 330 Wh/kg (540 Wh/l).

The basic idea of a polysulfide battery has already been mentioned in 1977 by Abraham et al. as a room-temperature analog to high-temperature sodium-sulfur battery [65]. Instead of molten sulfur, it was suggested to use dissolved sodium polysulfides. One year later, a similar idea has been proposed by same group for lithium [66]. These concepts were not further exploited and by the years, most research groups turned to cells based on solid carbon/sulfur electrodes (see Fig. 1, right). Recently, however, this approach is being reconsidered and a number of studies on polysulfide batteries have been published. For example, Yu and Manthiram et al. started to analyze the properties of polysulfide electrochemistry for sodium as negative electrode and reported better reaction kinetics for the reaction between long-chain polysulfides [63, 67]. For lithium, this system has been investigated and developed further as a flow battery concept with mobile polysulfide

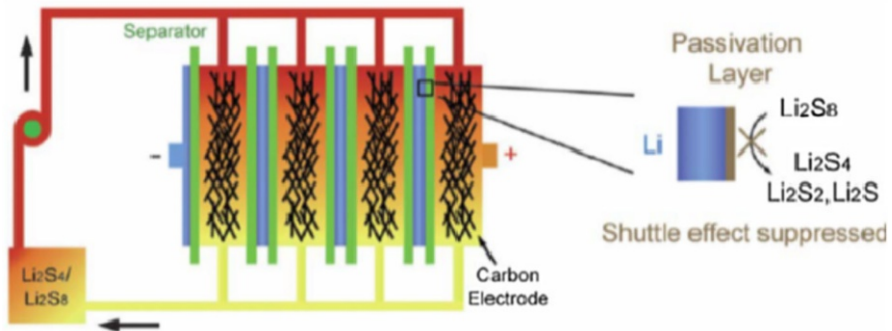


Fig. 6 Combination of Li–polysulfide cycling concept with dynamic flow electrolyte. The system works without a membrane. Reproduced from Ref. [64] with permission of the Royal Society of Chemistry

catholyte [64]. Interestingly, though no membrane was used, reliable cycling was possible (Fig. 6). In this case it is likely that excess sulfur temporarily formed a protective layer on the lithium electrode. Li et al. presented a lithium polysulfide cell operating with a mixed electrolyte system. An organic electrolyte was used in contact with the lithium electrode whereas an aqueous electrolyte was used for the positive electrode. The half cells were separated by a solid electrolyte membrane. Besides the cost advantage, water is able to dissolve larger amounts of polysulfides as well as Li_2S , which enlarges the operation window of polysulfide cells. Consequently, the obtainable capacity becomes much larger and have been found to exceed 1000 mAh/g [68]. Safety issues related to direct water exposure of lithium in case of membrane cracking, corrosion of the solid electrolyte in the aqueous solution, H_2S formation as well as water electrolysis are important challenges of this approach. It is worth mentioning that aqueous electrolytes have already been considered earlier for sulfur batteries. For example, Licht et al. studied aluminum–sulfur cells in the 1990s but they were not rechargeable [69, 70].

Overall, the main benefit of the polysulfide approach is the chance to realize cells with improved kinetics and hence high energy efficiency. Eventually, such cells can be designed in form of a semi-redox flow cell. On the contrary, only a (often small) fraction of the theoretical capacity of sulfur is accessible which intrinsically limits the energy density, not to mention the extra weight added in case of excess electrolyte is applied. The polysulfide cell concept is therefore only interesting for stationary energy storage.

2.3 All-Solid-State Cell Concept

All-solid-state battery concepts are playing a more and more prominent role in today's battery research thanks to their promises of higher energy density and improved safety compared to conventional LIB technology. As the name implies, all-solid-state cells do not contain any liquid. Electrodes and the electrolyte are all solid compounds that are mechanically pressed together. It is clear that the manufacturing of such cells is entirely different from conventional batteries. A

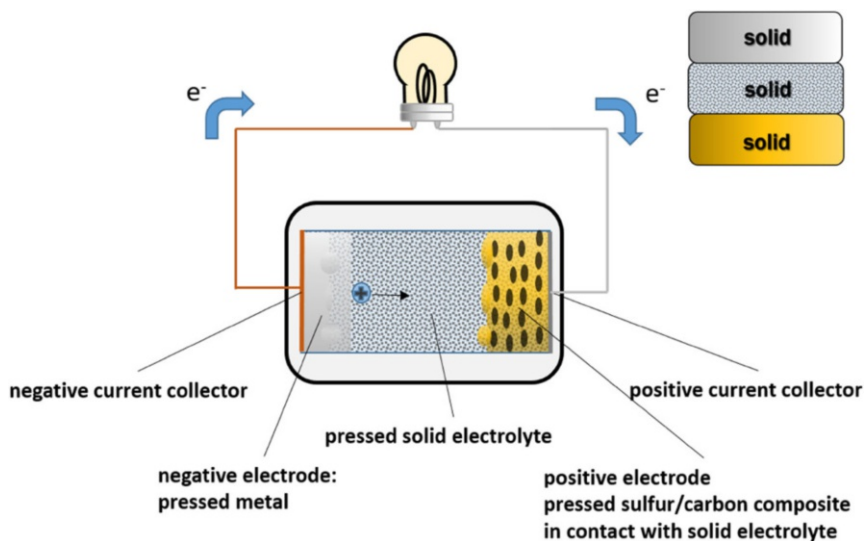


Fig. 7 Scheme of the all-solid-state concept. All reactants are solid at all times during cell cycling

major advantage of liquid electrolytes is that they can be easily injected into empty cells to contact both electrodes. The liquid electrolyte fills all free volume of the electrode and forms a continuous liquid/solid interface of large surface area that eases charge transfer. In solid-state cells, charge transfer is only possible over particle–particle contacts so suitable electrode design strategies are required to minimize the interface resistances. The solid electrolyte also functions as separator. For sulfur batteries, the development of all-solid-state cells is conceivable (Fig. 7) as well. The theoretical reaction mechanism during discharge remains the same. Oxidation of the metal at the negative electrode combined with formation of the corresponding metal sulfide at the positive electrode. The most important characteristic of all-solid-state metal–sulfur batteries is that the entire cell chemistry changes because polysulfide dissolution and shuttling cannot occur. It is also worth noting that the different metals of interest show a different number of thermodynamically stable intermediates (see Table 2). Whether this benefits or hinders the reversibility of the cell reaction remains to be clarified. Due to the insulating properties of sulfur and sulfides, the positive electrode requires conductive additives. In this case, it is not only conductive carbon to enable electronic transport but also solid electrolyte to enable the transport of the metal cations (unless the electrode is thin enough). The positive electrode is therefore usually a composite consisting of sulfur, solid electrolyte, and carbon.

The advantages of all-solid-state sulfur batteries are comparable to other all-solid-state concepts [9,10, 71]. Replacement of the volatile organic liquid electrolyte by an (ideally) non-flammable solid electrolyte is advantageous with respect to safety. The use of a solid electrolyte also holds greater promise to realize rechargeable batteries with metals as negative electrode. The common arguments

are that dendrite formation might be eliminated and that the electrode/electrolyte interface is more stable compared to liquid electrolytes where solid electrolyte interphase (SEI) formation takes place. Recent results, however, show that this is not necessarily the case [72–74]. Many solid electrolytes are found to be instable in contact with highly reductive metals and some that are considered stable have been found to function only because of an interphase formation [75, 76]. Dendrites, also, might grow through grain boundaries finally penetrating the solid electrolyte. The situation therefore is sometimes not too different compared to liquid electrolytes. Nevertheless, the recent progress in solid electrolytes [77, 78] provides new opportunities for designing batteries with improved properties—also with respect to metal–sulfur systems. For Mg, however, the chances are small because of the highly polarizing nature of the Mg^{2+} ion. Solid electrolytes with sufficiently high Mg^{2+} conductivity do not exist and are highly unlikely.

On the other hand, the solid-state approach is also linked to some specific challenges. Because all components are solid, volume changes during cell cycling will cause mechanical stress, eventually leading to crack formation and particle contact loss. The degree of volume expansion for the different reactions is shown in Table 1. Formation of Li_2S from sulfur is accompanied by a volume increase as high as 80%, for example. The situation becomes worse for the other alkali metals. It will therefore be challenging to cycle sulfur-rich electrodes in the solid state. Mechanical stress might be alleviated by porosity or by use of a soft matrix, although this comes with a number of obvious disadvantages. Another challenge is to fully utilize the active material. As stated before, the end members of the cell electrode reaction (sulfur, sulfides) are insulators. In case of larger particles, the reaction is likely restricted to the surface so the capacity yield is expected to be low. Nanosizing and uniform distribution of sulfur therefore becomes very important.

Research on all-solid-state sulfur batteries showed only moderate success so far. Only few publications have been reported within the last 15 years but the recent attention on solid-state batteries in general is also benefiting the research on sulfur solid-state systems. In 2004, a PEO-polymer containing LiTFSI-salt was discussed as a possible electrolyte for all-solid-state lithium–sulfur cells. The cells' performance was analyzed at 70 °C and an ionic conductivity of around 4.8×10^{-4} S/cm has been reported [41]. Three years later, a similar PEO-based electrolyte was used for solid-state sodium–sulfur cell system investigations. At temperatures around 90 °C, the polymer electrolyte provided an ionic conductivity of 3.38×10^{-4} S/cm [79]. General problems are an insufficient overall cell performance, instability of the electrolyte and a possible self-discharge due to partial electronic conductivity. Besides polymer electrolytes, ionically conductive ceramics and glasses are highly promising candidates for usage inside solid-state batteries. According to this, sulfidic glasses such as $\text{Li}_2\text{S}/\text{P}_2\text{S}_5$ or $\text{LiGeS}_4/\text{Li}_3\text{PS}_4$ (Thio-LISICON) are considered in recent research [38–40]. The Li^+ -ion conductivity of these compounds can exceed values of 1×10^{-3} S/cm even at room temperature. On the other hand, they are very reactive toward water let alone the possible evolution of toxic H_2S in case of leakage.

In summary, the all-solid-state concept for metal–sulfur batteries is still in its early stage of development. The issues related to the poor conductivity of sulfur and its compounds as well as the problems associated with the large volume expansion during sulfide formation are especially difficult to tackle in the solid state, however, the prospect of eliminating the shuttle mechanism is promising enough to consider this concept in the future.

2.4 High-Temperature Concept

High-temperature sulfur electrochemistry requires a cell concept with characteristics that strongly differ from the other presented concepts. Considering sulfur batteries, the term high temperature means that the operating temperature of the cell is always above the melting points of all reactants and intermediates. In the charged state, liquid metal is the active material of the negative electrode, while liquid sulfur is present at the positive electrode. Both electrode compartments are separated by a solid electrolyte. Although a planar design is imaginable (Fig. 8, top), the so-far commercialized sodium–sulfur batteries exhibit a tubular design (Fig. 8, bottom).

During discharge, metal is oxidized on the anode side and molten sulfur is subsequently reduced at the cathode side to form molten long-chain and finally molten short-chain polysulfides. It is important to realize that the melting points of sulfur ($T_m = 115\text{ °C}$) and the alkali metals lithium (181 °C), sodium (98 °C), and potassium (64 °C) are comparably low, making them ideal candidates for such a cell concept. On the other hand, sulfides have very high melting points ($T_m = 1372\text{ °C}$, 1168 °C and 948 °C for Li_2S , Na_2S and K_2S , respectively) so complete reduction is not conceivable. Cell discharge is therefore restricted to polysulfides that have intermediate melting points. The extent of the reaction therefore depends on the operating temperature, which is set at around 300 °C for the commercialized Na/S battery technology, for example. At this temperature, several Na–S long-chain polysulfides are liquid. Consequently, the practical capacity of the sulfur electrode is much lower than theoretically expected (see discussion below). Due to the high melting point of Mg (650 °C), this concept will likely not be applicable to Mg/S batteries.

The high-temperature battery concept comprises a couple of important advantages. An important aspect is that the reversibility of the metal electrode is improved, as no dendrite formation occurs. Moreover, the polysulfide shuttle mechanism is eliminated thanks to the solid electrolyte membrane. The use of liquid active materials also reduces the mechanical stress to the electrodes. The expected life time of these cells is therefore high. At last, the overall cell kinetics generally benefit from elevated temperatures.

On the other hand, the high-temperature concept faces some specific challenges. Obviously, all cell parts and components must resist higher temperatures over several years without any changes. The liquid active materials (alkali metal, sulfur, and polysulfides) are particularly aggressive, limiting the choice of materials for current collectors, solid electrolyte, sealing, and other cell-housing components. Moreover, the vapor pressure of the molten alkali metals and sulfur can cause

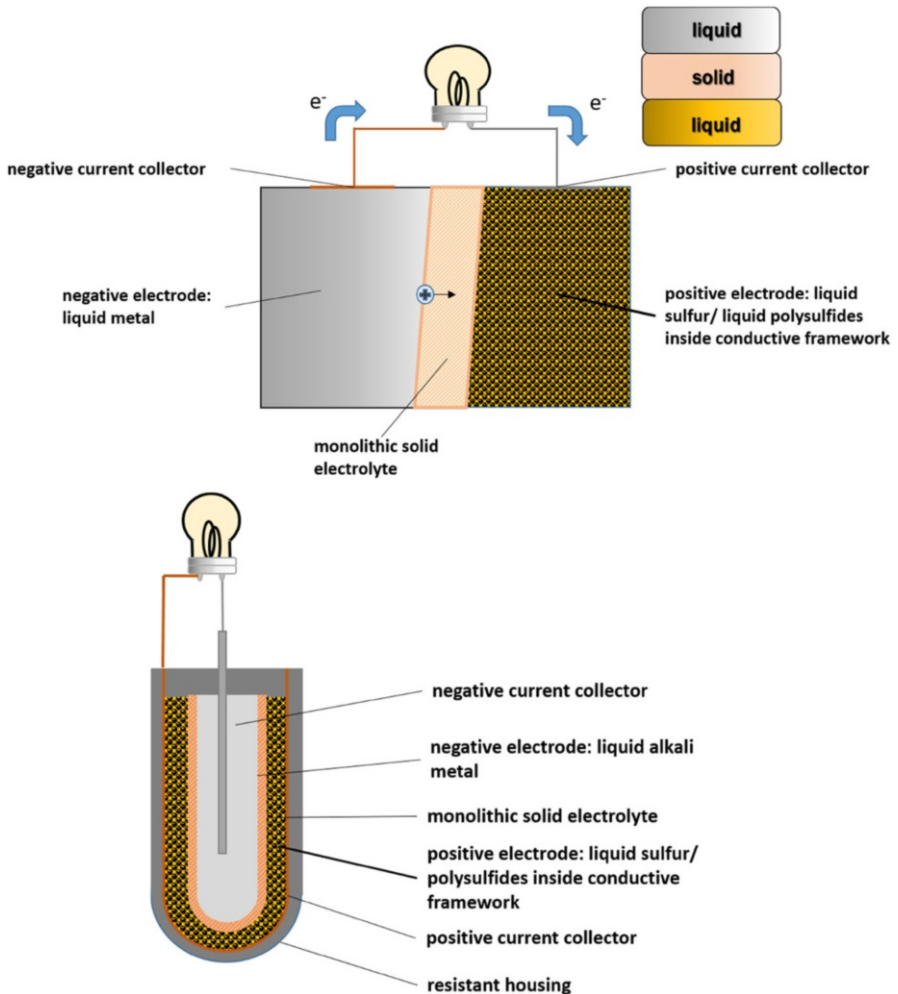


Fig. 8 *Top* Scheme of the high-temperature cell concept. Active materials are in molten state during cycling, while both electrodes are separated by an ion selective ceramic membrane. *Bottom* Tubular cell design that is used in commercialized high-temperature sodium–sulfur batteries

undesired transport and ageing mechanisms. Maintaining the high operating temperature also requires an optimized thermal management as otherwise the energy efficiency of the system becomes too low. For thermodynamic reasons, the cell voltage also slightly decreases with increasing temperature. The main challenge of the high temperature concept is related to safety. Leakage of the cell housing would lead to the release of highly reactive liquid metal or sulfur. Cracking of the solid electrolyte would cause a fast reaction between the electrodes active materials and finally thermal runaway. Developing reliable safety measures is therefore of utmost importance. Because of this, and the applied temperatures, high-temperature sulfur electrochemistry is suitable for stationary electrical energy storage only.

High-temperature sulfur batteries have been considered for several decades and research dates back to the late 1960s and 1970s where the high-temperature sodium–sulfur battery was suggested by Kummer and Weber (Ford Motor Co.) [80, 81]. The cell was originally designed for electric vehicles, although nowadays grid storage application is the main application. A number of companies developed this cell type, but presently, only NGK insulators Ltd. offers a commercial system (see Fig. 9). Analog cell concepts for lithium or other negative electrode materials have not been developed so far. Indeed, the high-temperature Na/S battery is the only metal sulfur battery that has been commercialized to date. An essential milestone and basic requirement was the discovery of Na- β'' -aluminate (NaAl_5O_8), a high-performance sodium ion-conducting ceramic [80–83]. This solid electrolyte possesses sufficient ionic conductivity as well as chemical stability for reliable usage inside high-temperature sodium–sulfur batteries. The basic sodium–sulfur battery, developed by Kummer and Weber, was based on a tubular Na- β'' -aluminate solid electrolyte. Aluminum was also used as current collector material. The operating temperature of 300 °C enables a reduction of sulfur to liquid polysulfides with an average stoichiometry of around Na_2S_3 , so the maximum gravimetric capacity is 557 mAh/g instead of 1672 mAh/g for complete sulfur reduction. Further reduction of Na_2S_3 would lead to the formation of solid Na_2S_2 ($T_m = 470$ °C), which has to be avoided. It is interesting to note that the formation of Na_2S_3 at 300 °C from molten sodium and sulfur corresponds to a theoretical cell voltage of 1.91 V, which is 180 mV lower than the same reaction at room temperature with all reactants in their solid state. The theoretical energy density at 300 °C therefore amounts to 721 Wh/kg. Practical values are in the range of 200 Wh/kg. These are still high values, although they are much lower from what one might expect from the values given in Table 1. An important advantage of the Na/S



Fig. 9 High-temperature sodium–sulfur battery park for grid scale electric energy storage purpose [84] (Reprinted with permission from http://www.energy-storage.news/blogs/sponsored-ngks-nas-grid-scale-batteries-in-depth_ February 2017)

battery is that the raw materials are inexpensive and abundant, which is an important requirement for future large-scale energy storage.

3 Challenges of Metal-Negative Electrodes

Considering capacity and cell voltage, the use of metals (Li, Na, K, Mg...) as negative electrodes is the most appealing option for any kind of battery. Safe operation of metal electrodes in rechargeable room-temperature batteries, however, is still an unsolved challenge to date (thin film batteries being an exception). This is mainly related to dendrite formation combined with the chronic instability towards liquid (and many solid) electrolytes [36, 85, 86]. Recent efforts in dendrite investigations show that suitable electrolyte modifications can minimize dendrite formation and electrolyte side reactions [87]. However, reliable control of metal plating under practical conditions still remains an unsolved challenge.

In today's LIBs, graphite is therefore used, although compared to a lithium electrode the capacity is much lower (372 mAh/g) and the cell voltage decreases by around 0.1 V. A few other negative electrodes such as $\text{Li}_4\text{Ti}_5\text{O}_{12}$ (LTO), silicon, tin, or other conversion reactions are considered for LIBs as well. The choice in negative electrodes for sulfur batteries, however, is even smaller. This is simply because the electrode potential of the sulfur electrode is relatively low. The combination of a sulfur positive electrode with an intercalation negative electrode would therefore deliver only small cell voltages. For example, the use of LTO (E^0 vs. $\text{Li}/\text{Li}^+ = 1.46$ V) in a Li/S battery would only deliver a maximum cell voltage of 0.78 V [88]. A high voltage, however, is very desirable considering power capability and to minimize the number of individual cells in a battery. The preferred choice for the negative electrodes in sulfur batteries is therefore the respective metal, i.e., Li, Na, K, Mg... as also shown in the sketches illustrating the cell concepts (see Figs. 2, 4, 6, 7). But even when using metals, the cell voltage (around 2 V or below) is much lower compared to commercialized LIB technology (close to 4 V), see Table 1. Anyway, the use of hard carbon, silicon, boron, or tin as negative electrode host material in sulfur batteries is being explored [89–94]. Although improvement in terms of safety might be possible, none of these compounds provides a clear advantage considering issues related to the shuttle mechanism and reactions with dissolved polysulfides.

As discussed above, developing metal electrodes for rechargeable room-temperature batteries is very demanding and has largely been unsuccessful for decades. The problems of dendrite formation and side reactions are intrinsic for the combination of an alkali metal and a liquid electrolyte and effective countermeasures are still desperately needed. Nevertheless, it is worth noting that rechargeable batteries with metal electrode are in application. These are all based on cell concepts without liquid electrolyte: Thin film lithium-ion batteries (operating at room temperature with LiPON as solid electrolyte [95, 96] a), the EV batteries of the BlueCar (≥ 60 °C with a polymer solid electrolyte) and finally the discussed high-temperature Na/S battery (≥ 300 °C). Overall, sulfur battery concepts without liquid electrolytes might have the greatest chance for operating with metal electrodes. A

very different type of anode was recently presented by Yu et al. who presented a liquid anode based on a dissolved sodium biphenyl compound. This unusual anode type provided a low potential of 0.09 V vs. Na/Na⁺ and its principal function was demonstrated in combination with a polysulfide cell [97]. Prospects of this approach, however, need to be studied in more detail.

4 Aspects of Magnesium–Sulfur and Potassium–Sulfur Cells

While most attention in sulfur batteries is given to Li/S and to some extent also Na/S systems (for a detailed comparison we refer to Ref. [28]), reports on Mg/S and K/S cells are very scarce. Lately, magnesium-ion batteries are also being reconsidered and therefore also the magnesium–sulfur cells. In contrast to the monovalent alkali ions, divalent ions are especially attractive considering the volumetric charge density. The capacity of magnesium metal by volume is 3834 mAh/cm³ compared to 2062 mAh/cm³ for Li and 1128 mAh/cm³ for Na, respectively. Magnesium is very abundant, non-toxic, and the density of the ideal discharge product MgS is significantly larger compared to the alkali metal sulfides, meaning the volume expansion during cell discharge (+36%) is smallest among all systems considered, see Table 1. Issues related to mechanical strain in the positive electrode are therefore less critical. Besides, magnesium is easier to handle than alkali metals, because it is not as sensitive to air and moisture.

A major disadvantage of a Mg–S cell is the inherently low theoretical cell voltage, which is only 1.77 V. Moreover, the lack of suitable electrolytes hampers a fast progress of magnesium batteries in general. Quite special electrolytes have to be considered instead. One option is the use of Grignard-like compounds in combination with AlCl₃ as Lewis acid. Usually, THF is used as solvent for this purposes [85]. Another possibility is the use of organo-metallic species. For magnesium–sulfur batteries, magnesium hexamethyldisilazide again combined with AlCl₃ (HMDS:AlCl₃) is discussed as electrolyte candidate in recent literature [98]. It is also reported that different magnesium salts like Mg-triflate can be dissolved in different ionic liquids, which are working as solvent or co-solvent [99].

Although research on the use of magnesium in batteries has recently become more popular, the focus is currently not on sulfur as a cathode material. One reason might be the unattractive low overall cell voltage. Another is that the already-difficult situation with the electrolytes becomes even more complex considering polysulfide formation. Therefore, it is unlikely that a magnesium–sulfur battery will have its breakthrough in the near future.

Potassium is also theoretically conceivable as a negative electrode material. In contrast to magnesium, potassium electrolyte solutions can be prepared easily with conventional salt in solvent methods. Because of the experiences with lithium and sodium, similar reaction mechanisms and challenges are expectable and hence, it can be introduced in all presented cell concepts. A potassium metal electrode provides 685.5 mAh/g (587 mAh/cm³), which is the lowest among the metals

discussed. Although the theoretical cell voltage of a K–S cell (1.88 V) is close to the one of the Na–S system, the theoretical energy density is not competitive. Actually, it is difficult to find any benefits in sulfur electrochemistry by introducing potassium as substitute for lithium or sodium. One advantage might be the low melting point of potassium for liquid electrode realization.

Only a few studies about potassium–sulfur cells have been published [100, 101]. An interesting example is a potassium–polysulfide cell, investigated at temperatures of around 150 °C [101]. The system is presented as an analog to the high-temperature sodium–sulfur battery, with the difference of lower operating temperature and the use of tetraglyme solvent ($T_b = 274$ °C) in the positive electrode compartment. Liquid potassium acts as a negative electrode, while a K- β'' -aluminate-based ceramic is used as solid electrolyte membrane. Overall, this cell represents a combination of high-temperature and polysulfide cell concept. As expected, higher cell voltages and lower capacities were obtained compared to high temperature Na/S cells, while the overall energy density is somewhat lower. Overall, the interest in K/S batteries seems more academic and a technological advantage over the other alkali metals is not apparent.

5 Conclusions

Thanks to its low cost and high theoretical capacity, sulfur is an extremely attractive element for electrical energy storage. Combined with a light metal counter electrode (Li, Na, K, Mg...), energy densities significantly exceeding lithium-ion technology are theoretically possible. Sulfur electrochemistry, however, is very complex and although research on metal–sulfur batteries has been initiated already decades ago, there was only limited progress over many years. Today, only the high-temperature sodium–sulfur battery is commercialized and used for grid storage. The renewed interest in electric vehicles revived research on the (ambient temperature) lithium–sulfur battery leading to intense research efforts worldwide within the last 10 years. More recently, also ambient temperature Na/S as well as K/S and Mg/S cells are being reconsidered.

Due to the peculiar properties of sulfur and its discharge products (poor conductivity, volume expansion, polysulfide shuttling, corrosion issues...), a conventional battery design is not suitable for achieving a performance that leads to commercially relevant results. The known challenges related to the use of metal electrodes in rechargeable batteries further add to the complexity for realizing metal–sulfur batteries. A range of alternative cell concepts has therefore been studied over the years in which sulfur is electrochemically converted in the solid, molten, or dissolved state. Advantages and disadvantages of these concepts were summarized and critically reviewed in this article. Table 3 summarizes these advantages and disadvantages. For all concepts, the use of an ion-selective membrane, either inorganic, organic, or as a composite, seems to be the key for rendering a long cycle life. Although progress has been made, the development of cost-effective membranes with excellent performance as well as their convenient integration into a full device is still needed for a major breakthrough. For this,

Table 3 Overview of cell concepts for batteries utilizing sulfur as active material: A comparison of advantages and restrictions

Cell concept	Advantages	Comments/restrictions
Conventional (Fig. 1)	Simple cell preparation	Volume effects Polysulfide shuttle Low overall lifetime
Conventional + membrane (Fig. 3)	High capacity yield Polysulfide shuttle alleviated	Volume effects
Polysulfide (Fig. 5)	No volume effects High energy efficiency Polysulfide shuttle alleviated	Polysulfide reactivity Low capacity yield (12–25%) Weight and volume penalty
All-solid-state (Fig. 7)	Safe operation Polysulfide shuttle suppressed	High impact of volume effects High sulfur dispersion necessary
High temperature (Fig. 8)	Proven technology (Na–S) Metal anode applicable Polysulfide shuttle suppressed	Restricted capacity yield (25–33%) Safety issues

suitable materials and processing strategies have to be developed to finally equal or surpass LIB technology in energy density or cost effectiveness.

Acknowledgements The authors acknowledge support from the State of Thuringia (Germany) within the ProExzellenz program.

References

- Dewulf J, Van der Vorst G, Denturck K, Van Langenhove H, Ghyoot W, Tytgat J et al (2010) Recycling rechargeable lithium ion batteries: critical analysis of natural resource savings. *Resour Conserv Recycl* 54(4):229–234
- Wadia C, Albertus P, Srinivasan V (2011) Resource constraints on the battery energy storage potential for grid and transportation applications. *J Power Sources* 196(3):1593–1598
- Larcher D, Tarascon JM (2015) Towards greener and more sustainable batteries for electrical energy storage. *Nat Chem* 7(1):19–29
- Grey CP, Tarascon JM (2017) Sustainability and in situ monitoring in battery development. *Nat Mater* 16(1):45–56
- Thielmann A, Sauer A, Wietschel M (2015) Gesamt-Roadmap Energiespeicher für die Elektromobilität 2030. Fraunhofer-Institute ISI, Karlsruhe
- Nykqvist B, Nilsson M (2015) Rapidly falling costs of battery packs for electric vehicles. *Nat Clim Chang* 5(4):329–332
- Nayak PK, Yang L, Brehm W, Adelhelm P (2017) From lithium-ion to sodium-ion batteries: a materials perspective. *Angew Chem Int Ed Engl*. doi:10.1002/anie.201703772
- Hu Y (2016) Batteries: Getting solid. *Nature Energy*. 1(4):16042. <http://www.nature.com/articles/nenergy201642>
- Janek J, Zeier W (2016) A solid future for battery development. *Nat Energy* 1:16141. doi:10.1038/nenergy.2016.141

10. Kato Y, Hori S, Saito T, Suzuki K, Hirayama M, Mitsui A, Yonemura M, Iba H, Kann R (2016) High-power all-solid-state batteries using sulfide superionic conductors. *Nat Energy* 1:16030. doi:[10.1038/nenergy.2016.30](https://doi.org/10.1038/nenergy.2016.30)
11. Aurbach D, McCloskey BD, Nazar LF, Bruce PG (2016) Advances in understanding mechanisms underpinning lithium–air batteries. *Nature Energy* 1(9):16128. doi:[10.1038/nenergy.2016.128](https://doi.org/10.1038/nenergy.2016.128)
12. Soloveichik G (2015) Flow Batteries: Current Status and Trends. *Chem Rev* 115:11533–11558. doi:[10.1021/cr500720t](https://doi.org/10.1021/cr500720t)
13. Winsberg J, Hagemann T, Janoschka T, Hager MD, Schubert US (2017) Redox-Flow Batteries: From Metals to Organic Redox-Active Materials. *Angew Chem Int Ed* 56(3):686–711. doi:[10.1002/anie.201604925](https://doi.org/10.1002/anie.201604925)
14. Hueso KB, Armand M, Rojo T (2013) High temperature sodium batteries: status, challenges and future trends. *Energy Environ Sci* 6:734–749. doi:[10.1039/C3EE24086J](https://doi.org/10.1039/C3EE24086J)
15. Yabuuchi N, Kubota K, Dahbi M, Komaba S (2014) Research Development on Sodium-Ion Batteries. *Chem Rev* 114(23):11636–11682. doi:[10.1021/cr500192f](https://doi.org/10.1021/cr500192f)
16. Sathiyam M, Rousse G, Ramesha K, Laisa CP, Vezin H, Sougrati MT et al (2013) Reversible anionic redox chemistry in high-capacity layered-oxide electrodes. *Nat Mater* 12(9):827–835
17. McCloskey BD, Garcia JM, Luntz AC (2014) Chemical and electrochemical differences in non-aqueous Li–O₂ and Na–O₂ batteries. *J Phys Chem Lett.* 5(7):1230–1235
18. Adelhelm P, Hartmann P, Bender CL, Busche M, Eufinger C, Janek J (2015) From lithium to sodium: cell chemistry of room-temperature sodium–air and sodium–sulfur batteries. *Beilstein J Nanotechnol* 6:1016–1055
19. OXIS Energy Ltd (2017) Cited 2017 March 19; Available from <https://oxisenergy.com/>. Accessed 19 Mar 2017
20. Raiss C, Peppeler K, Janek J, Adelhelm P (2014) Pitfalls in the characterization of sulfur/carbon nanocomposite materials for lithium–sulfur batteries. *Carbon* 79:245–255
21. Levin BDA, Zachman MJ, Werner JG, Sahore R, Nguyen KX, Han Y et al (2017) Characterization of sulfur and nanostructured sulfur battery cathodes in electron microscopy without sublimation artifacts. *Microsc Microanal* 23:15–162
22. Steudel R (2003) Inorganic Polysulfides S_n²⁻ and Radical Anions S_n^{·-}. In: Steudel R (ed) *Elemental sulfur and sulfur-rich compounds II. Topics in Current Chemistry*, vol 231. Springer, Berlin, Heidelberg. doi:[10.1007/b11909](https://doi.org/10.1007/b11909)
23. Mikhaylik YV, Akridge JR (2004) Polysulfide shuttle study in the Li/S battery system. *J Electrochem Soc* 151(11):A1969–A1976
24. Rehman S, Khan K, Zhao Y, Hou Y (2017) Nanostructured cathode materials for lithium–sulfur batteries: progress, challenges and perspectives. *J Mater Chem A* 5(7):3014–3038
25. Ji X, Lee KT, Nazar LF (2009) A highly ordered nanostructured carbon–sulfur cathode for lithium–sulfur batteries. *Nat Mater* 8(6):500–506
26. Holleman AF, Wiberg E, N. W. *Lehrbuch der Anorganischen Chemie*. 2007;102
27. Zhang SS (2013) Liquid electrolyte lithium/sulfur battery: fundamental chemistry, problems, and solutions. *J Power Sources* 231:153–162
28. Adelhelm P, Hartmann P, Bender CL, Busche M, Eufinger C, Janek J (2015) From lithium to sodium: cell chemistry of room-temperature sodium–air and sodium–sulfur batteries. *Beilstein J Nanotechnol* 6:1016–1055
29. Gao J, Lowe MA, Kiyu Y, Abuña HD (2011) Effects of liquid electrolytes on the charge-discharge performance of rechargeable lithium/sulfur batteries: electrochemical and in-situ X-ray absorption spectroscopic studies. *J Phys Chem C* 115(50):25132–25137
30. Yim T, Park M-S, Yu J-S, Kim KJ, Im KY, Kim J-H et al (2013) Effect of chemical reactivity of polysulfide toward carbonate-based electrolyte on the electrochemical performance of Li–S batteries. *Electrochim Acta* 107:454–460
31. Fan FY, Pan MS, Lau KC, Assary RS, Woodford WH, Curtiss LA et al (2016) Solvent effects on polysulfide redox kinetics and ionic conductivity in lithium–sulfur batteries. *J Electrochem Soc* 163(14):A3111–A3116
32. Zhang SS (2012) Binder based on polyelectrolyte for high capacity density lithium/sulfur battery. *J Electrochem Soc* 159(8):A1226–A1229
33. Wenzel S, Metelmann H, Raiss C, Durr AK, Janek J, Adelhelm P (2013) Thermodynamics and cell chemistry of room-temperature sodium/sulfur cells with liquid and liquid/solid electrolyte. *J Power Sources* 243:758–765

34. Elazari R, Salitra G, Garsuch A, Panchenko A, Aurbach D (2011) Sulfur-impregnated activated carbon fiber cloth as a binder-free cathode for rechargeable Li–S batteries. *Adv Mater* 23(47):5641
35. Hagen M, Dörfler S, Fanz P, Berger T, Speck R, Tübke J et al (2013) Development and costs calculation of lithium–sulfur cells with high sulfur load and binder free electrodes. *J Power Sources* 224:260–268
36. Xu W, Wang J, Ding F, Chen X, Nasybulin E, Zhang Y et al (2014) Lithium metal anodes for rechargeable batteries. *Energy Environ Sci* 7(2):513–537
37. Janek J, Adelhelm P (2013) Zukunftstechnologien. In: Korthauer R (ed) *Handbuch lithium-ionen-batterien*. Springer Berlin Heidelberg, Berlin, pp 199–217
38. Nagao M, Hayashi A, Tatsumisago M (2011) Sulfur–carbon composite electrode for all-solid-state Li/S battery with Li2S–P2S5 solid electrolyte. *Electrochim Acta* 56(17):6055–6059
39. Nagao M, Imade Y, Narisawa H, Kobayashi T, Watanabe R, Yokoi T et al (2013) All-solid-state Li–sulfur batteries with mesoporous electrode and thio-LISICON solid electrolyte. *J Power Sources* 222:237–242
40. Trevey JE, Gilsdorf JR, Stoldt CR, Lee SH, Liu P (2012) Electrochemical investigation of all-solid-state lithium batteries with a high capacity sulfur-based electrode. *J Electrochem Soc* 159(7):A1019–A1022
41. Yu X, Xie J, Yang J, Wang K (2004) All solid-state rechargeable lithium cells based on nano-sulfur composite cathodes. *J Power Sources* 132(1–2):181–186
42. Yamin HP (1983) E. Electrochemistry of a nonaqueous lithium/sulfur cell. *J Power Sources* 9(3):281–287
43. Ji X, Nazar LF (2010) Advances in Li–S batteries. *J Mater Chem* 20(44):9821–9826
44. Bresser D, Passerini S, Scrosati B (2013) Recent progress and remaining challenges in sulfur-based lithium secondary batteries—a review. *Chem Commun* 49(90):10545–10562
45. Evers S, Nazar LF (2013) New approaches for high energy density lithium–sulfur battery cathodes. *Acc Chem Res* 46(5):1135–1143
46. Yin YX, Xin S, Guo YG, Wan LJ (2013) Lithium–sulfur batteries: electrochemistry, materials, and prospects. *Angew Chem Int Ed* 52(50):13186–13200
47. Manthiram A, Fu YZ, Chung SH, Zu CX, Su YS (2014) Rechargeable lithium–sulfur batteries. *Chem Rev* 114(23):11751–11787
48. Lin Z, Liang CD (2015) Lithium–sulfur batteries: from liquid to solid cells. *J Mater Chem A* 3(3):936–958
49. Rosenman A, Markevich E, Salitra G, Aurbach D, Garsuch A, Chesneau FF (2015) Review on Li–sulfur battery systems: an integral perspective. *Adv Energy Mater* 5(16):1500212
50. Borchardt L, Oschatz M, Kaskel S (2016) Carbon Materials for lithium sulfur batteries—ten critical questions. *Chem Eur J* 22(22):7324–7351
51. Seh ZW, Sun YM, Zhang QF, Cui Y (2016) Designing high-energy lithium–sulfur batteries. *Chem Soc Rev* 45(20):5605–5634
52. Okamoto H (1995) The Li–S (lithium–sulfur) system. *J Phase Equilib* 16(1):94–97
53. Sangster J, Pelton AD (1997) The Na–S (sodium–sulfur) system. *J Phase Equilib* 18:89–96
54. Sangster J, Pelton AD (1997) The K–S (Potassium–Sulfur) system. *J Phase Equilib* 18:82–88
55. Predel B (1997) Mg–S (magnesium–sulfur). In: Madelung O (ed) *Li–Mg—Nd–Zr*. Springer Berlin Heidelberg, Berlin, p 1
56. Busche MR, Drossel T, Leichtweiss T, Weber DA, Falk M, Schneider M et al (2016) Dynamic formation of a solid-liquid electrolyte interphase and its consequences for hybrid-battery concepts. *Nat Chem* 8(5):426–434
57. Huang J-Q, Zhang Q, Peng H-J, Liu X-Y, Qian W-Z, Wei F (2014) Ionic shield for polysulfides towards highly-stable lithium–sulfur batteries. *Energy Environ Sci* 7(1):347–353
58. Yu X, Manthiram A (2016) Performance enhancement and mechanistic studies of room-temperature sodium–sulfur batteries with a carbon-coated functional Nafion separator and a Na₂S/activated carbon nanofiber cathode. *Chem Mater* 28(3):896–905
59. Bauer I, Thieme S, Brückner J, Althues H, Kaskel S (2014) Reduced polysulfide shuttle in lithium–sulfur batteries using Nafion-based separators. *J Power Sources* 251:417–422
60. Yu X, Joseph J, Manthiram A (2015) Polymer lithium–sulfur batteries with a Nafion membrane and an advanced sulfur electrode. *J Mater Chem A*. 3(30):15683–15691
61. Ceylan Cengiz E, Erdol Z, Sakar B, Aslan A, Ata A, Ozturk O et al (2017) Investigation of the effect of using Al₂O₃–Nafion barrier on room-temperature Na–S batteries. *J Phys Chem C* 121(28):15120–15126

62. Kim I, Park J-Y, Kim CH, Park J-W, Ahn J-P, Ahn J-H et al (2016) A room-temperature Na/S battery using a β'' alumina solid electrolyte separator, tetraethylene glycol dimethyl ether electrolyte, and a S/C composite cathode. *J Power Sources* 301:332–337
63. Yu X, Manthiram A (2014) Highly reversible room-temperature sulfur/long-chain sodium polysulfide batteries. *J Phys Chem Lett.* 5(11):1943–1947
64. Yang Y, Zheng G, Cui Y (2013) A membrane-free lithium/polysulfide semi-liquid battery for large-scale energy storage. *Energy Environ Sci* 6(5):1552
65. Abraham KM, Rauh RD, Brummer SB (1978) A low temperature NaS battery incorporating a soluble S cathode. *Electrochim Acta* 23:501–507
66. Rauh RD, Abraham KM, Pearson GF, Surprenant JK, Brummer SB (1979) A lithium/dissolved sulfur battery with an organic electrolyte. *J Electrochem Soc* 126(4):523–527
67. Yu X, Manthiram A (2014) Room-temperature sodium–sulfur batteries with liquid-phase sodium polysulfide catholytes and binder-free multiwall carbon nanotube fabric electrodes. *J Phys Chem C* 118(40):22952–22959
68. Li N, Weng Z, Wang Y, Li F, Cheng H-M, Zhou H (2014) An aqueous dissolved polysulfide cathode for lithium–sulfur batteries. *Energy Environ Sci* 7(10):3307–3312
69. Licht S. Sulfur/aluminum electrochemical batteries. Google Patents 1996
70. Licht S, Hwang J, Light TS, Dillon R (1997) The low current domain of the aluminum/sulfur battery. *J Electrochem Soc* 144(3):948–955
71. Kim JG, Son B, Mukherjee S, Schuppert N, Bates A, Kwon O et al (2015) A review of lithium and non-lithium based solid state batteries. *J Power Sources* 282:299–322
72. Hartmann P, Leichtweiss T, Busche MR, Schneider M, Reich M, Sann J et al (2013) Degradation of NASICON-type materials in contact with lithium metal: formation of mixed conducting interphases (MCI) on solid electrolytes. *J Phys Chem C* 117(41):21064–21074
73. Richards WD, Miara LJ, Wang Y, Kim JC, Ceder G (2016) Interface stability in solid-state batteries. *Chem Mater* 28(1):266–273
74. Zhu Y, He X, Mo Y (2016) First principles study on electrochemical and chemical stability of solid electrolyte-electrode interfaces in all-solid-state Li-ion batteries. *J Mater Chem A* 4(9):3253–3266
75. Schwoebel A, Hausbrand R, Jaegermann W (2015) Interface reactions between LiPON and lithium studied by in situ X-ray photoemission. *Solid State Ion* 273:51–54
76. Ma C, Cheng Y, Yin K, Luo J, Sharafi A, Sakamoto J et al (2016) Interfacial stability of Li metal–solid electrolyte elucidated via in situ electron microscopy. *Nano Lett* 16(11):7030–7036
77. Bachman JC, Muy S, Grimaud A, Chang HH, Pour N, Lux SF et al (2016) Inorganic solid-state electrolytes for lithium batteries: mechanisms and properties governing ion conduction. *Chem Rev* 116(1):140–162
78. Chen R, Qu W, Guo X, Li L, Wu F (2016) The pursuit of solid-state electrolytes for lithium batteries: from comprehensive insight to emerging horizons. *Mater Horiz* 3(6):487–516
79. Park C-W, Ryu H-S, Kim K-W, Ahn J-H, Lee J-Y, Ahn H-J (2007) Discharge properties of all-solid sodium–sulfur battery using poly (ethylene oxide) electrolyte. *J Power Sources* 165(1):450–454
80. Kummer JT, Weber N (1976) A sodium–sulfur secondary battery. SAE Technical Paper 670179
81. Kummer JT, Weber N (1968) Battery having a molten alkali metal anode and a molten sulfur cathode patent US3413150. 1968 Nov. 26
82. Fally P (1973) Some aspects of sodium–sulfur cell operation. *J Electrochem Soc.* 120(10):1292–1295
83. Whittingham MS, Huggins RA (1971) Measurement of sodium ion transport in beta alumina using reversible solid electrodes. *J Chem Phys* 54(1):414–416
84. NAS Energy Storage System (2017) Cited 2017 February 20. Available from:<https://ngk.co.jp>. Accessed 20 Feb 2017
85. Aurbach D, Zinigrad E, Cohen Y, Teller H (2002) A short review of failure mechanisms of lithium metal and lithiated graphite anodes in liquid electrolyte solutions. *Solid State Ion* 148:405–416
86. Kim H, Jeong G, Kim YU, Kim JH, Park CM, Sohn HJ (2013) Metallic anodes for next generation secondary batteries. *Chem Soc Rev* 42(23):9011–9034
87. Younesi R, Veith GM, Johansson P, Edström K, Vegge T (2015) Lithium salts for advanced lithium batteries: Li–metal, Li–O₂, and Li–S. *Energy Environ Sci* 8(7):1905–1922
88. Zhang W-J (2011) A review of the electrochemical performance of alloy anodes for lithium-ion batteries. *J Power Sources* 196(1):13–24

89. Brückner J, Thieme S, Böttger-Hiller F, Bauer I, Grossmann HT, Strubel P et al (2014) Carbon-based anodes for lithium sulfur full cells with high cycle stability. *Adv Func Mater* 24(9):1284–1289
90. Hassoun J, Kim J, Lee D-J, Jung H-G, Lee S-M, Sun Y-K et al (2012) A contribution to the progress of high energy batteries: a metal-free, lithium-ion, silicon–sulfur battery. *J Power Sources* 202:308–313
91. Yan Y, Yin Y-X, Xin S, Su J, Guo Y-G, Wan L-J (2013) High-safety lithium–sulfur battery with prelithiated Si/C anode and ionic liquid electrolyte. *Electrochim Acta* 91:58–61
92. Agostini M, Hassoun J, Liu J, Jeong M, Nara H, Momma T et al (2014) A lithium-ion sulfur battery based on a carbon-coated lithium–sulfide cathode and an electrodeposited silicon-based anode. *ACS Appl Mater Interfaces* 6(14):10924–10928
93. Agostini M, Hassoun J (2015) A lithium-ion sulfur battery using a polymer, polysulfide-added membrane. *Sci Rep.* 5:7591
94. Zhang X, Wang W, Wang A, Huang Y, Yuan K, Yu Z et al (2014) Improved cycle stability and high security of Li–B alloy anode for lithium–sulfur battery. *J Mater Chem A* 2(30):11660
95. Available from: <http://www.cytech.com/products-ips>. 2017. Cited 2017 March 19
96. Available from: http://www.st.com/content/st_com/en/products/power-management/battery-management-ics/enfilm-thin-film-batteries/ef700a39.html. 2017. Cited 2017 March 2017
97. Yu J, Hu YS, Pan F, Zhang Z, Wang Q, Li H et al (2017) A class of liquid anode for rechargeable batteries with ultralong cycle life. *Nat Commun* 8:14629
98. Zhao-Karger Z, Zhao X, Wang D, Diemant T, Behm RJ, Fichtner M (2015) Performance improvement of magnesium sulfur batteries with modified non-nucleophilic electrolytes. *Adv Energy Mater* 5(3):1401155
99. Cheek GT, O’Grady WE, El Abedin SZ, Moustafa EM, Endres F (2008) Studies on the electrodeposition of magnesium in ionic liquids. *J Electrochem Soc* 155(1):D91
100. Zhao Q, Hu Y, Zhang K, Chen J (2014) Potassium-sulfur batteries: a new member of room-temperature rechargeable metal-sulfur batteries. *Inorg Chem* 53(17):9000–9005
101. Lu X, Bowden ME, Sprenkle VL, Liu J (2015) A low cost, high energy density, and long cycle life potassium-sulfur battery for grid-scale energy storage. *Adv Mater* 27(39):5915–5922



Challenges and Prospect of Non-aqueous Non-alkali (NANA) Metal–Air Batteries

Danny Gelman^{1,2} · Boris Shvartsev² · Yair Ein-Eli^{1,2}

Received: 25 November 2015 / Accepted: 31 October 2016 / Published online: 22 November 2016
© Springer International Publishing Switzerland 2016

Abstract Non-aqueous non-alkali (NANA) metal–air battery technologies promise to provide electrochemical energy storage with the highest specific energy density. Metal–air battery technology is particularly advantageous being implemented in long-range electric vehicles. Up to now, almost all the efforts in the field are focused on Li–air cells, but other NANA metal–air battery technologies emerge. The major concern, which the research community should be dealing with, is the limited and rather poor rechargeability of these systems. The challenges we are covering in this review are related to the initial limited discharge capacities and cell performances. By comprehensively reviewing the studies conducted so far, we show that the implementation of advanced materials is a promising approach to increase metal–air performance and, particularly, metal surface activation as a prime achievement leading to respectful discharge currents. In this review, we address the most critical areas that need careful research attention in order to achieve progress in the understanding of the physical and electrochemical processes in non-aqueous electrolytes applied in beyond lithium and zinc air generation of metal–air battery systems.

Keywords Metal–air batteries · Non-aqueous · Magnesium–air · Aluminum–air · Silicon–air

D. Gelman and B. Shvartsev contributed equally to the present study.

Chapter 4 was originally published as Gelman, D., Shvartsev, B. & Ein-Eli, Y. Top Curr Chem (Z) (2016) 374: 82. DOI 10.1007/s41061-016-0080-9.

✉ Yair Ein-Eli
eineli@technion.ac.il

¹ The Nancy and Stephen Grand Technion Energy Program, Technion-Israeli Institute of Technology, 3200003 Haifa, Israel

² Department of Materials Science and Engineering, Technion-Israeli Institute of Technology, 3200003 Haifa, Israel

1 Introduction

Electrochemical power sources based on a metal anode immersed in an electrolyte capable of reacting with atmospheric oxygen have the highest energy density, as there is no need to store oxygen (the cathode active material) in the battery since it can be accessed from the ambient atmosphere. The current stage of research is focused on newly emerging chemistries, as one can find in (Li, Si, Al, Mg)-air cells. The main reason for the upsurge in attention is mainly attributed to the outstanding energetic capacities of these anode materials (3842 mAh/g for Li, 3816 mAh/g for Si, 2965 mAh/g for Al, 2204 mAh/g for Mg vs. only 815 mAh/g for Zn [1]). In past times, metal–oxygen power systems were all aqueous systems; the most employed system was Zn–air cell [1, 2]. This system ($\text{Zn} + 1/2\text{O}_2 \rightarrow \text{ZnO}$) has been investigated for many years, thanks to its relatively high specific capacity, as compared with cells based on common Zn battery chemistries [3, 4]; the kinetics of the cell reaction is limited by the cathode reaction [3]. Currently, for this specific metal–air system, the focus is on a possible rechargeability and cycling. For other newly researched batteries, such as lithium and sodium–air, a repeated discharge and charge processes for many cycles (essential for any use in a secondary cell) is still quite challenging [5, 6].

While the literature on Li–air [7–15] and Zn–air [2, 16–21] battery systems is quite extensive, with some excellent reviews on the subject, we will be focusing this review on the post Li and Zn-batteries era, and to be more specific, on non-aqueous non-alkali (NANA) metal–air batteries based on Mg, Al, and Si. Theoretical Nernst potential values of [Mg, Al and Si]/(metal ion) couples are fairly negative [22], and decomposition of aqueous electrolyte and a considerably high rate of anode corrosion [1] practically prohibit the use of aqueous electrolytes in the [Mg, Al and Si]-air systems. Thus, it is natural that the systems, which are the focus of the current research efforts, are metal–air systems utilizing non-aqueous electrolytes. We are referring to these systems as NANA metal–air batteries-non-aqueous non-alkali metal–air batteries. As stated earlier, currently, the major focus of the research is on alkali metal–air battery technology (Li [7–15] and Na–air systems [13, 23–26]), and the aim of the present work is to introduce to the reader other systems that may outperform the alkali metal–air battery. NANA metal–air systems are also of great interest, particularly because of the associated superior volumetric energy density and the substantially lower cost of Si, Al, and Mg if compared with the cost of Li or even Na metals.

The key factors for a proper utilization of the metals (Mg, Al, and Si) in NANA batteries, as anodes in power source devices, relates to the metal surface interaction with the electrolyte. The interaction properties, such as surface activity/passivity by dissolution of native oxide layer, surface modification, and the nature of the formed layer following the dissolution, are controlling suitability of the metal to serve as a proper fuel in the battery. For most of NANA metal–air batteries technologies being though off, the metals passivation layer on the surface is the main “killing factor”, preventing any possible interaction or processes at the metal/non-aqueous electrolyte interphase. Therefore, any further development of NANA metal–air

batteries calls for in-depth understanding of the behavior of such metals in non-aqueous electrolytes, the surface evolution and its interactions with the chosen electrolyte.

2 Non-aqueous Non-alkali (NANA) Metal–Air Batteries Research Objectives

The basic research objectives and initial challenges of the NANA-based batteries will be presented in this part. The retro-perspective view will allow the reader to understand concerns and challenges the community addressed in order to achieve the scientific advance in the NANA metal–air batteries up to today. In the case of the Mg–air battery system, the initiation of this research field was stimulated by Aurbach et al. [27], first reporting on a reversible Mg ion intercalation in Chevrel phase cathode structure in a non-aqueous Grignard-based medium. Following this report, a number of studies were conducted applying similar electrolytes in Mg-ion battery configuration [28, 29], which concluded the problematic stability of this type of electrolytes. In order to improve the stability, different and more durable electrolytic media were applied: room temperature ionic liquids (RTILs) and pseudo-Grignard type electrolytes. The initial research was focused on establishing the electrochemistry of Mg in these electrolytes, followed by attempts to apply the established results in batteries. The sluggish discharge abilities and reversibility (stripping and deposition) of magnesium anodes that is well known in commercial RTILs [30, 31] brought the researchers to the conclusion that an addition of Grignard organic compounds into the solution would improve the cell's performance. A similar approach was also applied and adopted in Mg–air cells, as it was established by Luder et al. [32, 33]. Another approach involves “tunable” electrolytes to fit the requirement of developing successful Mg–air batteries [6]. This approach is based mostly on synthesizing and investigating novel RTILs.

As it was established from the initial research in Al–air batteries, as far back as the 1960s, the utilization of aqueous alkaline-based electrolytes is hampered due to intrinsic issues, such as the tremendous corrosion and electrolyte degradation [34–37]. Additionally, a possible utilization of non-aqueous organic electrolytes, as media for Al-power sources, could not provide a suitable replacement. This fact is attributed to the stable oxide passivation of Al in organic solvents [38, 39]. Some attempts of surface activation in organic electrolytes were performed and reported [38–40], nevertheless without any real applications in power source devices. A different approach was conducted with the application of chloride-based ionic liquids, such as the EMImCl:AlCl₃ group. The ratio between the salts provides differences in the electrochemical behavior of Al metal. In this specific type of electrolytes, Al-ion batteries were initially reported [41–46] and a single report on Al–air power sources [47]. Although chloride-based ionic liquids media showed the ability of Al electrochemical dissolution and deposition, the recorded current densities were quite low [47, 48]. This fact, in addition to the problematic synthetic procedure and the high reactivity towards water of this specific class of electrolytes, hindered the use of such electrolyte compositions. A different chloro-free RTIL

electrolyte was introduced by Gelman and Shvartsev [49], utilizing EMIm(HF)_{2,3}F in a high-power and high-capacity Al–air battery.

The initial motivation for developing Si–air batteries was that such a battery system could be, in principle, an integrated power source in microelectronic applications, for instance, a lab on a chip. A small footprint and more compact battery design should be thought in order to enable a direct attachment to the electronic circuit. For such demanding applications, an Si–air battery may serve as an excellent solution, based on the fact that un-doped Si is practically inert to any electrochemical reaction [50], where the already-produced wafers are mostly doped and could be heavily doped, allowing to treat Si as a metallic substance. Additionally, Si suffered from severe parasitic corrosion reaction in conventional aqueous alkaline solutions [51, 52] and thus different types of electrolytes were applied; in this case, RTIL-based EMIm(HF)_{2,3}F. The initial studies on Si electrochemical behavior in this specific media showed its ability to electrochemically dissolve different Si types without the need of illumination [53, 54], allowing a utilization of wafers as anode materials. Based on this specific work, a research objective and the challenge of developing a full Si–air battery was addressed by Ein-Eli [55–60].

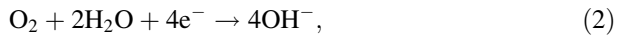
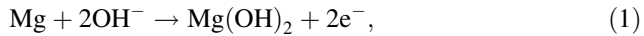
In the next sections, we briefly cover the technologies that are in the embryonic research stages, and that their commercial implementation may possibly take 20–30 years; among these technologies, one can include the Mg–air, Al–air, and Si–air batteries (2, 3, and 4 electrons transfer processes, respectively).

3 Nonaqueous Mg–Air Batteries

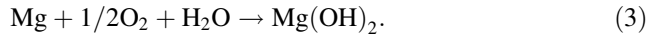
3.1 Introduction

Mg anode material has received increasing attention in battery-related applications in the recent decade [6]. This interest was stimulated for the following reasons [6, 61]: (1) availability of vast quantities in nature and well-established extraction methods; (2) low market cost; (3) Mg byproducts are mostly environmentally compatible; (4) a relatively low theoretical electrochemical equivalent (0.45 g/A h), high energy density (6450 W h/kg), and capacity (2200 mA h/g) [62, 63]; (5) a negative reduction potential (−2.37 V vs. SHE), and when taking into account the oxygen reduction potential in aqueous media, the theoretical cell voltage can be as high as 2.77 V.

Possible application of Mg batteries may be similar to Li-ion intercalation systems, where Mg ions “replace” the Li ions. The issues regarding the most appropriate and possible cathodes, as well as anodes for such systems, were already addressed in a variety of reports [6, 20, 28, 46, 64]. Magnesium, serving as an anode material in Mg–air batteries, is quite attractive for the automotive industry, where high capacity of the battery with a significantly lower cost of the system could promote a wider adoption of electric vehicles (EVs) [6]; indeed, past research works attempted to construct Mg–air batteries in aqueous media [20]. The main reactions in an aqueous Mg–air battery system were found to be [20]:



and, the overall reaction in aqueous media is:



While considering the application of Mg as an anode, similar challenges need to be overcome, as already presented for lithium and sodium anodes. Magnesium, as a reactive metal, is unstable in water, oxygen, and many of the organic compounds applied in battery technology. As a part of the corrosion reaction, a porous product layer on the Mg surface is constructed, and thus a further degradation of the metal, due to corrosion process, is expected. Moreover, the negative reduction potential of Mg, at -2.37 V vs. SHE [6], would allow a massive reduction of most electrolytes. Corrosion and self-discharge processes are common issues in systems utilizing reactive metals, interacting with the aqueous solutions. Magnesium hydroxide is formed with accompanied heat generation, caused by excessive cathode polarization and high self-discharge rates. This leads to increased vapor pressure, water loss, and dangerous thermal runaway conditions. Moreover, there is a loss in the cell stability and controllable discharge characteristics desired for practical use [20]. In alkaline electrolytes, Mg-hydroxide sinks in the cell as sludge and therefore the cell must be large enough to accommodate it [20]. At the beginning of the discharge process, a stable passivation surface layer is formed on the Mg surface and inhibits Mg corrosion, but gradually this film breaks down, causing instability in the working voltage [20].

Additional challenges are related to the Mg-based products at the air-cathode: based on Sawyer study [65], the divalent Mg^{2+} cation undergoes four-electron reaction with oxygen in organic solvents; meaning, during discharge, Mg-oxide (MgO) may be formed at the air electrode in non-aqueous Mg–O₂ batteries. Due to thermodynamically and electrochemical stability of the formed MgO, it cannot be decomposed by charging at ambient temperatures [66, 67]. Therefore, it is well accepted that a non-aqueous Mg–O₂ battery may only be regarded as a primary one at room temperature. For a secondary system (rechargeable cell), it is mandatory and required to have a catalyst for MgO decomposition.

3.2 Liquid-Based Cells

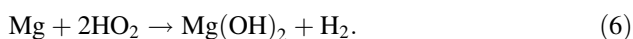
As a result of the limitations and challenges associated with the application of Mg anode in aqueous systems (as described above), further research in Mg high-energy-density batteries was focused on non-aqueous electrolyte systems [68].

3.2.1 Organic-Based Electrolytes

One of the most important aspects of the system is the evolving Mg anodes surface science. In particular, Mg dissolution/deposition processes and the interface

between the Mg surface and the electrolyte is very important for understanding the operation of rechargeable Mg cells. This subject is especially vital to Mg–air batteries, as the cathode is not based on Mg intercalation compounds, but rather an air–cathode, which drastically influencing the electrolyte composition and the Mg anode surface.

3.2.1.1 Organic Solutions with Regular Mg Salts One of the most prominent features in the electrochemistry of Mg is the presence of a passivation layer on the surface of the metal. This interphase between the bare Mg and the electrolytes is an ongoing subject for research. Initial efforts to address this subject were proposed by Peled et al. [69] in SOCl_2 electrolytes (inspired by a research in Li- SOCl_2 cells); it was suggested that a passivation layer with a low-Mg ion conductivity was formed on the Mg surfaces once exposed to or being in contact with the solution. Later efforts focused on the interphase and electrochemistry of Mg in standard organic electrolytes based on tetrahydrofuran (THF), propylene carbonate (PC), and acetonitrile (ACN) [70]. It was demonstrated, via Raman techniques, that even in completely inert conditions, traces of O_2 , CO_2 , and water react with the Mg surface to form a passivation layer, as illustrated in the following reaction schemes:



Additionally, when a fresh Mg surface was exposed to the electrolyte itself by mechanical means, the solvent molecules and anion salts were immediately reduced at the surface, forming insoluble and non-conducting films composed of organic and inorganic Mg-based salts such as $\text{Mg}(\text{ROCO}_2)_2$, Mg–Cl–O species, alkoxy species, and Mg_xBF_y type compounds [70]. However, while conducting cyclic voltammograms (CVs), it was found that this passivation layer is electrically and ionically non-conducting, in contrast to Li interphases, which have the ability to conduct Li ions [71]. Figure 1 presents the high anodic overpotentials of 0.7–0.9 V needed to break the passivation layer in order to achieve an electrochemical dissolution of Mg in THF and PC electrolytes.

The hysteresis observed in the anodic regions serves as an indication of surface transformation: the surface passivation breaks down, enabling much higher currents when potentials were swept back from an anodic vertex. However, upon returning to the open circuit potential (OCP) conditions, these passivation films were repaired and re-constructed. Moreover, due to the presence of non-conducting passivation films, deposition of Mg is practically impossible [70]. Because of these phenomena, it was concluded that organic electrolytes containing Mg salts would be less suitable for battery systems, especially a rechargeable one, including Mg–air batteries, where the charging process involves Mg deposition.

However, successful attempts were made to reach surface conditions where Mg dissolution and deposition could be accomplished at low over-potentials [70, 72].

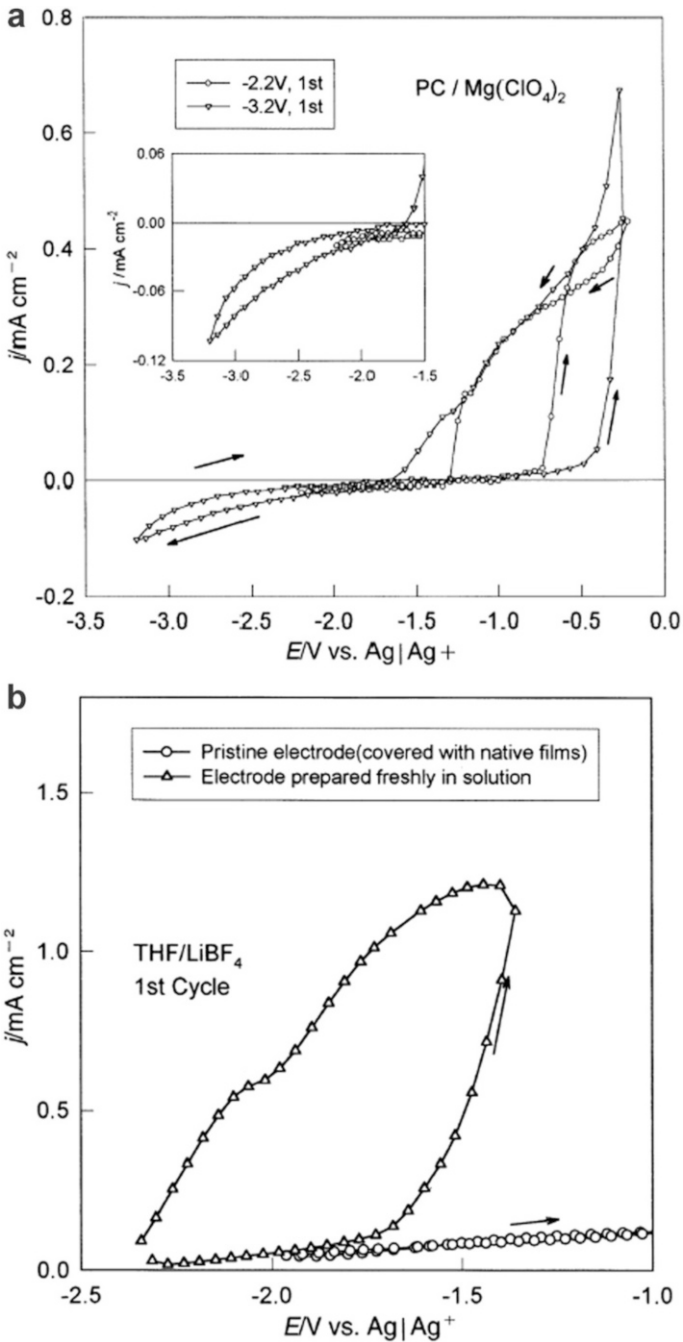


Fig. 1 Typical voltammetric behavior of Mg electrodes in PC and THF solutions. CV of Mg anode in **a** PC + 1 M $\text{Mg}(\text{ClO}_4)_2$ solutions (electrodes freshly prepared in solutions). First cycle CVs obtained at two different lower potential limits, -2.2 V and -3.3 vs. Ag/Ag^+ . **b** in THF/ LiBF_4 [70]. Reprinted from ref. [70]. Copyright 1999, with permission from Elsevier

When alkyl halides, such as bromoethane (EtBr) were added to the electrolyte, Mg dissolution and deposition were achieved with hardly any overvoltage, with anodic currents increasing with each CV cycle, as presented in Fig. 2. It was postulated that such species lead to a breakdown of surface films through a complicated process of EtBr reduction and Mg^{2+} migration, eventually forming Grignard salts, such as ethylmagnesium bromide (EtMgBr) in the electrolyte. In fact, the Mg surface was demonstrating so-called “film-free conditions” [70].

3.2.1.2 Ether Solutions with Organo-Magnesium Compounds An alternative approach in Mg battery electrolyte design is the application of THF with an addition of Grignard reagents of the RMgX type (R = buthyl, ethyl. X = Cl, Br). It was demonstrated that with the use of such reagents, the dissolution and deposition of Mg occurs with a rather small over-voltage, similar to the electrochemical behavior observed in EtBr, leading to Mg surface film-free conditions [70].

In order to investigate the nature and reaction mechanisms at the Mg surface, a number of analytical techniques were utilized. It was observed via EQCM experiments that during the first stages of Mg deposition process on a Mg anode, calculated values of mass per mol of electrons [g/mol (\bar{e})] were above the anticipated value of 12 (i.e., the mass equivalent of Mg) [70]. Thus, it was suggested that the deposition of Mg occurs in a complex process involving the adsorption of Mg species. It is known that in ether solutions containing dissolved RMgX (e.g., EtMgBr in THF) [72] the following equilibria exist:

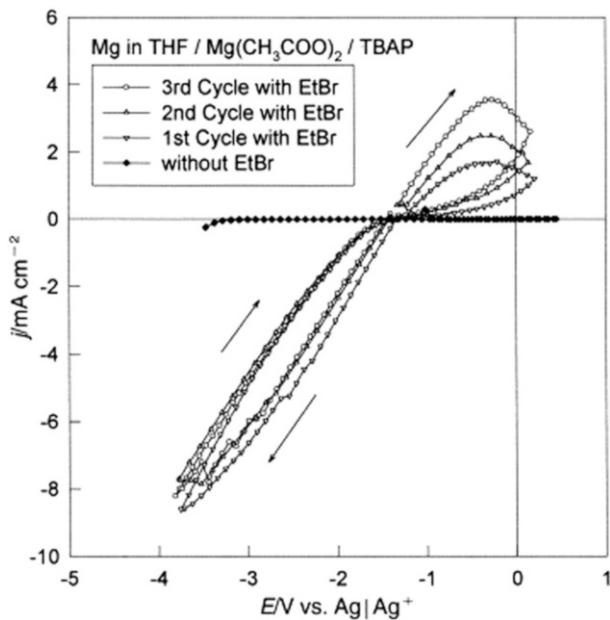
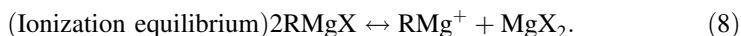
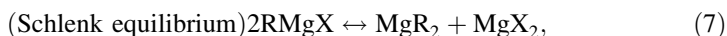
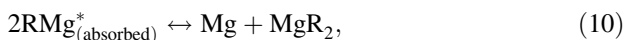


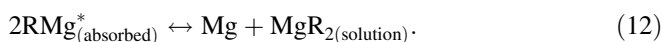
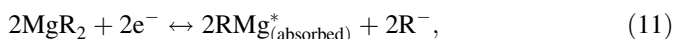
Fig. 2 CVs of Mg electrodes in THF, 0.1 M $(\text{CH}_3\text{CO}_2)_2\text{Mg}$, 1 M Bu_4NClO_4 in the absence and in the presence of EtBr, scan rate: 20 mV s^{-1} [70]. Reprinted from ref. [70]. Copyright 1999, with permission from Elsevier



Consequently, it was suggested by Aurbach [72] that the following complex deposition process occurs:



or,



Two phenomena regarding the surface of the Mg are observed when conducting an electrochemical impedance spectroscopy (EIS) in similar systems (BuMgCl/TBAPF₆ 0.5 M/THF, presented in Fig. 3): once a freshly deposited Mg surface is initially left to rest in the solution, the surface impedance increases over time, as deduced from the increase in the semi-circle radius [73]. Additionally, the lower the concentration of the Grignard salt, the lower the impedance on the surface (at equivalent resting times) that was recorded. This phenomenon is consistent with EQCM data and the suggested mechanism involving adsorption of Mg species on the surface. It was postulated that the reason for the time-dependent increase in the measured impedance was related to a build-up of an adsorption layer (with time) that is similar in its nature to the surface adsorption occurring during Mg deposition. This surface layer behavior was concluded to be unstable via subsequent CVs being conducted (applied after Mg deposition and in different rest periods, as described in Fig. 3). The layers disintegrated upon low anodic overpotentials during the CVs, in a similar pattern seen in previous studies [70]. Therefore, these layers were effectively conducting, despite the high impedance measured by EIS.

The instability and low conductivity of the electrolytes presented until now has led to the development of pseudo-Grignard-type solutions composed of charged acidic and basic components in an ethereal environment [6]. New organo-magnesium complexes of the Mg(AlCl_{3-n}R_{n'})₂ (R = butyl, ethyl etc.) type (abbreviated DCC) were synthesized and used instead of dissolved Grignard salts due to their higher anodic stability [63], while maintaining dissolution/deposition reversibility, rendering them more suitable for withstanding oxidation during charging processes in rechargeable Mg systems.

Other electrolyte modifications and upgrades include the addition of chloride salts (e.g., LiCl, tetrabutyl ammonium chloride) enabling a conductivity increase in THF-based DCC solutions [74], as shown in Fig. 4. Additional modifications include the use of PhMgCl–AlCl₃/THF instead of DCC, leading to an increase of electrolyte anodic stability [75].

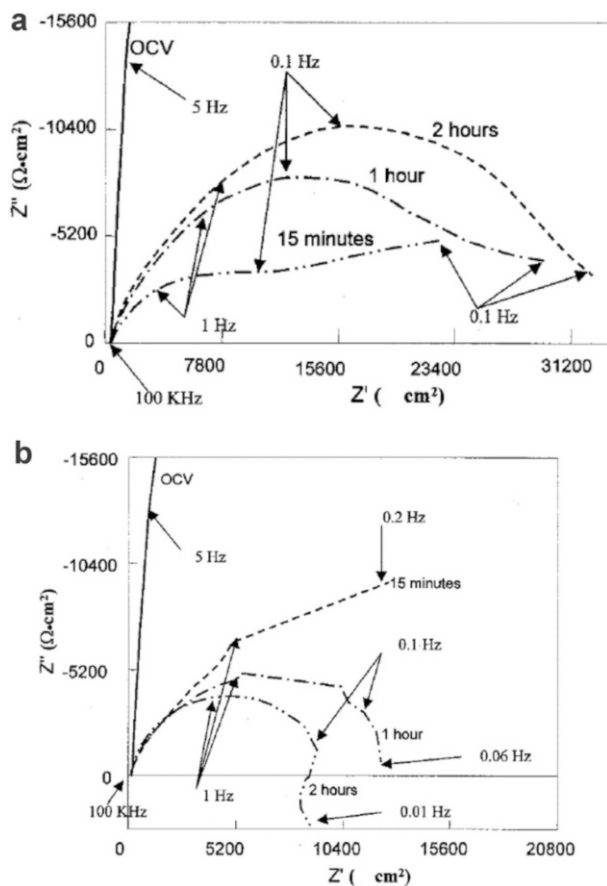


Fig. 3 Impedance spectra obtained from Au/QC (quartz crystal) electrodes after Mg deposition processes in EQCM experiments (5 min, 0.5 V vs. Mg R.E., 20–40 (g/cm²) in BuMgCl/TBAPF₆ 0.5 M/THF solutions during storage at OCV (0 V vs. Mg R.E.). **a** 1 M BuMgCl and **b** 0.1 M BuMgCl [72]. Reproduced with permission from the Electrochemical Society

3.2.1.3 Iodine-based electrolytes A completely different approach was adopted by Shiga et al. [76] introducing iodine–dimethylsulfoxide (I₂–DMSO) complex in a catalytic cycle for secondary Mg–O₂ batteries. The proposed mechanism suggests a charging of the MgO by combining decomposition under the influence of the I₂–DMSO complex with the 3I[−]/I₃[−] redox couple, as shown in Fig. 5. In the first step, the Mg iodide (MgI₂) formed during discharging at the cathode is electrochemically reduced to iodine, which interacts with DMSO to form a molecular complex. This I₂–DMSO complex reacts with MgO, formed by discharging at the cathode, and finally, this MgO precipitate separates into Mg ions (as MgI₂) and oxygen. The redox potential of 3I[−]/I₃[−] is near 2.0 V vs. Mg²⁺/Mg. These steps are cycled continuously until MgO is completely removed from the cathode at about 2.0 V. Oxygen would have been evolved if the process occurred according to Fig. 5 and iodine would react with MgO in a 1:1 molar ratio. The battery showed two steps

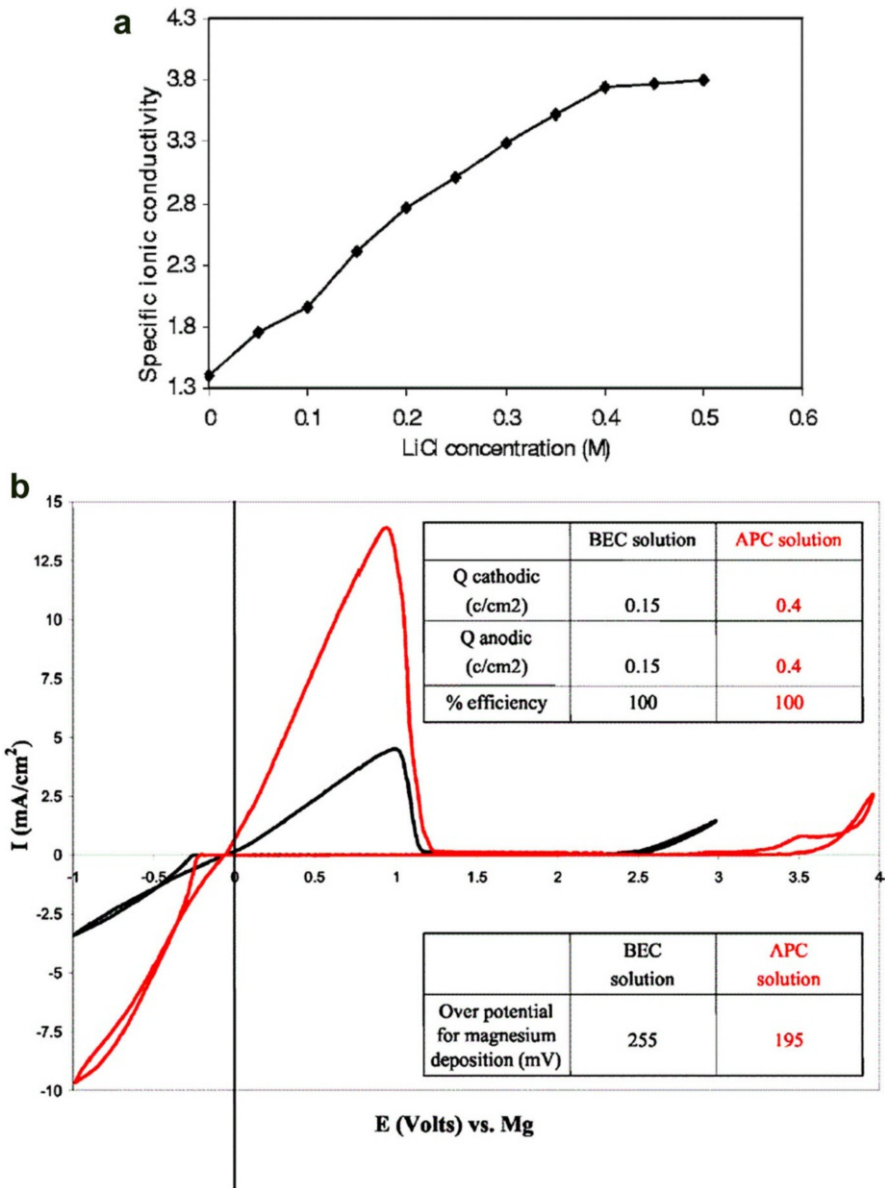


Fig. 4 **a** Conductivity (typical specific conductivity) vs. LiCl concentration curves for THF/DCC 0.25 M solutions [74]. **b** CV of 0.4 M PhMgCl–AlCl₃/THF solution compared to 0.25 M DCC/THF [75]. Reproduced with permission from the Electrochemical Society

associated with two discharge processes (during the first discharge), as can be seen in Fig. 5b. One should notice that Mg–O₂ battery discharge–charge curves were obtained at 60 °C [76]. The first stage, near the potential of 1.5 V, reflects the

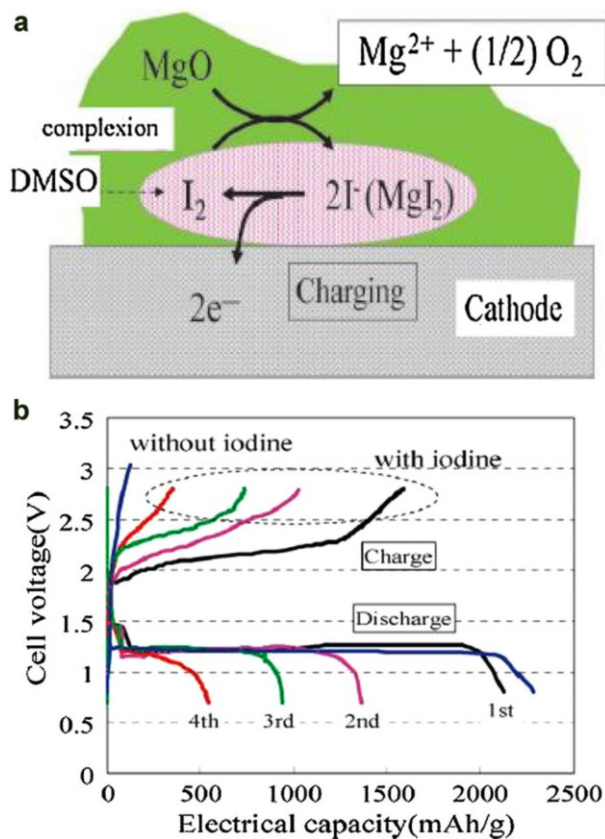


Fig. 5 **a** A proposed catalytic mechanism for the charging process. **b** Discharge–charge curves of the non-aqueous Mg–O₂ battery with iodine at 60 °C. The black, pink, green, and red lines correspond to the first, second, third, and fourth cycles, respectively. The blue line represents a discharging–charging profile in the absence of iodine [76]. Reprinted with permission from ref. [76]. Copyright 2013 Royal Society of Chemistry

reaction of Mg²⁺ with iodine (i.e., it acted as Mg–iodine battery), and represents the reduction of I₃ [76]:



The discharge capacity of the first stage (Mg–I₂) was 100 mA h g⁻¹, which was determined by the amount of dissolved iodine in the electrolyte. The second stage at about 1.25 V revealed the discharging of the Mg–O₂ couple [76]. A total discharge capacity of 2131 mA h g⁻¹ (cathode) was achieved (black line in Fig. 5b) [76]. The discharge voltage of the Mg–iodine and Mg–air couples was lower than the theoretical values calculated from the potentials of the iodine redox couple (+0.4 V vs. NHE) or four-electron reduction of oxygen (0.2 V vs. NHE) combined with the Mg²⁺/Mg (–2.37 V vs. NHE) potential. This voltage drop was attributed to the formation of a solid electrolyte interphase (SEI) on the Mg anode. The total charge

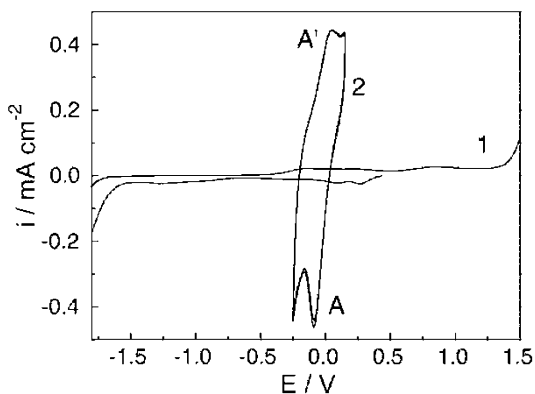
capacity was 1590 mA h g^{-1} , and the reversibility (against discharging) was calculated at 74.6%. The reversibility dropped drastically with an additional cycle [76]. In contrast, an Mg–O₂ battery without iodine had a large discharge capacity of 2280 mA h g^{-1} , but showed no charging behavior (blue line in Fig. 5b) [76]. The use of iodine-based electrolytes in the context of Mg–air (and even Mg–oxygen batteries) is a very interesting concept and as this technology approach is in its early stages, it is still premature to state its commercial applications.

3.2.2 Room-Temperature Ionic Liquids (RTILs)-Based Electrolytes

As a possible advance and natural continuity of the research on Mg anodes in power-source applications, RTILs were addressed as possible electrolytes in Mg-based batteries. This approach stemmed from the intent to utilize their advantages, listed earlier. During the last decade, the first attempts to research the electrochemistry of Mg in RTILs focused on dissolving Mg salts in this media and reporting the chemical and physical parameters of the established electrolytes. In contrast to the previously mentioned and discussed organic solutions, RTILs in general are reactive with Mg metal and in most cases a layer is formed at the Mg surface [30]. The layers are impermeable to Mg ions, in sharp contrast to Li SEI layers, meaning, Mg surfaces tend to be passivated upon any interaction with RTILs [30]. This passivating ability, occurring even under a potential bias, motivated many studies investigating RTILs as protective additives against Mg alloy corrosion [31]. Additionally, a number of electrochemical studies already suggested that Mg could be deposited and stripped from certain RTILs [77–81]. An example is the case of 1-butyl-3-methyl imidazolium tetrafluoroborate (abbreviated BMImBF₄) RTIL mixed with Mg(CF₃SO₃)₂ (Mg triflate) at relatively high concentrations (up to 1 M) [79]. In this electrolyte, reversible dissolution and deposition of Mg on a silver substrate was achieved, as shown in Fig. 6 (curve 2).

The same type of studies were repeated applying BMImBF₄ mixture with *N*-methyl-*N*-propylpiperidinium TFSI (PP₁₃-TFSI) [81], resulting with a similar evidence of deposition/dissolution. However, contrasting evidence to the dissolution/deposition cycles were also reported. In several studies [6, 30], various RTILs

Fig. 6 Cyclic voltammograms of BMImBF₄ without (curve 1) and with 1 M Mg(CF₃SO₃)₂ (curve 2) on silver plate anode at 50 mV/s (counter electrode: Mg, reference electrode: Pt) [79]. Reprinted from ref. [79]. Copyright 2005, with permission from Elsevier



systems were studied and the relevant Mg salts have been investigated. It should be noted that none of these systems were able to obtain reversible Mg deposition and dissolution, even in the systems with a significant Mg salt solubility. Again, this behavior was mainly due to Mg electrode surface passivation.

The ability to deposit and dissolve Mg from a wide series of RTIL-based electrolytes (identical and similar to those used in Figure), including three imidazolium-based RTILs with the different dissolved salts [MgCl_2 , $\text{Mg}(\text{CF}_3\text{SO}_3)_2$, $\text{Mg}(\text{ClO}_4)_2$, Bu_2Mg] was found to be negligible [30]. CVs studies, presented in Fig. 7, utilizing BMImBF_4 with 0.5 M $\text{Mg}(\text{CF}_3\text{SO}_3)_2$ as electrolyte, found that comparably only small Red/Ox current densities (related to Mg^{2+}/Mg) were obtained. Moreover, with each additional cycle, the cathodic peak current decreases. This was attributed to the growth of the passivation layer on the Mg surface, resulting from the reaction of Mg with the solution anions or water traces [30].

3.2.2.1 Grignard Reagents In an alternative approach, Mg ions can be added to ionic liquids not as a salt, but as Grignard reagent dissolved in ethers (e.g., THF). This approach is intuitive due to the ability to reversibly dissolve and deposit Mg from Grignard reagents in ethers, as discussed earlier. This approach is demonstrated in Fig. 8, where Grignard reagents were dissolved in THF and RTILs [82, 83] forming a “layer-free system” on the Mg surface. There is effectively no overvoltage for Mg dissolution and a small overvoltage for Mg deposition. In fact, the RTILs act as ionic strengtheners in the organic solvents, even when the RTIL is the main solvent.

RTILs with dissolved Grignard agents should not be good proton donors, because Grignard reagents are strong bases, and could react in an acid–base reaction. To that extent, RTILs based on pyrrolidinium cations are suitable for this purpose. In order for imidazolium cations to be suitable, there must be a substitution of an alkyl group instead of the hydrogen between the two nitrogen atoms in the cation [83]. Yoshimoto et al. [84] reported that the addition of *N,N*-diethyl-*N*-methyl-*N*-(2-

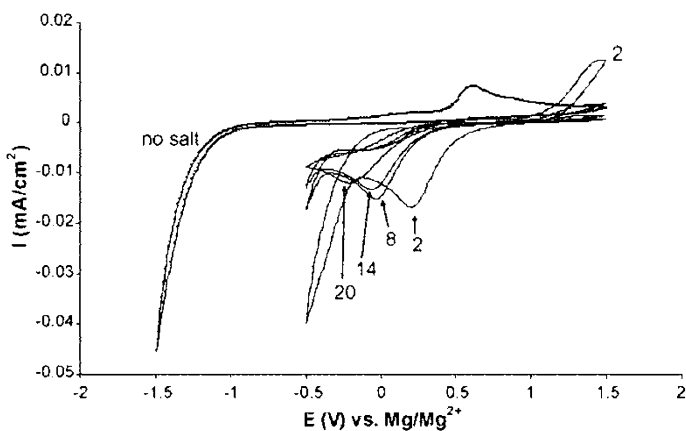


Fig. 7 Typical cyclic voltammograms measured with BMImBF_4 IL solutions and Pt working electrode at 50 mV/s. The CV related to the pure system (marked) and to solutions containing 0.5 M $\text{Mg}(\text{CF}_3\text{SO}_3)_2$ are presented, as indicated [30]. Reprinted from ref. [30]. Copyright 2007, with permission from Elsevier

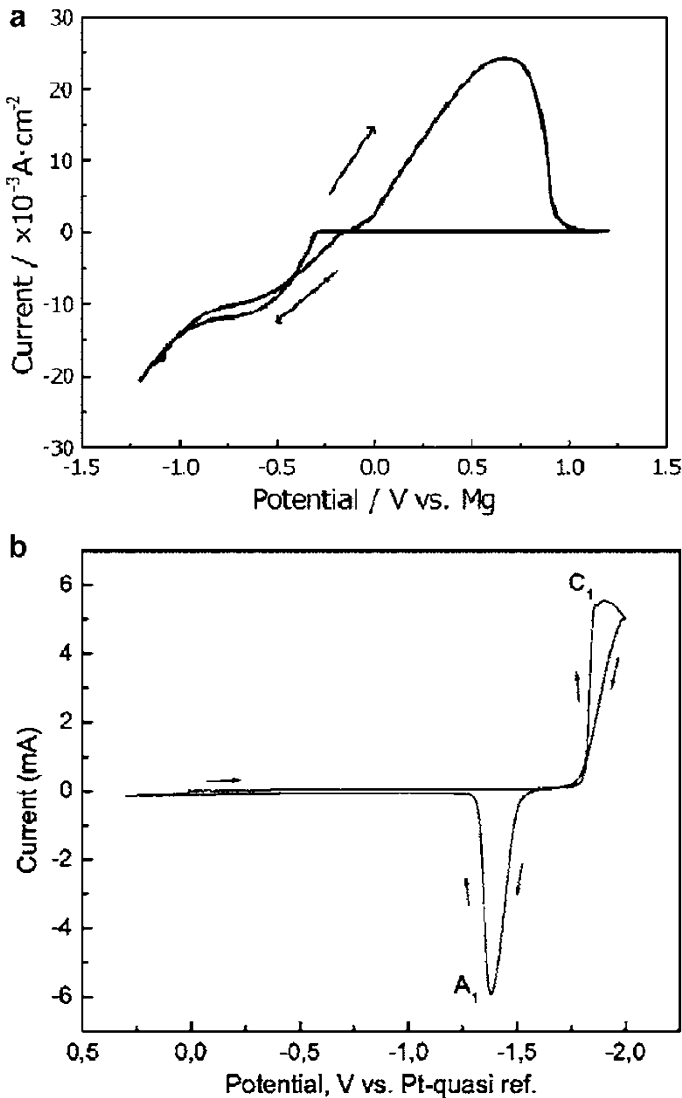


Fig. 8 **a** CV of a Ni substrate in the mixed electrolyte consisting of 1-ethyl 2,3, dimethyl imidazolium TFSI/MeMgBr/THF (equimolar amount of MeMgBr and IL salt) [83]. **b** CV with Pt substrate and 1:2 vol% mixture of Grignard reagent (2.0 M phenylmagnesium chloride in THF) and 1-butyl-1-methylpyrrolidinium TFSI ionic liquid at 100 °C. Scan rate: 10 mV/s [82]. Reprinted from ref. [83]. Copyright 2010, with permission from Elsevier and reproduced with permission from the Electrochemical Society

methoxyethyl)ammonium NTf₂ to ethereal Grignard solutions (EtMgBr–THF) showed improvement of cyclability, less electrolyte volatility, and a considerable coulombic efficiency of 93%. Kakibe et al. [83] achieved similar success utilizing bis(fluorosulfonyl)imide [FSI] anion and the same cation in a Grignard solution of MeMgBr–THF. The work showed that FSI anion was effective in improving the

cycling efficiency to above 90% in combination with the NTf_2 anion previously studied. Similar results were published by Yoshimoto et al. [85] where the effect of the alkyl chain on the Grignard molecule was addressed. As Kakibe et al. [83] reports, it was concluded that MeMgBr-THF with methyl-*N*-(2-methoxyethyl)ammonium NTf_2 produces a conductive solution that can support efficient cycling of Mg metal.

Luder et al. reported [32, 33] on the ability to electrochemically synthesize EtMgBr in ionic-liquid-based nonaqueous media. Utilization of high-boiling ether TEGDME could be used instead of the low-boiling THF that was demonstrated, without any influence on the reaction products. Mg surface electropolishing was observed visually and by SEM and AFM. This suggests a process involving Mg cation transport through a compact film composed of oxidized Mg and reduced solvent species. The described processes and phenomena could be used with numerous different reagents and parameters in a myriad of applications for the benefit of research on one hand, but also for the pharmaceutical and chemical industries on the other hand. Possible applications include industrial bulk Grignard synthesis in a controlled flowing framework, electrolyte synthesis for Mg batteries (especially Mg–air—had been demonstrated in this study) before and during discharge, and Mg electropolishing for surface finishing or the preparation of smooth substrates [32, 33].

3.2.2.2 Phosphonium Chloride Ionic Liquid Another type of RTILs was used by Khoo et al. [86], who studied Mg dissolution in $[\text{P}_{6,6,6,14}]\text{Cl}$, applying small amounts of H_2O as an additive, as part of a primary Mg–air cell discharge experiment. It was established that although H_2O may react with Mg, as expected from the active nature of the metal surface, it is a necessary ingredient for this RTIL electrolyte system. Khoo et al. [87] also studied the influence of H_2O presence in the RTIL. It was established that water presence combined with Mg^{2+} cation, originated from the anode discharge, provide the conditions for gel-like layer formation on the metal surface. The layer was found to be Mg cation conductive and stable for side reactions related to the cathodic processes in the air electrode, such as hydroxides formation. The gel-layer, white in color, was reported (based on elemental analysis and spectroscopic studies) to have $[\text{P}_{6,6,6,14}]\text{Cl}\cdot 2(\text{MgCl}_2)\cdot 37\text{H}_2\text{O}$ stoichiometry. Moreover, ex situ preparation of the same gel and then utilization of such in a battery cell as electrolyte, allowed dissolution reaction of Mg at 0.05 mA cm^{-2} for over 48 h (titanium mesh was used as the air electrode) [87]. In this research stage, the prepared gel electrolyte shows the ability to be utilized in primary Mg–air batteries. Nevertheless, the extended stability of Mg/electrolyte interface and the produced layer conductivity to Mg^{2+} cations may serve as a starting point for research on secondary Mg–air cells.

3.3 Polymer Electrolytes

Magnesium- O_2 cells (100% oxygen in contrast to $\sim 20\%$ oxygen in air) have been constructed with solid-state Mg ion conducting polymer electrolytes [88] soaked with ethylene-carbonate/propylene-carbonate with a dissolved $\text{Mg}(\text{ClO}_4)_2$ salt. The proposed reaction for a nonaqueous cell in dry conditions is:



Capacities in the range of 800–1400 A h g⁻¹ (charge per weight of active carbon in cathode) have been reached at various temperatures and water contents. In addition to the fact that 100% of O₂ was used instead of air, working voltages are quite low (<1.1 V) with inapplicable current densities of 0.075 mA cm⁻². Higher current densities in organic electrolytes with Mg salts are difficult to achieve due to their low conductivity, especially when soaked in solid polymer electrolytes [68, 88].

A different approach to polymer batteries was addressed by applying RTILs. Among the different types of ionic liquids, as already described above, an additional type is the one based on choline. These liquids are considered to be of low toxicity and may be utilized in a variety of biomedical applications [89–91]. The reason for this is related mostly to the fact that choline (more correctly cholinium) is a naturally occurring cation that can work as a cell-signaling agent [92]. Choline-based salts were studied recently in IL–gel systems, as a media for cancer therapy delivery [93]. Choline nitrate, [Ch][NO₃], was chosen in Jia et al.'s [93] work due to the low viscosity and high conductivity of this specific ionic liquid.

In this study [93], an integrated solid-state battery was demonstrated using a compact bio-battery system with the use of this thin-film gel electrolyte-based chitosan–choline nitrate, as shown in Fig. 9a. Bio-resorbable Mg alloy and biocompatible polypyrrole–*para*(toluene sulfonic acid) served as anode and cathode, respectively. The gel electrolyte was shown to be mechanically robust and provided a high ionic conductivity (Fig. 9b). An open-circuit voltage of 1.80 V and an output power of 3.9 W L⁻¹ was recorded [93]. This performance could be used to drive some low-power intermodulation distortion systems (IMDs) such as cardiac pacemakers or biomonitoring.

3.4 All Solid-State Cells

Inoishi et al. presented a concept of Mg–air solid oxide cells based on Ca-stabilized ZrO₂ as electrolyte, in a so-called “oxygen shuttle”-type battery [94]. The cell presented an open-circuit potential of 1.81 V with a discharge capacity of 1154 mA h g_{Mg}⁻¹ (52% of Mg theoretical capacity) [94]. In the same study, the researchers attributed the low-usage efficiency of Mg to the parasitic reaction of the Mg metal with the Al₂O₃ vessel; nevertheless, they assigned the discharge capacity of the full cell to magnesium oxidation. The measured transport number of ZrO₂-based oxide ion conductors was nearly unity over wide O₂ partial pressures. From the lower potential of Mg/MgO, in comparison to that of H₂/H₂O, oxygen concentration cell is achieved by a direct oxidation of Mg. Thus, oxygen simply permeates through the electrolyte [94]. The advantages of using oxide ion-conducting electrolyte will be described in detail in the silicon–air chapter. Moreover, when compared to the counter-diffusion of H₂ and H₂O, the diffusion of O₂ is much faster, allowing significantly greater power abilities than the H₂–air

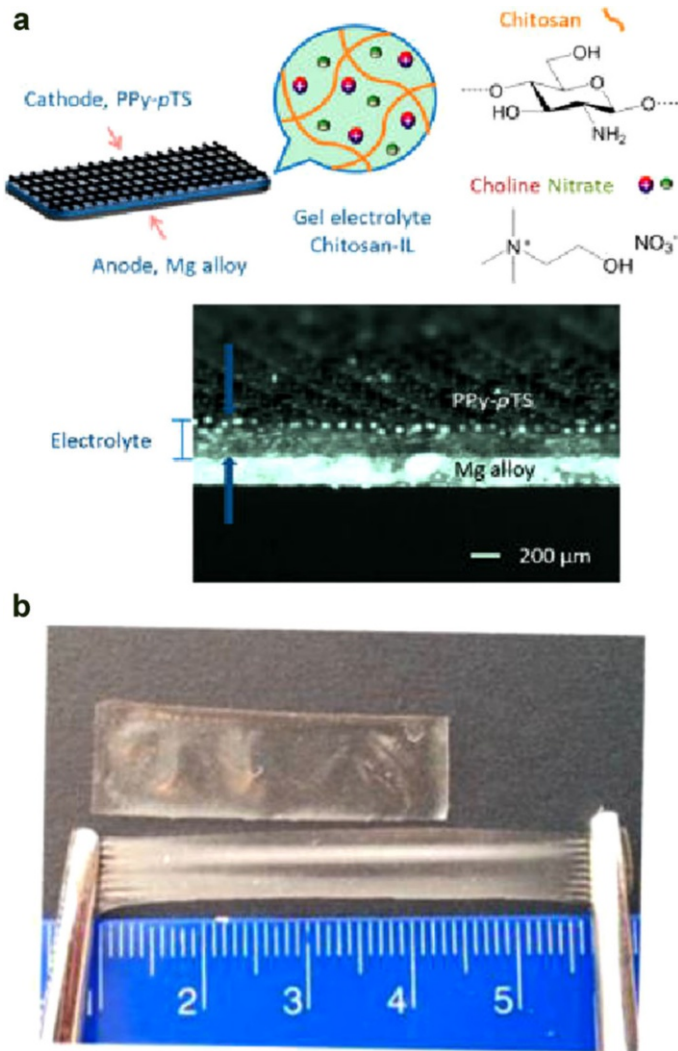


Fig. 9 **a** Schematic configuration and optical image of cross-sectional view (20° tilted) of the integrated solid-state Mg–air battery. **b** Digital image of a CS–[Ch][NO₃] (1:5) polymer electrolyte film demonstrating its mechanical robustness [93]. Reprinted with permission from ref. [93]. Copyright 2014 American Chemical Society

fuel cells [94]. Using an oxide ion conductor with a high-transport number of oxide ions, particularly in a reducing atmosphere, an increase in open-circuit potential and capacity is possible [94]. Additionally, a rechargeable Mg–air battery can be achieved by utilizing an electrolyte with superior stability in a reducing atmosphere or in contrast, lowering of the cell-operating temperature [94].

4 Nonaqueous Al–Air Batteries

4.1 Introduction

Aluminum–air batteries are being less researched compared to other NANA systems [6]. This fact is surprising when considering the commercial advantages of Al metal in power-source applications such as the abundance in earth crust [34, 37] and the low anode cost. In aqueous alkaline systems, an Al–air battery can provide an energy density of around 200 W h kg^{-1} for a full primary device [6, 34]. Additional advantages of Al–air cells are the low anode equivalent weight and the safety of cell ingredients [34, 49]. Moreover, Al and Al-based compounds are considered to be non-toxic and environmentally friendly [34, 35, 49]. An aluminum battery may be used in a variety of applications, such as field-portable emergency power supply, remote power applications, and last but not least, as a power source for electric transportation [35, 49]. On a theoretical level, Al possess half of the gasoline energy content per unit weight (8100 W h kg^{-1} for Al–air [35, 49, 95] and $13,000 \text{ W h kg}^{-1}$ for gasoline [8]) and three times the energy per unit volume ($21,870 \text{ W h L}^{-1}$ for Al–air and 9700 W h L^{-1} for gasoline [96]). In the case of electric vehicles (EVs), state-of-the-art utilization can approach 1700 W h kg^{-1} [8]. For aqueous Al–air batteries, reports as early as 1960s exist with two main efforts and technologies being the focus of the research in the last 50 years: alkaline or saline electrolytes [34, 35, 49]. Aluminum anode should exhibit, thermodynamically, a potential of -1.66 V in saline and -2.35 V in alkaline solutions [35, 49]. In practice, Al electrode operates at significantly lower potentials, due to a voltage delay attributed to oxide/hydroxide films. Additionally, in aqueous media, Al undergoes tremendous parasitic corrosion reactions. This lowers the Al-metal utilization and coulombic efficiency, leading to a massive hydrogen gas production and evolution [35, 49]. Additional challenge considered aqueous media relates specifically to alkaline electrolytes; as part of the discharge reaction, a progressive consumption of hydroxyl ions occurs near the anode, bringing the electrolyte into saturation with aluminate. At the end of the discharge process, the concentration exceeds the super-saturation level, and a precipitation of crystalline Al hydroxide occurs, leading to a loss of the ionic conductivity [35, 49].

When one thinks of the possibility of rechargeable Al–air batteries in aqueous media, some essential issues should be considered. In alkaline electrolytes, Al hydroxide ($\text{Al}(\text{OH})_3$) is produced along with alumina (Al_2O_3) as discharge products. While hydroxide-based discharge products are considered as recyclable, the alumina is not. Additionally, in moderate alkaline solutions, Al_2O_3 may be formed on the anode surface as a passivation layer, preventing long-term operation. In concentrated alkaline electrolytes, the previously addressed corrosion reactions hamper the cell stability. Moreover, hydrogen evolution reaction in these specific solutions occurs much before any possible Al deposition [34], meaning, in order to operate secondary Al–air cells non-aqueous electrolytes should be addressed and studied.

4.2 Liquid-Based Cells

4.2.1 Alcohols

The only known attempts, in the best of our knowledge, to apply non-aqueous solution in Al–air cells consider alcohols. Alcohols used as solvents for both aqueous and non-aqueous alkaline KOH electrolytes utilizing Al as an anode. The solvents include methanol [97, 98], ethanol [99], and propanol [100]. Without water, no hydrogen evolution occurs due to extended electrolyte stability. Additionally, under open-circuit conditions, the corrosion current densities were measured at low values of $0.0976 \text{ mA cm}^{-2}$, in a 4 M KOH solutions at 25 °C [99]. Nevertheless, due to decreases in the ionic conductivity of the electrolyte and extended passivation of the surface, almost no Al electrochemical dissolution is possible [97, 101]. In order to improve the dissolution rate, water–alcohol mixtures may be applied, with some increase in the currents, yet below the values achieved in only aqueous solutions. One should note that the experiments conducted with pure Al (99.9995%), rather than with alloys, as different behavior may be anticipated [34]. The electrolyte stability at the air–cathode side is considered a critical issue is Al–air cell implementation. In the case of Pt-based catalyst in the air cathode, methanol- and ethanol-based electrolytes were found to be unsuitable, as they are oxidized, releasing carbon dioxide gas [102, 103]. Other catalysts, such as tungsten carbide-silver composite (Ag-W₂C/C) [104] and a La_{0.6}Ca_{0.4}CoO₃ perovskite were also studied and used with some success in alkaline alcohol–water mixtures as oxygen reduction reaction (ORR) catalysts [105].

4.2.2 Ionic Liquid Electrolytes

As previously explained, aqueous-based Al–air batteries can be used only as primary power sources due to the fact that Al cannot be electrodeposited in this specific media [106, 107]. Therefore, possible electrolytes for rechargeable Al–air batteries are the aprotic ones such as ionic liquids [107].

4.2.2.1 Chloroaluminate Ionic Liquids Chloroaluminate-based liquids are a so-called “first” generation of RTILs and they are already in use for Al electrodeposition [48, 106, 108].

The synthetic procedure for manufacturing chloroaluminates is based on combining highly hygroscopic AlCl₃ with a suitable organic chloride such as *N*-butylpyridinium chloride (N-BPC) and 1-ethyl-3-methylimidazolium chloride (EMImCl) [109]. The utilization of such electrolytes in Al-based power sources was already presented by several researchers [34]. One of the main disadvantages of this kind of solutions is the difficult preparation procedure, related to a highly exothermic reaction between 1-ethyl-3-methylimidazolium chloride (EMImCl) and AlCl₃, which increases the overall substance price and decreases the safety of the electrolytes [110, 111]. For other possible cations, such as trimethylphenyl ammonium (chloride), the cost and the safety are substantially improved, albeit

some decrease in the performances is evident [112]. The ionic conductivity of EMImAlCl₄ is 0.017 S cm⁻¹ [110], inferior to aqueous solutions electrolytes, such as alkaline KOH (0.7 S cm⁻¹ for 7 M KOH at 30 °C) [113, 114]. Nevertheless, due to their extreme hygroscopicity, all chloroaluminate-based ionic liquids must be handled under an inert-gas atmosphere or at least under dry air [106, 115, 116]. Thus, this type of RTIL is quite challenging to be utilized in Al–air batteries, unless the cell could be sealed completely and only an O₂-permeation would be allowed through the air–cathode membrane [117]. Additionally, cycling the AlCl₃/EMImCl (as part of dissolution/deposition reaction) at the Al surface, results in changes in its composition, leading to a dramatic limit of the cell cyclability [34]. Revel et al.'s recent study [47] presented Al–air in AlCl₃/EMImCl mixture and the battery exhibits a low-self discharge rate. The cell capacity was measured to be 71 mA h cm⁻² at 0.1 mA cm⁻², similar to previous reports in Li–air and superior to any known data in Li-ion cells [47]. As presented there, the cell can sustain current densities of up to 0.6 mA cm⁻² [47]. In addition, it was concluded that charging such a system is possible, but with a limitation, attributed to the air electrode and the over-potential (charge) was found to be above the stability limit of the electrolyte. The presented results of this specific work are somewhat contradicting the previously explained inherent challenges related to utilization of chloroaluminates in Al–air batteries. Mostly, the extreme hygroscopicity of these liquids was not addressed at all by the authors, and the problems involved in development of such electrolyte-based batteries were not disclosed.

A different type of cathode, besides air, may be used when Al power sources are studied in chloroaluminates media. The cathodes that are under intense focus of the research community are operated by a reversible electrochemical intercalation of Al³⁺ [46]. Many of the cathodic materials utilized in secondary Al batteries include Chevrel phase Mo₆Se₈, V₂O₅, Ag halides, and various manganese oxides, which were previously applied as cathodes in Mg battery research [41–46, 118]. Nevertheless, secondary Al cells based on the suggested cathodic materials suffer severely from a low open-circuit potential in comparison to the Mg parallels. Although this subject is not in the scope of this review, it is important to notice that the vast majority of these studies used EMImCl/AlCl₃ as the electrolyte of choice.

4.2.2.2 Alternative Ionic Liquids The “second” generation of RTILs, which are air- and water-stable ionic liquids such as 1-butyl-1-methylpyrrolidinium bis(trifluoromethylsulfonyl)imide BMPTFSI, 1-ethyl-3-methylimidazolium bis(trifluoromethylsulfonyl)amide EMImTFSI and (trihexyl-tetradecyl)phosphonium bis(trifluoromethylsulfonyl) imide P_{14,6,6,6}TFSI [106], may serve as a possible alternative for Al–air batteries electrolytes. With an addition of AlCl₃ to these solvents, a successive Al deposition and dissolution cycles were reported, as shown in Fig. 10. Charge efficiencies of 100, 4 and 87%, respectively, were measured at 25 °C [106]. It was marked that EMImTFSI results were superior to the other two liquids, because of its lower viscosity. This electrolyte allowed higher discharge current density up to 12 mA cm⁻² compared to 0.1 mA cm⁻² for BMPTFSI and 0.4 mA cm⁻² for P_{14,6,6,6}TFSI [106].

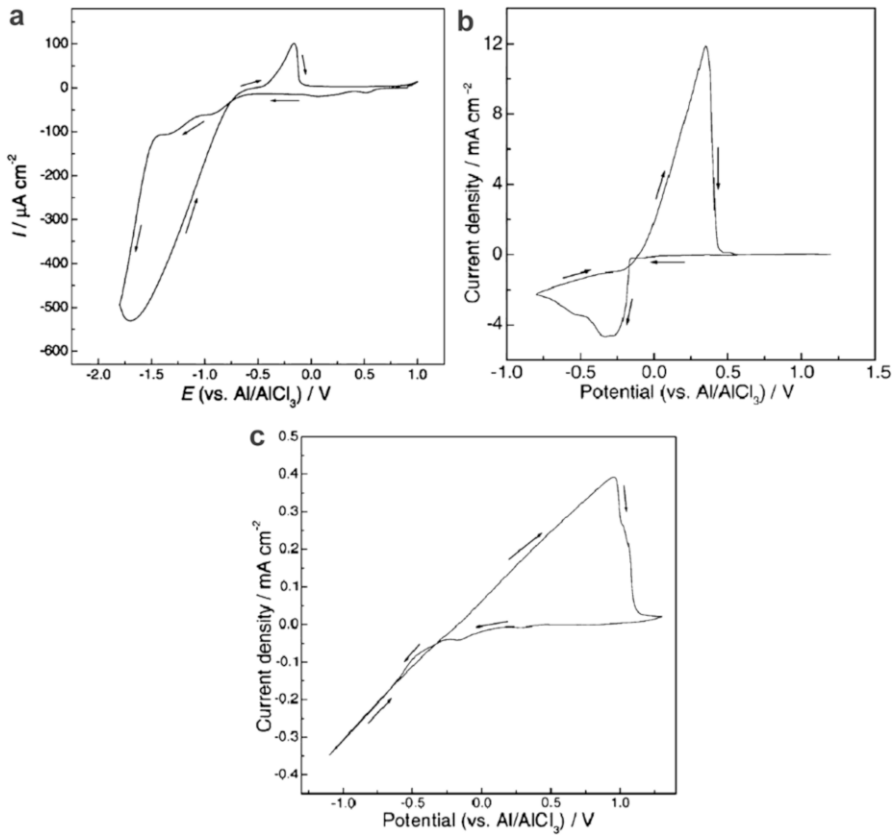


Fig. 10 Cyclic voltammograms recorded on Au substrate at 25 °C in the ionic liquid (scan rate: 10 mV/s): **a** 1-butyl-1-methyl pyrrolidinium-bis(trifluoromethylsulfonyl)imide containing AlCl_3 1.6 M (from the upper phase of the mixture). **b** 1-Ethyl-3-methyl imidazolium bis(trifluoromethylsulfonyl)imide saturated with AlCl_3 (from the upper phase of the mixture). **c** Trihexyl-tetradecyl phosphonium Tf_2N containing 4 M AlCl_3 [106]. Copyright 2006 Wiley-VCH Verlag GmbH & Co. KGaA, Weinheim. Reproduced with permission from ref. [106]

A very different approach to the conventional practice in Al-based power source was reported by Gelman et al. [49]. This study was performed without any use of AlCl_3 or in fact any chloro-based materials at all. In the work, a 1-ethyl-3-methylimidazolium oligo-fluoro-hydrogenate $\text{EMIm}(\text{HF})_{2.3}\text{F}$ RTIL was applied and used. The produced Al–air cells were able to sustain current densities up to 1.5 mA cm^{-2} , achieving capacities above 140 mA h cm^{-2} utilizing as much as 70% of the theoretical Al energetic capacity, as presented in Fig. 11a [49]. These values correspond to tremendous energy densities of 2300 W h kg^{-1} and 6200 W h L^{-1} . As a reaction discharge product, only Al_2O_3 was detected at the air electrode, coupling the oxygen reduction coupled with migrated Al ions, as shown in Fig. 11b [49].

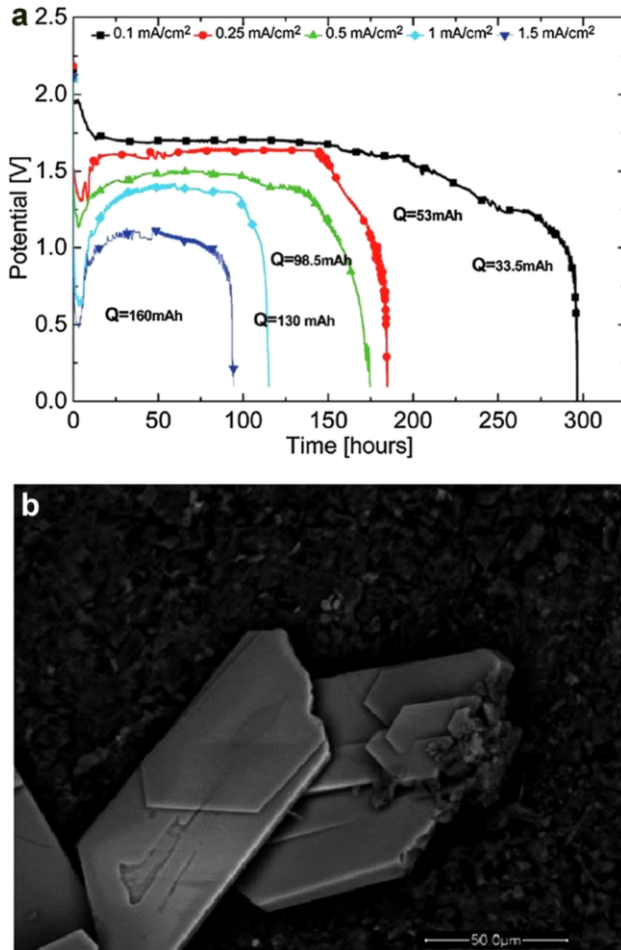


Fig. 11 **a** Al–air battery discharge profiles at different current densities of 0.1 (black square); 0.25 (red circle); 0.5 (green up-based triangle); 1 (cyan diamond), and 1.5 mA·cm⁻² (blue down-based triangle). **b** Back-scattered electron (BSE) SEM micrographs of air cathode electrode surface after discharge at 1.5 mA cm⁻² [49]. Reprinted with permission from ref. [49]. Copyright 2014 Royal Society of Chemistry

4.3 All Solid-State Cell

No significant reports on solid-state Al–air batteries in non-aqueous media were found, as far as we are aware of. It is not reasonable to apply and implement the oxygen-shuttle concept with Ca-stabilized ZrO₂ (CSZ), as the electrolyte, shown for various metals–air in the previous report by Inoishi et al. [119], since Al ion may poison the oxygen ion conducting membrane [120]. A possible approach can be adopted from the all solid-state Si–air battery, which utilizes HEMA polymer [56] as the polymer electrolyte soaked with EMIm(HF)_{2.3}F ionic liquid.

5 Nonaqueous Silicon–Air Batteries

5.1 Introduction

A highly promising battery system, based on its high theoretical specific energy of 8470 Wh kg^{-1} and an energy density of $21,090 \text{ Wh L}^{-1}$, is Si–air [56]. The battery theoretical capacity, 3.816 Ah kg^{-1} , is very close to the well-studied, Li–air 3.86 Ah kg^{-1} . The Si–air battery system, first reported in 2009 [57], provides an operating voltage of 0.8–1.1 V, under loading of $0.01\text{--}0.3 \text{ mA cm}^{-2}$. Opposite to Li–air, the Si-based battery does not exhibit many of the environmental and safety issues as partially hampered Li-based battery development. In the case of Si anode, ambient atmosphere does not affect in any way the system stability and safety, since the ionic liquid-based electrolyte is non-volatile. In addition, the discharge product, being SiO_2 , can be disposed or recycled [56].

5.2 Liquid-Based Cells

The work by Cohn et al. [55–60] addresses the study and development of a rather new and unique non-aqueous Si–oxygen couple. This system is comprised of a single-crystal Si wafer as the anode and EMIm(HF) $_{2.3}$ F room temperature ionic liquid (RTIL) as the electrolyte. It has been identified that the most appropriate Si type to serve as the anodic active material is heavily doped n-type. Heavily doped n-type Si benefits from a low self-discharge rate (with corrosion rate of 0.078 nm/min), together with cell potentials, varies from 1.1 to 0.8 V, with current densities of $0.01\text{--}0.3 \text{ mA cm}^{-2}$, as shown in Fig. 12 [58].

EDX and XPS examinations confirm the sedimentation of SiO_2 over the air electrode [58]. This deposit is considered to cause pore clogging in the active carbon layer of the air electrode, leading to a decrease in available active sites for oxygen

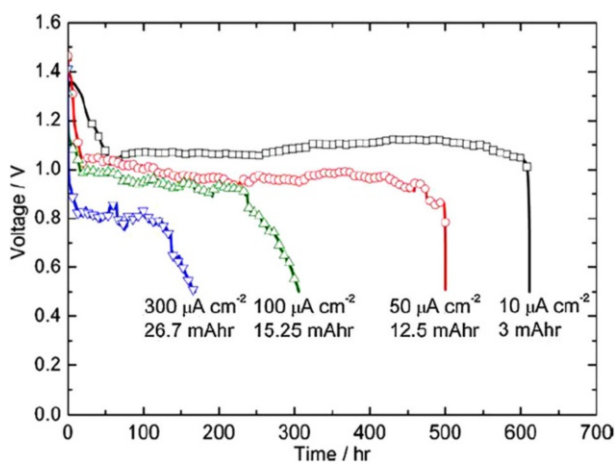


Fig. 12 Discharge plots of Si–air cells using EMIm(HF) $_{2.3}$ F RTIL electrolyte at different constant current densities [58]. Reprinted from ref. [58]. Copyright 2010, with permission from Elsevier

reduction, which contributes to lower performance of the air cathode. A suggested model is presented in Fig. 13 for low and high discharge currents [58].

Water addition to EMIm(HF)_{2,3}F electrolyte had a massive impact on the discharge performance of Si–air batteries [59]. Variations in the volumetric water content in the electrolyte significantly influence the discharge mechanism and capacity of Si–air batteries [59]. Maximum cell discharge capacity was obtained with the addition of 15 vol% of water, where the capacity was increased by 35% compared to the capacity obtained with a pure RTIL electrolyte. This improvement is attributed to a shift in SiO₂ reaction zone, leading to a distribution of the SiO₂ formation zones; now, some of it is being formed in the bulk electrolyte, in contradiction to a formation solely at the air electrode with a pure RTIL electrolyte. Water-uptake studies showed that the hydrophilic EMIm(HF)_{2,3}F RTIL can sustain a high amount of water and can be operated under an extremely humid environment [59]. Operating in a humid environment not only did not degrade the Si–air cell performance dramatically, but rather contributed to an impressive increase in the discharge capacity. However, the addition of water encouraged the formation of an oxide passivation layer on the Si substrate, which resulted in higher cell impedance [59]. The water content had an effect on the surface morphology of the Si anode as well. A porous structure was obtained with and without water in the electrolyte, as shown in Fig. 14 [59]; however, the surface etching mechanism was not identical in both cases. The results reinforce the fact that water is formed and plays a major role in the discharge process of Si–air batteries, and thus, greatly affects the cell's efficiency.

Si–air battery studies [55–60] were performed mostly on MnO₂-catalyzed air cathodes. A model was proposed showing that the air cathode was not only blocked by SiO₂ reduction products upon discharge but also experienced a major

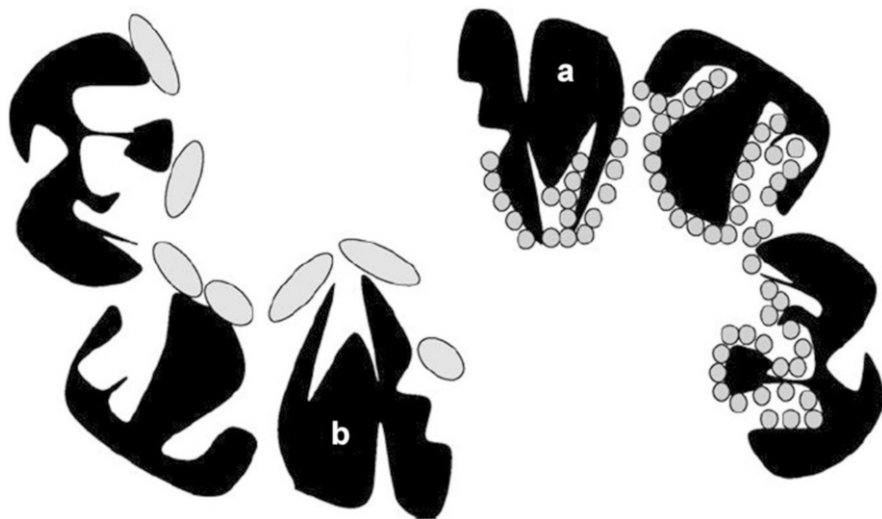


Fig. 13 A model for SiO₂ reaction product deposition on porous carbon air electrode. **a** Low discharge currents and **b** high discharge currents [58]. Reprinted from ref. [58]. Copyright 2010, with permission from Elsevier

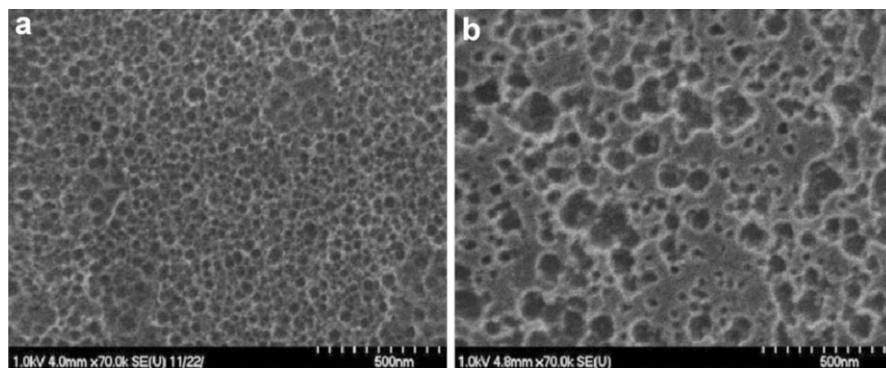


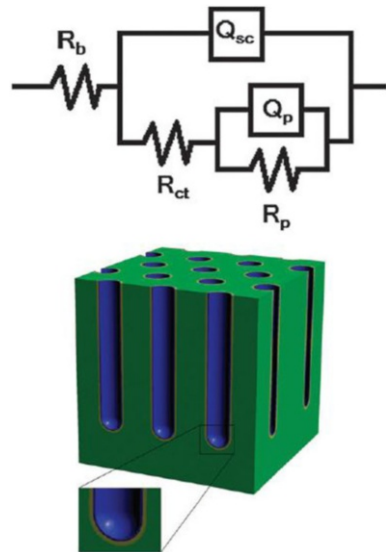
Fig. 14 HRSEM micrographs of the Si wafer anode obtained after discharge at a current density of 0.3 mA cm^{-2} at different capacities and electrolytes: **a** $18.34 \text{ mAh cm}^{-2}$, pure RTIL; **b** $18.34 \text{ mAh cm}^{-2}$, 15 vol% of H_2O in the RTIL [59]. Copyright 2011 Wiley-VCH Verlag GmbH & Co. KGaA, Weinheim. Reproduced with permission from ref. [59]

modification in the MnO_2 catalyst nature via the formation of a MnF_2 surface layer. This modification greatly influences Si–air battery performance and provides an additional explanation to the limited discharge capacity and inhibited cell discharge [60]. Electrochemical impedance spectroscopy (EIS) studies along the discharge process were applied to characterize the interfaces between the battery’s electrodes and electrolyte, and to describe the better explain the discharge profile of a Si–air battery. Flat-band measurements showed that n-type Si was under depletion during battery discharge [55, 121].

EIS results showed a negligible impedance contribution of the processes at the air cathode compared to the Si anode side. The impedance data, in terms of an electrical equivalent circuit, revealed the parameters related to space charge capacitance and charge transfer, and indicated that the active electrochemical area remained unchanged, even though the formation of porous structure was observed. Furthermore, the capacitance of the space charge layer was well correlated with the doping concentration of the Si anode. Comparing the potential profile of the complete Si–air cell to that of the distinctly two electrodes half-cells, provided experimental evidence for the domination and the negative impact (in terms of capacity and voltage drop of the Si–air cell) of the Si anode over the air cathode. The discharge capacity of the Si–air battery can be significantly increased by replacing the discharged inactivated Si anode towards the end of the discharge process. A suggested mechanism for anodic etching of Si in $\text{EMIm}(\text{HF})_{2.3}\text{F}$ RTIL, based on an electron-injecting surface complex, is shown in Fig. 15 [55].

A silicon–air battery based on $\text{EMIm}(\text{HF})_{2.3}\text{F}$ room temperature ionic liquid as the electrolyte is attractive for a wide range of applications, starting from micro electro-mechanical systems and up to large mechanically rechargeable batteries.

Fig. 15 Equivalent circuit chosen to model the impedance behavior of an Si–air battery, and Schematics of porous anode surface. *Inset* exhibits two surface layers; the *inner* represents the space charge layer and the *outer* represents the oxide layer [55]. Reprinted with permission from ref. [55]. Copyright 2013 Royal Society of Chemistry



5.3 Gel Polymer-Based Electrolyte

Gel polymer electrolytes (GPE) have attracted much attention as electrolytes for many solid-state electrochemical devices, such as chemical sensors [122], solar cells [123], and mainly Li batteries [7, 124, 125]. GPEs are formed by incorporating a liquid electrolyte into a polymeric matrix; therefore, the conduction mechanism in polymer gels is similar to the one observed in liquid electrolytes, with the advantage of a solid structure. The GPEs are thus highly safe, shape-flexible, mechanically stable, and display only a modest loss in ionic conductivity upon operation. The most common polymer matrices used for GPEs are poly-methylmethacrylate (PMMA), poly-vinylidene fluoride (PVdF), poly-ethylene oxide (PEO), and poly-acrylonitrile (PAN). GPEs for Li-ion electrolytes, containing the polymeric matrices mentioned above, show typical ionic conductivity of the order of 1 mS cm^{-1} , at room temperature. Within the massive introduction of RTILs into electrochemical applications, the combination of these interesting liquids together with polymers, in order to form gel-like electrolyte, is widely investigated [126–128].

Tsuda et al. explored the feasibility of various combinations of EMIm(HF)_{2,3}F: polymer composites, in terms of ionic conductivity, air stability, and electrochemical window [129]. The compounds 2-hydroxyethyl methacrylate (HEMA), vinyl acetate, 1-vinyl imidazole, and methyl methacrylate were used as monomers. From all of the above, the only successive combination was identified to be the mixture of EMIm(HF)_{2,3}F and HEMA, which polymerized into a transparent gel. It was found that the conductivity of the GPE decreased dramatically with a decrease in RTIL molar content in the mixture. For 60 mol% RTIL, at room temperature, the conductivity was found to be 23 mS cm^{-1} , compared to 100 mS cm^{-1} for the neat RTIL. The apparent electrochemical window of the 50 mol% RTIL mixture was found to be 0.3 V wider than for the pure RTIL. No

change was observed in the cyclic voltammogram for the 50 mol% RTIL mixture after 1 week of exposure to air, indicating a stability of the mixture in contact with air [129].

Applying the previously suggested method of composite polymer electrolyte, Cohn et al. [56] implemented and studied EMIm(HF)_{2.3}F RTIL and HEMA polymer in different compositions (shown in Fig. 16a), from 40 to 70 mol% of RTIL. The constructed freestanding membranes were proven to be mechanically stable, having a uniform structure, without any evidence of aggregation or phase separation. The applied compositions were thermally stable up to a temperature of 270 °C. In addition, it was observed that the electrolyte ionic transport number increases with an increase in RTIL content in the GPE. Moreover, all the polymer electrolytes were

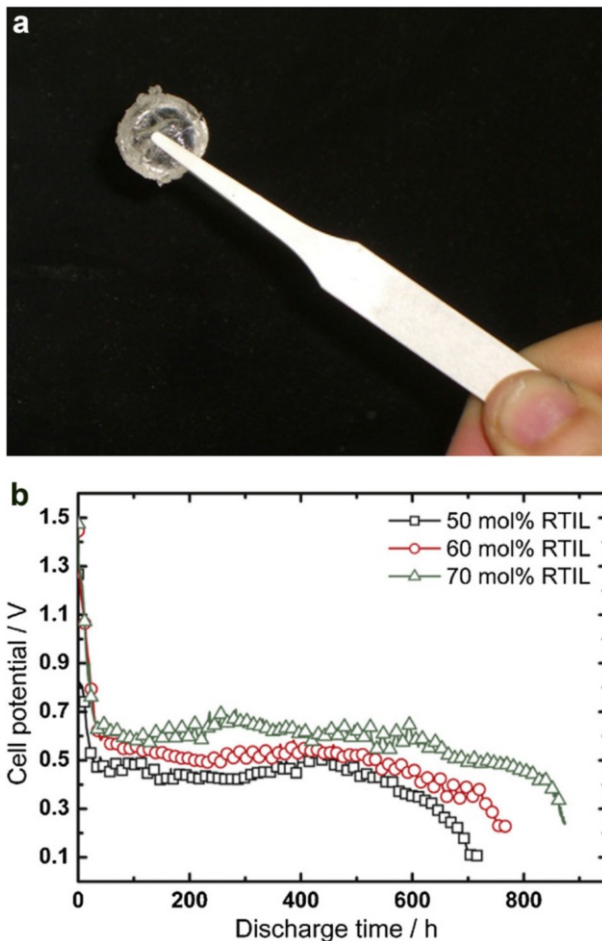


Fig. 16 **a** Photograph of a EMIm(HF)_{2.3}F RTIL/HEMA polymer gel electrolyte. **b** Galvanostatic discharge curves of Si–air cell, comprised of Si wafer anode, air cathode and EMIm(HF)_{2.3}F RTIL–HEMA (70 mol% RTIL gel polymer electrolyte) [56]. Reprinted from ref. [56]. Copyright 2011, with permission from Elsevier

found to exhibit an ionic transport number close to unity, implying an ionic conduction as the charge transfer mechanism across the GPE. It was also found that the GPEs have good compatibility with both the Si anode and the air cathode [56].

Si–air batteries utilizing polymer gel electrolytes, based on EMIm(HF)_{2.3}F RTIL and HEMA polymer, were operated under a discharge current density of 0.1 mA cm⁻². The results show relatively long discharge times, up to 850 h (Fig. 16b). However, the operating voltage is lower with respect to a cell discharge utilizing the ionic liquid alone [58], due to a general lower ionic conductivity of the polymer electrolyte compared with the pure RTIL. Another challenge in this system was found to be a lack of intimate contact between the Si-based anode and the air cathode, as the reacted anode surface area was lower than expected. GPE-based Si–air batteries can be utilized for powering low-power devices because of the associated high specific energies [56].

5.4 All Solid-State Cells

Producing and developing a rechargeable Si–air battery-based liquid or gel electrolytes was found to be difficult and challenging due to the problematic Si oxide electrochemical reducing process, related strongly to its high stability and high theoretical oxidation potential [55, 57, 130]. The work by Inoishi et al. [131] reports on an application of an oxide ion conductor as the electrolyte in a Si–air rechargeable battery based on the oxygen shuttle concept. Based on this study [131], the oxide ionic conductor method has advantages in metal–air batteries. Solid oxide ion conductors are chemically stable, in a wide range of potentials, meaning that only negligible decomposition or reaction of the electrolyte with other materials occurs. Additionally, due to the low vapor pressure, the evaporation of the electrolyte is not an issue, opposite to liquid electrolytes such as carbonates or ethers. Finally, the temperature stability of these materials allows operating conditions in a range of temperatures as wide as 373–1273 K [131]. According to Gibbs free energy consideration of the reactions, it is expected that Si will be reduced or oxidized at elevated temperatures. Such application of oxide ion conductor in a Si–air battery at a reasonably elevated temperature should allow reversible cell operation [131].

A rechargeable battery based on an oxygen shuttle concept and using a ZrO₂ oxide ion conductor stabilized with CaO (CSZ), in which oxygen permeates through an electrolyte both during discharge and charge as the result of electrochemical pumping. The schematic cell structure is shown in Fig. 17a [131]. The open-circuit voltage was measured at 1.34 V, in an intermediate value between the theoretical potentials of Si/SiO (0.958 V) and Si/SiO₂ (1.821 V) [131]. It was assumed that the voltage is a mixed potential assigned for both formation SiO₂ and SiO formation. It was also shown by XRD studies that reaction in Eq. (15) appears to be the dominant process in the Si–air battery, with minor contribution from reaction in Eq. (16) [131].

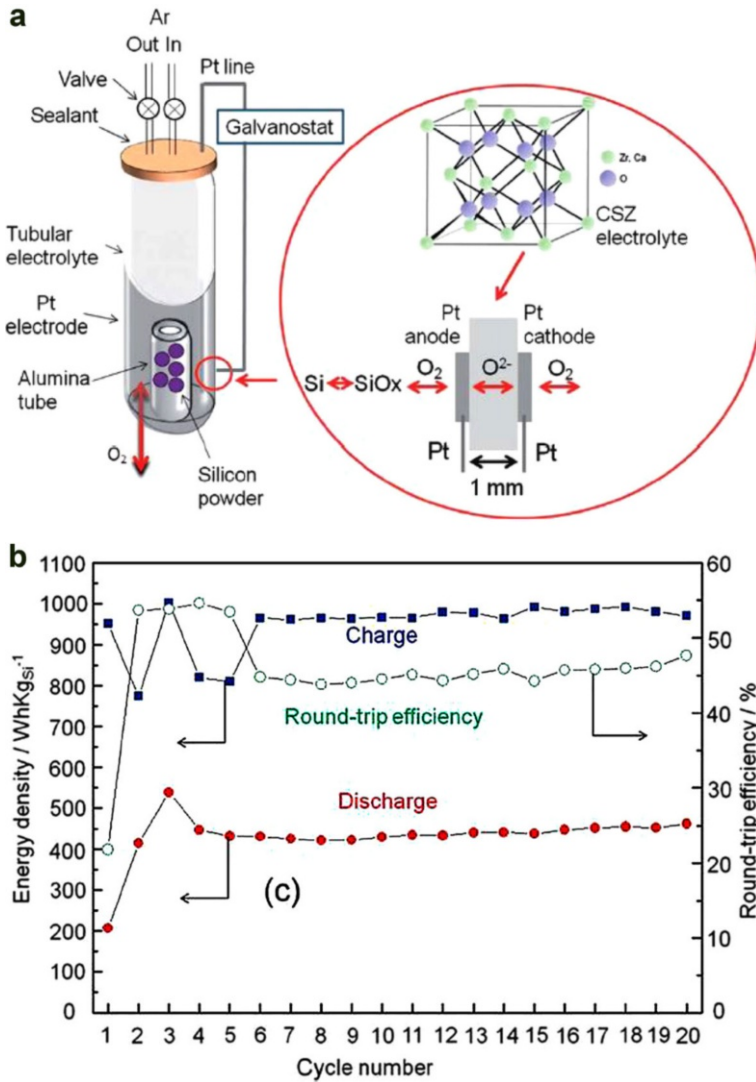


Fig. 17 **a** Schematic view of a Si–air battery with a Pt/CSZ/Pt cell. The cell used is a tubular type of Pt/Ca_{0.055}Zr_{0.945}O₂/Pt. **b** Charge–discharge properties of a Si–air battery (energy density and round-trip efficiency) [131]. Reprinted with permission from ref. [131]. Copyright 2013 Royal Society of Chemistry



The charge–discharge behavior was measured with the use of a Pt/Ca-stabilized zirconia (CSZ)/Pt cell with Si at 1073 K. The capacity for the first discharge cycle was around 368 mA h g_{Si}⁻¹, but an increase of capacity up to 701 mA h g_{Si}⁻¹ was recorded for the third discharge. Figure 17b shows the energy density and round-trip

efficiency. The energy density was measured to be larger than $400 \text{ W h kg}_{\text{Si}}^{-1}$, nevertheless the efficiency was only around 45%. These results are inferior to the already established performances of other rechargeable systems [131].

6 An Overview: Conclusions and Perspective

6.1 General

In this manuscript, a number of leading metal–air systems, which are the next generation of the Li and Zn–air batteries, were reviewed. The most common feature to all NANA systems is the fact that their true implementation can be achieved only by using non-aqueous electrolytes. The first and foremost important issue regarding any possible utilization relates to the interaction between anode and electrolyte. The conditions necessary to create an effective battery should include simultaneously two different surface conditions in the contact between the anode and electrolyte: (1) the activation of the anode surface by the electrolyte—meaning removing the layer of oxide layer and allowing active metal dissolution (discharge), (2) relatively low corrosion rates (orders of magnitude lower than the discharge) in order to enable efficient battery. Thus, the main challenges with all NANA systems is achieving both activation of the anode surfaces and at the time, allowing simultaneously reversible metal deposition (at the anode) and metal-oxide reduction, releasing oxygen at the cathode.

While reviewing the studies in the NANA batteries field, it could be seen that there is no uniform or unified methodology of research. There are attempts to get directly to the application itself (battery) and there is less focus on the scientific aspects of the single component or possible interactions components. This fact obstructs the possible progress in the research of many areas in NANA metal–air battery systems. This is in contrast to the current research in lithium and sodium–air batteries. In these two systems, scrupulous scientific work is conducted and usually comparisons between the two are applied. This leads to a deeper and better understanding of the involved mechanism and it of course more effective.

6.2 Magnesium–Air Battery System

Although Mg–air battery research should be the most advance compare system compared to the other NANA batteries, based on the intensive studies in the field of Mg-ion battery, there is only a few reports on full Mg–air cells. The initial studies on electrolyte developing for reversible Mg processes were centered on Grignard base materials (RMgX , where R = alkyl, aryl group and X = halide) or very similar analogous, dissolved in an organic solvents. Due to the problematic stability and considerably low conductivity, pseudo-Grignard systems were developed, composing charged acidic and basic components in ethereal solutions. Although these novel organic electrolytes show adequate conductivity and good electrochemical stability, these solutions are still volatile and mostly unstable in an ambient environment. This was one of the reasons to combine the Grignard-based

organic electrolytes with RTILs, thus improving the conductivity on one hand and decreasing the volatility on the other hand.

A variety of standard and well-known ionic liquids react with Mg and forms on its surface a layer of products. The constructed layer is generally hampers Mg diffusion through it and instead rather passivates the surface; meaning, instead of SEI as it forms in Li in organic media, a passivation layer is the outcome of Mg interaction with RTILs. With the fact that a vast number of possible commercially available RTILs proved to be unstable with Mg, possible “tailoring” of the chemistry has not yet been explored in detail. With better understanding of the required chemistry, one can assume that a suitable RTIL could be synthesized. Such ionic liquid should provide the conditions for proper Mg electrochemistry by either stability in the Mg potential or by constructing a suitable permeable to Mg ions SEI layer. Thus, novel electrolytes, especially ionic liquids, should be synthesized and investigated for developing successful Mg–air batteries.

6.3 Aluminum–Air Battery System

In alkaline media self-discharge, accompanied by considerable amount of heat generate and vast hydrogen generation results in a high rate of water loss and electrolyte dehydration what also the Al anode shelf life. To overcome this problem, the use of different non-aqueous electrolytes was suggested and conducted. The main challenge in non-aqueous media was and still is an activation of Al surface. Thus, the main electrolytes that have been used for this matter are the ones based on chlorides, and more specifically on Al chloride (AlCl_3). The use of Al chloride (AlCl_3)-based electrolytes are not restricted to the field of Al–air but also relevant and applicable in other Al-based power sources, without any real success. The leap in successful utilization of Al as anode in a variety of battery systems could be made with synthesizing, and studies of non-chloride containing electrolytes, which should have improved chemical and humidity stability.

6.4 Silicon–Air Battery System

Surprisingly enough, only a few solutions have been studied as electrolytes for Si–air batteries. The huge potential of using Si wafers as anode and powering independently the devices integrated directly on it brings this type of batteries as needed future solution in microelectronics and MEMS industries. One of the major applications of Si–air would be its integration into lab-on-a-chip device. The use of oligo-fluoro-hydrogenate RTIL as the electrolyte for Si–air batteries was groundbreaking, as it allows the development of a primary system. It seems that currently this RTIL is the most important component for any future development and commercialization of sustainable solid-state Si–air battery based on the utilization of a HEMA polymer.

6.5 All Solid-State Metal–Air Battery Systems

The area of solid-state batteries is highly important in order to introduce stable, durable, and most importantly, safe batteries. Not so many reports have been

Table 1 A summary of the different types of NANA batteries

Type	Anode	Cathode	Electrolyte	Temperature/ C	OCV/V	Discharge current densities/ mA cm ⁻²	Discharge capacity	Discharge voltage characteristics	Rechargeability ^a	References
Liquid	Mg	Carbon cathode sandwiched between two Pt mesh grids at 2 atm	0.5 mol/l Mg(ClO ₄) ₂ solution in DMSO	60	1.4 (estimation)	0.078	2280 mAh g ⁻¹	One plateau at 1.25 V	Non	[76]
	Mg	Carbon cathode sandwiched between two Pt mesh grids at 2 atm	0.5 mol/l Mg(ClO ₄) ₂ solution in DMSO and iodine in the solutions was between 0.026 and 0.086 mol/l	60	1.7 (estimation)	0.078	2131 mAh g ⁻¹ (first cycle)	First plateau near 1.5 V Second plateau at 1.25 V	Very limited, four cycles rapid decline of the capacity	[76]
	Mg (>99.8%)	Porous carbon-based air electrode with MnO ₂ as a catalyst	mixing BMPTFSI, THF, and EtBr in a volumetric ratio of 1:1:0.3	25	1.9	0.1	345 mAh g ⁻¹	Large voltage deep (of ~200 mV) at the first 10% discharge capacity Declining plateau at 0.1 mA cm ⁻²	Not mentioned	[33]

Table 1 continued

Type	Anode	Cathode	Electrolyte	Temperature/ C	OCV/ V	Discharge current densities/ mA cm^{-2}	Discharge capacity cm^{-2}	Discharge voltage characteristics	Rechargeability ^a	References
	Al plate (99.999%)	Porous carbon-based air electrode with MnO_2 as a catalyst	$\text{AlCl}_3/$ EMImCl	25	1.6	0.05 up to 0.6	71 mAh cm^{-2}	0.8 V at 0.05 mA cm^{-2} 0.7 V at 0.1 mA cm^{-2} 0.5 V at 0.3 mA cm^{-2} Declining plateau at 0.6 mA cm^{-2}	Possible ^b	[47]
	Al foil (99.997%)	Porous carbon-based air electrode with MnO_2 as a catalyst	$\text{EMIm}(\text{HF})_{2.3}\text{F}$	25	2.1	0.1 up to 1.5	140 mAh cm^{-2}	Voltage deep (for 4 h) at 0.25 - 1.5 mA cm^{-2} 1.7 V at 0.1 mA cm^{-2} 1.5 V at 0.25 mA cm^{-2} 1.45 V at 0.5 mA cm^{-2} 1.35 V at 1 mA cm^{-2} 1.1 V at 1.5 mA cm^{-2}	Possible	[49]

Table 1 continued

Type	Anode	Cathode	Electrolyte	Temperature/ C	OCV/V	Discharge current densities/ mA cm ⁻²	Discharge capacity	Discharge voltage characteristics	Rechargeability ^a	References
	Single-crystal (100) heavily doped n-type Si wafers	Porous carbon-based air electrode with MnO ₂ as a catalyst	EMIm(HF) _{2.3} F	25	1.45	0.01 up to 0.3	53.4 mAh cm ⁻²	1.1 V at 0.01 mA cm ⁻² 0.95 V at 0.05 mA cm ⁻² 0.9 V at 0.1 mA cm ⁻² 0.8 V at 0.3 mA cm ⁻²	Non	[58]
Polymer	Mg alloy (AZ31)	PPy film	CS-[Ch][NO ₃] polymer electrolyte film	25	1.80–1.71	0.01 up to 0.1	1.55 mAh cm ⁻²	1.4 V at 0.01 mA cm ⁻² 1.2 V at 0.05 mA cm ⁻²	Non	[93]
	Single-crystal (100) heavily doped n-type Si wafers	Porous carbon-based air electrode with MnO ₂ as a catalyst	EMIm(HF) _{2.3} F and 2-hydroxyethyl methacrylate polymer	25	1.45	0.1	85 mAh cm ⁻²	Declining plateau at 0.05 and 0.1 mA cm ⁻² 0.5 V at 50%/mol RTIL 0.55 V at 60%/mol RTIL 0.6 V at 70%/mol RTIL	Non	[56]

Table 1 continued

Type	Anode	Cathode	Electrolyte	Temperature/ C	OCV/V	Discharge current densities/ mA cm^{-2}	Discharge capacity	Discharge voltage characteristics	Rechargeability ^a	References
Solid	Mg	Pt paste	Ca-stabilized ZrO_2 solid electrolyte	800	1.81 V	0.077	1154 $\text{mAh gr}_{\text{Mg}}^{-1}$	~ 1.1	Not mentioned	[94]
	Si powder on Pt paste	Pt paste	Ca-stabilized ZrO_2 solid electrolyte	800	1.34 V	0.04	701 $\text{mAh gr}_{\text{Si}}^{-1}$	~ 1	20 cycles	[131]

^a Based on the reference description

^b Seems problematic due to the high hygroscopicity and reactivity of the electrolyte

published until now in the field of all solid-state Mg, Al, Si–air battery systems. A variety of metal–air systems have been studied and reported by Ishihara and his coworkers. The systems are incorporating and utilizing an oxide ion-conducting electrolyte based on the oxygen shuttle concept and most of the cells employ Ca stabilized ZrO_2 .

6.6 Full Cell Comparison

To the best of our knowledge, there are a quite small number of studies showing full operational non-aqueous metal–air cells utilizing Mg, Al, Si metals as an anode. This is in contrast to Li, Na–air systems where the amount of produced research is enormous. This is not surprising in lieu of the major challenges that have been previously thoroughly described. Table 1 summarizes the performers of NANA-based battery cells.

From Table 1, one can conclude that rechargability of NANA is still not an issue due to the fact that even primary Mg, Al, Si–air battery performances are still a substantial challenge. Mg, as a metal of choice, was applied greatly than the other metals in full battery configurations. The main reason for this is that Mg anode was already studied with different media and electrolytes for a utilization in Mg-ion systems. Nevertheless, when similar solutions were applied in Mg–air batteries, the results were, in most cases, insufficient. The reason for this is mainly due to the high reactivity and instability of the electrolyte in the presence of oxygen. In terms of electrolytes, RTILs can be used as a promising media for utilization in NANA metal–air batteries and can also serve as a future platform for such rechargeable systems.

In considering a rechargeable system for Si and Al–air battery technologies, one should plan and design functional electro-catalysts, enabling a reversible reduction of the formed metal oxides. This in-turn would enable breaking the strong metal (Al, Si)-oxygen bonds, leading to a reduction of the metal cation and a release of oxygen. Yet, such an electrocatalyst is not to be found, and a major effort should be directed towards such material development.

Acknowledgements This research work was financially supported by the Israel Science Foundation (ISF) Grant No. 1701/12, by Israel National Center for Electrochemical Propulsion (INREP-ISF) and by the Nancy and Stephen Grand Technion Energy Program (GTEP).

References

1. Kraytsberg A, Ein-Eli Y (2013) The impact of nano-scaled materials on advanced metal–air battery systems. *Nano Energy* 2(4):468–480
2. Li Y, Dai H (2014) Recent advances in zinc–air batteries. *Chem Soc Rev* 43(15):5257–5275
3. Linda D, Reddy T (2001) *Handbook of batteries*, 3rd edn. McGraw-Hill Companies Inc., Maidenhead
4. Zhang XG (1996) *Corrosion and electrochemistry of zinc*. Springer, USA
5. Goldstein J, Brown I, Koretz B (1999) New developments in the Electric Fuel Ltd. zinc/air system. *J Power Sources* 80(1):171–179
6. Kar M, Simons TJ, Forsyth M, MacFarlane DR (2014) Ionic liquid electrolytes as a platform for rechargeable metal–air batteries: a perspective. *Phys Chem Chem Phys* 16(35):18658–18674

7. Balaish M, Kraysberg A, Ein-Eli Y (2014) A critical review on lithium–air battery electrolytes. *Phys Chem Chem Phys* 16(7):2801–2822
8. Girishkumar G, McCloskey B, Luntz A, Swanson S, Wilcke W (2010) Lithium–air battery: promise and challenges. *J Phys Chem Lett* 1(14):2193–2203
9. Kraysberg A, Ein-Eli Y (2011) Review on Li–air batteries—opportunities, limitations and perspective. *J Power Sources* 196(3):886–893
10. Abraham K, Jiang Z (1996) A polymer electrolyte-based rechargeable lithium/oxygen battery. *J Electrochem Soc* 143(1):1–5
11. Choi R, Jung J, Kim G et al (2014) Ultra-low overpotential and high rate capability in Li–O₂ batteries through surface atom arrangement of PdCu nanocatalysts. *Energy Environ Sci* 7(4):1362–1368
12. Kowalczyk I, Read J, Salomon M (2007) Li–air batteries: a classic example of limitations owing to solubilities. *Pure Appl Chem* 79(5):851–860
13. Peled E, Golodnitsky D, Mazor H, Goor M, Avshalomov S (2011) Parameter analysis of a practical lithium- and sodium–air electric vehicle battery. *J Power Sources* 196(16):6835–6840
14. Read J, Mutolo K, Ervin M et al (2003) Oxygen transport properties of organic electrolytes and performance of lithium/oxygen battery. *J Electrochem Soc* 150(10):A1351–A1356
15. Wu D, Guo Z, Yin X et al (2014) Metal-organic frameworks as cathode materials for Li–O₂ batteries. *Adv Mater* 26(20):3258–3262
16. Caramia V, Bozzini B (2014) Materials science aspects of zinc–air batteries: a review. *Mater Renew Sustain Energy* 3(2):1–12
17. Chakkaravarthy C, Waheed A, Udupa H (1981) Zinc–air alkaline batteries—a review. *J Power Sources* 6(3):203–228
18. Cheng F, Chen J (2012) Metal–air batteries: from oxygen reduction electrochemistry to cathode catalysts. *Chem Soc Rev* 41(6):2172–2192
19. Lee J, Tai Kim S, Cao R et al (2011) Metal–air batteries with high energy density: Li–air versus Zn–air. *Adv Energy Mater* 1(1):34–50
20. Rahman MA, Wang X, Wen C (2013) High energy density metal–air batteries: a review. *J Electrochem Soc* 160(10):A1759–A1771
21. Cao R, Lee J, Liu M, Cho J (2012) Recent progress in Non-precious catalysts for metal–air batteries. *Adv Energy Mater* 2(7):816–829
22. Pourbaix M (1974) Atlas of electrochemical equilibria in aqueous solutions. M. Pourbaix, published 1974 by NACE, p 644
23. Hartmann P, Bender CL, Vračar M et al (2013) A rechargeable room-temperature sodium superoxide (NaO₂) battery. *Nat Mater* 12(3):228–232
24. Kang S, Mo Y, Ong SP, Ceder G (2014) Nanoscale stabilization of sodium oxides: implications for Na–O₂ batteries. *Nano Lett* 14(2):1016–1020
25. Liu W, Sun Q, Yang Y, Xie J, Fu Z (2013) An enhanced electrochemical performance of a sodium–air battery with graphene nanosheets as air electrode catalysts. *Chem Commun* 49(19):1951–1953
26. Xia C, Black R, Fernandes R, Adams B, Nazar LF (2015) The critical role of phase-transfer catalysis in aprotic sodium oxygen batteries. *Nat Chem* 7(6):496–501
27. Aurbach D, Lu Z, Schechter A et al (2000) Prototype systems for rechargeable magnesium batteries. *Nature* 407(6805):724–727
28. Muldoon J, Bucur CB, Oliver AG et al (2012) Electrolyte roadblocks to a magnesium rechargeable battery. *Energy Environ Sci* 5(3):5941–5950
29. Aurbach D, Weissman I, Gofer Y, Levi E (2003) Nonaqueous magnesium electrochemistry and its application in secondary batteries. *Chem Rec* 3(1):61–73
30. Amir N, Vestfrid Y, Chusid O, Gofer Y, Aurbach D (2007) Progress in nonaqueous magnesium electrochemistry. *J Power Sources* 174(2):1234–1240
31. Howlett P, Khoo T, Mooketsi G, Efthimiadis J, MacFarlane D, Forsyth M (2010) The effect of potential bias on the formation of ionic liquid generated surface films on mg alloys. *Electrochim Acta* 55(7):2377–2383
32. Luder D, Kraysberg A, Ein-Eli Y (2014) Catalyst-free electrochemical Grignard reagent synthesis with room-temperature ionic liquids. *ChemElectroChem* 1(2):362–365
33. Luder D, Ein-Eli Y (2014) Electrochemical Grignard reagent synthesis for ionic-liquid-based magnesium–air batteries. *ChemElectroChem* 1(8):1319–1326
34. Egan D, Ponce de León C, Wood R, Jones R, Stokes K, Walsh F (2013) Developments in electrode materials and electrolytes for aluminium–air batteries. *J Power Sources* 236:293–310

35. Li Q, Bjerrum NJ (2002) QR aluminum as anode for energy storage and conversion: a review. *J Power Sources* 110(1):1–10
36. Mokhtar M, Talib MZM, Majlan EH et al (2015) Recent developments in materials for aluminum–air batteries: a review. *J Ind Eng Chem* 32:1–20
37. Gelman D, Lasman I, Elfimchev S, Starosvetsky D, Ein-Eli Y (2015) Aluminum corrosion mitigation in alkaline electrolytes containing hybrid inorganic/organic inhibitor system for power sources applications. *J Power Sources* 285:100–108
38. Licht S, Levitin G, Yarnitzky C, Tel-Vered R (1999) The organic phase for aluminum batteries. *Electrochem Solid State Lett* 2(6):262–264
39. Licht S, Tel-Vered R, Levitin G, Yarnitzky C (2000) Solution activators of aluminum electrochemistry in organic media. *J Electrochem Soc* 147(2):496–501
40. Rybalka K, Beketaeva L (1993) Anodic dissolution of aluminium in nonaqueous electrolytes. *J Power Sources* 42(3):377–380
41. Geng L, Lv G, Xing X, Guo J (2015) Reversible electrochemical intercalation of aluminum in Mo₆S₈. *Chem Mater* 27(14):4926–4929
42. Jayaprakash N, Das SK, Archer LA (2011) The rechargeable aluminum-ion battery. *Chem Commun* 47(47):12610–12612
43. Lin M, Gong M, Lu B et al (2015) An ultrafast rechargeable aluminium-ion battery. *Nature* 520:324–328
44. Rani JV, Kanakaiah V, Dadmal T, Rao MS, Bhavanarushi S (2013) Fluorinated natural graphite cathode for rechargeable ionic liquid based aluminum–ion battery. *J Electrochem Soc* 160(10):A1781–A1784
45. Wang W, Jiang B, Xiong W et al (2013) A new cathode material for super-valent battery based on aluminium ion intercalation and deintercalation. *Sci Rep* 3:3383
46. Muldoon J, Bucur CB, Gregory T (2014) Quest for nonaqueous multivalent secondary batteries: magnesium and beyond. *Chem Rev* 114(23):11683–11720
47. Revel R, Audichon T, Gonzalez S (2014) Non-aqueous aluminium–air battery based on ionic liquid electrolyte. *J Power Sources* 272:415–421
48. Endres F, El Abedin SZ (2006) Air and water stable ionic liquids in physical chemistry. *Phys Chem Chem Phys* 8(18):2101–2116
49. Gelman D, Shvartsev B, Ein-Eli Y (2014) Aluminum–air battery based on an ionic liquid electrolyte. *J Mater Chem A* 2(47):20237–20242
50. Zhang XG (2001) *Electrochemistry of silicon and its oxide*. Springer, New York
51. Seidel H, Csepregi L, Heuberger A, Baumgärtel H (1990) Anisotropic etching of crystalline silicon in alkaline solutions II. influence of dopants. *J Electrochem Soc* 137(11):3626–3632
52. Glembocki O, Palik E, De Guel G, Kendall D (1991) Hydration model for the molarity dependence of the etch rate of Si in aqueous alkali hydroxides. *J Electrochem Soc* 138(4):1055–1063
53. Raz O, Starosvetsky D, Tsuda T, Nohira T, Hagiwara R, Ein-Eli Y (2007) Macroporous silicon formation on N-Si in room-temperature fluorohydrogenate ionic liquid. *Electrochem Solid State Lett* 10(3):D25–D28
54. Raz O, Shmueli Z, Hagiwara R, Ein-Eli Y (2010) Porous silicon formation in fluorohydrogenate ionic liquids. *J Electrochem Soc* 157(3):H281–H286
55. Cohn G, Eichel RA, Ein-Eli Y (2013) New insight into the discharge mechanism of silicon–air batteries using electrochemical impedance spectroscopy. *Phys Chem Chem Phys* 15(9):3256–3263
56. Cohn G, Altberg A, Macdonald DD, Ein-Eli Y (2011) A silicon–air battery utilizing a composite polymer electrolyte. *Electrochim Acta* 58:161–164
57. Cohn G, Starosvetsky D, Hagiwara R, Macdonald DD, Ein-Eli Y (2009) Silicon–air batteries. *Electrochem Commun* 11(10):1916–1918
58. Cohn G, Ein-Eli Y (2010) Study and development of non-aqueous silicon–air battery. *J Power Sources* 195(15):4963–4970
59. Cohn G, MacDonald DD, Ein-Eli Y (2011) Remarkable impact of water on the discharge performance of a silicon–air battery. *ChemSusChem* 4(8):1124–1129
60. Jakes P, Cohn G, Ein-Eli Y, Scheiba F, Ehrenberg H, Eichel R (2012) Limitation of discharge capacity and mechanisms of air-electrode deactivation in silicon–air batteries. *ChemSusChem* 5(11):2278–2285
61. Blurton KF, Sammells AF (1979) Metal/air batteries: their status and potential—a review. *J Power Sources* 4(4):263–279

62. Sathyanarayana S, Munichandraiah N (1981) A new magnesium–air cell for long-life applications. *J Appl Electrochem* 11(1):33–39
63. Aurbach D, Schechter A, Moshkovich M, Cohen Y (2001) On the mechanisms of reversible magnesium deposition processes. *J Electrochem Soc* 148(9):A1004–A1014
64. Aurbach D, Suresh GS, Levi E et al (2007) Progress in rechargeable magnesium battery technology. *Adv Mater* 19(23):4260–4267
65. Sawyer DT, Valentine JS (1981) How super is superoxide? *Acc Chem Res* 14(12):393–400
66. Mohamed M, Yabe T, Baasandash C et al (2008) Laser-induced magnesium production from magnesium oxide using reducing agents. *J Appl Phys* 104(11):113110
67. Rongti L, Wei P, Sano M (2003) Kinetics and mechanism of carbothermic reduction of magnesia. *Metall Mater Trans B* 34(4):433–437
68. Aurbach D (1999) *Nonaqueous electrochemistry*. CRC Press, Boca Raton
69. Peled E, Straze H (1977) The kinetics of the magnesium electrode in thionyl chloride solutions. *J Electrochem Soc* 124(7):1030–1035
70. Lu Z, Schechter A, Moshkovich M, Aurbach D (1999) On the electrochemical behavior of magnesium electrodes in polar aprotic electrolyte solutions. *J Electroanal Chem* 466(2):203–217
71. Peled E (1979) The electrochemical behavior of alkali and alkaline earth metals in nonaqueous battery systems—the solid electrolyte interphase model. *J Electrochem Soc* 126(12):2047–2051
72. Aurbach D, Moshkovich M, Schechter A, Turgeman R (2000) Magnesium deposition and dissolution processes in ethereal Grignard salt solutions using simultaneous EQCM-EIS and in situ FTIR spectroscopy. *Electrochem Solid State Lett* 3(1):31–34
73. Bard AJ, Faulkner LR (1980) *Electrochemical methods: fundamentals and applications*, vol 2. Wiley, New York
74. Gofer Y, Chusid O, Gizbar H et al (2006) Improved electrolyte solutions for rechargeable magnesium batteries. *Electrochem Solid State Lett* 9(5):A257–A260
75. Mizrahi O, Amir N, Pollak E et al (2008) Electrolyte solutions with a wide electrochemical window for rechargeable magnesium batteries. *J Electrochem Soc* 155(2):A103–A109
76. Shiga T, Hase Y, Kato Y, Inoue M, Takechi K (2013) A rechargeable non-aqueous Mg–O₂ battery. *Chem Commun* 49(80):9152–9154
77. Feng Z, NuLi Y, Wang J, Yang J (2006) Study of key factors influencing electrochemical reversibility of magnesium deposition and dissolution. *J Electrochem Soc* 153(10):C689–C693
78. NuLi Y, Yang J, Wang J, Xu J, Wang P (2005) Electrochemical magnesium deposition and dissolution with high efficiency in ionic liquid. *Electrochem Solid State Lett* 8(11):C166–C169
79. NuLi Y, Yang J, Wu R (2005) Reversible deposition and dissolution of magnesium from BMIMBF₄ ionic liquid. *Electrochem Commun* 7(11):1105–1110
80. NuLi Y, Yang J, Wang P (2006) Electrodeposition of magnesium film from BMIMBF₄ ionic liquid. *Appl Surf Sci* 252(23):8086–8090
81. Wang P, NuLi Y, Yang J, Feng Z (2006) Mixed ionic liquids as electrolyte for reversible deposition and dissolution of magnesium. *Surf Coat Technol* 201(6):3783–3787
82. Cheek G, O’Grady W, El Abedin SZ, Moustafa E, Endres F (2008) Studies on the electrodeposition of magnesium in ionic liquids. *J Electrochem Soc* 155(1):D91–D95
83. Kakibe T, Yoshimoto N, Egashira M, Morita M (2010) Optimization of cation structure of imidazolium-based ionic liquids as ionic solvents for rechargeable magnesium batteries. *Electrochem Commun* 12(11):1630–1633
84. Yoshimoto N, Matsumoto M, Egashira M, Morita M (2010) Mixed electrolyte consisting of ethylmagnesiumbromide with ionic liquid for rechargeable magnesium electrode. *J Power Sources* 195(7):2096–2098
85. Yoshimoto N, Hotta K, Egashira M, Morita M (2012) Electrochemical behavior of magnesium in mixed solutions consisting of ionic liquid and alkylmagnesiumbromides with different alkyl-chains. *Electrochemistry* 80(10):774–776
86. Khoo T, Howlett PC, Tsagouria M, MacFarlane DR, Forsyth M (2011) The potential for ionic liquid electrolytes to stabilise the magnesium interface for magnesium/air batteries. *Electrochim Acta* 58:583–588
87. Khoo T, Somers A, Torriero AA, MacFarlane DR, Howlett PC, Forsyth M (2013) Discharge behaviour and interfacial properties of a magnesium battery incorporating trihexyl (tetradecyl) phosphonium based ionic liquid electrolytes. *Electrochim Acta* 87:701–708
88. Abraham K (2008) A brief history of non-aqueous metal–air batteries. *ECS Trans* 3(42):67–71

89. Curto VF, Scheuermann S, Owens RM et al (2014) Probing the specific ion effects of biocompatible hydrated choline ionic liquids on lactate oxidase biofunctionality in sensor applications. *Phys Chem Chem Phys* 16(5):1841–1849
90. Fukaya Y, Iizuka Y, Sekikawa K, Ohno H (2007) Bio ionic liquids: room temperature ionic liquids composed wholly of biomaterials. *Green Chem* 9(11):1155–1157
91. Vijayaraghavan R, Thompson B, MacFarlane D et al (2009) Biocompatibility of choline salts as crosslinking agents for collagen based biomaterials. *Chem Commun* 46(2):294–296
92. Weaver KD, Kim HJ, Sun J, MacFarlane DR, Elliott GD (2010) Cyto-toxicity and biocompatibility of a family of choline phosphate ionic liquids designed for pharmaceutical applications. *Green Chem* 12(3):507–513
93. Jia X, Yang Y, Wang C et al (2014) Biocompatible ionic Liquid-Biopolymer electrolyte-enabled thin and compact magnesium–air batteries. *ACS Appl Mater Interfaces* 6(23):21110–21117
94. Inoishi A, Ju Y, Ida S, Ishihara T (2013) Mg–air oxygen shuttle batteries using a ZrO₂-based oxide ion-conducting electrolyte. *Chem Commun* 49(41):4691–4693
95. Yang S, Knickle H (2002) Design and analysis of aluminum/air battery system for electric vehicles. *J Power Sources* 112(1):162–173
96. Pistoia G (2014) Lithium-ion batteries: advances and applications. Elsevier, Amsterdam
97. Wang J, Wang J, Shao H, Zhang J, Cao C (2007) The corrosion and electrochemical behaviour of pure aluminium in alkaline methanol solutions. *J Appl Electrochem* 37(6):753–758
98. Abd-El-Nabey B, Khalil N, Khamis E (1984) Alkaline corrosion of aluminium in water-organic solvent mixtures. *Surf Technol* 22(4):367–376
99. Shao H, Wang J, Wang X, Zhang J, Cao C (2004) Anodic dissolution of aluminium in KOH ethanol solutions. *Electrochem Commun* 6(1):6–9
100. Mukherjee A, Basumallick IN (1996) Complex behaviour of aluminium dissolution in alkaline aqueous 2-propanol solution. *J Power Sources* 58(2):183–187
101. Wang J, Wang J, Shao H et al (2009) The corrosion and electrochemical behavior of pure aluminium in additive-containing alkaline methanol–water mixed solutions. *Mater Corros* 60(4):269–273
102. Spendelov JS, Wieckowski A (2007) Electrocatalysis of oxygen reduction and small alcohol oxidation in alkaline media. *Phys Chem Chem Phys* 9(21):2654–2675
103. Lai SC, Koper MT (2009) Ethanol electro-oxidation on platinum in alkaline media. *Phys Chem Chem Phys* 11(44):10446–10456
104. Meng H, Shen PK (2006) Novel Pt-free catalyst for oxygen electroreduction. *Electrochem Commun* 8(4):588–594
105. Li C, Ji W, Chen J, Tao Z (2007) Metallic aluminium nanorods: synthesis via vapor-deposition and applications in Al/air batteries. *Chem Mater* 19(24):5812–5814
106. Zein El Abedin S, Moustafa E, Hempelmann R, Natter H, Endres F (2006) RAA 25 electrodeposition of nano- and microcrystalline aluminium in three different air and water stable ionic liquids. *ChemPhysChem* 7(7):1535–1543
107. Galova M (1980) Electrodeposition of aluminium from organic aprotic solvents. *Surf Technol* 11(5):357–369
108. Moustafa E, Zein El Abedin S, Shkurankov A et al (2007) Electrodeposition of Al in 1-butyl-1-methylpyrrolidinium bis (trifluoromethylsulfonyl) amide and 1-ethyl-3-methylimidazolium bis (trifluoromethylsulfonyl) amide ionic liquids: in situ STM and EQCM studies. *J Phys Chem B* 111(18):4693–4704
109. Abbott AP, Qiu F, Abood HM, Ali MR, Ryder KS (2010) Double layer, diluent and anode effects upon the electrodeposition of aluminium from chloroaluminate based ionic liquids. *Phys Chem Chem Phys* 12(8):1862–1872
110. Jiang T, Chollier Brym M, Dubé G, Lasia A, Brisard G (2006) RAA179 electrodeposition of aluminium from ionic liquids: part i—electrodeposition and surface morphology of aluminium from aluminium chloride (AlCl₃)–1-ethyl-3-methylimidazolium chloride ([EMIm] Cl) ionic liquids. *Surf Coat Technol* 201(1):1–9
111. Zhao Y, VanderNoot T (1997) RAA 180 electrodeposition of aluminium from nonaqueous organic electrolytic systems and room temperature molten salts. *Electrochim Acta* 42(1):3–13
112. Zhao Y, VanderNoot T (1997) Electrodeposition of aluminium from room temperature AlCl₃–TMPAC molten salts. *Electrochim Acta* 42(11):1639–1643
113. Gilliam R, Graydon J, Kirk D, Thorpe S (2007) A review of specific conductivities of potassium hydroxide solutions for various concentrations and temperatures. *Int J Hydrog Energy* 32(3):359–364

114. See DM, White RE (1997) Temperature and concentration dependence of the specific conductivity of concentrated solutions of potassium hydroxide. *J Chem Eng Data* 42(6):1266–1268
115. El Abedin SZ, Moustafa E, Hempelmann R, Natter H, Endres F (2005) Additive free electrodeposition of nanocrystalline aluminium in a water and air stable ionic liquid. *Electrochem Commun* 7(11):1111–1116
116. Plechkova NV, Seddon KR (2008) Applications of ionic liquids in the chemical industry. *Chem Soc Rev* 37(1):123–150
117. Zhang J, Xu W, Li X, Liu W (2010) Air dehydration membranes for nonaqueous lithium–air batteries. *J Electrochem Soc* 157(8):A940–A946
118. Reed L, Ortiz S, Xiong M, Menke E (2015) A rechargeable aluminum-ion battery utilizing a copper hexacyanoferrate cathode in an organic electrolyte. *Chem Commun* 51(76):14397–14400
119. Inoishi A, Kim H, Sakai T, Ju Y, Ida S, Ishihara T (2015) Discharge performance of solid-state oxygen shuttle metal–air battery using ca-stabilized ZrO₂ electrolyte. *ChemSusChem* 8(7):1264–1269
120. Isaacs J, Taricco F, Michaud V, Mortensen A (1991) Chemical stability of zirconia-stabilized alumina fibers during pressure infiltration by aluminum. *Metall Trans A* 22(12):2855–2862
121. Shvartsev B, Cohn G, Shasha H, Eichel R, Ein-Eli Y (2013) Reference electrode assembly and its use in the study of fluorohydrogenate ionic liquid silicon electrochemistry. *Phys Chem Chem Phys* 15(41):17837–17845
122. Rotariu L, Zamfir L, Bala C (2010) Low potential thiocholine oxidation at carbon nanotube-ionic liquid gel sensor. *Sens Actuators B Chem* 150(1):73–79
123. Wang Y (2009) Recent research progress on polymer electrolytes for dye-sensitized solar cells. *Solar Energy Mater Solar Cells* 93(8):1167–1175
124. Fergus JW (2010) Ceramic and polymeric solid electrolytes for lithium-ion batteries. *J Power Sources* 195(15):4554–4569
125. Stephan AM (2006) Review on gel polymer electrolytes for lithium batteries. *Eur Polym J* 42(1):21–42
126. Egashira M, Todo H, Yoshimoto N, Morita M (2008) Lithium ion conduction in ionic liquid-based gel polymer electrolyte. *J Power Sources* 178(2):729–735
127. Kumar D, Hashmi S (2010) Ionic liquid based sodium ion conducting gel polymer electrolytes. *Solid State Ionics* 181(8):416–423
128. Ferrari S, Quartarone E, Mustarelli P et al (2010) Lithium ion conducting PVdF-HFP composite gel electrolytes based on *N*-methoxyethyl-*N*-methylpyrrolidinium bis (trifluoromethanesulfonyl)-imide ionic liquid. *J Power Sources* 195(2):559–566
129. Tsuda T, Nohira T, Nakamori Y, Matsumoto K, Hagiwara R, Ito Y (2002) A highly conductive composite electrolyte consisting of polymer and room temperature molten fluorohydrogenates. *Solid State Ion* 149(3):295–298
130. Zhong X, Zhang H, Liu Y et al (2012) High-capacity silicon–air battery in alkaline solution. *ChemSusChem* 5(1):177–180
131. Inoishi A, Sakai T, Ju Y, Ida S, Ishihara T (2013) A rechargeable Si–air solid state oxygen shuttle battery incorporating an oxide ion conductor. *J Mater Chem A* 1(48):15212–15215



Challenges Considering the Degradation of Cell Components in Commercial Lithium-Ion Cells: A Review and Evaluation of Present Systems

Karin Kleiner¹ · Helmut Ehrenberg¹

Received: 24 April 2016 / Accepted: 8 April 2017 / Published online: 3 May 2017
© Springer International Publishing Switzerland 2017

Abstract Owing to the high energy and power density of lithium-ion cells (1200 Wh kg⁻¹ and 200 Wh kg⁻¹) and due to their compact design, they are used as energy storage devices in many contemporary mobile applications such as telecommunication systems, notebooks and domestic appliances. Meanwhile their application is not limited only to consumer electronics, they are also standard in hybrid electric (HEVs) and electric vehicles (EVs). However, the profitable application of lithium-ion cells in the automobile industry requires lower costs, lower safety risks, a higher specific energy density and a longer lifetime under everyday conditions. All these aspects are directly or indirectly related to the degradation of the materials in a lithium-ion cell. One possibility for reducing the costs is a second life application of the cells after their usage in (H)EVs. In order to enable this, the safety risks at the end of life of a cell operated in a vehicle have to be reliably predicted. This requires a fundamental knowledge about underlying material degradations during operation. The safety risk of a lithium-ion cell increases during operation because the voltage windows in which the electrodes are cycled shift, resulting in a higher possibility that at least one electrode is operated in a meta- or unstable state. Furthermore, higher impedances due to material degradations lead to increasing heat generation and therefore to an increase in the risk of failure. Higher energy densities can be achieved by raising the end of charge voltage of a cell, causing additional safety risks because many cathode materials tend to decompose at high voltages. Another possibility for achieving higher energy densities is to use

Chapter 5 was originally published as Kleiner, K. & Ehrenberg, H. Top Curr Chem (Z) (2017) 375: 54. DOI 10.1007/s41061-017-0139-2.

✉ Karin Kleiner
karin.kleiner@tum.de

¹ Karlsruhe Institute of Technology (KIT), Institute for Applied Materials-Energy Storage Systems (IAM-ESS), 76344 Eggenstein-Leopoldshafen, Germany

nickel-rich or lithium-excess cathode materials, since cathodes are currently limiting the capacity of lithium-ion cells. But these systems show a poor cycling stability (a higher degradation rate). The lifetime of a lithium-ion cell is limited by the degradation of the individual cell components. Although the degradation of materials is the key consideration in achieving lower costs, a higher safety standard, higher energy densities and a longer lifetime, the degradation of the individual cell components in dependence on the operation conditions has hardly been investigated and is poorly understood. The present work reviews known material degradations in commercial lithium-ion cells, shows a way to analyze such degradations in dependence on the operation conditions and describes how these degradation processes lead to observed performance drops.

Keywords Degradation of Li-ion batteries · Cell components · Safety risks · Second life application

1 Introduction

Since the market introduction of lithium-ion cells in 1991 by SONY, the demand has increased continuously from around 5000 MWh in 2000 to around 50,000 MWh in 2014 [1]. The worldwide demand for lithium-ion cells is driven mainly by consumer electronics and power tools. Recent efforts to reduce CO₂ emissions, especially in Western Europe and in the US, led to an expanded production of hybrid- and electric-vehicles (H-/EV), in which a lithium-ion power unit is implemented. With the application of lithium-ion batteries in the automobile industry, new lifetime requirements are affiliated. While the product life cycle of consumer electronics is often shorter than two years, the lifetime of lithium-ion cells in an electric or hybrid electric vehicle should reach or even exceed ten years [2]. However, material degradations still limit the lifetime of lithium-ion cells to shorter periods of usage. Under harsh cycling conditions such as high currents, high temperatures, high states-of-charge (SoC) and high depths-of-discharge (DoD), the end-of-life (EoL) of commercial lithium-ion cells can be reached much faster than required [3]. There are two dominating degradation processes: the degradation of active materials and the formation/growth of corrosion layers [3–9]. In order elucidate the origin of these degradations, the thermodynamic reasons for material degradation are discussed in Sect. 2.

Section 2.2 reviews which kind of material degradations are observed in commercial lithium-ion cells. This section focuses on the anodic corrosion layer growth and fatigue as well as on structural changes of cathode materials.

The issue of corrosion layer formation on the anode surface (solid electrolyte interface, SEI) has been known since 1979, when Peled described the instability of organic electrolytes at anodic potentials lower than 0.8 V vs Li⁺/Li [10]. Since the market introduction of lithium-ion cells, much efforts has been put into the stabilization of the SEI, which ideally prevents the reduction of electrolyte components during cycling [11–14]. However, even the initial formation of the corrosion layer consumes a lot of active lithium, which is lost for the ongoing cycling. Therefore, the formation of the SEI reduces the specific capacity on the cell

level. Furthermore, the volumetric work of the negative electrode upon cycling causes cracks in the active material which increase the surface area and result in an ongoing formation of the SEI during the entire lifetime of a cell [6, 11]. Exfoliation and self-discharge reactions lead additionally to SEI formation reactions and therefore to the consumption of active lithium [11].

The degradation of cathode materials within commercial lithium-ion cells depends on the type of material. In general, three types of cathode materials are used: Layered oxides of the type LiMO_2 ($M = \text{Ni, Co, Mn, Al}$), spinels of the type LiM_2O_4 ($M = \text{Ni, Mn}$) and LiFePO_4 with an olivine structure. Layered oxides have a high energy density but they show a poor power density [2, 15]. In general they suffer from changes in the surface structure upon cycling, which lead to an impedance rise [15]. Furthermore, the materials are unstable in highly delithiated states. High states of charge and high temperatures accelerate the degradation processes. In contrast to layered oxides, spinels show good power but poor energy density [2]. Manganese-containing spinels (the most often used spinel-type electrodes in commercial lithium-ion cells) suffer from Mn-dissolution. Two mechanisms are proposed and discussed: Either Mn^{3+} disproportionates to Mn^{4+} and Mn^{2+} at low states of charge (and Mn^{2+} can dissolve) or HF is formed out of the conducting salt LiPF_6 (most used lithium-ion-providing salt in commercial lithium-ion batteries), which reacts in an acidic corrosion reaction with the spinel structure [7, 20]. High temperatures lead to an acceleration of the Mn-dissolution. LiFePO_4 seems to be more stable, but both the energy and the power density of this polyanion compound are relatively low compared to the layered oxides and the spinels. According to the different advantages and disadvantages of the cathode materials, they are used for different applications: e.g. layered oxides are used in power units for electric vehicles, where the energy density plays an important role. Spinel fits better to an application in hybrid electric vehicles, where the power density is more important. In the field of stationary energy storage systems the lifetime is a crucial point and therefore LiFePO_4 would be a good choice.

The degradation of the electrochemical inactive components like the separator, the current collectors and the binder play a minor role considering the performance drop during degradation of a commercial lithium-ion cell. Nevertheless, these issues are also briefly reviewed and discussed in Sect. 2.2.

While the abovementioned degradation processes have been extensively studied, the interactions of the single processes in the full-cell are poorly understood [8, 9]. With the degradation of the active material and the formation of corrosion layers, the distribution of active lithium, the state of charge (SoC) of the cathode relative to the SoC of the anode, changes. This means that in spite of a constant cell voltage, the potential windows for the individual electrodes change. The cutoff voltages for stable and safe operation of a full cell are given by the cell suppliers. The cell voltage is determined as the difference between the cathode potential (or the cathode voltage, measured against a reference) and the anode potential (or anode voltage versus the same reference). In case the potential curves of the electrodes are shifted against each other due to the formation of corrosion layers, or one electrode curve is compressed due to a loss of active material, the upper and lower cutoff voltages can be derived from two points on the potential curves, for which at least one electrode is not stable anymore. As a consequence, the cell will degrade faster

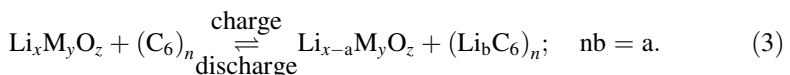
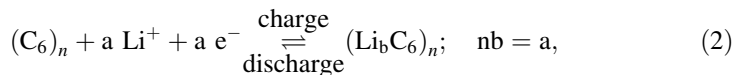
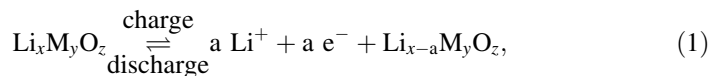
due to irreversible side reactions. The question as to which degradation process dominates in a full cell and how degradation processes depend on operation conditions is widely unclear [21].

Not only does the degradation of cell components limit the lifetime of commercial lithium-ion cells, it also increases the risk of a failure and therefore the risk of a thermal runaway, an uncontrolled discharge reaction of a lithium-ion cell [22]. The starting reactions of a thermal runaway are decomposition reactions of SEI components, which can be induced by a short circuit, harsh operation conditions and/or an increase in temperature due to high impedances. The decomposition reactions are highly exothermic, whereby the system is heated up and the protection layer (SEI) disappears. Further electrolyte components reach the anode surface and are reduced, which also generates additional heat. During the SEI and electrolyte decomposition, flammable gases are evolved. Above 130 °C the common polymeric separator melts, which causes a short circuit, resulting in the start of cathode decomposition, accompanied by the formation of oxygen gas (layered oxides and spinels). At this point, the flammable gases start to burn. However, to start such a reaction cascade a high temperature is necessary [23]. Especially due to cathode degradations the impedance increases upon cycling [16, 17]. This leads to a lower cycling efficiency and the heat production increases. Furthermore, high amounts of SEI products, formed during cycling, provide a lot of energy, which can be evolved as heat during exothermic decomposition reactions.

2 Results and Discussion

2.1 Basic Electrochemistry

The origin of material degradations in lithium-ion cells is driven by thermodynamics. This section addresses the basic thermodynamics in lithium-ion batteries and discusses under which conditions cell materials are unstable. The basic reactions during charge and discharge of a lithium-ion cell are shown in Eqs. (1–3), whereby (1) and (2) describe the half-cell reactions of the individual electrodes and (3) is the resulting full-cell reaction:



If lithium-ion and electron conductors are separated by a lithium-ion conductor but electronic insulator, charge separation (polarization) takes place (Fig. 1). Depending on the half-cell potentials, the amount of separated charges varies.

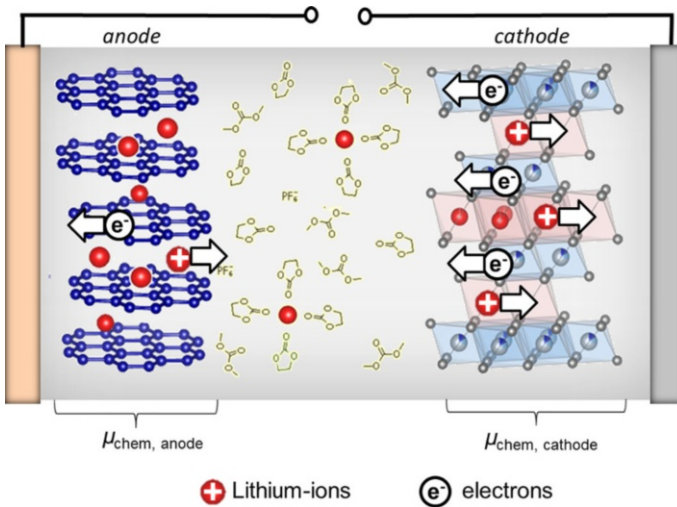


Fig. 1 Schematic illustration of the charge separation within the solid electrodes of a lithium-ion battery

The mobile charge carriers (mcc) lead to a chemical potential of the electrodes, which differs from the standard potential μ_{mcc}^0 in an ideal solution by the natural logarithm of the activities a_{mcc} multiplied by the absolute temperature T and the universal gas constant R , Eq. (4). The activity of a species (here: lithium ions Li^+ or electrons e^-) is its concentration times a correction factor, in which shielding effects due to differences between the ideal and the real environment around the mcc are considered.

$$\mu_{chem,i} = \mu_{Li^+}^0 + \mu_{e^-}^0 + RT \cdot \ln(a_{Li^+} \cdot a_{e^-}). \quad (4)$$

Due to differing amounts of mobile charge carriers, which are characteristic for each material, the chemical potential of the anode and the cathode differs, Eq. (5). Note that the term “anode” is used for the material which operates at lower potentials and “cathode” for the material which operates at higher potentials. In contrast, in electrochemistry the “cathode” and “anode” are the electrodes at which the reduction or oxidation takes place, respectively. In case of a lithium-ion cell, both definitions match only for the discharge at which the reaction proceeds voluntarily.

$$\mu_{chem, anode} \neq \mu_{chem, cathode}. \quad (5)$$

The chemical Gibbs free energy $\Delta G'$ is the sum over the chemical potentials $\mu_{chem,i}$ of the individual electrodes i multiplied with the stoichiometric factor ν_i given by Eq. (6).

$$\Delta G' = \sum_i v_i \cdot \mu_{\text{chem}, i} \neq 0. \quad (6)$$

In general, the difference in the Gibbs free energy ΔG is the work obtainable from an isothermic and isobaric system, as it is ideally present in lithium-ion cells. However, $\Delta G'$ describes only the energy of the system, which is obtainable due to the different concentrations of mobile charge carriers in the anode and cathode. Because of the electronically isolating separator, the diffusion of charge carriers to compensate the different lithium-ion and electron concentrations is impeded. The charge separation (or polarization) leads to a voltage between the electrodes, which can be measured as the open-circuit voltage (OCV) between the anode and the cathode (Fig. 2).

In order to describe the whole Gibbs free energy ΔG of the system, its electric energy $zF\phi_i$ has to be considered, as well. ϕ_i is the Galvani-potential of the electrode i . The difference in the Galvani-potential of the cathode and the anode, multiplied by the amount of exchanged electrons z per full-cell reaction (3) and Faraday's constant F gives the maximum work which a lithium-ion cell can deliver. The Gibbs free energy of the system thus can be reformulated as in Eq. (7).

$$\Delta G = \sum_i v_i \cdot (\mu_{\text{chem}, i} - zF\phi_i) = 0. \quad (7)$$

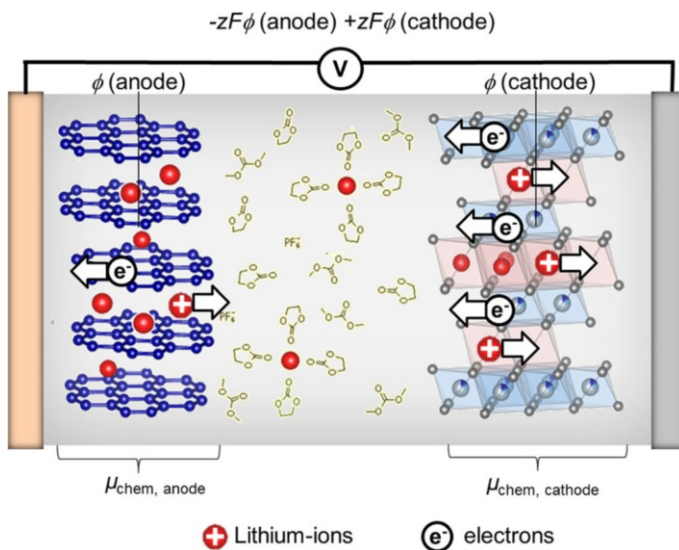


Fig. 2 The difference in the Galvani-potential of the two electrodes gives the open-circuit voltage (OCV), which results from the separation of charges within the individual electrodes. The intrinsic amount of mobile charges is characteristic for each material and determines its Galvani-potential ϕ . A counter electrode is necessary to determine the Galvani-potential of an electrode

The difference in the Galvani-potential (multiplied with zF) acts against the difference in the chemical potential (Eq. (5)). Therefore, the Gibbs free energy is zero (Eq. (7)) and the system is in equilibrium. The separation of the anode and the cathode parts in Eq. (8) results in Eq. (9). The chemical potential of an electrode plus its Galvani-potential (multiplied with zF) gives the electrochemical potential $\tilde{\mu}_i$ of an electrode i , Eq. (10).

$$\mu_{\text{chem, cathode}} - \mu_{\text{chem, anode}} = zF\phi_{\text{cathode}} - zF\phi_{\text{anode}}, \quad (8)$$

$$\mu_{\text{chem, cathode}} - zF\phi_{\text{cathode}} = \mu_{\text{chem, anode}} - zF\phi_{\text{anode}}, \quad (9)$$

$$\tilde{\mu}_i = \mu_{\text{chem, i}} - zF\phi_i. \quad (10)$$

If an external voltage is applied to the cell or the outer electronic circuit is closed (with a resistance in between), the differences in the amount of mobile charge carriers lead to a diffusion of lithium ions and electrons till the difference in the Galvani-potential is zero (closed circuit) or till the difference in the chemical potential compensates the applied voltage (difference in the Galvani-potential). The relation between the anode and the cathode electrochemical potentials as described above applies only if no reactions other than (1–3) take place. If the HOMO (highest occupied molecular orbital) or LUMO (lowest unoccupied molecular orbital) of an actual electrochemically inactive cell component lies for some reason between the chemical potential of the cathode and the anode, this cell component is either reduced or oxidized. Operation conditions such as the temperature and the SoC can change the LUMO and the HOMO level or the chemical potential (the Fermi Level) of a cell component. Further kinetic issues, mainly determined by the applied current, introduce inhomogeneities within the electrodes and spatially resolved degradations are observed. Therefore, stability and degradation related issues depend severely on operating conditions. Examples of side reactions, which are potential dependent and in most cases irreversible, are electrolyte decompositions, which lead to a growth of corrosion layers, dendrite formation, self-discharge, binder decomposition, transition-metal dissolutions and surface-near composition changes in the active materials. Besides, undesired oxidation and reduction reactions high temperatures can lead to a loss of porosity in the polymer-separator. Cracks, formed due to volume changes of the active materials upon cycling, may lead to isolated particles and make the reformation of the solid electrolyte passivation layers necessary.

2.2 Material Issues Related to Degradation

A widely used lithium-ion cell design consists of an anode (mostly graphite) and a cathode (layered oxides, spinels or phosphoolivines) separated by an electronically insulating, but electrolyte penetrating and thereby ionic-conducting polymer (laminated polypropylene/polyethylene/polypropylene). The ionic conductivity between the anode and the cathode arises from the electrolyte, which is commonly LiPF_6 , dissolved in organic, carbonate based solvents. A schematic illustration of a

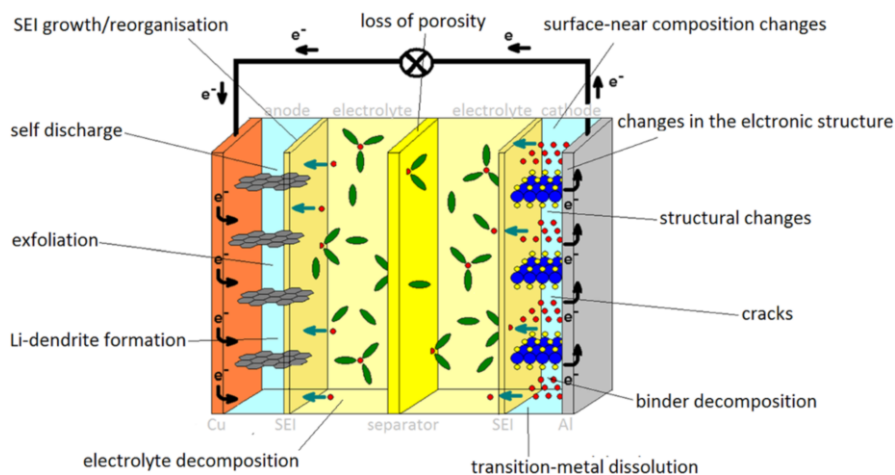


Fig. 3 Illustration of specific degradation processes related to various cell components (anode, cathode, electrolyte, separator, current collectors and corrosion/interface layers) in a lithium-ion cell. The schematic drawing of the cell was inspired by Xu et al. [11]

lithium-ion cell, which is inspired by Xu et al. [11], is given in Fig. 3. A huge variety of different degradation processes in lithium-ion cells are known and concern all cell components [6–9]. In the following sections the different types of degradation reactions are briefly introduced and explained.

2.2.1 SEI Growth/Reorganization

Much effort has been put into the investigation of the graphite electrolyte interface [6, 11, 24–30]. Graphite (and almost all other active materials) performs periodic volumetric work during cycling. This can be observed either with atomic force microscopy or by a change in the lattice parameters of the unit cell (powder or neutron diffraction analysis) [31, 32]. Even if a highly passivating and stable solid electrolyte interface (SEI) is formed on the anode surface during the initial cycles, the expansion of the graphite particles during subsequent cycling leads to small cracks in the SEI [6]. Additional electrolyte molecules can percolate through the protective film, reach the anode surface and become reduced at anodic potential below 0.8 V versus Li^+/Li [5]. Therefore, the SEI is continuously growing upon cycling. Figure 4 shows scanning electron microscopy (SEM) pictures of a calendaric aged and a fatigued graphite surface. While the calendaric aged surface shows well defined contours and characteristic structures of graphite, the fatigued surface appears smooth. Amorphous parts within the particles are identified which can probably be attributed to SEI decomposition products.

The protection layer is formed from electrolyte decomposition products and lithium ions (immobilized lithium salts) [27, 33]. Due to charge neutrality these lithium ions originate from the amount of lithium that is transferred from the cathode to the anode, and vice versa, upon cycling. SEI formation or growth can only include the consumption of lithium ions from the electrolyte if a PF_6^- counter

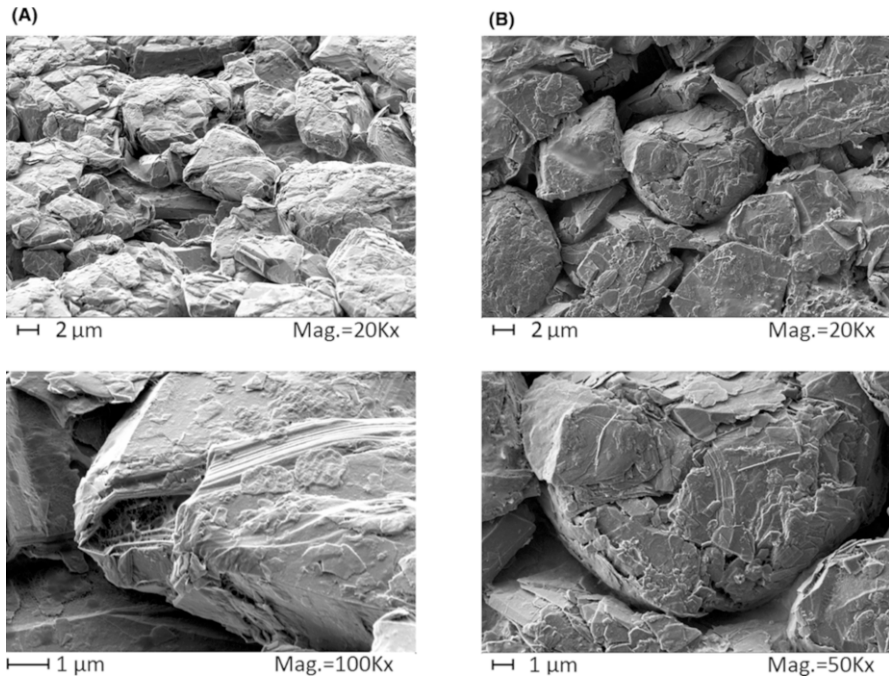


Fig. 4 Scanning electron microscopy pictures of calendaric aged (a) and cycled graphite (b). The calendaric aged sample was stored for 34 weeks at room temperature (30% SOC) while the fatigued sample was cycled with 8C, at 50 °C and between 79 and 81% SOC. The samples are from a 7 Ah commercial lithium-ion battery

anion is immobilized, too [21]. The amount of active lithium dictates the capacity of a full-cell within a fixed upper and lower cutoff voltage. Lithium ions consumed during SEI formation or growth are missing in the subsequent (de-)intercalation process, because the amount of transferable lithium (from the cathode) is limited. Therefore, the SEI growth leads necessarily and directly to capacity losses [34]. Many researchers also propose that the increasing surface film causes an increase in impedance [6, 8, 29, 35]. However, in our studies of commercial 7 and 20 Ah lithium-ion cells, a decrease in the graphite impedance with increasing fatigue was observed. These results hold for all investigated cells, although much more active lithium was consumed during cycling on the anode surface of the fatigued cells compared to the corresponding pristine cells [3, 21]. The reason is probably the increasing surface area which accompanies fatigue. This may accelerate the (de-)intercalation reaction more than the SEI growth hinders the (de-)intercalation process.

2.2.2 Self Discharge

Fewer efforts have been made to understand self-discharge processes in lithium-ion cells, although these processes are partially irreversible and can also lead to SEI

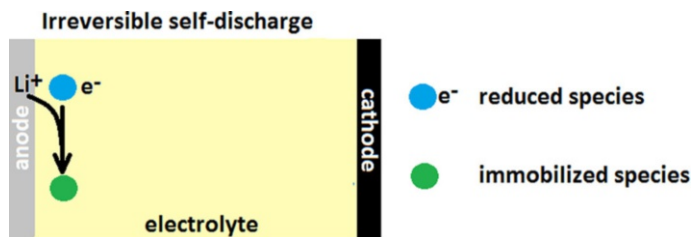


Fig. 5 Irreversible reduction of electrolyte molecules at the anode surface during storage. Due to charge neutrality, a lithium ion diffuses towards the reduced molecule and forms an immobilized salt

growth [36, 37]. Compared to other battery technologies, the self-discharge rates of lithium-ion cells are relatively low (lithium-ion cell: 2–3% per month; nickel-hydrogen: roughly 1% per day [38]). In principle, self-discharge reactions can be divided into reversible reactions, where the capacity can be gained back in the subsequent charge or discharge, and irreversible reactions, which decrease the cell capacity [36]. Besides mechanical issues (poor electronic or ionic isolation between cell components) the reduction of electrolyte molecules on the graphite surface during storage is the most dominant process affecting self-discharge in lithium-ion cells, illustrated in Fig. 5 [37]. The reductive decomposition of electrolyte molecules (the electron is provided by the graphite) during storage leads to lithium-ion diffusion from the graphite bulk towards the electrode–electrolyte interface to preserve charge neutrality. Once lithium ions have reached the surface, they form immobilized lithium salts with electrolyte decomposition products. For the subsequent (de-)intercalation these lithium ions are lost, thus leading to an irreversible capacity loss.

Shuttle mechanisms have been discussed as reasons for reversible self-discharge effects. The upper picture in Fig. 6 illustrates the principle of a reversible shuttle process. Byproducts of the electrolyte SEI formation or other electrolyte components are reduced on the anode and oxidized on the cathode within the applied voltage window. Oxalate is one such molecule. It can be formed out of CO_2 on the anode, dissolves in the electrolyte and is oxidized back to CO_2 on the cathode [39]. This process is a reversible shuttle mechanism. However, if oxalate or CO_2 reacts further to Li_2CO_3 , the process becomes irreversible (Fig. 6, middle and bottom picture). Active lithium is immobilized in Li_2CO_3 which leads again to capacity losses [40].

2.2.3 Exfoliation

If the passivation layer on the anode surface, which is formed of electrolyte molecules and additives, covers the anode surface incompletely, exfoliation can take place [6, 11]. The exfoliation process is illustrated in Fig. 7. Between 1.5 V and 0.8 V (graphite vs Li^+/Li) solvated lithium ions can be intercalated between two graphite layers (Fig. 7b) [24, 32]. At voltages lower than 0.8 V vs Li^+/Li , the molecules of the solvation shell will be reduced [5, 41]. Carbonates, which built up the solvation sheath, react towards gas formation within the graphite network (Fig. 7c) [42]. Equations (11) and (12) show the reduction process of

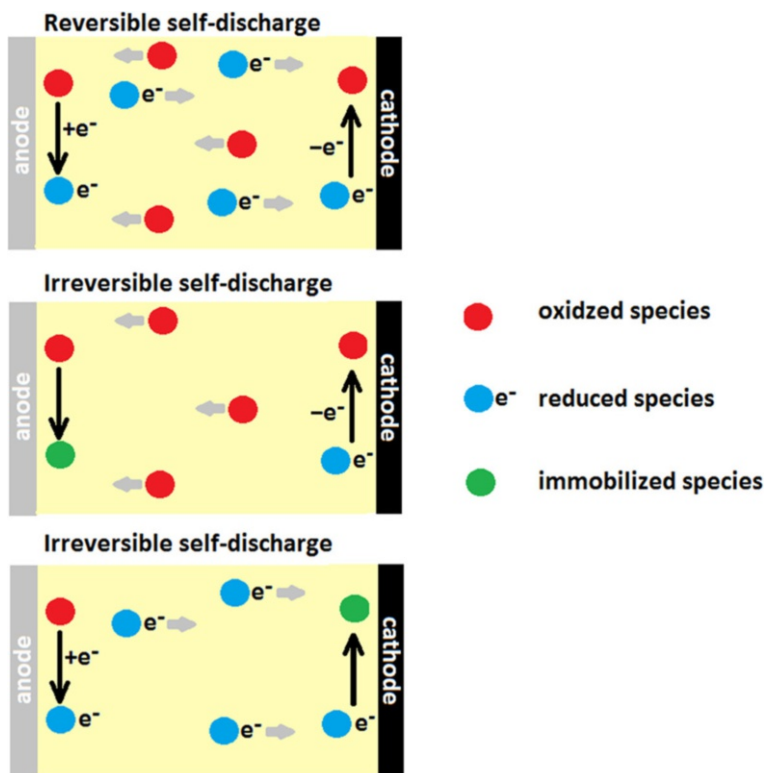
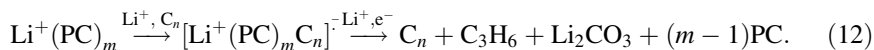
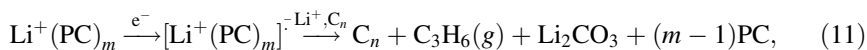


Fig. 6 Reversible shuttle mechanism, which leads to self-discharge without any capacity loss (*upper part*), and how this mechanism can proceed to irreversible self-discharge processes (*two lower parts*)

propylencarbonate as published by Xu et al. [11]. The gaseous products expand and cause cracks in the material.



Further carbonates, which reach the graphite surface at voltages lower than 0.8 V versus lithium, become reduced rather than intercalated. Figure 8 shows a scanning electron microscopy image of exfoliated graphite. A focused ion beam cut was made perpendicular to the surface. The particles are traversed by cavities, which are characteristic for exfoliated graphite. Before cutting, the surface was covered with gold by sputtering in order to prevent false interpretation due to deposits of the cutting process on the particle surfaces.

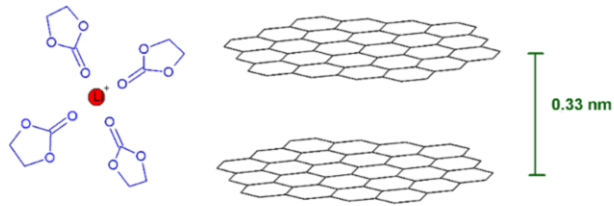
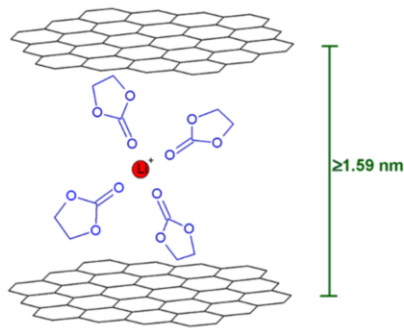
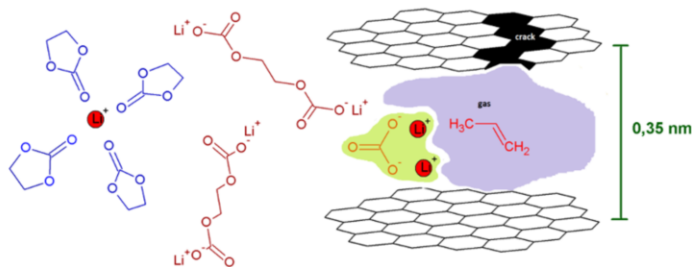
(A) >1.5 V graphite versus lithium**(B)** 1.5 V – 0.8 V graphite versus lithium**(C)** < 0.8 V graphite versus lithium

Fig. 7 At graphite voltages higher than 1.5 V versus lithium, the distance between the graphite layers is smaller than the solvated lithium complex (a). At voltages lower than 1.5 V, the distance between the graphite layers increases and solvated lithium ions are intercalated (b) [24, 32]

Exfoliation is prevented by ethylene carbonate (EC) based electrolytes or by additives such as vinylidene carbonate (VC), which form a relatively stable and completely covering surface film on the anode surface within the first formation cycles [11]. The diffusion of electrolyte molecules through this layer is impeded, so the electrolyte

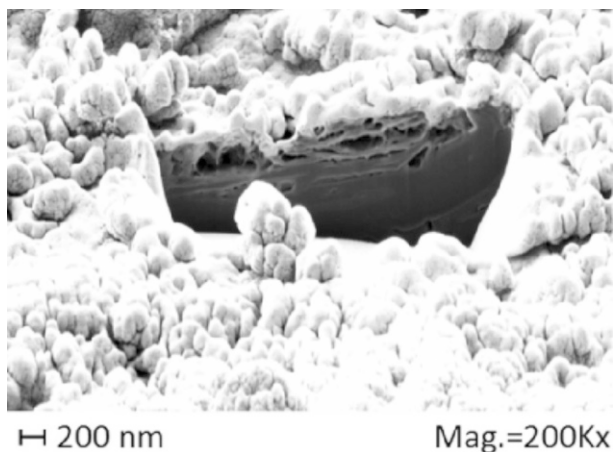


Fig. 8 Scanning electron microscopy image of exfoliated graphite. The light surface film is gold, which was sputtered on top of the graphite surface to prevent false interpretation of deposit products from the focused ion beam cut into the surface. The sample was cycled with 8C, at 50 °C for 34 weeks before the FIB preparation

molecules do not reach the anode surface. This is a mutual stabilization of the electrolyte against reduction on one hand and of the graphite against exfoliation on the other.

2.2.4 *Li-Dendrite Formation*

Lithium-dendrite formation means deposition of elementary lithium with a relatively large surface area. If the concentration of lithium ions at the graphite electrolyte interface becomes higher than the saturation of the electrolyte by lithium ions, elementary lithium deposits on the graphite surface [43]. The concentration can overshoot the saturation limit due to high currents [44] or low temperatures [29]. High currents lead to higher polarization effects. This means a higher amount of Li and PF_6^- ions at positions close enough to the graphite surface for an electron exchange. The critical amount of lithium ions close to the surface, the amount necessary to initiate dendrite formation, can therefore be reached by increasing the current per surface area up to a critical value [45]. At low temperatures the lithium intercalation process becomes slower and the polarization effects increase, as well. Furthermore, at kinks and steps on the surface the amount of lithium ions is locally higher compared to normal surface planes due to lithium diffusion along the surface [46]. Due to the inhomogeneous lithium concentration along the surface, the probability of lithium deposition at defects is higher [47–49]. Moreover, the kinetics of the intercalation are slowed down with an increasing state of charge of the anode. As a consequence, the polarization effects increase with higher SoCs and, therefore, dendrite formation becomes more likely. Additionally, overpotentials of the dendrite formation process highly depend on the characteristics of the graphite surface, on the temperature, on the surface area of the dendrites and on the lithium-ion concentration [29, 50]. The surface area of the dendrites formed at a graphitic

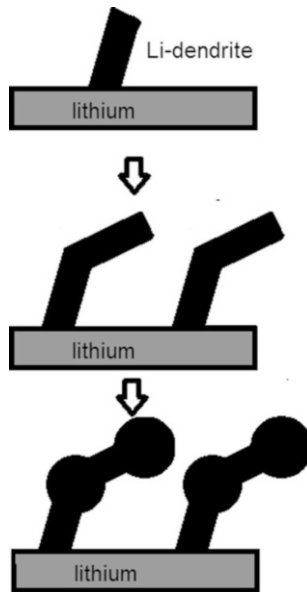


Fig. 9 Lithium dendrite formation following the example of Yamaki et al. [51, 52]. The deposition of elementary lithium leads to the formation of whiskers, which are deformed. If the diffusion of lithium ions towards the solid electrolyte interface becomes limited by the presence of the dendrites, lithium ions deposit at the tip of the whiskers and at kink sites

surface increases continuously. Therefore, the overpotentials decrease very rapidly once the onset of lithium dendrite formation is reached. Figure 9 is a schematic illustration of lithium-dendrite formation following the example of Yamaki et al. [51, 52]. The inhomogeneous deposition of lithium causes stress within the electrode, leading to a deformation of the dendrite whiskers. If the amount of deposited lithium limits the lithium-ion diffusion through the electrode–electrolyte interface, the incoming lithium ions start to deposit at the tip and kink points of the whisker, too.

Lithium deposition on graphite is partially reversible. At higher anodic potentials (> 0.06 V vs lithium) dendritic lithium (if it is still electronically contacted to the current collector) can dissolve again as lithium ions. However, during such processes parts of the dendrites can become electronically isolated and become widely distributed. The arboreal growth of lithium dendrites and the spread of isolated, elementary lithium can lead to short circuits and therefore can initiate a thermal runaway. As long as elementary lithium is oxidized as fast as it is deposited on the anode-surface, no imminent danger of lithium dendrites exists. In common practice, the anode capacity per surface collector area is oversized compared to the cathode capacity so that the graphite is cycled roughly between 0.06 and 0.9 V [21] and elementary lithium can dissolve during the entire cycle. The ratio of negative to positive electrode capacity (n/p ratio) is therefore an important parameter which ensures cell safety (considering lithium dendrite formation) [53]. However, for

kinetic reasons, harsh operation conditions can lead to lithium dendrite formation on a graphite surface even though the potential is high enough for lithium dissolution [29, 54]. With an increasing amount of lithium ions migrating through the anodic surface (increasing charge throughput) the risk of lithium dendrite formation increases, as well.

2.2.5 Electrolyte Decomposition

As long as the electrodes are in direct contact with the liquid electrolyte, the electrolyte molecules are thermodynamically stable only if their highest occupied molecular orbital (HOMO) has a lower energy than the lowest energy of an unoccupied electronic state of the cathode and the lowest unoccupied molecular orbital (LUMO) has a higher energy than the highest electronic state of the anode. However, as shown in Fig. 10, at voltages lower than 0.8 V vs lithium (normal anode potentials), commonly used carbonate-based electrolytes are not stable [5]. A passivation layer, consisting of electrolyte decomposition products, is formed within a few cycles. This passivation layer ideally impedes the transfer of electrons to electrolyte components and prevents an ongoing electrolyte reduction during operation. This protection of the electrolyte is schematically shown in Fig. 10, by a red arrow. However, the formation of such a protective layer depends on the operation conditions in the initial cycles (formation cycles) as well as in the ongoing cycles [35]. Vinylidene carbonate is commonly used to form a stable protection layer on the anode surface. This additive forms polymeric species on the anode surface but still allows the penetration of the polymer film by lithium ions. Therefore, the formation of the protection layer does not lead to an impedance rise [55]. At temperatures higher than 60 °C the composition of the protection layers alters and additional electrolyte molecules reach the surface, leading to an ongoing

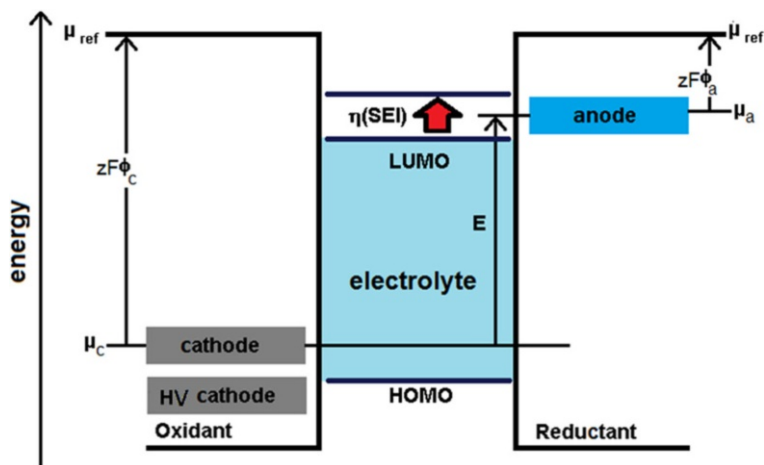


Fig. 10 Energy diagram showing the highest occupied molecular orbital (HOMO) and the lowest unoccupied molecular orbital (LUMO) of the organic electrolyte in comparison to the chemical potential of the electrodes [5]

reduction of electrolyte molecules [55]. If the electrodes undergo volume changes, crack formation (see Sect. 2.2.9) occurs. This makes necessary an additional formation of corrosion layers during normal operation of lithium-ion cells.

Figure 11 gives some insight into the basic chemistry of electrolyte decomposition reactions and the discussed reaction pathways. The reviews [6, 11, 56] provide further insights into this topic. The initial reaction, which causes electrolyte decomposition, is probably the decomposition of the conductive salt LiPF_6 , which is used in most of the commercial lithium-ion batteries (reaction (13)) [39, 57, 58].



The balance of this reaction is on the left side. With increasing temperature the amount of LiF and PF_5 is slightly increased. If PF_5 further reacts with electrolyte molecules, the concentration of PF_5 is reduced and reaction (13) proceeds further from the left to the right to approach or preserve equilibrium conditions.

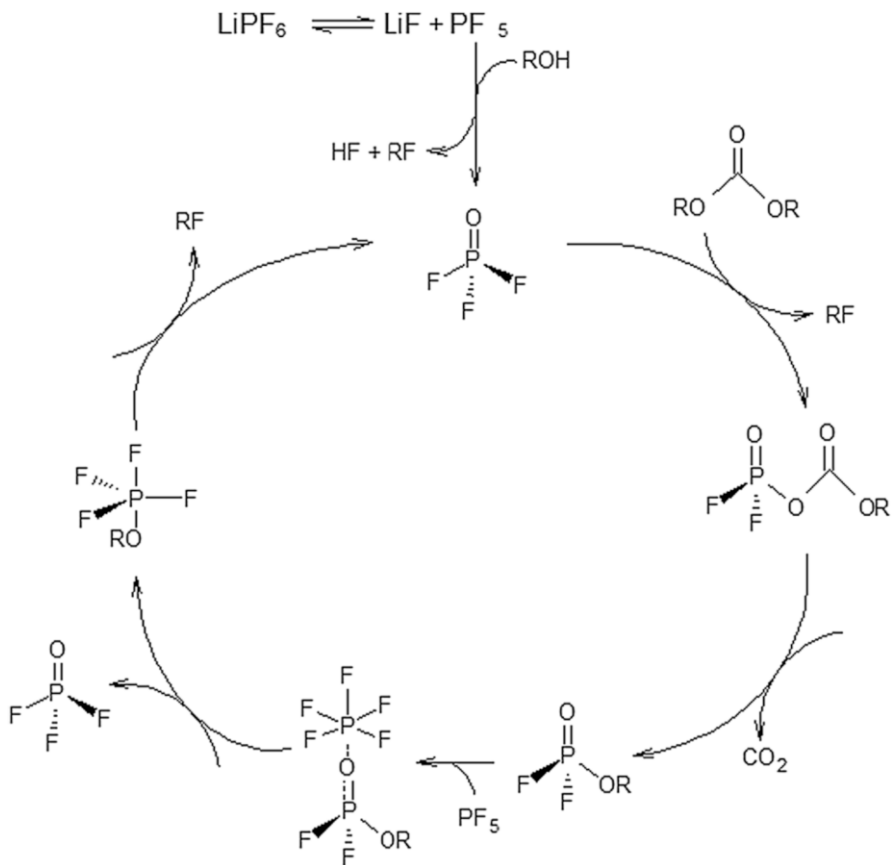


Fig. 11 Reaction of PF_5 with trace impurities of alcohols to POF_3 . POF_3 can react further with linear carbonates such as diethyl carbonate towards ethyl fluorophosphate. This reacts with PF_5 to POF_3 as a splitting group as proposed by Campion et al. [59]

Figure 11 shows the reaction of PF_5 with trace impurities of water or alcohol to POF_3 [59].

POF_3 can further react with ethylene-carbonate (EC) to oligoethylene oxides capped with alkyl fluoride and fluorophosphates (Fig. 12). This reaction proceeds via a ring opening reaction with radical intermediate states [11, 14]. There is some question as to whether these radical intermediate states are actually present in real cells or the intermediate species are adsorbed on the electrode surface and the reaction is electrochemically catalysed (as is known in the case of fuel cells and often shown in the field of catalysis). This seems to be an important point because on the electrode surface, such a reaction can proceed electrochemically while only chemical pathways can be considered in a solution. Therefore, more efforts should be put into understanding where the reactions take place.

Considering new, high voltage materials for application in lithium-ion batteries, the chemical potential of the cathode is shifted below the HOMO of the electrolyte (Fig. 10) and therefore protection is necessary against oxidative electrolyte decomposition reactions or the development of new electrolyte systems. This challenge still remains unsolved [5].

2.2.6 Loss of Porosity

The main function of a separator is to prevent electronic transport while allowing ionic conduction. In commercial lithium-ion cells a 3-layer polypropylene/polyethylene/polypropylene (PE/PP/PE) separator is commonly used. The electrolyte can penetrate the polymers through the porous structure, which allows ionic conductivity between the anode and the cathode. While polypropylene (PP) ensures mechanical stability, polyethylene (PE) serves to shut down the cell during overheating up to 130 °C (melting point of PE) [60]. PP only starts to melt at 165 °C. Polypropylene loses its porosity upon heating to 110 °C (ionic conductivity

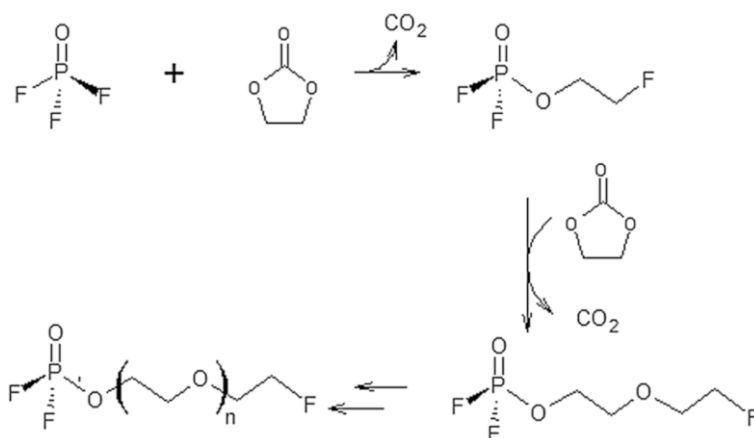
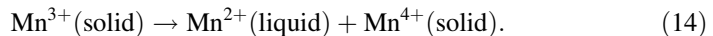


Fig. 12 Reaction of ethylene carbonate with POF_3 to oligoethylene oxides capped with fluoride and fluorophosphates end groups as proposed by Campion et al. [59]

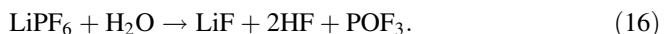
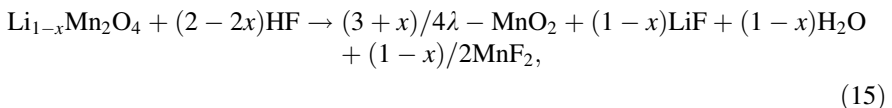
through the pores decreases around 2%) [61] and it shrinks around 2–5% [60]. At this temperature, the deformation of PP is not very pronounced and it can serve for stability. Therefore, the separator (PE/PP/PE) can prevent a thermal runaway up to 130 °C. However, even at lower temperatures the polymers can lose their porosity, which leads to an impedance rise of lithium-ion batteries during operation [62]. Further dissolved transition-metal ions or dismantled active material can diffuse through the separator and block pores [63].

2.2.7 Transition-Metal Dissolution

Transition-metal dissolution has been observed for manganese-containing cathode materials (spinel and layered oxides). The dissolution of other transition metals such as nickel and cobalt has also been observed in the case of NCM [64]. Layered oxides which do not contain manganese do not show transition metal dissolution [7]. There are two different proposed reaction mechanisms that lead to transition-metal dissolution [65]. The first is the disproportionation of Mn [3] described in Eq. (14). This mechanism was proposed by Hunter et al. in order to explain the conversion of LiMn_2O_4 (Mn^{3+} , Mn^{4+}) into λ - MnO_2 (Mn^{4+}) and MnO (Mn^{2+}) in the presence of water [66].



The mechanism described in Eq. (7) is the dominant aging mechanism considering spinel structures which are stored at high temperatures [7]. Mn^{3+} is present at low states of charge of the spinel LiMn_2O_4 (Mn^{3+} , Mn^{4+}) or structural analogous. Therefore, the disproportionation reaction proceeds only at low states of charge. In layered oxides such as $\text{LiNi}_{1/3}\text{Co}_{1/3}\text{Mn}_{1/3}\text{O}_2$ (Ni^{2+} , Co^{3+} , Mn^{4+} , NCM) the presence of Mn^{3+} is attributed to the presence of trace amounts of oxygen vacancies and Mn^{3+} is oxidized to Mn^{4+} at higher states of charge. However, the dissolution of manganese in many layered oxides, as well as in some spinels, is mainly observed at high states of charge [20, 65, 67, 68]. Another reaction mechanism ascribes the manganese dissolution to acid corrosion (HF and organic acids), reaction (19) [7, 65].



The proposed reaction mechanism is given in Fig. 13 [20]. According to Eq. (20) the apparently consumed HF is reproduced due to the formation of water, which reacts again with LiPF_6 . The transition-metal dissolution will stop only if water or HF is consumed in other side reactions. This kind of degradation can be reduced by surface coatings that protect the material from HF attacks [69–72]. NCM and other high voltage materials show a strong increase of manganese dissolution if the upper

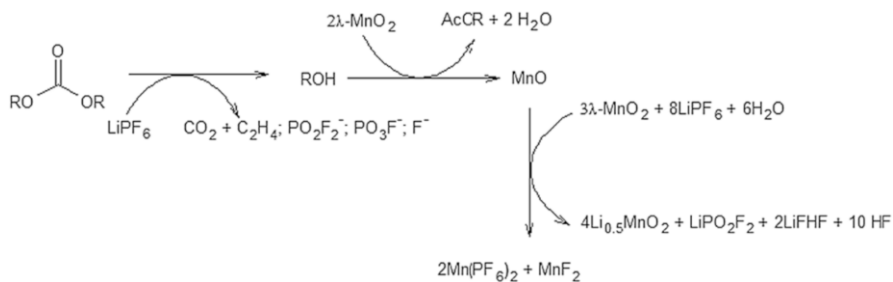


Fig. 13 Proposed reaction mechanism of the manganese dissolution process at high states of charge. The reaction scheme includes the formation of an alcohol out of carbonates, while LiPF_6 is consumed [20]. However, this reaction step is poorly understood [7]

cutoff voltage is above 4.5 V [64]. This might be related to the decomposition reaction of the conducting salt LiPF_6 with an onset around 4.5 V. However, the oxidative decomposition of LiPF_6 or PF_5 , a decomposition product of LiPF_6 , is poorly understood [7]. Evidence that the dissolution of manganese coincides with the decomposition of LiPF_6 is derived from studies with various conductive salts [7, 20, 73].

2.2.8 Binder Decomposition

The battery efficiency as well as the long term stability of a lithium-ion battery depend highly on the electrode manufacturing [74]. In this process, a binder is dissolved in a solvent and, together with the active material (plus conductive carbon), it forms an ink, which can be coated on a current collector (metal foil). The obtained wet film is dried and the binder forms a (polymer-) network that acts as a glue between the particles and the current collector. Thereby the binders need to disperse homogeneously in the inks in order to form a very homogeneous (polymer-) network [75, 76]. During cycling the binder has to accommodate volumetric changes of the active material. Especially for materials which undergo large volumetric changes (e.g. silicon anodes or alloys) the binder plays a key role in preventing massive cracking and a subsequent flake off of the active material [76, 77]. It goes without saying that binders also need to be chemically stable in contact with electrolytes and in the applied potential window and that they should have good elastomeric properties. Furthermore, cohesive strengths between the active material and the binder are reported to be an important factor for improving the stability of coated electrodes [78]. Degradation reactions of the binders can lead to poor connectivity between the single particles, and also between the current collector and the active material, which is associated with delamination (see also Sect. 2.2.9). As a consequence, the internal resistance of the lithium-ion cell increases. Moreover, active material can become partially isolated, leading to capacity losses.

Polyvinylidene fluoride (PvdF) is commonly used as binder for positive electrodes [79, 80]. However, it shows relatively poor elastic elongation compared to cross-linking polymers or elastomeric binders [81, 82]. Although PvdF was

thought to be stable under the chemical and electrochemical conditions present in a lithium-ion cell, detailed X-ray photo electron spectroscopy (XPS) and electrochemical studies reveal that PvdF undergoes corrosion reactions upon cycling that affect the capacity retention and the coulombic efficiency of the cathodes [80]. However, detailed studies about the dependency of these decomposition reactions on the potential or the state of charge of the cathodes are missing, not least due to a lack of analytical tools. Binder decomposition reactions are often negligible compared to the degradations of other cell-components and, (beside the potential- or state-of-charge dependency) depend also on impurities in the electrolyte and the temperature [83, 84]. Nevertheless, comparative studies between binder-free and binder-containing electrodes provide clear evidence that PvdF is not as electrochemically inactive as commonly assumed [84]. It has been shown that cathode corrosion occurs especially at contact points between the active material and the binder. A deeper understanding of the detailed degradation mechanism is still missing [3]. Fewer studies are performed to investigate alternative binders for cathode materials since PvdF seems to be stable enough for currently used cathode materials. Nevertheless, Manickham et al. showed that PTFE (Polytetrafluoroethylene) offers better cycling stability while cycling transition metal phosphates [80].

The embedding of silicon (and other conversion type electrodes) into graphite forced investigations of new binders with enhanced elastic properties in order to accommodate the large volumetric work performed by these alloys upon cycling [85]. The introduction of Carboxymethylcellulose (CMC) as a binder in 2003 was a breakthrough, due not only to the better elongation properties of the systems but also to the more environmentally friendly water based manufacturing process [86]. Nowadays styrene butadiene rubber (SBR) in combination with CMC is commercially the most used binder for graphite, the almost solely used anode material in commercial lithium-ion batteries. Formerly used fluorinated binders such as PvdF or polytetrafluoroethylene (PTFE) showed reactions with lithium towards LiF formation at low potentials, while SBR-CMC binders are almost inert under these conditions [8, 77, 87–89]. However, scanning electron microscopy (SEM) pictures of a fatigued graphite sample suggest that SBR-CMC binders are not completely inert during cycling (Fig. 14), though they show an improved coulombic efficiency compared to PvdF [90].

In considering different binders, the environmental friendliness of the manufacturing is important [91, 92]. While PvdF is dissolved in *N*-methylpyrrolidone (NMP) during electrode manufacturing, SBR-CMC binders can be dissolved in water. A water based electrode coating has clear advantages over the NMP based process. The negative CO₂ balance of the NMP-production and the toxicity of NMP is harmful for the environment. In addition the production and disposal of NMP is very cost intensive. However, most commercially used cathode materials (layered oxides such as LiCoO₂) are unstable in contact with water [93]. Nevertheless, a detailed study of the decomposition and the cycling stability of these materials coated with water based binders is still missing. Furthermore, it has already been shown that the dissolution of transition metals from layered oxides can be suppressed by a variation

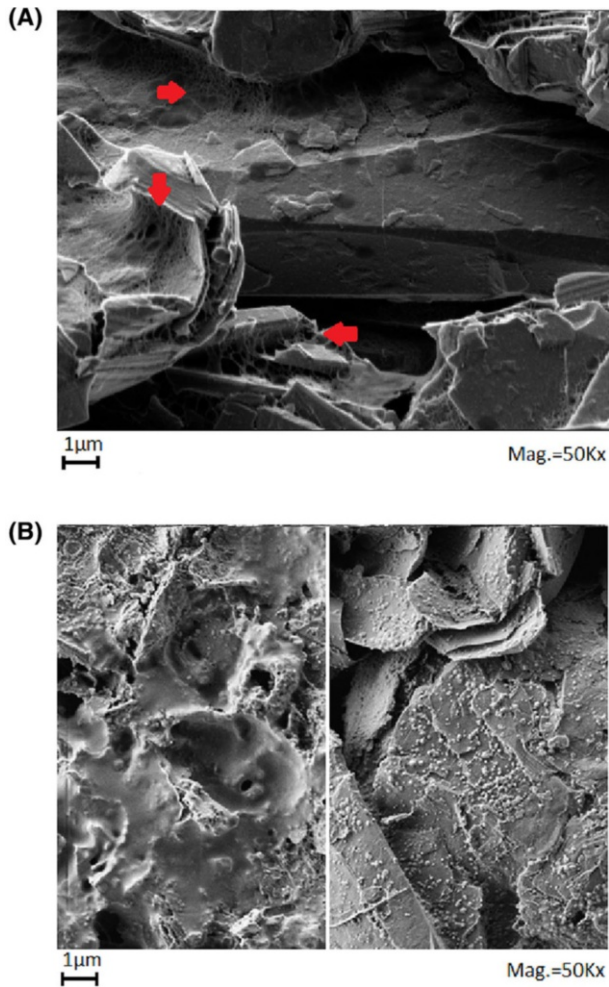


Fig. 14 Scanning electron microscopy image of a pristine (a) and a fatigued graphite surface (b). On pristine surfaces binder structures can be identified marked with red arrows. However, the sample fatigued with an 8C rate, at 50 °C for 34 weeks, shows deposits on the surface, and binder structures can no longer be identified

of the pH-value of the solution [94, 95]. Other cathode materials, e.g. LiFePO_4 , are more stable in aqueous solutions [96, 97].

2.2.9 Cracks

Structural changes in the active materials during cycling (whether a gradual change of lattice parameters or a reconstructive first-order phase transition) can lead to crack formation (Fig. 15). Cracks can affect just the contact between particles or can occur within particles. Both types of cracks may lead to electronically isolated particles and therefore to capacity losses. When cracks occur, lithium (de-

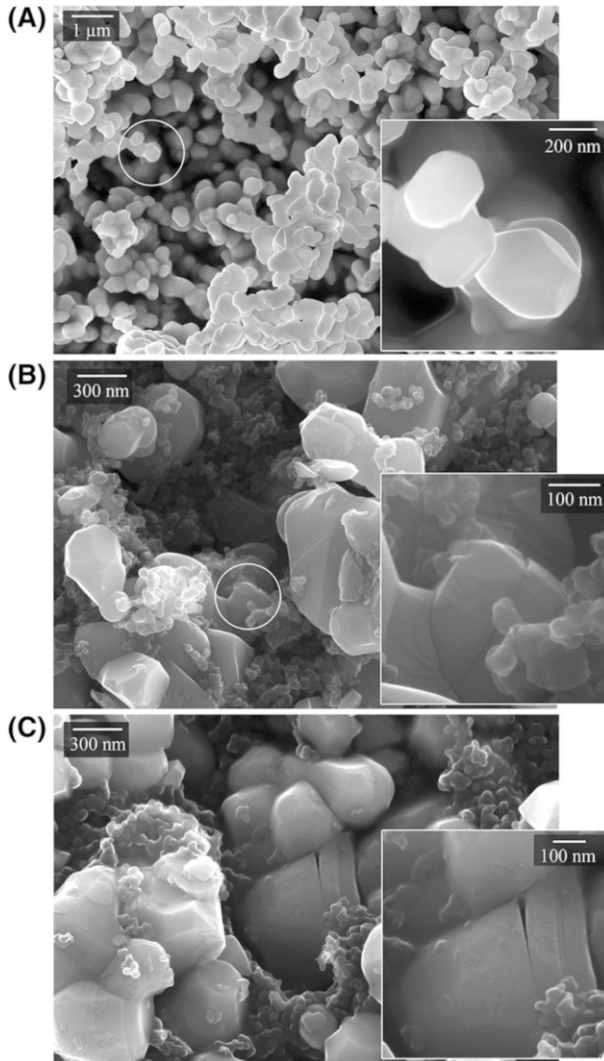


Fig. 15 SEM images of as-prepared $\text{LiNi}_{1/3}\text{Co}_{1/3}\text{Mn}_{1/3}\text{O}_2$ powder (a), and after 10 cycles at 0.1C rate in the potential range 3.0–4.2 V vs Li^+/Li in the charged state (b) and discharged state (c) [100]

)intercalation is accelerated with an increasing surface because the electrolyte can penetrate a larger surface area. Crack formation is more pronounced at high C-rates, broad depth of discharge (DoD) and for larger particles [98, 99].

Lithium diffusion within layered cathode materials is in the range of 10^{-8} till $10^{-15} \text{ cm}^2\text{s}^{-1}$, determined with the galvanostatic intermittent titration technique (GITT) [16, 101]. All cathode materials behave like semiconductors with an electronic conductivity of 10^{-3} Scm^{-1} [101, 102]. Electronic conductivity is a function of the temperature (Arrhenius type behavior) [101]. This leads to the conclusion that the lithium-ion transport within the material is the limiting process

[101]. However, some cathode materials (e.g. LiCoO_2 and LiMn_2O_4) show phase transformations during cycling which can lead to a variation in the electronic conductivity of about three orders of magnitude [103].

2.2.10 Structural Changes

The insertion or deintercalation of lithium ions from or into a host structure is accompanied by changes in the lattice parameters and sometimes with changes in the geometry of the unit cell, as well [19, 104–106]. In order to consider fatigue of electrodes due to structural changes, their thermodynamic and kinetic stability must be considered at different states of charge, which means different lithium contents within the host structure. According to the different types of structural changes which can occur in electrodes during operation, the following reactions can be observed:

- Solid solution reaction
- Two-phase reaction
- Irreversible phase transformation

The first and the second types of reaction are ideally reversible and describe the charge and discharge reactions of electrodes. The different working mechanisms can be distinguished with respect to the underlying structural changes during lithiation and delithiation. The change of Li-content can take place continuously in one phase like a solid solution or as a two-phase mechanism. In the latter case the overall change of lithium in the electrode is accompanied by a change in the phase ratio of a lithium-rich and a lithium-poor (or lithium-free) phase. Both mechanisms are ideally reversible and can easily be distinguished from the voltage versus state-of-charge profile: while the voltage changes continuously for a one-phase mechanism (the Gibbs free energy ΔG , Eq. (7), varies with the lithium content), a two-phase mechanism is reflected in a constant voltage plateau as long as both phases coexist. Two phases in contact with each other can only exist if their difference in the Gibbs free energy ΔG , and therefore the change in the electrode potential ($\Delta\phi_i$), equals zero. The most important example for a two-phase mechanism is LiFePO_4 , which coexists with FePO_4 during cycling [107, 108]. All layered oxides are considered to react via a solid solution type mechanism. However, in situ analysis of the reflection patterns (synchrotron measurements) provide evidence that even layered oxides run through a two-phase reaction during cycling, although these two phases coexist in only a small voltage window and the phase content of the less active (inactive) phase decreases (vanishes) with a decreasing lithium content [104].

The de-/intercalation of lithium ions from or into a host structure can lead to irreversible phase transformations (the third type of structural change). The knowledge of the underlying de-/intercalation type can be used to understand how the different mechanisms can lead to irreversible structural changes. Both de-/intercalation mechanisms have an impact on the mechanical stress as a consequence of the structural changes; in a one-phase mechanism a gradual change of lattice

parameters takes place. Therefore, the exchange of charge carriers can proceed relatively quickly because there is no need for the breaking and reconstruction of phase boundaries [105]. The geometry of the host structure is maintained during almost the entire de-/lithiation, but the dimensions of the unit cell change. Therefore, the host structure might become instable at some states of charge. Layered oxides, for example (although they do not react ideally as a solid solution but this mechanism comes closest to it) become instable in delithiated states due to repulsive interactions of oxygen atoms in opposite transition metal layers (Fig. 16) [109, 110].

Li_xCoO_2 -rich structures tend to transform from a rhombohedral to a monoclinic structure at lithium contents x lower than 0.5 [111]. A structural decomposition of Li_xNiO_2 -rich materials starts at lithium contents x lower than 0.35 [112, 113]. According to this, nickel based cathode materials exhibit higher, reversible capacities compared to cobalt-containing materials if both materials are operated in a voltage window in which the materials are stable (Ni-based 180 mAhg^{-1} , Co-based 150 mAhg^{-1}). In order to understand the differences, the dimensions of the isostructural lattice of the materials are considered; cobalt has a larger ionic radius compared to nickel [18]. This leads to a higher octahedral-site-stabilization-energy, which is determined by the electronic configuration of the transition metals (Co^{3+} , low spin $3d^6$: $t_{2g}^6 e_g^0 -21.33 \text{ Dq}$, Ni^{3+} , $3d^7$: $t_{2g}^6 e_g^1 -12.67 \text{ Dq}$). Further, Co^{3+} is in a low spin state and therefore its radius increases during oxidation due to the occupation of t_{2g} orbitals. This results in a higher energy barrier for cobalt migration, which prevents disordering of lithium and cobalt [15, 18, 114]. Therefore, the separation of the cobalt and lithium layers is almost ideal while nickel (with a radius similar to lithium ions especially for the 2^+ state) tend to occupy lithium sites, as well (Fig. 17). Even during sample preparation, LiNiO_2 forms a lithium-deficient phase $\text{Li}_{1-x}\text{Ni}_{1+x}\text{O}_2$ with a high degree of cation disorder. Stoichiometric LiNiO_2 is very difficult to prepare and for example obtained from NaNiO_2 by a cation exchange reaction. Beside Ni and Co based layered oxides, the structure can also contain manganese. Manganese is more electronegative compared to nickel and in manganese and nickel containing electrodes (layered LiMnO_2 is not

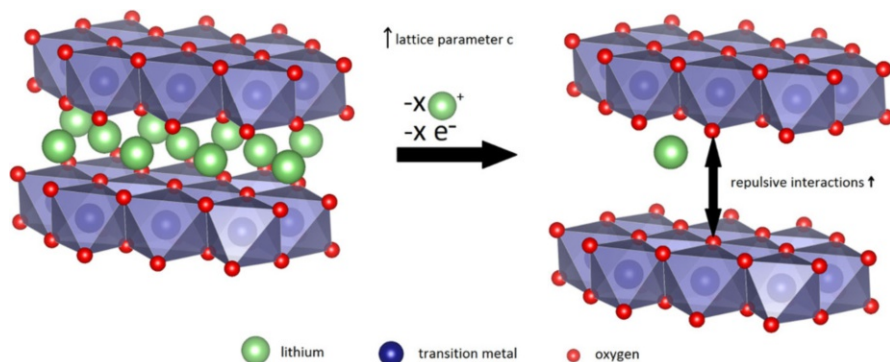


Fig. 16 Layered lithium-transition metal oxides upon delithiation: The lattice expands in the c -direction during delithiation due to repulsive interactions of oxygen atoms from opposite transition metal layers

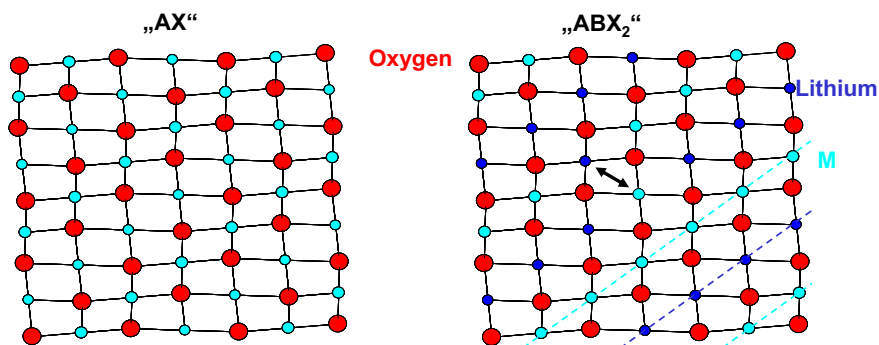


Fig. 17 Illustration of the cation distribution in the layered oxides LiMO_2 ($M = \text{Ni, Co, Mn}$ or Al). LiMeO_2 as an ABX_2 superstructure shown on the left-hand side, derived from the rock-salt type AX on the right by splitting the cation A-site into two alternating layers, A and B. A rhombohedral LiMO_2 structure results from this cation ordering and the different sizes of the A and B ions. However, a partial mixing of A and B ions is very common; one example is marked in the *right-hand side* by the *arrow*

stable under standard conditions) manganese exists in a 4^+ -state while nickel has an oxidation state of 2^+ [115]. As discussed above, Ni^{2+} has a radius very similar to lithium ions and therefore it can occupy lithium sites [116]. The degree of disorder for which manganese and nickel containing materials are still stable is similar or even higher compared to Ni-rich materials.

On the one hand the cation disorder may stabilize the delithiated structure because the repulsive interactions of the oxygen atoms, in opposite transition metal layers destabilizing the structure during deintercalation, are reduced (Fig. 16). On the other hand, the transition metal disorder can be irreversible, in which case it is a very crucial limitation for the electrochemical performance of such materials. The smaller 3d-transition metals in the lithium layers hinder lithium-ion mobility (Fig. 18).

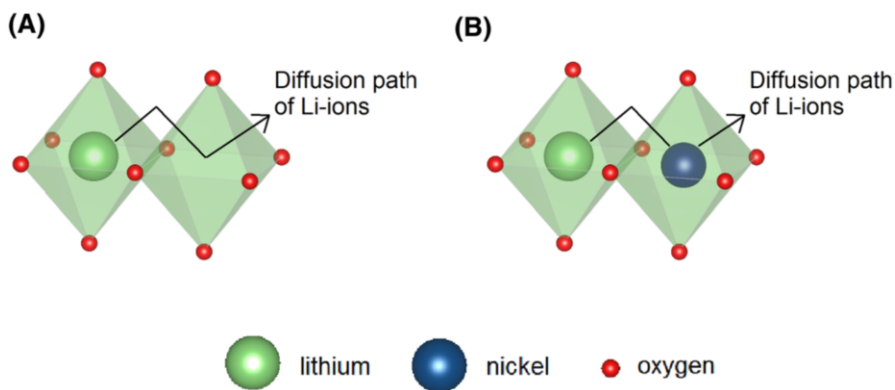


Fig. 18 Schematic illustration of a lithium-octahedrons in layered oxides (a) and the lithium diffusion pathway, depicted by a *black arrow*. The occupation of empty lithium sites by nickel, which blocks the lithium diffusion within the structure, is shown in (b)

In contrast to the abovementioned (dis-)order as an explanation for the different degrees of stability of layered oxides upon delithiation, several authors argue with the differences in the density of states between cobalt and nickel [5, 15, 117]. According to this explanation the difference in the chemical stability can be related to the band structures of the materials (Fig. 19). The Co^{3+} t_{2g} band overlaps with the O 2p band. If the lithium content becomes low enough ($x < 0.5$ in Li_xCoO_2) the electrons are removed from the O 2p band rather than from the Co^{3+} t_{2g} band. This results in oxygen release from the structure. A rearrangement of the structural components is the consequence of this oxygen oxidation reaction. The Ni t_{2g} band touches the O 2p band (barely) and therefore oxygen release occurs at lower x values in Li_xNiO_2 [19, 118]. However, this argument ignores the fact that in both the nickel and cobalt-containing layered oxides, the transition metal–oxygen-bond has a highly covalent character and, therefore, a reversible oxidation of oxygen starts from the lithiated (discharged) state on and proceeds over the entire charge (a detailed discussion is given in Sect. 2.2.11) [16, 119, 120]. Nevertheless, even a partial oxidation of oxygen (which starts in the lithiated state) can lead to oxygen release from the structure at more delithiated states if the diffusion pathways for oxygen atoms are short compared to the time for which the material is held in the delithiated state (diffusion coefficient of oxygen is much lower compared to lithium ions: $\ll 10^{-15}$ cm^2/s). At high levels of delithiation (for commercial cathode materials in the overcharged state), oxygen release takes place and the materials become intrinsically unstable. This is reflected by the shrinking of the unit cell c -axis parameter because of less repulsion between the oxygen layers (Fig. 16). The highly delithiated compounds become thermally unstable and have a tendency to release oxygen as in a thermal runaway.

The previous section addressed structural changes of layered oxides during de/intercalation. These materials react almost as a solid solution. In this section the fatigue accompanied by a two-phase reaction will be discussed. A reconstructive first-order phase transition is necessary for the coexistence of two phases in the two-

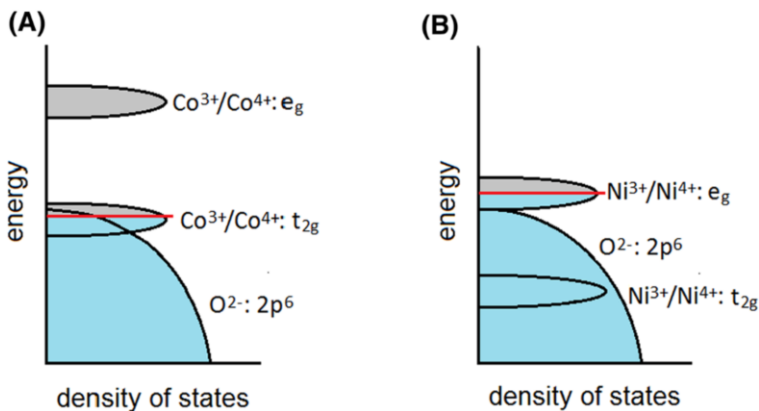


Fig. 19 Schematic illustration of the density of states of LiCoO_2 (a) and LiNiO_2 (b). Note that these pictures are simplified. Real band structures are much more complicated

phase mechanism. For the deintercalation of lithium ions, breaking and reconstruction of phase boundaries is necessary. This is attached to an activation energy which has to be overcome. Therefore, the kinetics of the de-/intercalation are slower compared to a solid solution reaction and side reactions become more dominant. Senyshyn et al. and Levi et al. showed, for example, that the charge and discharge of graphite proceeds via the coexistence of more than one phase [121, 122]. Therefore, the lithium intercalation is relatively slow and lithium dendrite formation (Sect. 2.2.4), as well as the irreversible decomposition of electrolyte molecules, can take place (Sect. 2.2.5). In contrast to a solid solution reaction, the phases formed in a two-phase reaction are mostly stable at all states of charge and, therefore, phase transformations (beside the desired ones) are rarely observed. An example of a cathode material which runs through an irreversible phase transformations during the coexistence of two phases is $\text{Li}_x\text{Mn}_2\text{O}_4$ [123–125]. During delithiation a transition from a tetragonal to a cubic structure takes place. The tetragonal structure shows a Jahn–Teller distortion because of a single electron in the e.g. orbital of the high spin Mn^{3+} state ($t_{2g}^3 e_g^1$) [124, 126]. This phase transition is accompanied by an increase of the c/a ratio (c and a are lattice parameters of the unit cell) of about 16% and a volumetric increase of about 6.5% [15]. These changes in the symmetry are too severe to maintain structural integrity. Structural rearrangements are the results leading to irreversible structural changes as shown by Tran et al. [127, 128]. Structural changes during lithiation and delithiation of spinels and other cathode materials are pushed back with the substitution of nickel, cobalt and manganese by di- or trivalent cations such as Cr, Al, Mg [129, 130].

2.2.11 Changes in the Electronic Structure

In Sect. 2.2.10 it was shown that severe structural changes occur upon lithiation or delithiation of a host structure. Changes in the dimensions and/or geometry of the lattice are accompanied by changes in the electronic structure, which dictate the charge diffusion processes. In order to understand this relationship, the electron distribution within transition metal oxides is considered first. In layered oxides and spinels the transition metal ions are placed in oxygen octahedrons. In a very simple viewing the electronic structure can therefore be described by ligand field theory (Fig. 20). Every oxygen atom has a 2p orbital which points towards a transition metal. The 3d orbitals of the transition metal pointing in the direction of the 2p orbitals are increased in energy due to repulsive interactions of electrons in these orbitals, while the other orbitals are lower in energy.

According to ligand field theory, the electronic configuration of a transition metal (TM) in an oxygen octahedron is $\text{TM } 3d^x \text{ O } 2p^6$ (x depends on the kind of transition metal and on the state-of-charge of the material). However, X-ray absorption spectroscopy (XAS) measurements at the O K edge show that electrons can be excited from the K-shell (1 s orbital of oxygen) into the L shell (O 2p orbitals of oxygen), even though the L-shell is completely occupied according to the ligand field theory. Therefore, the simple picture derived from the ligand field theory must be reviewed. It is well known in the field of XAS that a charge transfer from the

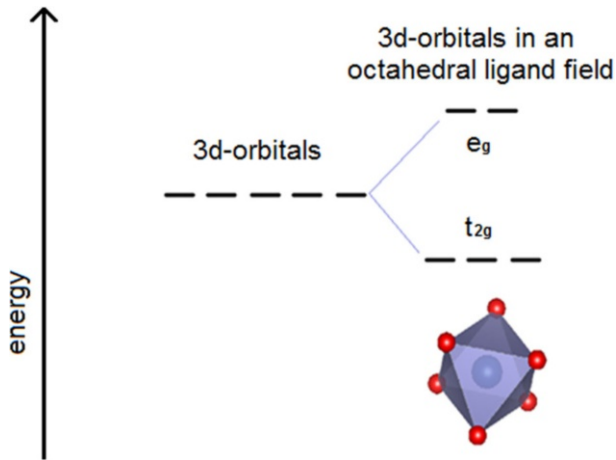


Fig. 20 Breaking of the Ni 3d orbital degeneracy due to the presence of six oxygen ligands around a transition metal ion (principle of the ligand field theory)

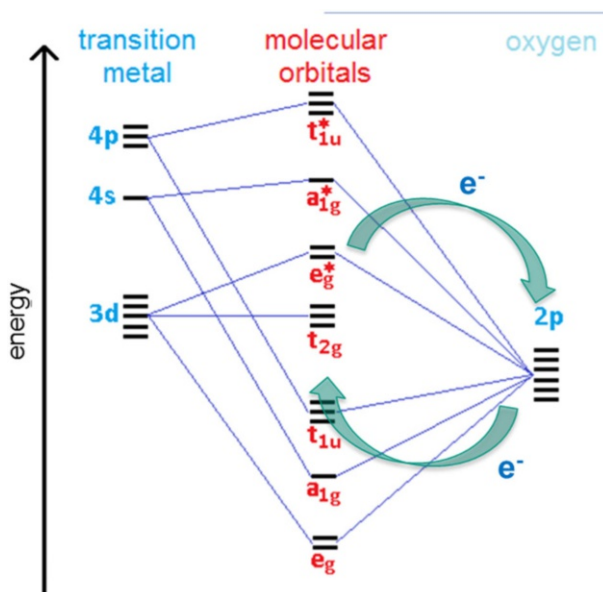


Fig. 21 Molecular orbital scheme of a transition metal surrounded by six oxygen ligands as described in [15]. According to XAS results, an exchange of electrons between the transition metals nickel, cobalt and manganese must be allowed. Therefore, the transition metal–oxygen bond has a covalent character

transition metal 3d towards the O 2p orbitals can take place. This can be described by molecular orbital schemes (Fig. 21).

The charge transfer of electrons between 3d and 2p orbitals can be seen as a covalent characteristic of the transition metal–oxygen bond and this, indeed, means that the electronic configuration of transition metal oxides has to be reformulated as

follows: $\text{TM } 3d^x \text{ O } 2p^6 \rightleftharpoons \text{TM } 3d^{x+1} \text{ O } 2p^5$. This configuration has electron vacancies at the oxygen sites and shows interactions between the transition metal 3d-orbitals and the O 2p orbitals, which enable the transition from a 1 s into a 2p orbital. The density of states is derived from an almost infinitesimal amount of overlapping 3d and 2p orbitals of the atoms within a solid (Fig. 22). The red area describes the variation in the Fermi Level due to the electron exchange during lithium-ion intercalation or deintercalation.

As mentioned in Sect. 2.2.10 the discussion about the density of states of lithium-transition metal-oxides often ignores the TM 3d-O 2p-interactions. These interactions are delocalized over the entire structure of the transition metal oxides because the oxygen atoms form a bridge between the transition metal octahedrons. This delocalization leads to the high energy densities of the materials, but it also carries the risk of oxygen release from the host structure due to the continuous oxidation of oxygen. For commercial applications, higher energy densities are often achieved by increasing the end of charge voltage. However, this is at the expense of the lifetime of a lithium-ion cell because this favors oxygen release from the structure and other degradation mechanisms. As shown by Rozier et al. for ruthenium containing layered oxides, the covalent interactions between the oxygen atoms and the transition metals can be highlighted in the density of states by dashed instead of solid lines (Fig. 23) [131]. The oxygen 2p and the transition metal 3d orbitals are combined to one molecular orbital and the oxidation/reduction of the transition metals, as well as the oxygen atoms, cohere.

The electronic structure of transition metals and oxygen atoms in cathode materials changes during cycling [16, 132–134]. In order to understand the context between the changes in the electronic structure and the electrochemical performance of an electrode, the lithium diffusion pathway in a solid electrode has to be considered. In layered lithium-transition metal-oxides, lithium moves via an

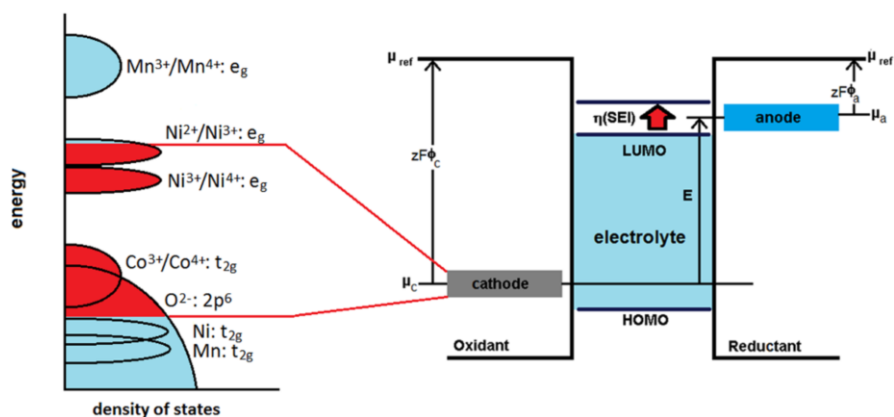


Fig. 22 The energy as a function of the density of states (left side), depicting from which molecular orbitals electrons are transferred during charge and discharge of $\text{LiNi}_{1/3}\text{Co}_{1/3}\text{Mn}_{1/3}\text{O}_2$ [117]. The description of the stability window of cathode materials is more complicated than that derived from simple thermodynamic considerations. The HOMO (or the Fermi Level) of a cathode material changes during cycling, and thereby the structure, can become unstable

Fig. 23 Density of states for lithium-transition metal-oxides: The *dashed lines* between overlapping states of different atoms show the interactions between the underlying orbitals and therefore the covalent character between the elements to which these orbitals belong

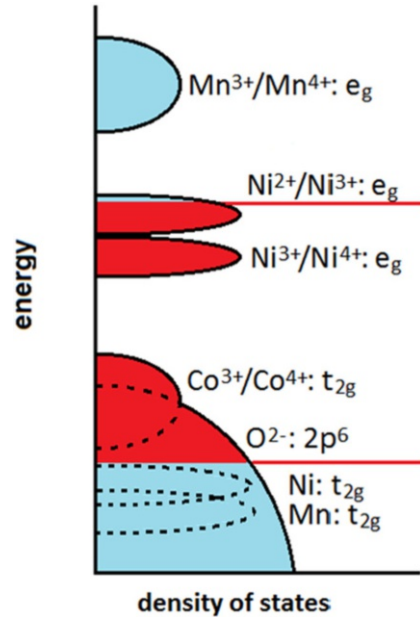
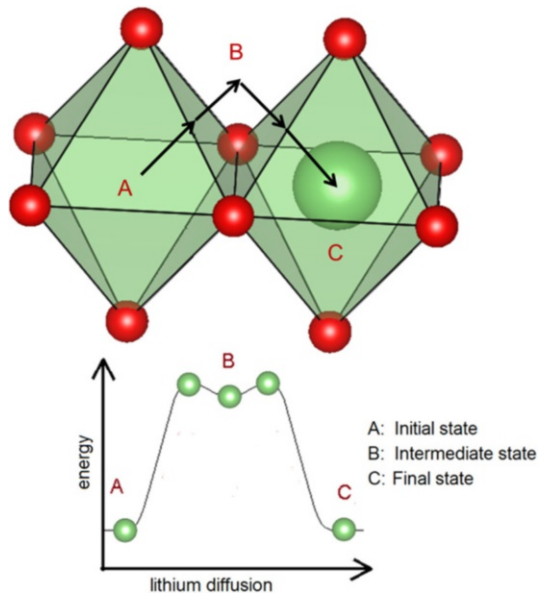


Fig. 24 Lithium diffusion pathway in layered transition metal oxides and the energy diagram of the migration. The lithium ion moves from *A* via the intermediate tetrahedral site *B* into the neighboring octahedral site *C*



intermediate, tetrahedral site into a neighboring octahedral site (Fig. 24) [135]. In this process, the interactions between the lithium-ion and three oxygen atoms (the triangle plane of the tetrahedron) have to be overcome twice.

The interactions between oxygen and lithium ions depend, of course, on the amount of lithium ions next to the unoccupied octahedron in which the lithium ion migrates (Fig. 25) [16, 132]. If oxygen is oxidized from 2- towards 1-, the attractive lithium-oxygen interactions become smaller and the energy barrier for lithium diffusion decreases, as well.

Fatigued cathode materials often show an increase in overpotentials, and the onset of the redox process is delayed (starts at higher applied voltages in the charge and at lower applied voltages in the discharge), as depicted in Fig. 26 and shown in [16]. An increase of overpotentials can be induced by surface-near structural changes (mainly observed in Ni-rich layered oxides), showing an increase of disorder (lithium excess and nickel rich layered oxides) or the formation of a passivation layer on the electrodes. While the activation barrier decreases if the oxygen oxidation starts (in pristine materials it starts immediately), it stays constant at low states of charge till the oxidation sets in. Therefore, the overpotentials slow down the reaction kinetics and the deintercalation (charge) may become incomplete. If the charge is incomplete, the subsequent discharge also shows a lower capacity compared to the pristine material.

2.2.12 Surface-Near Composition Changes

Changes in the surface-near composition are the dominant aging process in layered nickel-rich cathodes, leading to an impedance rise and therefore to capacity losses [16, 119]. In contrast, the isostructural LiCoO_2 does not show such degradations [136]. However, nickel-rich layered oxides (including NCA) provide the highest capacity of the present commercial cathodes (around 180 mAhg^{-1} [15, 137]). Although the structural changes in the bulk are almost impeded by the partial substitution of nickel with cobalt and aluminium [7, 104], high temperatures, high currents, high depths of discharge and high states of charge (presence of lithium vacancies [16, 119]) lead to nickel motion into empty lithium sites, and therefore to changes in the specific cation distribution, especially in surface-near regions [16, 17, 138]. The restriction to the surface probably has kinetic causes [16, 104]. During operation, outer parts of the particles become more delithiated compared to inner parts due to slow lithium-ion diffusion kinetics within the host structure

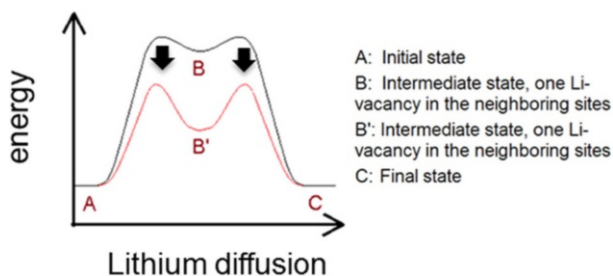


Fig. 25 Energy diagram of the lithium diffusion pathway in layered oxides before and after the oxidation of the materials has started

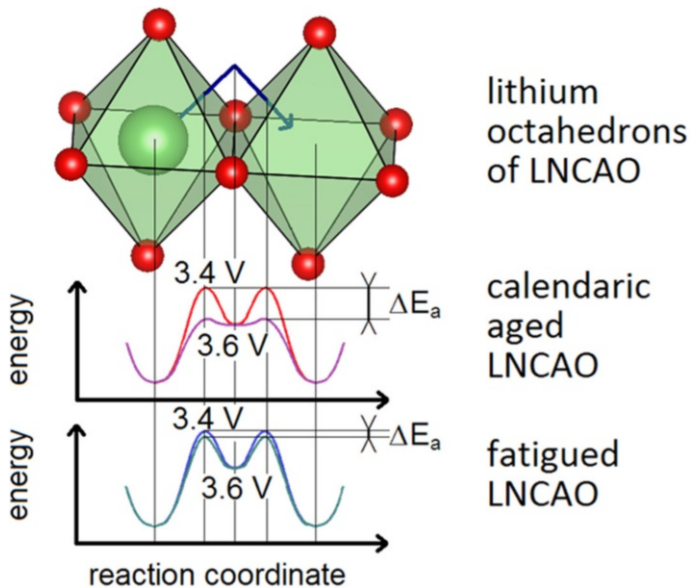


Fig. 26 Energy diagrams of lithium migration in a layered oxide (LNCAO, $\text{LiNi}_{0.8}\text{Co}_{0.15}\text{Al}_{0.05}\text{O}_2$) at two different applied voltages according to [16]. While the energy barrier of the calendaric aged material decreases from 3.4 to 3.6 V during charge, the energy barrier of the fatigued materials stays constant

[16, 104]. With ongoing oxidation, the highly delithiated surface-near parts of the layered oxides are rearranged. Soft X-ray absorption studies have revealed that oxygen is oxidized simultaneously with nickel during charge (see Sect. 2.2.11) [16, 119, 134, 139]. The presence of pre-edges in the O K X-ray absorption spectra confirms 3d-O 2p interactions, and therefore a covalent character of the nickel-oxygen bond. Otherwise, excitations of electrons from the O K core level into O 2p states are not possible due to the full occupation of the O 2p states. These interactions are probably the reason for promoted oxygen release, once nickel-ions are structurally disordered and a NiO-like structure with divalent nickel is formed. This process is irreversible and the small nickel-ions in the lithium layers (0.69 Å for Ni^{2+} and 0.76 Å for Li^+ in octahedral coordination [140]) block the lithium diffusion pathways, which causes the observed impedance rise. Oxygen diffusion within semiconductors such as layered oxides is rather slow compared to lithium-ion conductivity, and thus oxygen is only evolved from surface-near parts of the particles [101, 141].

2.3 Capacity Loss in Full Cells

In the following section the influences of SEI formation and degradations of active material on the full-cell capacity are discussed. Changes in the lithium distribution during cycling play a crucial role in the performance drop of lithium-ion cells. The SEI formation in the initial cycle and the immobilization of active lithium is illustrated in Fig. 27. In the left part of the figures, the lithium distribution within a

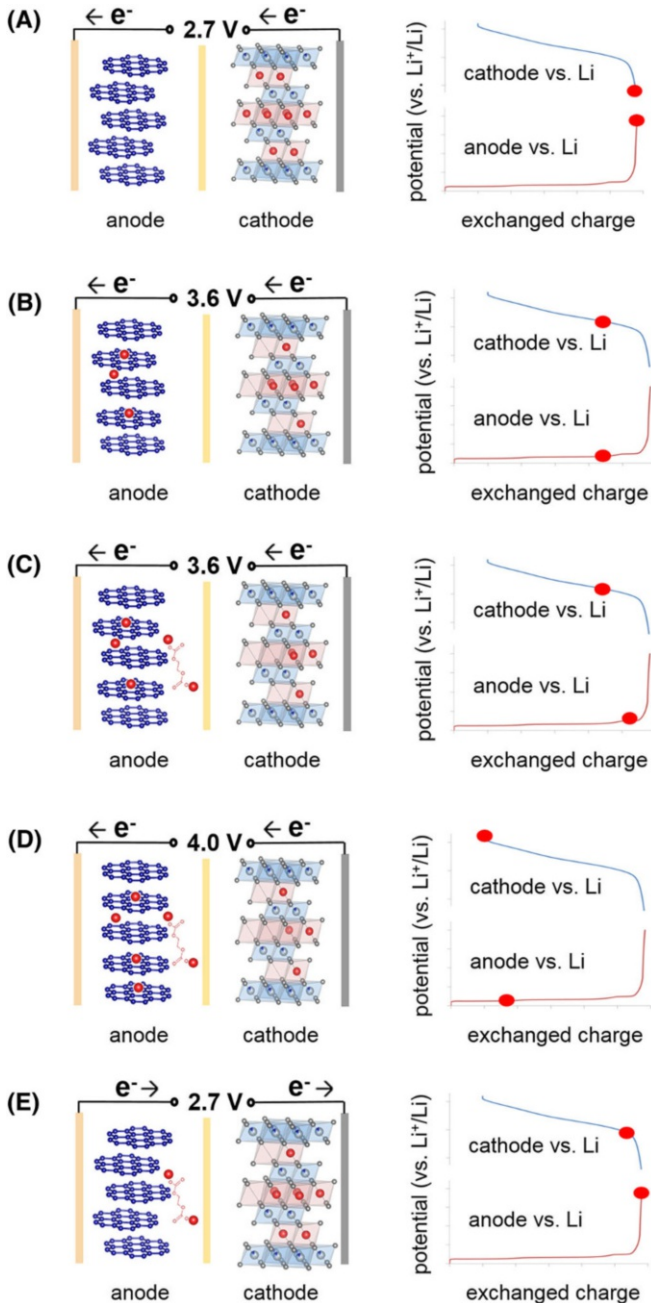


Fig. 27 First cycle of pristine LNCAO vs pristine graphite. The *left* parts of the pictures show the transfer of lithium between graphite and LNCAO. In the *right* parts, the potential curves of graphite and LNCAO are depicted. The *red circles* give the relative states-of-charge of the active materials. While the figures **a** till **d** show the first charging process, figure **e** illustrates the active lithium distribution after the first discharge process

full-cell is given for a distinct, applied voltage. In the right part of the figures, the potential curves of the individual electrodes are shown as measured against a reference electrode. The red points on the curves mark the states-of-charge of the cathode and the anode. Before cycling the materials all lithium is localized in the positive electrode. This means the cathode is fully lithiated and the anode is fully delithiated (Fig. 27a). In Fig. 28a the individual electrode potential curves (where blue is the positive electrode and red the negative) are shown. During charge lithium is deintercalated from the cathode and intercalated into the anode (Fig. 27b). However, at about 3.6 V (cathode vs anode) or 0.8 V graphite vs lithium, the electrolyte components are not stable and become reduced if they reach the anode surface (Fig. 27c) [5]. In order to ensure charge neutrality in the graphite, intercalated lithium ions diffuse to the outside of the particles and form immobilized

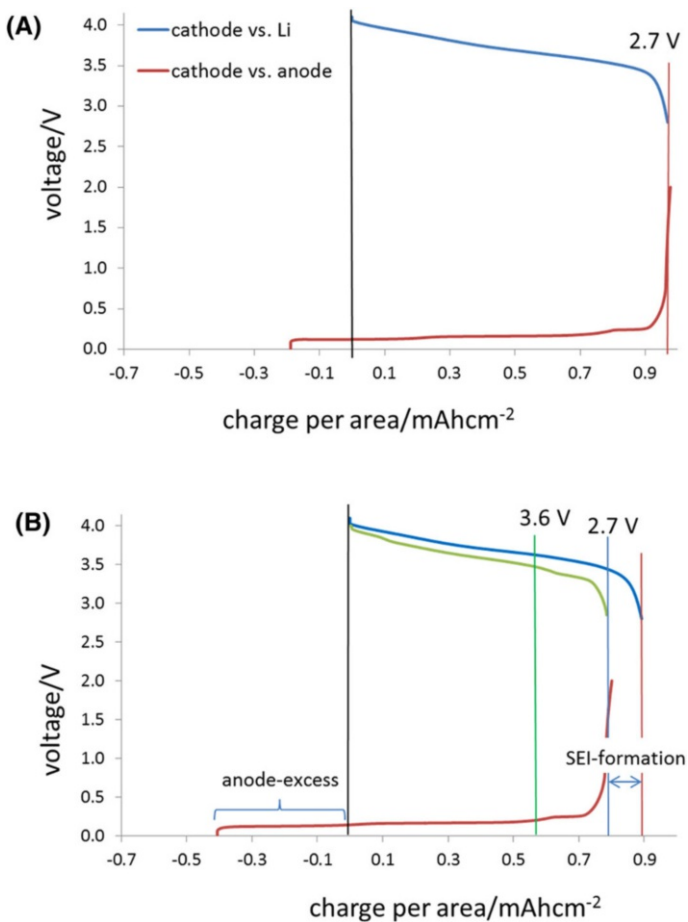


Fig. 28 Electrode potential and full-cell voltage curve before the SEI formation process (a). The relative positions of the electrode half-cell potential curves are chosen arbitrarily. The relative position of the potentials curves after the formation cycles are shown in b. The negative exchanged charge at the anode side is virtual and reflects the excess of anode capacity with respect to the cathode

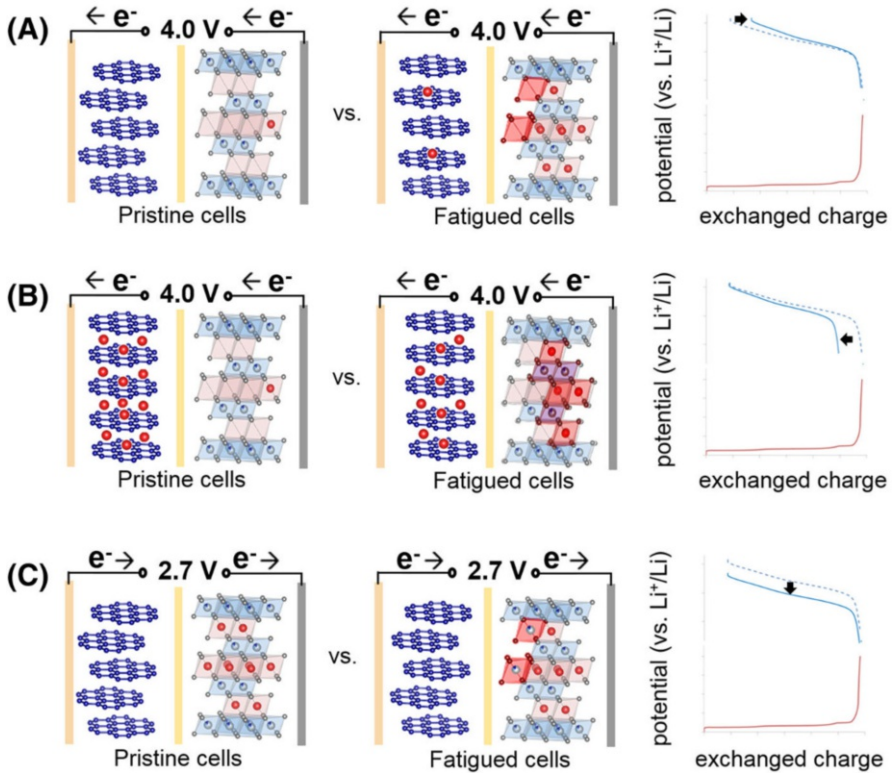


Fig. 29 Capacity losses of the cathode material can be observed if the amount of active lithium is reduced. Therefore, the cathode material can either not be fully charged (a) or discharged (b). It is also possible that both scenarios can be observed within one electrode. c shows voltage fade of the cathode material, which can also occur due to degradation

lithium salts with the electrolyte decomposition products. Therefore, the SoC of the graphite decreases while the SoC of the cathode remains constant (Fig. 27c, right diagram (red dots)). Shifting the potential curves relative to each other till the red dots lie on one vertical line leads to the new and real full-cell curve (cathode minus anode potential curve), which is illustrated in Fig. 28b. Figure 28a is somewhat virtual, because at voltages higher than 3.6 V (cathode versus anode) the SEI formation starts immediately and therefore the electrode potentials curves are shifted relative to each other. The capacity of the cathode (marked by the red line in Fig. 28b) subtracted by the capacity of the full cell (marked by the blue line at 2.7 V in Fig. 28b) gives the amount of former active lithium, which is consumed in the SEI-formation process and causes an irreversible capacity loss due to SEI formation. This shift in the potential curves remains during the following charge and discharge (Fig. 27d, e). At the end of discharge the anode is fully delithiated, but empty sites in the cathode are still present (Fig. 27e); the end of charge potential of the anode and the end of discharge potential of the cathode has increased while the full-cell

capacity has decreased. The shift of the voltage window means different potentials at the anode and cathode, in spite of the same cutoff-voltages on cell level. This can lead to operation conditions in which either the cathode or the anode is not stable anymore. Besides the initial SEI formation, cracks, self discharge reactions, dendrite formation and exfoliation can lead to additional lithium consumption (SEI formation) during normal operation as described in Sect. 2.2.4.

Besides SEI formation, capacity losses due to the degradation of the cathode material can also lead to changes in the relative distribution of active lithium in a full-cell, which is shown in Fig. 29. The capacity of a full-cell is commonly limited by the cathode material due to safety issues (Sect. 2.2.4), and therefore cathode degradations immediately affect the full cell capacity. Degradations of the cathode material lead to a compression of the respective potential curve, which is either compressed towards the positive charge direction (loss of empty lithium sites, Fig. 29a) or towards the negative charge direction (loss of lithiated lithium sites, Fig. 29b). Besides capacity losses, degradation of the cathode material can also lead to voltage fade, which is illustrated in Fig. 29c. The discharge curve of the cathode is thereby shifted downwards [16, 142]. As discussed for the SEI formation process, the relative changes of the potential curves of the electrodes change the cutoff voltages of the electrodes. This can lead to operation conditions at which at least one of the electrodes is not stable and therefore irreversible side reactions can take place or become more dominant.

High states of charge accelerate structural changes in the cathode material, e.g. layered oxides tend to release oxygen [15, 16]. High SoCs in combination with high temperatures accelerate manganese dissolution from spinel structures and manganese containing layered oxides [7, 129]. The shift of the graphite potential curve towards the negative charge direction as well as the compression of the cathode potential curve towards the positive charge direction lead to a higher end-of-charge potential at the cathode (and all degradation reactions occurring at high states of charge are accelerated), because the cutoff-criteria refer to the full cell voltage. The full cell voltage is the difference between the cathode and anode potentials and is specified by the cell supplier (normally not adapted to fatigue). In contrast, low states of charge accelerate manganese disproportionation, which is observed in Mn-containing spinels and also leads to manganese dissolution. The compression of the cathode potential curve towards the negative charge direction leads to a lower end-of-discharge potential at the cathode and to an increase of Mn^{3+} disproportionation reactions. The shift of the anode potential curve towards the negative charge direction leads to an increase of the potential in the delithiated state of graphite at the end of discharge. Therefore, graphite potentials for the intercalation of solvated lithium ions (1.5–0.8 V graphite vs lithium) might be reached and successive exfoliation might occur. If the anode potential is further shifted to higher potentials, copper dissolution can take place. This will lead to copper-dendrite formation and, further, to a short circuit in the cell.

2.4 Degradation as a Safety Risk

Since the market introduction of lithium-ion cells in 1991, accidents in which lithium-ion batteries spontaneously start to burn have been very rare. Nevertheless, some reports have attracted great attention. In this chapter the risk of such an accident, the so called “thermal runaway”, is discussed considering the degradation of lithium-ion cells and its effect upon operation. Regardless of whether the thermal runaway is caused by a short circuit, high currents/high voltages, overcharge or material degradations, all of these factors first lead to an overheating of the system and initiate highly exothermic decomposition reactions. Therefore, a crucial point considering the safety issue of a lithium-ion cell is the heat mitigation during operation. The temperature of a cell is determined by the amount of heat generated during operation and the amount of heat which is removed from the system at the same time. The heat generation rate proceeds in an exponential function while the heat removal rate can be described by a linear function, both shown in Fig. 30 [22, 23]. If the cell is cycled at low temperatures (point A on the heat generation line), more heat is produced than removed from the system till point B is reached. At this point, the heat generation and removal rate are equal and the system runs at a stable temperature. If the system is operated at point C (Fig. 30), more heat is removed than produced. Therefore, a thermal runaway is impossible. If the system is operated at point D, more heat is generated than removed, and therefore a continuous rise of the temperature is observed. At the end of this continuous increase a thermal runaway will take place.

The cycling efficiency (integral over the charge minus the integral over the discharge curve) usually decreases during operation. Layered oxides, especially,

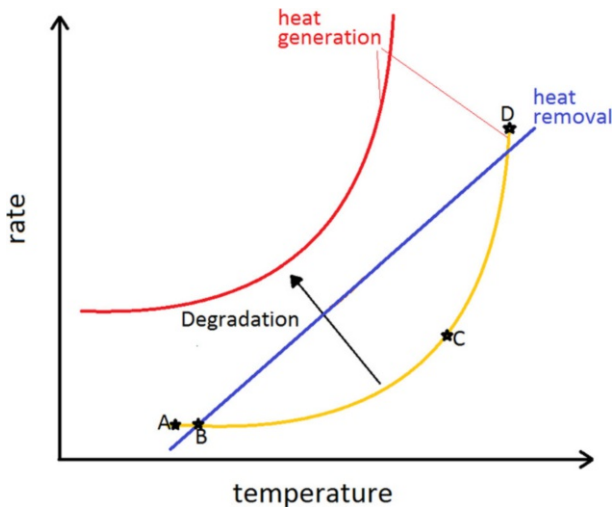
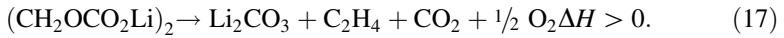
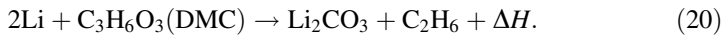
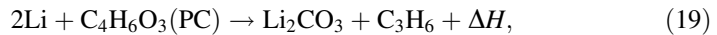
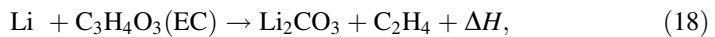


Fig. 30 Schematic illustration of heat generation and removal rates in a lithium-ion cell or battery in dependence on the temperature of the system and the state of health (SOH) [22]. During degradation, the cycling efficiency decreases and therefore the heat generation increases

show an increase of the impedance during cycling, mostly caused by changes in the surface morphology of the particles, therefore, the heat generation rate increases (Fig. 30, red curve). If the heat generation curve lies completely above the heat removal line, no stable operation point for the system exists. That is why the risk of overheating the system increases with increasing degradation. If once the system reaches a temperature above 90 °C, highly exothermic decomposition reactions of SEI-products start (Fig. 31). The decomposition of an ethylenecarbonate based SEI-product is given in Reaction (17).



In the absence of the protection layer, further electrolyte molecules reach the anode surface and decompose as well in exothermic reactions, Eq. (18–20).



All these decomposition reactions lead to the formation of flammable gases, although no fire is observed at this time due to the absence of oxygen. However, the pressure and the temperature continue to increase. The heat generated during this exothermic reaction depends on the amount of SEI products present, which increases during fatigue and aging of a lithium-ion cell. Therefore, the state of health of the battery is again a crucial point. If once the temperature increases above 120 °C, the separator (in most of the cases polypropylene, polyethylene, polypropylene) starts to melt. Without a separator a short circuit is created and the cathode material starts to decompose. The reactions (21–23) illustrate this breakdown for the case of LiCoO_2 [22].

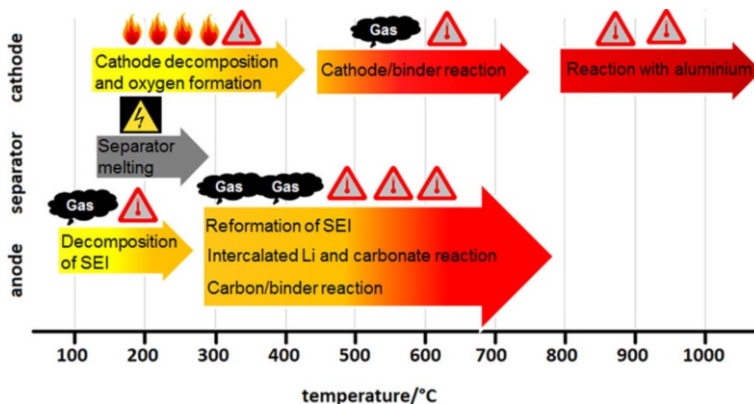
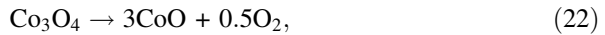
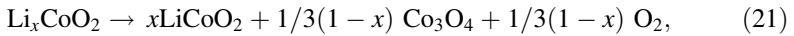


Fig. 31 Schematic representation of the proceeding of a thermal runaway in a lithium-ionlithium-ion cell in dependence on the temperature of the system [143]



During the structural breakdown of layered oxides or spinels, elementary oxygen is evolved and the cell starts to burn. With a further increase in temperature, binder decomposition reactions and aluminium (now melted) reactions take place.

3 Summary and Outlook

After a short introduction into the basic thermodynamics of lithium-ion cells, the most relevant degradation mechanisms of cell components were discussed. This included SEI formation, growth, aging and fatigue, structural changes of cathode materials upon cycling and fatigue of electrochemically inactive cell components such as the current collector, the binder and the separator. A relation between loss of active lithium and capacity losses on full-cell level were derived from the individual electrode potentials in dependence on the specific states of charge and health. Composition and structural changes in both surface-near regions and the bulk of cathode materials were considered with respect to an increase in the cell impedance and capacity losses. The importance of a solid knowledge about the underlying degradation mechanisms for the evaluation of safety risks was outlined. The increasing field of second life applications will trigger the need for even more sophisticated lifetime models with much more knowledge about fatigue and failure mechanisms in lithium-ion cells at their end-of-life. The individual cell designs and their effect on the homogeneous charge and discharge behavior of the cells will become highly relevant, which is already indicated by in operando studies. The optimization of lithium-ion batteries with respect to lifetime and cost efficiency will also depend on detailed information about the underlying degradation mechanisms. Much more work is needed to deduce such processes in more detail and to combine all information into suitable models to predict performance parameters in fresh, aged and fatigued cells under different operation conditions with a sufficient reliability.

References

1. Pillot C (2013) Li-ion battery material market review and forecasts 2012–2025. In: Avicenne energy, 3rd israeli power sources conference, May 29–30, 2013
2. Andre D, Kim S-J, Lamp P, Lux SF, Maglia F, Paschos O, Stiaszny B (2015) Future generations of cathode materials: an automotive industry perspective. *J Mater Chem A* 3:6709–6732
3. Kleiner K (2014) Chemical investigation of aging mechanisms in lithium-ion batteries; PhD thesis, Cuvillier Verlag Göttingen
4. Broussely M, Biensan P, Bonhomme F, Blanchard P, Herreyre S, Nechev K, Staniewicz RJJ (2005) Main aging mechanisms in Li Ion batteries. *J Power Sources* 146(1–2):90–96

5. Goodenough JB, Kim Y (2010) Challenges for rechargeable Li batteries. *Chem Mater* 22(3):587–603
6. Aurbach D, Zinigrad E, Cohen Y, Teller H (2002) A short review of failure mechanisms of lithium metal and lithiated graphite anodes in liquid electrolyte solutions. *Solid state ion* 148(3–4):405–416
7. Wohlfahrt-Mehrens M, Vogler C, Garche J (2004) Aging mechanisms of lithium cathode materials. *J Power Sources* 127:58–64
8. Vetter J, Novák P, Wagner MR, Veit C, Möller K-C, Besenhard JO, Winter M, Wohlfahrt-Mehrens M, Vogler C, Hammouche A (2005) Ageing mechanisms in lithium-ion batteries. *J Power Sources* 147(1–2):269–281
9. Arora P, White RE, Doyle M (1998) Capacity fade mechanisms and side reactions in lithium-ion batteries. *J Electrochem Soc* 145(10):3647–3667
10. Peled E (1979) The electrochemical behavior of alkali and alkaline earth metals in nonaqueous battery systems—the solid electrolyte interphase model. *J Electrochem Soc* 126(12):2047–2051
11. Xu K (2004) Nonaqueous liquid electrolytes for lithium-based rechargeable batteries. *Chem Rev* 104(10):4303–4417
12. Peled E, Bar Tow D, Merson A, Gladkikh A, Burstein L, Golodnitsky D (2001) Composition, Depth profiles and lateral distribution of materials in the SEI built on HOPG-TOF SIMS and XPS studies. *J Power Sources* 98:52–57
13. Aurbach D, Levi MD, Levi E, Schechter A (1997) Failure and stabilization mechanisms of graphite electrodes. *J Phys Chem B* 101(12):2195–2206
14. Aurbach D, Gofar Y, Ben-Zion M, Aped P (1992) The behaviour of lithium electrodes in propylene and ethylene carbonate: The major factors that influence Li cycling efficiency. *J Electroanal Chem* 339(1–2):451–471
15. Nazri G-A, Pistoia G (eds) (2003) *Lithium batteries-science and technology*. Springer, New York
16. Kleiner K, Melke J, Merz M, Jakes P, Nagel P, Schuppler S, Liebau V, Ehrenberg H (2015) Unraveling the degradation process of LiNi_{0.8}Co_{0.15}Al_{0.05}O₂ electrodes in commercial lithium ion batteries by electronic structure investigations. *ACS Appl Mater Interfaces* 7:19589–19600
17. Kojima Y, Muto S, Tatsumi K, Kondo H, Oka H, Horibuchi K, Ukyo Y (2011) Degradation analysis of a Ni-based layered positive-electrode active material cycled at elevated temperatures studied by scanning transmission electron microscopy and electron energy-loss spectroscopy. *J Power Sources* 196(18):7721–7727
18. Hausbrand R, Cherkashinin G, Ehrenberg H, Grötting M, Albe K, Jaegermann W (2015) Fundamental degradation mechanisms of layered oxide Li-Ion battery cathode materials: methodology, insights and novel approaches. *Mater Sci Eng B* 192:3–25
19. Laubach S, Laubach S, Schmidt PC, Ensling D, Schmid S, Jaegermann W, Thissen A, Nikolowski K, Ehrenberg H (2009) Changes in the crystal and electronic structure of LiCoO₂ and LiNiO₂ upon Li intercalation and de-intercalation. *Phys Chem Chem Phys* 11:3278–3289
20. Aoshima T, Okahara K, Kiyohara C, Shizuka K (2001) Mechanisms of manganese spinels dissolution and capacity fade at high temperature. *J Power Sources* 97–98:377–380
21. Kleiner K, Jackes P, Liebau V, Scharner S, Ehrenberg H (2016) Changes of the balancing between anode and cathode due to fatigue in commercial lithium-ion cells. *J Power Sources* 317:25–34
22. Wang Q, Ping P, Zhao X, Chu G, Sun J, Chen C (2012) Thermal runaway caused fire and explosion of lithium ion battery. *J Power Sources* 208:210–224
23. Hoesel M (1960) *Some problems in chemical kinetics and reactivity*, vol 1. Princeton University Press, Princeton
24. Xu K, Lam Y, Zhang SS, Jow TR, Curtis TB (2007) Solvation sheath of Li⁺ in nonaqueous electrolytes and its implication of graphite/electrolyte interface chemistry. *J Phys Chem C* 111(20):7411–7421
25. Xu K (2009) Whether EC and PC differ in interphasial chemistry on graphitic anode and how. *J Electrochem Soc* 156(9):A751
26. Aurbach D, Daroux ML, Faguy PW, Yeager E (1987) Identification of surface films formed on lithium in propylene carbonate solutions. *J Electrochem Soc* 134(7):1611–1620
27. Augustsson A, Herstedt M, Guo J-H, Edström K, Zhunag GV, Ross PN, Rubensson J-E, Nordgren J (2004) Solid electrolyte interphase on graphite Li-Ion battery anodes studied by soft X-ray spectroscopy. *Phys Chem Chem Phys* 6(16):4185–4189
28. Malmgren S, Rensmo H, Gustafsson T, Gorgoi M, Edström K (2010) Nondestructive depth profiling of the solid electrolyte interphase on LiFePO₄. *ECS Trans* 25(36):201–210

29. Li Z, Huang J, Yann Liaw B, Metzler V, Zhang J (2014) A review of lithium deposition in lithium-ion and lithium metal secondary batteries. *J Power Sources* 254:168–182
30. Agubra V, Fergus J (2013) Lithium ion battery anode aging mechanisms. *Materials* (Basel). 6(4):1310–1325
31. Koltypin M, Cohen YS, Markovsky B, Cohen Y, Aurbach D (2002) The study of lithium insertion-deinsertion processes into composite graphite electrodes by in situ atomic force microscopy (AFM). *Electrochem Commun* 4:17–23
32. Wagner MR, Albering JH, Moeller K-C, Besenhard JO, Winter M (2005) XRD evidence for the electrochemical formation of Li^+ (PC)yCn⁻ in PC-based electrolytes. *Electrochem Commun* 7(9):947–952
33. Aurbach D (1993) In situ FTIR spectroelectrochemical studies of surface films formed on Li and nonactive electrodes at low potentials in Li salt solutions containing CO[sub 2]. *J Electrochem Soc* 140(11):L155
34. Broussely M, Herreyre S, Biensan P, Kasztejna P, Nechev K, Staniewicz R (2001) Aging mechanism in Li Ion cells and calendar life predictions. *J Power Sources* 97–98:13–21
35. Verma P, Maire P, Novák P (2010) A review of the features and analyses of the solid electrolyte interphase in Li-Ion batteries. *Electrochim Acta* 55(22):6332–6341
36. Yazami R, Reynier Y (2002) Mechanism of self-discharge in graphite–lithium anode. *Electrochim Acta* 47(8):1217–1223
37. Utsunomiya T, Hatozaki O, Yoshimoto N, Egashira M, Morita M (2011) Self-discharge behavior and its temperature dependence of carbon electrodes in lithium-ion batteries. *J Power Sources* 196(20):8598–8603
38. Zhu Y, Wang C (2010) Galvanostatic intermittent titration technique for phase-transformation electrodes. *J Phys Chem C* 114(6):2830–2841
39. Sloop SE, Kerr JB, Kinoshita K (2003) The role of Li-Ion battery electrolyte reactivity in performance decline and self-discharge. *J Power Sources* 119–121:330–337
40. Sugiyama J, Mukai K, Ikedo Y, Nozaki H, Russo PL, Andreica D, Amato A, Ariyoshi K, Ohzuku T (2009) Static magnetic order on the triangular lattice in with. *Phys B Condens Matter* 404(5–7):663–666
41. Wang Y, Nakamura S, Tasaki K, Balbuena PB (2002) Theoretical studies to understand surface chemistry on carbon anodes for lithium-ion batteries: how does vinylene carbonate play its role as an electrolyte additive? *J Am Chem Soc* 124(16):4408–4421
42. Aurbach D (2003) Electrode–solution interactions in Li-ion batteries: a short summary and new insights. *J Power Sources* 119–121:497–503
43. Steiger J, Richter G, Wenk M, Kramer D, Mönig R (2015) Comparison of the growth of lithium filaments and dendrites under different conditions. *Electrochem Commun* 50:11–14
44. Orsini F, du Pasquier A, Beaudouin B, Tarascon JM, Trentin M, Langenhuizen N, de Beer E, Notten P (1999) In situ SEM study of the interfaces in plastic lithium cells. *J Power Sources* 81–82:918–921
45. Brissot C (1999) In situ concentration cartography in the neighborhood of dendrites growing in lithium/polymer-electrolyte/lithium cells. *J Electrochem Soc* 146(12):4393
46. Kleiner K, Comas-Vives A, Naderian M, Mueller JE, Fantauzzi D, Mesgar M, Keith JA, Anton J, Jacob T (2011) Multiscale modeling of Au-Island ripening on Au(100). *Adv Phys Chem* 2011:1–11
47. Steiger J, Kramer D, Mönig R (2014) Mechanisms of dendritic growth investigated by in situ light microscopy during electrodeposition and dissolution of lithium. *J Power Sources* 261:112–119
48. Steiger J, Kramer D, Mönig R (2014) Microscopic observations of the formation, growth and shrinkage of lithium moss during electrodeposition and dissolution. *Electrochim Acta* 136:529–536
49. Morigaki K, Ohta A (1998) Analysis of the surface of lithium in organic electrolyte by atomic force microscopy, fourier transform infrared spectroscopy and scanning auger electron microscopy. *J Power Sources* 76:159–166
50. Diggle JW, Despic AR, Bockris JO (1969) The mechanism of the dendritic electrocrystallization of zinc. *J Electrochem Soc* 116(11):1503
51. Yamaki J, Tobishima S, Hayashi K, Saito K, Nemoto Y, Arakawa MA (1998) Consideration of the morphology of electrochemically deposited lithium in an organic electrolyte. *J Power Sources* 74:219–227
52. Yamaki J-I, Tobishima S-I (2011) Rechargeable lithium anodes. In: Besenhard JO (ed) *Handbook of battery materials*, 2nd edn. Wiley-VCH Verlag GmbH & Co, Weinheim

53. Kim C-S, Jeong KM, Kim K, Yi C-W (2015) Effects of capacity ratios between anode and cathode on electrochemical properties for lithium polymer batteries. *Electrochim Acta* 155:431–436
54. Purushothaman BK, Landau U (2006) Rapid charging of lithium-ion batteries using pulsed currents a theoretical analysis. *J Electrochem Soc* 153:A533–A542
55. Jow RT, Xu K, Borodin O, Ue M (2014) Electrolytes for lithium and lithium-ion batteries, modern Asp. Springer, New York
56. Krueger S, Kloepsch R, Li J, Nowak S, Passerini S, Winter M (2013) How do reactions at the anode/electrolyte interface determine the cathode performance in lithium-ion batteries? *J Electrochem Soc* 160(4):A542–A548
57. Kawamura T, Okada S, Yamaki J (2006) Decomposition reaction of LiPF₆-based electrolytes for lithium ion cells. *J Power Sources* 156(2):547–554
58. Sloop SE, Pugh JK, Wang S, Kerr JB, Kinoshita K (2001) Chemical reactivity of PF₅ and LiPF₆ in ethylene carbonate/dimethyl carbonate solutions. *Electrochem Solid State Lett* 4(4):A42
59. Campion CL, Li W, Lucht BL (2005) Thermal decomposition of LiPF₆-based electrolytes for lithium-ion batteries. *J Electrochem Soc* 152(12):A2327
60. Zhang SS (2007) A review on the separators of liquid electrolyte li-ion batteries. *J Power Sources* 164:351–364
61. Baginska M, Blaiszik BJ, Merriman RJ, Sottos NR, Moore JS, White SR (2012) Autonomic shutdown of lithium-ion batteries using thermoresponsive microspheres. *Adv Energy Mater* 2:583–590
62. Love CT (2011) Thermomechanical analysis and durability of commercial micro-porous polymer Li-Ion battery separators. *J Power Sources* 196(5):2905–2912
63. Norin L, Kostecki R, McLarnon F (2002) Study of membrane degradation in high-power lithium-ion cells. *Electrochem Solid State Lett* 5:A67
64. Gallus DR, Schmitz R, Wagner R, Hoffmann B, Nowak S, Cekic-Laskovic I, Schmitz RW, Winter M (2014) The influence of different conducting salts on the metal dissolution and capacity fading of NCM cathode material. *Electrochim Acta* 134:393–398
65. Zheng H, Sun Q, Liu G, Song X, Battaglia VS (2012) Correlation between dissolution behavior and electrochemical cycling performance for LiNi_{1/3}Co_{1/3}Mn_{1/3}O₂-based cells. *J Power Sources* 207:134–140
66. Hunter JC (1981) Preparation of a new crystal form of manganese dioxide: λ -MnO₂. *J Solid State Chem* 39:142–147
67. Jang DH, Shin YJ, Oh SM (1996) Dissolution of spinel oxides and capacity losses in 4 V. *J Electrochem Soc* 143(7):2204–2211
68. Aurbach D, Levi MD, Gamulski K, Markovsky B, Salitra G, Levi E, Heider U, Heider L, Oesten R (1999) Capacity fading of Li₁Mn₂O₄ spinel electrodes studied by XRD and electroanalytical techniques. *J Power Sources* 81–82:472–479
69. Yang K, Fan L-Z, Guo J, Qu X (2012) Significant improvement of electrochemical properties of AlF₃-coated LiNi_{0.5}Co_{0.2}Mn_{0.3}O₂ cathode materials. *Electrochim Acta* 63:363–368
70. Li GR, Feng X, Ding Y, Ye SH, Gao XP (2012) AlF₃-coated Li(Li_{0.17}Ni_{0.25}Mn_{0.58})O₂ as cathode material for Li-Ion batteries. *Electrochim Acta* 78:308–315
71. Lee SH, Koo BK, Kim J-C, Kim KM (2008) Effect of Co₃(PO₄)₂ coating on Li[Co_{0.1}Ni_{0.15}Li_{0.2}Mn_{0.55}]O₂ cathode material for lithium rechargeable batteries. *J Power Sources* 184:276–283
72. Chen Z, Qin Y, Amine K, Sun Y-K (2010) Role of surface coating on cathode materials for lithium-ion batteries. *J Mater Chem* 20:7606
73. Martha SK, Sclar H, Szmuk Framowitz Z, Kovacheva D, Saliyski N, Gofer Y, Sharon P, Golik E, Markovsky B, Aurbach D (2009) A comparative study of electrodes comprising nanometric and submicron particles of LiNi_{0.50}Mn_{0.50}O₂, LiNi_{0.33}Mn_{0.33}Co_{0.33}O₂, and LiNi_{0.40}Mn_{0.40}Co_{0.20}O₂ layered compounds. *J Power Sources* 189:248–255
74. Jansen A, Kahaian A, Kepler K, Nelson P, Amine K, Dees D, Vissers D, Thackeray M (1999) Development of a high-power lithium-ion battery. *J Power Sources* 81–82:902–905
75. Li J, Lewis RB, Dahn JR (2007) Sodium carboxymethyl cellulose. *Electrochem Solid State Lett* 10(2):A17
76. Zhang WJ (2011) A Review of the electrochemical performance of alloy anodes for lithium-ion batteries. *J Power Sources* 196(1):13–24

77. Buqa H, Holzapfel M, Krumeich F, Veit C, Novák P (2006) Study of styrene butadiene rubber and sodium methyl cellulose as binder for negative electrodes in lithium-ion batteries. *J Power Sources* 161:617–622
78. Hochgatterer NS, Schweiger MR, Koller S, Raimann PR, Wöhrle T, Wurm C, Winter M (2008) Silicon/graphite composite electrodes for high-capacity anodes: influence of binder chemistry on cycling stability. *Electrochem Solid-State Lett* 11(5):A76
79. Xu J, Chou S-L, Gu Q, Liu H-K, Dou S-X (2013) The effect of different binders on electrochemical properties of $\text{LiNi}_{1/3}\text{Mn}_{1/3}\text{Co}_{1/3}\text{O}_2$ cathode material in lithium ion batteries. *J Power Sources* 225:172–178
80. Manickam M, Takata M (2003) Effect of cathode binder on capacity retention and cycle life in transition metal phosphate of a rechargeable lithium battery. *Electrochim Acta* 48(8):957–963
81. Chen Z, Chevrier V, Christensen L, Dahn JR (2004) Design of amorphous alloy electrodes for Li-Ion batteries. *Electrochem Solid State Lett* 7(10):A310
82. Liu W-R, Yang M-H, Wu H-C, Chiao SM, Wu N-L (2005) Enhanced cycle life of Si anode for Li-Ion batteries by using modified elastomeric binder. *Electrochem Solid State Lett* 8(2):A100
83. Markevich E, Salitra G, Aurbach D (2005) Influence of the PVdF binder on the stability of LiCoO_2 electrodes. *Electrochem Commun* 7(12):1298–1304
84. Aurbach D, Markovsky B, Salitra G, Markevich E, Talyossef Y, Koltypin M, Nazar L, Ellis B, Kovacheva D (2007) Review on electrode–electrolyte solution interactions, related to cathode materials for Li-Ion batteries. *J Power Sources* 165:491–499
85. Lee J-H, Paik U, Hackley VA, Choi Y-M (2005) Effect of carboxymethyl cellulose on aqueous processing of natural graphite negative electrodes and their electrochemical performance for lithium batteries. *J Electrochem Soc* 152(9):A1763
86. Choi Y-M, Paik U, Kim K-H (2003) Application No. P2003-0040085
87. Spotnitz R, Franklin J (2003) Abuse behavior of high-power, lithium-ion cells. *J Power Sources* 113:81–100
88. Li G (1996) The influence of polytetrafluorethylene reduction on the capacity loss of the carbon anode for lithium ion batteries. *Solid State Ion* 90:221–225
89. Maleki H, Deng G, Kerzhner-Haller I (2000) Thermal stability studies of binder materials in anodes for lithium ion batteries. *J Electrochem Soc* 147(12):4470–4475
90. Buqa H, Goers D, Spahr ME, Novak P (2003) The influence of graphite surface modification on the exfoliation during electrochemical lithium insertion. *J Solid State Electrochem* 8(1):79–80
91. Zackrisson M, Avellan L, Orlenius J (2010) Life cycle assessment of lithium-ion batteries for plug-in hybrid electric vehicles-critical issues. *J Clean Prod* 18(15):1517–1527
92. Kim GT, Jeong SS, Joost M, Rocca E, Winter M, Passerini S, Balducci A (2011) Use of natural binders and ionic liquid electrolytes for greener and safer lithium-ion batteries. *J Power Sources* 196(4):2187–2194
93. Saeki S, Lee J, Zhang Q, Saito F (2004) Co-Grinding LiCoO_2 with PVC and water leaching of metal chlorides formed in ground product. *Int J Miner Process* 74:S373–S378
94. Li C-C, Lee J-T, Tung Y-L, Yang C-R (2007) Effects of pH on the dispersion and cell performance of LiCoO_2 cathodes based on the aqueous process. *J Mater Sci* 42(14):5773–5777
95. Chou S-L, Pan Y, Wang J-Z, Liu H-K, Dou S-X (2014) Small things make a big difference: binder effects on the performance of Li and Na batteries. *Phys Chem Chem Phys* 16(38):20347–20359
96. Guerfi A, Kaneko M, Petitclerc M, Mori M, Zaghbi K (2007) LiFePO_4 water-soluble binder electrode for li-ion batteries. *J Power Sources* 163(2):1047–1052
97. Porcher W, Lestriez B, Jouanneau S, Guyomard D (2009) Design of aqueous processed thick LiFePO_4 composite electrodes for high-energy lithium battery. *J Electrochem Soc* 156(3):A133
98. Li J, Murphy E, Winnick J, Kohl PA (2001) Studies on the cycle life of commercial lithium ion batteries during rapid charge-discharge cycling. *J Power Sources* 102:294–301
99. Chen D, Indris S, Schulz M, Gamer B, Mönig R (2011) In situ scanning electron microscopy on lithium-ion battery electrodes using an ionic liquid. *J Power Sources* 196(15):6382–6387
100. Kızıldağ-Yavuz N, Herklotz M, Hashem AM, Abuzeid HM, Schwarz B, Ehrenberg H, Mauger A, Julien CM (2013) Synthesis, structural, magnetic and electrochemical properties of $\text{LiNi}_{1/3}\text{Mn}_{1/3}\text{Co}_{1/3}\text{O}_2$ Prepared by a sol–gel method using table sugar as chelating agent. *Electrochim Acta* 113:313–321
101. Park M, Zhang X, Chung M, Less GB, Sastry AM (2010) A review of conduction phenomena in Li-Ion batteries. *J Power Sources* 195(24):7904–7929

102. Amin R, Ravnsbæk DB, Chiang Y-M (2015) Characterization of electronic and ionic transport in $\text{Li}_{1-x}\text{Ni}_{0.8}\text{Co}_{0.15}\text{Al}_{0.05}\text{O}_2$ (NCA). *J Electrochem Soc* 162(7):A1163–A1169
103. Nobili F, Croce F, Scrosati B, Marassi R (2001) Electronic and electrochemical properties of $\text{Li}_x\text{Ni}_{1-y}\text{Co}_y\text{O}_2$ cathodes studied by impedance spectroscopy. *Chem Mater* 13:1642–1646
104. Kleiner K, Dixon D, Jakes P, Melke J, Murat Y, Roth C, Nikolowski K, Liebau V, Ehrenberg H (2015) Fatigue of $\text{LiNi}_{0.8}\text{Co}_{0.15}\text{Al}_{0.05}\text{O}_2$ in commercial Li ion batteries. *J Power Sources* 273:70–82
105. Xiao J, Yu X, Zheng J, Zhou Y, Gao F, Chen X, Bai J, Yang XQ, Zhang JG (2013) Interplay between two-phase and solid solution reactions in high voltage spinel cathode material for lithium ion batteries. *J Power Sources* 242:736–741
106. Senyshyn A, Mühlbauer MJ, Nikolowski K, Pirling T, Ehrenberg H (2012) “In-operando” neutron scattering studies on Li-Ion batteries. *J Power Sources* 203:126–129
107. Padhi A, Nanjundaswamy K, Goodenough J (1997) Phospho-Olivines as positive-electrode materials for rechargeable lithium batteries. *J Electrochem Soc* 144:1188–1194
108. Brunetti G, Robert D, Bayle-Guillemaud P, Rouvière JL, Rauch EF, Martin JF, Colin JF, Bertin F, Cayron C (2011) Confirmation of the Domino-Cascade model by $\text{LiFePO}_4/\text{FePO}_4$ precession electron diffraction. *Chem Mater* 23:4515–4524
109. Manthiram A, Sivaramkrishnan V (2001) Chemical and structural instabilities of LiCoO_2 cathodes at deep lithium extraction. Materials science and engineering program, ETC 9.104, Austin
110. Arunkumar TA, Alvarez E, Manthiram A (2008) Chemical and structural instability of the chemically delithiated (1–Z) $\text{Li Li}_{1/3}\text{Mn}_{2/3}$ O-2 center dot(z) $\text{Li Co}_{1-y}\text{Ni}_y$ O-2 ($0 \leq Y \leq 1$ and $0 \leq Z \leq 1$) Solid Solution Cathodes. *J Mater Chem* 18:190–198
111. Reimers JN, Dahn JR (1992) Electrochemical and in situ X-ray diffraction studies of lithium intercalation in Li_xCoO_2 . *J Electroanal Chem* 139(8):2–8
112. Ohzuku T, Ueda A, Nagayama M (1993) electrochemistry and structural chemistry of LiNiO_2 (R3 m) for 4 volt secondary lithium cells. *J Electrochem Soc* 140(7):1862–1870
113. Ohzuku T, Ueda A, Kouguchi M (1995) Synthesis and characterization of $\text{LiAl}_{1/4}\text{Ni}_{3/4}\text{O}_2$ (R-3m) for lithium-ion (shuttlecock) batteries. *J Electrochem Soc* 142(12):4033–4039
114. Choi S, Manthiram A (2002) Factors influencing the layered to spinel-like phase transition in layered oxide cathodes. *J Electrochem Soc* 149:A1157
115. Kang S (2002) Layered $\text{Li}(\text{Ni}_{0.5-x}\text{Mn}_{0.5-x}\text{M}_2x)\text{O}_2$ ($M' = \text{Co}, \text{Al}, \text{Ti}; x = 0, 0.025$) cathode materials for Li-Ion rechargeable batteries. *J Power Sources* 112(1):41–48
116. Jiang M, Key B, Meng YS, Grey CP (2009) Electrochemical and structural study of the layered, “Li-excess” lithium-ion battery electrode material $\text{Li}[\text{Li}_{1/9}\text{Ni}_{1/3}\text{Mn}_{5/9}]\text{O}_2$. *Chem Mater* 21(13):2733–2745
117. Hong J, Gwon H, Jung S-K, Ku K, Kang K (2015) Review—lithium-excess layered cathodes for lithium rechargeable batteries. *J Electrochem Soc* 162(14):A2447–A2467
118. Chebiam RV, Prado F, Manthiram A (2001) Soft chemistry synthesis and characterization of layered $\text{Li}_{1-x}\text{Ni}_{1-y}\text{Co}_y\text{O}_{2-\delta}$ ($0 \leq x \leq 1$ and $0 \leq y \leq 1$). *Chem Mater* 5:2951–2957
119. Yoon W-S, Chung KY, McBreen J, Fischer DA, Yang X-Q (2007) electronic structural changes of the electrochemically Li-Ion Deintercalated $\text{LiNi}_{0.8}\text{Co}_{0.15}\text{Al}_{0.05}\text{O}_2$ cathode material investigated by X-ray absorption spectroscopy. *J Power Sources* 174(2):1015–1020
120. Montoro L, Abbate M, Almeida E, Rosolen J (1999) Electronic structure of the transition metal ions in LiCoO_2 , LiNiO_2 and $\text{LiCo}_{0.5}\text{Ni}_{0.5}\text{O}_2$. *Chem Phys Lett* 309(1–2):14–18
121. Senyshyn A, Dolotko O, Mühlbauer MJ, Nikolowski K, Fuess H, Ehrenberg H (2013) Lithium intercalation into graphitic carbons revisited: experimental evidence for twisted bilayer behavior. *J Electrochem Soc* 160(5):A3198–A3205
122. Levi MD, Wang C, Markevich E, Aurbach D, Chvoj Z (2003) Noteworthy electroanalytical features of the stage 4 to stage 3 phase transition in lithiated graphite. *J Solid State Electrochem* 8(1):40–43
123. Ohzuku T, Kitagawa M, Hitai T (1990) Electrochemistry of manganese dioxide in lithium non-aqueous Cell II. X-ray diffractonal and electrochemical characterization on deep discharge products of electrolytic manganese dioxide. *J Electrochem Soc* 137(3):40–46
124. Shao-horn Y, Hackney SA, Kahaian AJ, Kepler KD, Skinner E, Vaughan JT, Thackeray MM (1999) Structural fatigue in spinel electrodes in Li R Li X W Mn 2 X O 4 cells. *J Power Sources* 81–82:496–499
125. Aurbach D, Levi M, Gamulski K, Markovsky B, Salitra G, Levi E, Heider U, Heider L, Oesten R (1999) Capacity fading of $\text{Li}_x\text{Mn}_2\text{O}_4$ spinel electrodes studied by XRD and electroanalytical techniques. *J Power Sources* 81–82:472–479

126. Chung KY, Kim KB (2004) Investigations into capacity fading as a result of a Jahn-Teller distortion in 4 V LiMn_2O_4 thin film electrodes. *Electrochim Acta* 49:3327–3337
127. Ikeno H, de Groot FMF, Stavitski E, Tanaka I (2009) Multiplet calculations of L(2,3) X-Ray absorption near-edge structures for 3d transition-metal compounds. *J Phys Condens Matter* 21(10):104208
128. Tran N, Croguennec L, Menetrier M, Weill F, Biensan P, Jordy C, Delmas C (2008) Mechanisms associated with the “Plateau” observed at high voltage for the overlithiated $\text{Li-1.12}(\text{Ni}_{0.425}\text{Mn}_{0.425}\text{Co}_{0.15})\text{O}_2$ system. *Chem Mater* 20(6):4815–4825
129. Wohlfahrt-Mehrens M, Butz A, Oesten R, Arnold G, Hemmer RP, Huggins RA (1997) The influence of doping on the operation of lithium manganese oxide spinel. *J Power Sources* 68(2):582–585
130. Guao Y, Dahn JR (1996) Synthesis and characterization of $\text{Li}_1 + \text{Mn}_2\text{O}_4$ for Li-Ion battery applications. *J Electrochem Soc* 143(1):100–114
131. Rozier P, Tarascon JM (2015) Review—Li-Rich layered oxide cathodes for next-generation Li-Ion batteries: chances and challenges. *J Electrochem Soc* 162(14):A2490–A2499
132. Montoro LA, Rosolen JM (2004) The role of structural and electronic alterations on the lithium diffusion in $\text{Li}_x\text{Co}_{0.5}\text{Ni}_{0.5}\text{O}_2$. *Electrochim Acta* 49(19):3243–3249
133. Yoon W, Kim K, Kim M, Lee M, Shin H, Lee J, Lee J (2002) Oxygen contribution on Li-Ion intercalation—deintercalation in LiCoO_2 investigated by O K-edge and Co L-edge X-ray absorption spectroscopy. *J Phys Chem B* 106:2526–2532
134. Kobayashi H, Arachi Y, Emura S, Tatsumi K (2007) Investigation on lithium de-intercalation mechanism for $\text{LiNi}_{0.45}\text{Mn}_{0.45}\text{Al}_{0.1}\text{O}_2$. *Solid State Ion* 178:1101–1105
135. Van der Ven A, Ceder G (2000) Lithium diffusion mechanisms in layered intercalation compounds. *J Power Sources* 97–98:529–531
136. Moses AW, Flores HGG, Kim J-G, Langell MA (2007) Surface properties of LiCoO_2 , LiNiO_2 and $\text{LiNi}_{1-x}\text{Co}_x\text{O}_2$. *Appl Surf Sci* 253:4782–4791
137. Han CJ, Yoon JH, Cho WL, Jang H (2004) Electrochemical properties of $\text{LiNi}_{0.8}\text{Co}_{0.2-x}\text{Al}_x\text{O}_2$ prepared by a sol-gel method. *J Power Sources* 136(1):132–138
138. Yang XQ, Sun X, McBreen J (1999) New findings on the phase transitions in $\text{Li}_{1-x}\text{NiO}_2$: in situ synchrotron X-ray diffraction studies. *Electrochem Commun* 1(6):227–232
139. Saito Y, Shikano M, Kobayashi H (2011) State of charge (SOC) dependence of lithium carbonate on $\text{LiNi}_{0.8}\text{Co}_{0.15}\text{Al}_{0.05}\text{O}_2$ electrode for lithium-ion batteries. *J Power Sources* 196(16):6889–6892
140. Shannon RD (1976) Revised effective ionic radii and systematic studies of interatomic distances in halides and chalcogenides. *Acta Cryst* A32:751–767
141. Maier J (ed) (2000) *Festkörper-Fehler Und Funktion*. Teubner Studienbücher, Leipzig
142. Amalraj F, Talianker M, Markovsky B, Sharon D, Burlaka L, Shafir G, Zinigrad E, Haik O, Aurbach D, Lampert J, Schulz-Dobrick M, Garsuch A (2012) Study of the lithium-rich integrated compound ${}_x\text{Li}_2\text{MnO}_3(1-x)\text{LiMO}_2$ (X around 0.5; $M = \text{Mn, Ni, Co}$; 2:2:1) and its electrochemical activity as positive electrode in lithium cells. *J Electrochem Soc* 160(2):A324–A337
143. Chanson C, Wiaux J-P (2013) Safety of lithium-ion batteries. The European Association for advanced rechargeable batteries. Belgium, Brussels, p 25